# Re-inforcing nano-particle integration into metal AM and produced part characterisation

By

André Mussatto

B.Eng, M.Eng

A thesis submitted in fulfilment of the requirements for the degree of

Doctor of Philosophy (PhD)

from

Dublin City University

School of Mechanical and Manufacturing Engineering

Supervisors

Prof. Dermot Brabazon

Dr. Yan Delauré

Prof. Greg Hughes

May 2022

## Declaration

I hereby certify that this material, which I now submit for assessment on the programme of study leading to the award of PhD is entirely my own work, that I have exercised reasonable care to ensure that the work is original, and does not to the best of my knowledge breach any law of copyright, and has not been taken from the work of others save and to the extent that such work has been cited and acknowledged within the text of my work.

Signed: Andre Mussatto ID No.: 12707669 Date: 25-04-2022

## Acknowledgements

Firstly, I would like to acknowledge the help, support and encouragement that I received from my supervisors Prof. Dermot Brabazon, Dr. Yan Delauré and Prof. Greg Hughes.

I would like to thank my research colleagues, who I had the pleasure to work alongside with, for passing on their knowledge and for providing valuable scientific input and support.

Thanks also to the staff in the school of Mechanical and Manufacturing Engineering, Nano Research Facility and Research Project Administration.

I would like to thank Dr. Ronan Mac Loughlin from Aerogen Galway for his contribution and support to the nebulising project.

I would like also to acknowledge Science Foundation Ireland for the financial support of this project.

Finally, my sincere thanks to my family and friends for their motivation and encouragement. I dedicate this work to them.

# Table of Contents

## List of Figures

## List of Tables

## List of Publications

1. Mussatto, A., Ahad, I. U., Mousavian, R. T., Delaure, Y., and Brabazon, D., 2020, **"Advanced Production Routes for Metal Matrix Composites,"** Engineering Reports, e12330. https://doi.org/10.1002/eng2.12330

2. Mussatto, A., Groarke, R., A-Hameed, A., Ahad, I. U. I., Vijayaraghavan, R. K., O'Neill, A., McNally, P., Delaure, Y., and Brabazon, D., 2019, **"Evaluation via Powder Metallurgy of Nano-Reinforced Iron Powders Developed for Selective Laser Melting Applications,"** Materials & Design, 182, 108046. https://doi.org/10.1016/j.matdes.2019.108046

3. Mussatto, A., Groarke, R., O'Neill, A., Obeidi, M. A., Delaure, Y., and Brabazon, D., 2021, "**Influences of Powder Morphology and Spreading Parameters on the Powder Bed Topography Uniformity in Powder Bed Fusion Metal Additive Manufacturing,"** Additive Manufacturing, 38, 101807. https://doi.org/10.1016/j.addma.2020.101807

4. Mussatto, A., Groarke, R., Vijayaraghavan, R. K., Hughes, C., Obeidi, M. A., Doğu, M. N., Yalçin, M. A., McNally, P. J., Delaure, Y., and Brabazon, D., 2022, **"Assessing Dependency of Part Properties on the Printing Location in Laser-Powder Bed Fusion Metal Additive Manufacturing,"** Materials Today Communications, 30, 103209. https://doi.org/10.1016/j.mtcomm.2022.103209

5. Mussatto, A., Groarke, R., Vijayaraghavan, R. K., Obeidi, M. A., McNally, P. J., Nicolosi, V., Delaure, Y., and Brabazon, D., **"Laser-powder bed fusion of silicon carbide reinforced 316L stainless steel using a sinusoidal laser scanning strategy",** Journal of Materials Research and Technology, 18, pp. 2672-2698. https://doi.org/10.1016/j.jmrt.2022.03.170

6. Mussatto, A., Groarke, R., Vijayaraghavan, R. K., Obeidi, M. A., MacLoughlin, R., McNally, P. J., Nicolosi, V., Delaure, Y., and Brabazon, D., 2022, **"Laser-Powder Bed Fusion in-Process Dispersion of Reinforcing Ceramic Nanoparticles onto Powder Beds via Colloid Nebulisation,"** Materials Chemistry and Physics, 126245. https://doi.org/10.1016/j.matchemphys.2022.126245

7. Obeidi, M. A., Mussatto, A., Groarke, R., Vijayaraghavan, R. K., Conway, A., Rossi Kaschel, F., McCarthy, E., Clarkin, O., O'Connor, R., and Brabazon, D., 2020, "**Comprehensive Assessment of Spatter Material Generated during Selective Laser Melting of Stainless Steel,**" Materials Today Communications, 25, 101294. https://doi.org/10.1016/j.mtcomm.2020.101294

8. Obeidi, M. A., Mussatto, A., Dogu, M. N., Sreenilayam, S. P., McCarthy, E., Ahad, I. U., Keaveney, S., and Brabazon, D., 2022, **"Laser Surface Polishing of Ti-6Al-4V Parts Manufactured by Laser Powder Bed Fusion,"** Surface and Coatings Technology, 128179. https://doi.org/10.1016/j.surfcoat.2022.128179

9. Groarke, R., Danilenkoff, C., Karam, S., McCarthy, E., Michel, B., Mussatto, A., Sloane, J., O' Neill, A., Raghavendra, R., and Brabazon, D., 2020, "**316L Stainless Steel Powders for Additive Manufacturing: Relationships of Powder Rheology, Size, Size Distribution to Part Properties,"** Materials, 13(23), 5537. https://doi.org/10.3390/ma13235537

10. Gorji, N. E., O'Connor, R., Mussatto, A., Snelgrove, M., González, P. G. M., and Brabazon, D., 2019, "**Recyclability of Stainless Steel (316 L) Powder within the Additive Manufacturing Process,**" Materialia, 8, 100489. https://doi.org/10.1016/j.mtla.2019.100489

11. Liu, J., Silveira, J., Groarke, R., Parab, S., Singh, H., McCarthy, E., Karazi, S., Mussatto, A., Houghtaling, J., Ahad, I. U., Naher, S., and Brabazon, D., 2019, "**Effect of Powder Metallurgy Synthesis Parameters for Pure Aluminium on Resultant Mechanical Properties**," International Journal of Material Forming, 12(1), pp. 79–87. https://doi.org/10.1007/s12289-018-1408-5

## List of Oral Presentations

1. Mussatto, A., Brabazon, D., "**Re-inforcing nano-particle integration into metal AM and produced part characterisation**" 2nd International Symposium on Small-scale Intelligent Manufacturing Systems, Cavan, Ireland, April 2018.
2. Mussatto, A., Brabazon, D., "**Advanced production routes for metal matrix composites**", 21st International Conference on Advances in Materials & Processing Technologies, Dublin, Ireland, September 2018.
3. Mussatto, A., Brabazon, D., "**Metal matrix composites: Processing and challenges**", I-Form Gathering, virtual event, November 2020.

## List of Poster Presentations

1. Mussatto, A., Brabazon, D., **"Go with the flow - The ideal rheological characteristics of powders for powder bed based metal 3D printing**", Irish Postgraduate Research Conference, Dublin, Ireland, November 2018. *Awarded runner-up prize for poster presentation.*

2. Mussatto, A., Freeland, B., Brabazon, D., "**Morphological characteristics of silicon carbide nanostructures synthesised via pulsed laser ablation in deionised water**", I-Form Industry Partner Event, University College Dublin, Dublin, Ireland, December 2019.

3. Mussatto, A., **"Diatoms**", Expose Your Research photography competition, Dublin City University, Dublin, Ireland, October 2018.

4. Groarke R., Chekotu J C., Obeidi, M. A., Mussatto A., O'Toole K., Brabazon D., "**Additive manufacturing of nitinol heat exchanger**", I-Form Industry Partner Event, University College Dublin, Dublin, Ireland, December 2019.

# Abstract

**André Mussatto**

**Re-inforcing nano-particle integration into metal AM and produced part characterisation**

Metal matrix composites (MMCs) are an important class of materials replacing monolithic alloys in applications where high specific strength and temperature and wear resistance are critical. However, the ductility of the matrix is very often negatively affected by the presence of the harder reinforcing phase and the existing production routes can be of high cost or difficult to implement either due to complex part design or the requirement for specialised equipment. Recently, the additive manufacturing technique known as laser-powder bed fusion (L-PBF) has proved a promising method for manufacturing MMCs as it promises to suppress several of the existing challenges concerning MMC production.

The focus of this thesis is on the fabrication and characterisation of stainless steel 316L nanometre-scale silicon carbide and tungsten carbide reinforced MMCs, in an attempt to bring understanding and solutions to current issues concerning MMCs production and their integrity. Firstly, two aspects of L-PBF currently lacking in knowledge and that have implications on MMCs integrity were studied: assessment of part-properties dependency of on the printing location across the build platform in L-PBF, and identification of influencing factors and assessment of the optimal powder spreading conditions within the L-PBF system. Secondly a feedstock powder for L-PBF of MMCs, driven by the requirements of a homogeneous mixture and improve powder rheology, was developed and tested using the simple and cost effective route of powder metallurgy. Thirdly, the developed powder and the optimised parameters in the L-PBF of MMCs were examined. Lastly, a commercial L-PBF system was implemented to work with a colloid form of feedstock material, as well as powdered form, during the manufacturing of MMCs. Several relevant material characterisation techniques were utilised to assess the feedstock materials and the prepared samples so that meaningful scientific information could be obtained and detailed explanations of these results presented.

# Chapter 1

# Introduction

## 1.1 Metal Matrix Composites

Probably one of the most important achievements in materials science and technology comes from the developments of new materials and processes capable of meeting very specific requirements [1]. Over the last 50 years or so, metal matrix composites (MMCs) have emerged as an important class of materials. During this period, a considerable research effort has been focused towards a better understanding of their potential and limitations [2]. Nowadays MMCs are increasingly found in many production applications. This is because, compared to metals and alloys, MMCs can offer numerous advantages, such as higher specific strength and higher elevated temperature resistance [3]. However, their impact toughness, ductility, thermal fatigue and oxidation resistance are very often inferior than the matrix material itself [4]. Also, the fabrication of MMCs today is still difficult for parts requiring complex design or specific material property requirements.

## 1.2 Powder Metallurgy

Powder metallurgy (PM) is a route of production, processing, and consolidation of fine particles to make a solid metal [5]. It is considered a practical and economical production route for making high quality non-complex net shaped or near net shaped components from powders. PM is also a low energy intensity technology that generates low waste, and very often it is preferred to conventional melting technologies to produce and process high melting point metals, ceramics and composites. PM comprises a family of production technologies, and these generally involve all or most of the following steps: production of powder, mixing of powders, pressing of powder into a compact and sintering of the compact, then followed by secondary operations such as machining and finishing, when required [6,7]. Modern PM commenced in the 1920s and it is today still widely practiced by many industries due to its unique capabilities and advantages. Similarly, PM has been and is a cheap and simple technology used in research for developing new materials [8].

### 1.3 Laser-Powder Bed Fusion

Recently emerged as a subject of intense worldwide attention, laser-powder bed fusion (L-PBF) is a state of the art additive manufacturing technology designed to use high power density laser to melt and fuse metallic powders together in the creation of functional parts [9]. L-PBF involves a number of steps and these generally are: creation of a computer aided designed (CAD) model that fully describes the geometry to be build, conversion of the CAD model to stereolithography (STL) file format, transfer of the STL file to the L-PBF machine, machine setup and set build parameters, build the three dimensional (3D) geometry through layer by layer consolidation of the deposited powder layers, removal of the printed part from the L-PBF machine, part cleaning and supports removal. Depending on the application, parts may undergo additional post processing such as surface finishing, heat treatment, machining and painting [10].

L-PBF is capable of fabricating fully dense complex functional parts of high structural integrity at a competitive cost [11]. However, meltpool stability is critical for the quality of fabricated parts. Meltpool instability can lead to micro-particles formation and ejection, irregular or discontinuous tracks, balling, humping and porosity. Additionally, shrinkage tend to occur during liquid to solid transformation, and thus accumulating stresses that could lead to distortion and even delamination of final parts [12]. Therefore, proper care is required in the selection of both powder depositing and laser processing parameters to determine a suitable process window and minimise the likelihood of detrimental phenomena from happening.

### 1.4 Thesis Aim and Objectives

The aim of this thesis was to integrate ceramic reinforcing nanoparticles into metal via L-PBF for the production of MMCs with a view to understanding the material properties, metallurgy and process characteristics needed to obtain optimal and reliable properties. To this end, the aim of this thesis was achieved through the following specific objectives:

1. Investigate the effect of the printing location on part property variability.
2. Assess the influencing factors on L-PBF powder bed formation.
3. Development of a feedstock powder for L-PBF of MMCs.
4. Development of a novel scanning strategy for L-PBF MMC production.
5. Implementation of a L-PBF machine to print MMCs using in-situ aerosol-deposited nano-scale reinforcements.

### 1.5 Thesis Format and Outline

This thesis is a collection of published research papers and submitted manuscripts with original contribution to the literature. The candidate contribution to the resulting publications was the following:

| Chapter | Publication Title | Status | Candidate contribution |
|---|---|---|---|
| 3 | Assessing dependency of part properties on the printing location in laser-powder bed fusion metal additive manufacturing | Published, Materials Today Communications, 2022 | First author, corresponding author, project administration, conceptualisation, methodology, investigation, data curation, formal analysis, visualisation, writing - original draft, writing - review & editing |
| 4 | Influences of powder morphology and spreading parameters on the powder bed topography uniformity in powder bed fusion metal additive manufacturing | Published, Additive Manufacturing, 2021 | First author, corresponding author, project administration, conceptualisation, methodology, investigation, formal analysis, writing - original draft, writing - review & editing |
| 5 | Evaluation via powder metallurgy of nano-reinforced iron powders developed for selective laser melting applications | Published, Materials & Design, 2019 | First author, corresponding author, project administration, conceptualisation, methodology, investigation, data curation, formal analysis, visualisation, writing - original draft, writing - review and editing |

| Chapter | Publication Title | Status | Candidate contribution |
|---|---|---|---|
| 6 | Laser-powder bed fusion of silicon carbide reinforced 316L stainless steel using a sinusoidal laser scanning strategy | Published, Journal of Materials Research and Technology, 2022 | First author, corresponding author, project administration, conceptualisation, methodology, investigation, data curation, formal analysis, visualisation, writing - original draft, writing - review & editing |
| 7 | Laser-powder bed fusion in-process dispersion of reinforcing ceramic nanoparticles onto powder beds via colloid nebulisation | Published, Materials Chemistry and Physics, 2022 | First author, corresponding author, project administration, conceptualisation, methodology, investigation, data curation, formal analysis, visualisation, writing - original draft, writing - review & editing |

This thesis has been laid out in a progressive manner and is comprised of eight chapters. The following is a brief of the contents of each chapter:

**Chapter 1** introduces several subjects the thesis encompasses and summarises the objectives of the thesis.

**Chapter 2** reviews the necessary background and presents previous work carried out in the field, highlighting challenges, shortcomings and need for further work.

**Chapter 3** presents a comprehensive investigation on the contribution of the location parameter to the repeatability (build-to-build) and variability (within a build) issues in L-PBF printed parts.

**Chapter 4** addresses the knowledge gap of powder spreadability in L-PBF. Powder bed is the foundation to print quality parts and spreadability is a key governing factor. This chapter investigates powder spreading parameters and phenomena influencing powder bed uniformity.

**Chapter 5** focuses on the development of a feedstock powder for L-PBF of MMCs, driven by the following requirements: a homogeneous mixture, improve powder rheology and increase meltpool stability.

**Chapter 6** introduces a feasible solution to accomplish advancements in L-PBF of MMCs. A novel scanning strategy was developed and employed in an attempt to address ductility issues, as well as to reduce energy consumption and lead times related to L-PBF MMC production.

**Chapter 7** presents a multi-feedstock material printing methodology for L-PBF of MMCs. This methodology is also inclined to provide a potential for the development of MMCs with a single step production process.

**Chapter 8** summarises the most important findings of this work and provides recommendations for further research work.

# Chapter 2

# Literature Review

## 2.1 Metallic Powders for Laser-Powder Bed Fusion

A vast list of metals and alloys are processable via laser-powder bed fusion (L-PBF). Generally, the selection of a material of interest is made based on desired requirements of the final product. Factors such as the capability of powder particles to absorb energy radiation is crucial for the L-PBF process [13]. Material properties such as thermal conductivity and specific heat determines the thermal behaviour that powders would present. The thermal conductivity and coefficient of thermal expansion properties of the powder, both influence residual stresses during the solidification of molten material. The chemical composition of the powder is also important as it determines the general behaviour of the material.

### 2.1.1 Production Routes

There are several traditional routes for producing metallic powders. However, due to the development and growth of additive manufacturing processes such as L-PBF, the metal powder industry has evolved in order to achieve physical properties of powder material that meets strict metallurgical requirements. Atomisation is generally viewed as the best route due to geometrical properties of the powder particles that can be achieved. For this reason, atomised powders are widely used within L-PBF.

#### 2.1.1.1 Water Atomisation

Water atomisation generally consists of melting, atomisation, solidification and cooling stages. Metal powders produced with this route are typically irregular in morphology which reduces both flow and packing properties. However, by adjusting atomisation parameters, materials with high surface tension such as nickel can be produced to a near spherical morphology. Water atomisation is applicable to all metals that can be melted, and its powders are widely used in the powder metallurgy (PM) and welding industries [14,15].

#### 2.1.1.2 Gas Atomisation

Gas atomisation and water atomisation have the same theory for producing powders. However, gas atomisation uses gas as atomising media. Hence, enabling the production of clean and highly spherical powders of homogeneous microstructure. This is the reason for gas atomisation being the main process for producing metal powders for L-PBF [16,17].

### 2.1.2 Powder Characteristics

#### 2.1.2.1 Particle Size and Morphology

The quality of metal powder plays an important role in the L-PBF process. It can have a significant influence on mechanical properties, build consistency and production of defects on components. Particle size and distribution has an obvious impact on the minimum layer thickness and resolution of the finest detail in the component, and it influences greatly the powder bed density, energy input required to melt particles and surface roughness of the final component [18,19]. It was reported that powders with a large particle size distribution and a high fraction of fine particles led to the production of components with higher density [20,21]. However, the problem with such powder distribution is that smaller particles may evaporate before the larger particles fully melt [22]. Powder particles between 30 µm and 150 µm are suitable for the L-PBF technology [23]. Powders with narrower width of particle size are known to enable production of components with higher mechanical properties and dimensional accuracy, this is because such powders can lead to a much more stable meltpool behaviour [24,25].

The ideal powder characteristics that are sought for both powder fed and powder bed systems are of a spherical morphology, a smooth surface and a controlled size distribution. This is because such powder characteristics are beneficial to powder fluidity and also help forming uniform and consistent powder layers in powder bed systems. The presence of excessive amounts of surface pores and or closed pores with entrapped gas can negatively affect the L-PBF process and the properties of printed parts. Therefore, porous powders must be avoided [26].

#### 2.1.2.2 Powder Packing Density

Powder layer density plays a decisive role in the density of final parts and related part properties. The particles morphology, size and size distribution are factors that directly

influence the powder packing density [27]. High packing density can be achieved by using a multimodal powder distribution since a high fine fraction fills in voids between large particles. However, small particles reduce the fluidity of the powder, and less packing is achieved with increasing particle size. Therefore, a compromise in the particle size distribution is required in order to obtain both good flow properties and high packing density [28]. Moreover, the packing density of a powder has a positive correlation and is sensitive to the applied layer thickness [29]. Powder with smooth, clean and dry particles is another important requirement to achieve a high powder packing density [27].

#### 2.1.2.3 Flow Properties

Powder flowability is an umbrella term describing the complex behaviour of powder when it is subjected to stress or mobilised. Figure 2.1 shows the multiple aspects of powder flow. Flowability is an inherent flow property, and flow properties are specific bulk characteristics and properties of a powder that can affect flow, which are influenced by the powder properties and the interaction between powder particles. Particle size distribution, morphology, density and humidity level are the main parameters influencing powder flowability. The correlation between powder properties and flowability is well established. It implies that the narrowing of the particle size distribution increases flowability and that flowability generally improves with coarser particles [30,31]. Powder flowability is an important parameter for L-PBF systems as it effects the consistency of powder feeding with the process.

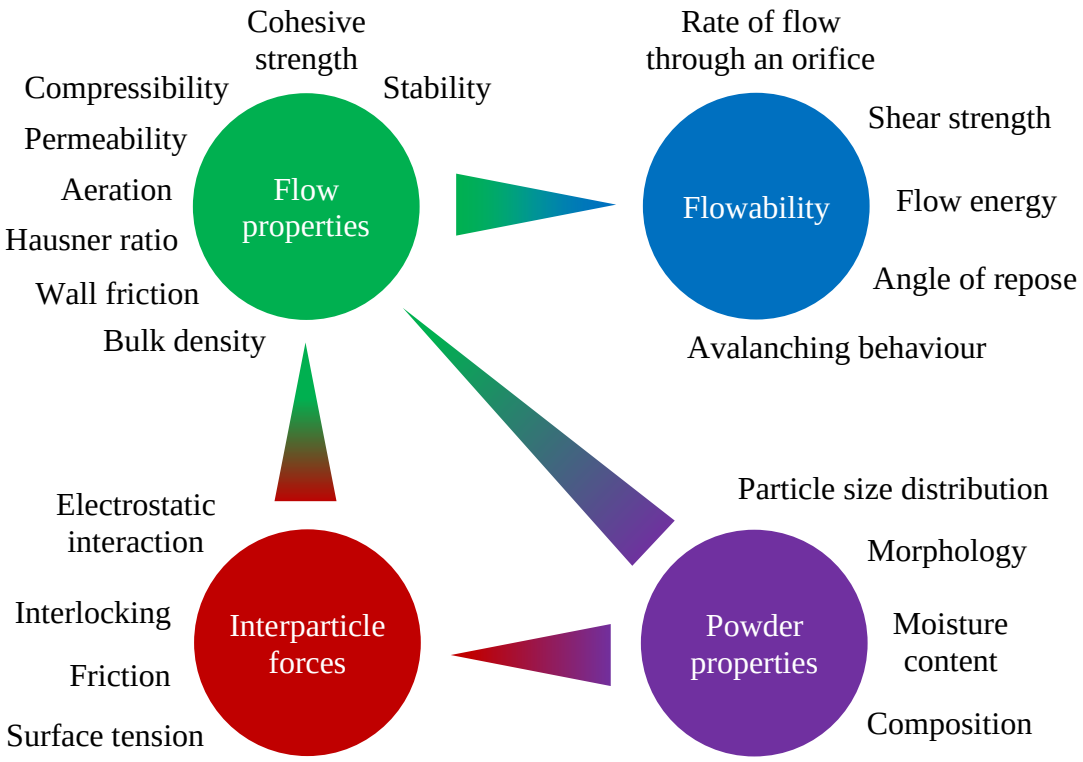


**Figure 2.1** Schematic visualisation of connection between the terms flow properties, flowability and respective influencing parameters [32].

#### 2.1.2.4 Powder Composition

Characteristics of materials, especially those that control the thermal responses, wettability and mechanical properties, originate from chemical composition. The chemical, thermal and physical properties influence the laser melting behaviour of a powder. The chemical composition also influences particles moisture absorption profiles and interparticle forces [30,33]. Typically, the particles of gas atomised powders have the same chemical property throughout. However, finer particles tend to have higher oxygen content due to the higher specific surface. Regarding the chemical composition, it is important to consider the effect of interstitial elements, such as oxygen, nitrogen, carbon and sulphur, as they can influence the melting kinetics of the powder by interfering with the surface tension of the meltpool resulting in Marangoni flow, which can have a negative influence on the porosity and properties of printed components [17,26].

#### 2.1.2.5 Laser Absorption

The laser absorption of a material is a complex phenomenon that describes the interaction of laser light with a material. The absorption of photons on the material surface causes a transformation into thermal energy [34]. Basically, the absorbance depends on a number

of different factors related to laser source and material. Typically, the laser wavelength, intensity, angle of incidence, polarisation and the material chemical composition, surface roughness, surface oxides, contaminations and temperature have important roles in the laser absorption [35–37]. Usually, for most L-PBF printers, a laser wavelength approaching 1064 nm is used which may or may not be optimum for specific metals [38]. The intrinsic absorbance of metals is generally temperature dependent and rises with increasing temperature [39]. It is also known that powder particle size also influences laser absorption. A higher laser energy absorption rate tends to be achieved with finer particles than coarser particles [25]. Absorption is also dependent upon the surface texture and roughness of the particles. Typically, when there are finer powder particles the fraction of laser absorption is enhanced as this can cause multiple reflection and absoption of the laser light [40]. However, it should be noted that the correlation with absorption of these parameters is very complex.

## 2.2 Metal Matrix Composites

Metals and their alloys are used in many engineering applications but with recent advancements in MMCs an endless array of enhancement possibilities are presented. The properties of MMCs can be designed to fulfil requirements that are specific to and dependent on the application.

### 2.2.1 Matrix Material

In MMCs, the matrix material plays an important role as it provides support for the reinforcement, assists in carrying the loads and provides stability to the composite structure. Additionally, the matrix material must enable bonding with the reinforcement material, withstand the surrounding environment, be able to deform elastically under load and restrict the development and propagation of cracks [41,42]. Density, ductility and strength retention at elevated temperature are important factors considered when selecting a matrix material. The selection of a suitable matrix material also depends on the type of reinforcement and amenability for production [43,44].

To date, numerous metals have been used as matrices. However, the most important have been aluminium, magnesium, titanium, iron, copper and their alloys. Table 2.1 demonstrates examples from the literature where such matrices were employed as base material during production of MMCs. Additionally, it reports what matrix properties were enhanced based on the used reinforcement material and manufacturing process. The

property enhancement possible with MMCs replaced various traditional materials. Hence, MMCs are accepted in numerous applications like gears, bearings, brake discs, brake drums, brake pads, piston rings, connecting rods, valves, valve seats, crankshafts, turbochargers, helicopter rotors, rotating blade sleeves, aircraft landing gear, flight control hydraulic manifold, engine exhaust flaps, turbine shafts, compressor rotors, rotor bling, fan blades, augmenter links, electrical connectors, wires, printed circuits, electronic casing, satellite structures, orthopaedic implants, petrochemical condenser plates, tubes, rivets, propellers, heat exchangers, heat sinks and magnetic windings [45–66].

**Table 2.1** Typical matrices, reinforcements, manufacturing processes and enhanced matrix properties.

| Base Metal | Matrix | Reinforcement | Manufacturing Process | Enhanced Property | Ref. |
|---|---|---|---|---|---|
| Al | 6061-T6 | $Al_2O_3$ | Friction Stirring | Hardness | [67] |
| Al | ZL114A | Ti–6Al–4V | Casting | Yield strength | [68] |
| Al | Pure Al | CNTs | Powder metallurgy + hot extrusion | Yield and tensile strength | [69] |
| Al | Pure Al | AlN | Hot Extrusion | Ultimate tensile strength | [70] |
| Al | 6082 | SiC | Stir + squeeze casting | Tensile properties | [71] |
| Al | Pure Al | W + tungsten aluminide | Pulsed current processing | Hardness | [72] |
| Al | 7178 | $ZrB_2$ | Stir casting | Yield, tensile and flexural strength, hardness and corrosion resistance | [73] |
| Al | 5052 | $Al_{0.6}CoCrFeNi$ | Vacuum hot pressing sintering | Hardness and Young's modulus | [74] |
| Al | AlSi10Mg | Graphene | Lase-powder bed fusion | Yield strength and hardness | [75] |
| Al | Pure Al | CNTs + SiC | Spark plasma sintering + hot extrusion | Ultimate tensile strength | [76] |

| Base Metal | Matrix | Reinforcement | Manufacturing Process | Enhanced Property | Ref. |
|---|---|---|---|---|---|
| Mg | Mg-6Zn | GNPs | Stir and pressure casting + hot extrusion | Young's modulus, yield and ultimate tensile strength | [77] |
| Mg | AZ31 | Ti | Friction Stirring | Yield and ultimate tensile strength | [78] |
| Mg | Pure Mg | Fullerene | Powder metallurgy | Tensile and compressive properties, hardness, wear and corrosion resistance | [79] |
| Mg | ZE41 | $TiB_2$ | Stir casting | Young's modulus, yield and ultimate tensile strength and hardness | [80] |
| Mg | Pure Mg | Bredigite ($Ca_7MgSi_4O_{16}$) | Powder metallurgy | Biodegradation rate, abilities of cell attachment and viability, compressive strength and hardness | [81] |
| Mg | AZ91 | TiC +$TiB_2$ | Stir casting | Yield and ultimate tensile strength | [82] |
| Mg | Pure Mg | ZnO | Powder metallurgy + hot extrusion | Ultimate tensile and compressive strength, tensile failure strain and wear resistance | [83] |
| Mg | AZ91 | SiC | Stir casting + hot forging + hot extrusion | Thermal stability, hardness, Young's modulus, yield and ultimate tensile strength | [84] |
| Mg | AZ91D | SiC | Laser-powder bed fusion | Compressive yield strength | [85] |

| Base Metal | Matrix | Reinforcement | Manufacturing Process | Enhanced Property | Ref. |
|---|---|---|---|---|---|
| | | | | and ultimate tensile strength | |
| Mg | AZ 91 | $Al_2O_3$ | Squeeze casting | Creep resistance | [86] |
| Ti | Pure Ti | $B_4C$ | Rapid hot pressing | Young's modulus and specific stiffness | [87] |
| Ti | Ti-6Al-4V | $B_4C$ | Direct metal deposition | Hardness and elevated temperature Young's modulus and ultimate tensile strength | [88] |
| Ti | Ti-1100 | TiB | Powder metallurgy + hot working | Tensile yield strength | [89] |
| Ti | Pure Ti | GNPs | Spark plasma sintering | Hardness and ultimate tensile strength | [90] |
| Ti | Ti-6Al-4V | TiC | Laser-powder bed fusion | Strength and plasticity | [91] |
| Ti | TA15 | $Ti_2AlC$ | Spark plasma sintering | Hardness, wear resistance, tensile, and compressive strength | [92] |
| Ti | Pure Ti | Diamond | Spark plasma sintering | Hardness, wear resistance and compressive strength | [93] |
| Ti | Ti-6Al-4V | GNFs | Powder metallurgy | Young's modulus, yield and ultimate tensile strength | [94] |
| Ti | Ti-6Al-4V | TiB | Spark plasma sintering | Yield and ultimate tensile strength | [95] |

| Base Metal | Matrix | Reinforcement | Manufacturing Process | Enhanced Property | Ref. |
|---|---|---|---|---|---|
| Ti | Pure Ti | TiB + TiC | Powder metallurgy + hot extrusion | wear resistance and Friction coefficient | [96] |
| Fe | 316L | $M_7C_3$ | Spark plasma sintering | Wear resistant | [97] |
| Fe | APM 2311 | TiC | Hot isostatic pressing | Abrasive wear and toughness | [98] |
| Fe | 304 | $TiB_2$ | Hot isostatic pressing | Sliding wear | [99] |
| Fe | High chromium cast iron | $Al_2O_3 + ZrO_2$ | Squeeze casting | Impact wear resistance | [100] |
| Fe | 316L | $AlCr_2$ | Powder metallurgy | Tensile strength and intergranular corrosion | [101] |
| Fe | 316L | $CeO_2$ | Laser-powder bed fusion | Yield strength | [102] |
| Fe | Low carbon steel | $TiB_2$ | Casting | Specific stiffness | [103] |
| Fe | Tool steel | WC | Laser-powder bed fusion | Compressive and tensile strength | [104] |
| Fe | Pure Fe | SiC | Hot isostatic pressing | Tensile strength and hardness | [105] |
| Fe | Fe-5Cu-3Sn | $ZrO_2 + MoS_2$ | Powder metallurgy | Hardness and tribology | [106] |
| Cu | Pure Cu | CNTs | Electroless deposition + spark plasma sintering | Yield strength and hardness | [107] |
| Cu | Pure Cu | GNSs | Vacuum hot press sintering | Electrical conductivity and hardness | [108] |
| Cu | Pure Cu | CNTs | Spark plasma sintering | Ultimate tensile strength, elongation at | [109] |

| Base Metal | Matrix | Reinforcement | Manufacturing Process | Enhanced Property | Ref. |
|---|---|---|---|---|---|
| | | | | break and hardness | |
| Cu | Cu-18Zn | SiC | Powder metallurgy | Hardness and compressive yield strength | [110] |
| Cu | Pure Cu | $Ti_2AlN$ | Vacuum hot press sintering | Hardness and flexural strength | [111] |
| Cu | Pure Cu | $TiO_2$ | Spark plasma sintering + hot extrusion | Yield and ultimate tensile strength and hardness | [112] |
| Cu | Pure Cu | $TiB_2$ | Friction Stirring | Hardness and wear resistance | [113] |
| Cu | Pure Cu | Fe + graphite | Powder metallurgy | Hardness, wear resistance and friction coefficient | [114] |
| Cu | Pure Cu | SiC + $Sc_2W_3O_{12}$ | Vacuum hot press sintering | Hardness and thermal expansion and conductivity | [115] |
| Cu | Pure Cu | GNSs + Ni | Chemical reaction + Vacuum hot press sintering | Hardness, wear resistance and friction coefficient | [116] |

Stainless steels are widely used as structural materials. They are of great interest in the industry for their corrosion resistance, ductility and easy formability and fabrication. In comparison to other alloys, stainless steels normally provides good resistance to oxidation and resistance to creep at high temperatures [117,118]. An example is the austenitic stainless steel 316L, which chemical composition and properties are shown in Table 2.2. Stainless steel 316L contains high levels of nickel and chromium. Chromium hardens, toughens and increases resistance to corrosion and nickel stabilises the austenitic structure and improves ductility and toughness and enhance corrosion resistance at high temperatures [119,120]. The low levels of carbon increases immunity from boundary carbide precipitation, minimises the potential of formation of chromium carbide and enhances the alloy ductility. Stainless steel 316L also contains molybdenum which

provides an appreciable resistance to pitting corrosion. Unfortunately, this alloy cannot harden via thermal treatment since its elemental composition strongly stabilises the austenitic structure and does not allow structural transformation. Therefore, its hardness and strength is attained during its manufacture and formation. However, they can be increased with mechanical treatments such as work hardening and shot peening [121–123]. Nevertheless, the application of stainless steel 316L has been limited because of its poor wear resistance and strength both at low and high temperatures [124,125]

**Table 2.2** Composition and properties of austenite stainless steel 316L [126–128].

| **Chemical Composition** | | | | | | | | | |
|---|---|---|---|---|---|---|---|---|---|
| Fe | Cr | Ni | Mo | Mn | Si | N | C | S | P |
| Balance % | 16-18 % | 10-14 % | 2-3 % | 0-2 % | 0-1 % | 0-0.1 % | 0-0.03 % | 0-0.03 % | 0-0.05 % |

| **Mechanical properties** | |
|---|---|
| Compressive Strength | 310 MPa |
| Ultimate Tensile Strength | 558 MPa |
| Modulus of Elasticity | 193 GPa |
| Vickers Hardness | 213 HV |

| **Physical Properties** | |
|---|---|
| Density | 8027 kg/m$^3$ |
| Melting Temperature | 1371 - 1399 °C |
| Thermal Conductivity | 16.2 - 21.4 W/mK |
| Thermal Expansion Coefficient | 16.6 - 19.4 x10$^{-6}$/K |
| Absorptivity of Laser Light | 36 - 55 % |

### 2.2.2 Reinforcement Material

In comparison to fibres and whiskers, particles are the most common and least expensive form of reinforcement. They are relatively easy to process and compatible with most conventional processing routes. Generally, the distribution of particles in the composite matrix is random. With this, compared to other forms of reinforcement, particulate reinforced MMCs exhibit relatively isotropic properties [129]. The main issue with production of particulate reinforced MMCs is the low wettability of the reinforcement

with the molten metal matrix. Powder particles may also agglomerate and form clusters, thus preventing them from being homogeneously dispersed throughout the matrix [130]. This is the case of nano reinforcements, which are susceptible to agglomeration due to high value of surface energy. In order to overcome these problems an appropriate MMC production route must be selected [44].

In particulate reinforced MMCs, the reinforcing particles are bonded with the matrix and they have the ability to restrict dislocation movement in the matrix material, grain growth and grain boundary slip at high temperatures. Due to this and the combination of their increased physical strength, in effect, the matrix composite is strengthened. The strengthening mechanism (dispersion hardening/strengthening) depends on particle diameter, inter-particle distance, reinforcement volume fraction, as well as the matrix and reinforcement properties [131–135]. Particulate reinforcement like Boron Carbide ($B_4C$), Silicone Carbide (SiC) and Titanium Carbide (TiC) offer numerous desirable properties such as high specific stiffness, good wear resistance and high strength at high temperatures [136]. However, the ductility of composites is very often negatively affected by the presence of such a second harder phase. Yet, this may be overcome through proactive design of the composite and production routes [137,138,44].

SiC is a non-oxide ceramic which has a high potential for advanced structural applications, as well as for electronic devices and production of composite materials. These applications are possible because of the unique properties of SiC such as good oxidation resistance, high temperature strength, outstanding corrosion resistance and excellent wear and thermal shock resistance. Together with superior electrical properties, good chemical stability, low coefficient of thermal expansion and high thermal conductivity [139,140]. Table 2.3 compares some of the most important physical, thermal and mechanical properties of SiC with TiC and tungsten carbide (WC).

**Table 2.3** A comparison of the properties of selected ceramic MMC reinforcement materials.

| **Properties** | **SiC** | **TiC** | **WC** |
|---|---|---|---|
| Density (kg/m$^3$) | 3210 [141] | 4930 [142] | 15720 [142] |
| Melting Point (°C) | 2830 [143] | 3180 [144] | 2750 [145] |
| Thermal Conductivity (W/mK) | 490 [146] | 43 [142] | 19 [142] |
| Thermal Expansion Coefficient (x10$^{-6}$/K) | 2.9 [141] | 8.6 [142] | 3.9 [142] |
| Young's Modulus (GPa) | 694 [147] | 450 [142] | 720 [148] |
| Hardness (GPa) | 25 [149] | 28 [150] | 22 [151] |
| Compressive Strength (GPa) | 1.9 [152] | 1.3 [153] | 2.7 [151] |
| Tensile Strength (GPa) | 1.03 [152] | 0.5 [153] | 0.3 [153] |

### 2.2.3 Interface

The interface is a bridge between the matrix and reinforcement, hence it largely controls the properties of the composite. Strong interfacial bonds allow distribution and transfer of load from the matrix to the reinforcement, whereas week interfacial bonds fail before any effective stress transfer to the reinforcement occurs. The interface has a large surface area within MMCs, therefore it must not degrade during processing and withstand both high temperature and corrosive environments. However, the high chemical gradient of the matrix and reinforcement induce reactions. Chemical reactions can change the matrix composition and lead to a strong interfacial bond. Additionally, they can form a brittle reaction product, which is highly detrimental to the performance of the composite. The interface between matrix and reinforcement affects not only strength, toughness, stiffness and ductility of composites but also other proprieties such as thermal conductivity, coefficient of thermal expansion and fatigue [154–156].

### 2.2.4 Processing

The selection of a particular processing route depends on several factors such as property requirements, envisaged application and the economics of fabrication. Additionally, it is important to take into consideration the fact that different processing routes can lead to completely different composite characteristics, even though the same composition and

amounts of the constituents are used [157]. Many processes are available for production of MMCs. Where for these, the reinforcing material can be either created in-situ or introduced as an ex-situ phase. In-situ synthesising is that where the dispersed phase is created within the matrix, typically by the occurrence of a chemical reaction which is often exothermic [158,159]. Differently, ex-situ is where the reinforcement phase is synthesised separately before its insertion into the matrix [160,161,44].

The advantages of in-situ tend to be very process and property specific. However, in general, in-situ provides a more homogeneous distribution of the dispersed phase particles, and the reinforcement surfaces and the reinforcement-matrix interfaces are more likely to be free of contamination. This route also tends to ensure better bonding between the particle and matrix, and allows the introduction of a large volume fraction and a small size reinforcement. Essentially, in-situ processes provide a strong interfacial bonding, better mechanical properties and less degradation in high temperature applications. However, in-situ reinforcement materials are limited to only those that are thermodynamically stable in a particular matrix. Also, the size and shape of particles are determined by the kinetics of the process during the nucleation and growth activities. Nevertheless, in-situ processing of composites is cost effective and scalable, but commercial applications are still limited by the unpredictability of the reactions and the insufficient knowledge concerning its processes [162–165,44].

The properties of ex-situ processed composites greatly depend on the volume fraction of the reinforcement, and in terms of processing, ex-situ enable production of bulk materials that exhibit isotropic characteristics. For this reason and also because of ease of production and modest production cost, ex-situ is widely preferred over in-situ. However, ex-situ processing has limitations which are mainly due to poor wettability of the reinforcement and reactions at reinforcement-matrix interface. Ex-situ processing also imposes difficulties to overcome in terms of homogeneous incorporation of the reinforcement into the matrix. One of the main reasons is because of Van der Waals and electrostatic forces in the liquid mixing process which leads to particle agglomeration and clustering [166–171,44].

### 2.3 Powder Metallurgy

PM is a well-developed technique that involves a small number of energy efficient steps. Its processes are suitable for synthesis of micro- and nano-ceramic reinforced MMCs

[172]. Additionally, it is considered one of the best routes for preparing MMCs, because it can eliminate problems such as non-uniform distribution of reinforcement, insufficient wetting and weak interfacial bonding between matrix and reinforcement materials faced by most of other conventional routes [173–176].

### 2.3.1 Powder Mixing

In powder metallurgy, mixing is a technique used to combine powders of different chemistries and to produce homogeneous mixtures in order to obtain a uniform quality and proper technological properties of the processed powders. Mixing of powders can be performed by a variety of mechanical methods, but for mixing materials such as metals and ceramics together, mixing mechanisms such as the rotating drum, double cone and V-type mixers are normally employed [177]. The rotating drum mixing mechanism is the simplest type of powder mixer. In this mechanism, the powders to be mixed are added to the drum and then the drum is set into rotation motion. The powders are lifted by the rotation of the drum and mixing take place in the cascading down. The volume of powder in the drum must not be too large to give sufficient freedom of motion to powders to mix. The amount of time that powders are mixed should be sufficient to obtain a uniform distribution of materials. Overmixing leads to particle distribution homogeneity deterioration and reduces flow characteristics of the mixture [178,179].

### 2.3.2 Powder Compaction

Powder compaction is the process of converting loose powder into a geometric form. This creates a part called a green compact as it is not yet fully processed. Powder compaction is commonly done at room temperature using a uniaxial hydraulic press. The opposing punches of the press squeeze the powders contained in the die giving rise to densification. In the first stage of powder pressing, densification is accomplished by repacking of the powders into a more efficient arrangement with filling of large pores within the powders microstructure. This also results in an increase in the number of contact points between particles. As pressure increases the point contacts undergo elastic deformation storing a residual elastic energy in the compact. As compression continues, these contact points experience cold pressure welding thus giving the green compact structural integrity. The final stage is characterised by contact enlargement through plastic deformation of particles. Further increase of pressure leads to strain hardening of the particles and new contacts are formed as the voids between particles collapse. The density continues to

increase until the green density is reached. Even though the maximum density of the pressed powders is reached, voids still exist extensively in the green compact. In metal powder compaction the interlocking and cold welding at particle surfaces are the main factors governing the green strength of the compacted mass [124,131].

The green density and compaction pressure are related functions. As the compacting pressure increases the compact density approaches the bulk compression, which refers to the density of the metal in its bulk form. The optimum compacting pressure required depends on a number of factors such as particle characteristics and particle shape. The effect of particle characteristics has a significant impact on the compact density, as the shape, size and density of the particles affect the apparent density, which decides the die fill during compaction. In metal powder compaction, to obtain superior interlocking and hence high green strength irregular shaped particles are preferred [124,180].

In powder compaction, friction is an important factor to consider as it opposes movement of particles during pressing. Friction at die wall is high and decreases in the direction to the centre of the die. During compaction, the movement of the particles is in the compaction direction, but as a result of die wall friction they also move in the direction of least resistance. This causes a non-uniform distribution of density in green compacts and increase wear on the tools. Friction between the surfaces of the particles impact on powder flowability and impede the consolidation of the powder. These result in inconsistent compaction, porosity and density in the green compact. In order to improve compaction conditions and reduce the friction internal lubrication is used. A good lubricant is the one that leads to uniform distribution of density. Lubricants can be mixed with powders in a small proportion. Lubrication in excess will prevent proper compaction of powder and collect in interparticle spaces. The typical lubricants used with metal powders are ethylene bisstearamide, zinc stearate, wax and boron nitride. The addition of lubricants reduce the particles surface to surface contacts which has a negative effect on the powders green strength [124,180,181].

It is often necessary to homogeneously disperse a binder in the powder to increase the green strength of the compact, as the green compact needs to be strong enough to be handled. Binders are also used to improve flowability and increase compactability of powders. Some polymeric binders can cause gas contamination and increase the carbon

content during sintering. These problems are minimised when choosing binders such as Polyethylene glycol and Polyvinyl alcohol [144,182].

### 2.3.3 Compact Sintering

Sintering is a process during which a green compact undergoes heat treatment to bond its metallic particles, without achieving a melting point. Sintering is usually carried out at temperature between 0.7 and 0.9 of the melting point of the powder metal [183]. If the green compact is made up of several materials, sintering temperature may be elevated near to or slightly higher than the melting point of the material with the lowest melting point. The essential phenomena of sintering are porosity decrease and strength increase. Sintering is carried out for various reasons but primarily to achieve adequate dimensional tolerance, good corrosion resistance and improved mechanical properties [124,131,184].

During sintering of metallic powders, a number of changes at microscopic scale occurs. The contact point between particles is where particle bonding initiates. Eventually, these contact points grow into necks, such that the initial particles lose their identity and pores are interconnected. With continued sintering, the pores between particles are reduced in size as the grain boundaries are extended from pore to pore. In the last stage, the porosity does not change but pore channel closure occurs as consequence of grain boundaries development in the neck regions. Therefore, sintering process involves: particles surface and grain boundary diffusion as temperature rises, liquid and vapour phase material transport and plastic flow of particles, densification resulting from an increase of the particles contact area and decrease of porosity, and recrystallisation and grain growth between particles at the contact area [124,131,185].

The main variables in sintering are temperature, time and furnace atmosphere. Sintering temperature and time depend mainly on the material and product sought characteristics. The sintering atmosphere has a significant influence on the sintering process. Therefore, proper control of the furnace atmosphere is important in order to obtain optimum properties. In modern sintering practice, the function of a controlled atmosphere is to prevent oxidation of the powder, reduce existing oxides, assist removing lubricants and binders, adjust impurity levels, control the level of carbon content, assist heat transfer, enhance sintering rate and promote densification [180,186].

## 2.4 Laser-Powder Bed Fusion

L-PBF is an outstanding manufacturing technology growing to maturity and showing great promise for manufacturing sophisticated products. However, it will never fully replace conventional manufacturing technologies. To compensate for the additional cost, high energy use and low productivity, one or more of the advantages offered by L-PBF such as fast manufacturing, weight reduction, geometry complexity, design flexibility and product quality need to be exploited. L-PBF is a unique fabrication technology for creating metallic, ceramic and composite products, which has the potential to impact the designs and applications in multiple fields such as aerospace, automotive, energy, electronics and biomedical [187].

### 2.4.1 Process Mechanism

The processing of a powder into a component via L-PBF involves spreading a thin layer of powder onto the building platform. Then, the laser beam scans a corresponding cross-section on the powder bed which selectively melts and solidifies as a bulk mass, thus start forming a solid component. Thereafter, the building platform is lowered and the cycle is repeated until the final layer has been processed and the component is completed. This process has been shown schematically in Figure 2.2.

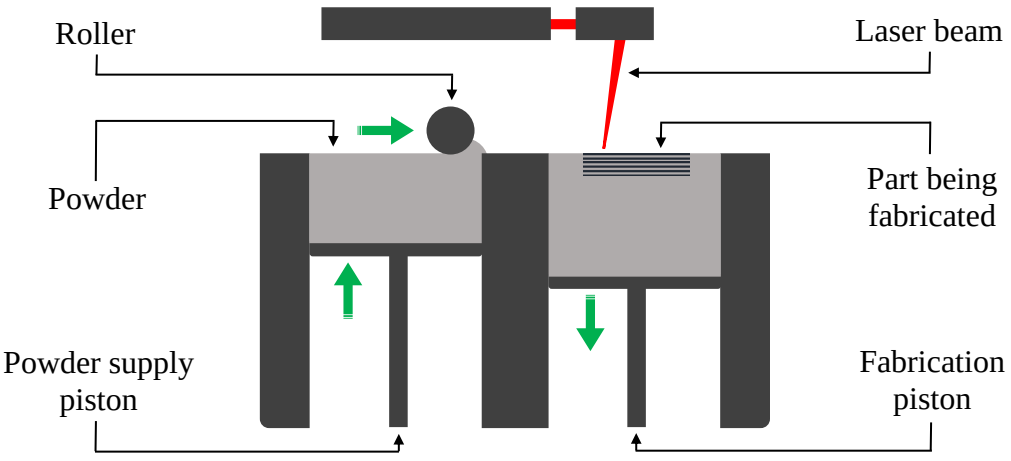


**Figure 2.2** Schematic diagram illustrating a typical laser-powder bed fusion arrangement.

L-PBF is an integrated process involving materials, physics and manufacturing. Hence, its working efficiency and quality of printed parts are highly influenced by a large number of processing parameters.

### 2.4.2 Control Parameters

L-PBF is accompanied by complexity and a large number of critical parameters influence the process and thus the mechanical properties and final quality of printed parts. In order to be able to control the process better and to produce parts with desired properties, identifying important inputs and understanding their relationship with and effects on the output is required. This can be achieved by understanding the design space using simulation and or exploring the design space using experimentation. Both are equally challenging due to the fact that there are a such large number of parameters influencing the process [188]. The effect of hatch distance, scanning speed and layer thickness on the L-PBF process and on the quality of printed parts will be discussed in the next sections.

#### 2.4.2.1 Hatch Distance

The hatch distance is one of the parameters determining the overlap rate of subsequent tracks, i.e. increasing the hatch distance reduces the overlap rate. The overlap indicates the areas influenced by repeated melting with the laser beam. In L-PBF, track overlapping is necessary in order to produce continuous metallurgical bonding entity [189]. Insufficient overlap is a cause of formation of the un-melted powders between scan tracks. Therefore, lack of fusion defects are normally distributed between scan tracks and deposited layers [190–192]. Excessive overlap ratios make previous scan tracks heat sinks of laser energy, and also lead to occurrence of swelling material above the plane of powder distribution and melting, hence deteriorating surface quality as well as decreasing relative density of parts. It is speculated from the literature that a sufficient overlap ratio is very case specific, but it usually ranges from 40 to 60 percent [189,193–195].

#### 2.4.2.2 Scanning Speed

The scanning speed influences the irradiation time on the powder bed per unit area. At high scanning speeds the meltpool depth is lower and the scanned line width is narrower because of meltpool faster solidification rate. Fast cooling can cause formation of cracks and layers delamination due to thermal gradients. Too fast scanning speeds may result in uncompleted molten powder and a discontinuous meltpool, hence increasing porosity. Also, an increase of the scanning speed tends to reduce surface roughness and improve dimensional accuracy. On the other hand, if the scanning speed is too low the spheroidisation phenomenon can occur and cause metal particles to agglomerate and bond, which then leads to an irregular meltpool cross-section. This eventually causes a

large number of defects in the part. Whereas, a low scanning speed tends to generate and cause residual stresses in the part. However, it allows production of parts with higher density [196–200].

#### 2.4.2.3 Layer Thickness

In L-PBF, the minimum layer thickness and the minimal feature size that can be built are constrained by the particle size. Typically, the layer thickness ranges from 30 to 150 μm [201]. The most efficient method to increase build rate is using a thicker powder layer with a high scanning speed and a high laser power. To melt thicker layer of powder higher energy density is required. However, excessively high laser energies lead to process instabilities. Nevertheless, such instabilities may be avoided by increasing the laser beam diameter in conjunction with laser power. The layer thickness is an important parameter for the densification of parts. Thicker layer thickness generally leads to residual micropores and low density parts. Whereas, thinner layer thickness improves part density because the melting between layers is better. The characteristics of the moving meltpool such as mass transfer, heat transfer and cooling rate are directly influenced by layer thickness. Therefore, the layer thickness has a strong influence on microstructural outcome and surface roughness. The literature has shown that thinner layer thickness lead to higher tensile strength and hardness and that thicker layer thickness lead to weaker bonding between layers, dimensional errors and higher plasticity [202–207].

### 2.4.3 MeltPool

Laser irradiation on the powder surface causes material to heat up and melt, hence forming a liquid meltpool on the top of previously solidified material. The size and shape of the meltpool greatly impact on the quality of track formation, which are mainly controlled by the scanning speed and the laser power. The meltpool fluid behaviour strongly influences the movement of molten material, surface tension, heat transfer and internal structure of solidified part. In addition, various physical phenomena can affect the molten pool and prevent the formation of a consistent structure along the scanning direction. Therefore, understanding the meltpool behaviour is critical in controlling printed parts properties [208–211].

Microstructural studies on the meltpool showed that the penetration depth increases with low scanning speed and that at high scanning speed with low laser power the track width reduces and slowly becomes discontinuous, thus it results in balling [212]. The

Marangoni effect has great effect on the mass and heat transfer within the meltpool and on the pool geometry. In the presence of Marangoni effect, the meltpool becomes wide and shallow, while in its absence the meltpool becomes narrower and deeper [213,214]. Therefore, formability, microstructure and mechanical properties depend on the meltpool mode. Figure 2.3 shows a schematic representing heat history during keyhole mode and conduction mode [215]. The melting mode has a dominant role in determining the geometry and morphology of molten pools, and it can be controlled by varying the scanning speed, laser power and layer thickness. Conduction mode can provide a wider processing window, good formability, few forming defects (spatter, porosity and crack) and high process stability, while if keyhole mode does not lead to increased porosity can impart a better combination of ductility and strength. These two modes have therefore their own advantages and disadvantages and the preference of one over the other is dependent on the specific material type, part design and process parameter case in hand [214,216].

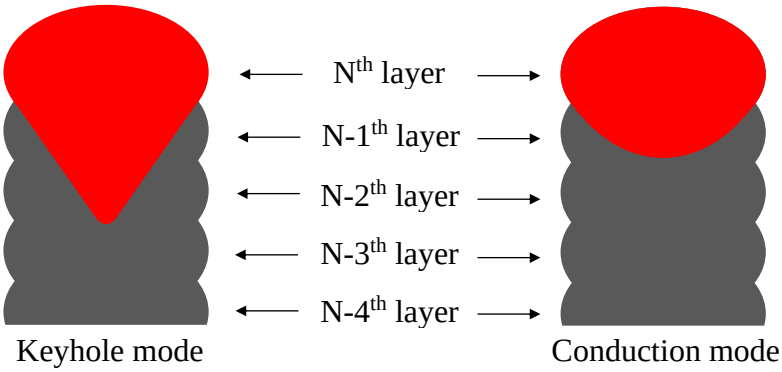


**Figure 2.3** Schematic representation of meltpool keyhole mode and conductive mode.

#### 2.4.3.1 Vaporisation

High thermal irradiation energy generated by the laser source is absorbed by the exposed powder particles which forms a meltpool [217]. A plasma plume consisting of ionised gas and metal is usually visible above the meltpool, Figure 2.4. When the temperature of the meltpool becomes greater than the boiling point of the molten material, vaporisation occurs [218]. The vaporisation induces an immense pressure which results in a shock wave which then generates a recoil momentum on the molten material forming a vapour cavity [219]. Consequently, this causes the ejection of molten material and a change in the meltpool shape [220]. Additionally, vapour can also condense on the lens and

attenuate or refract the laser beam [221]. Therefore, material vaporisation should be avoided.

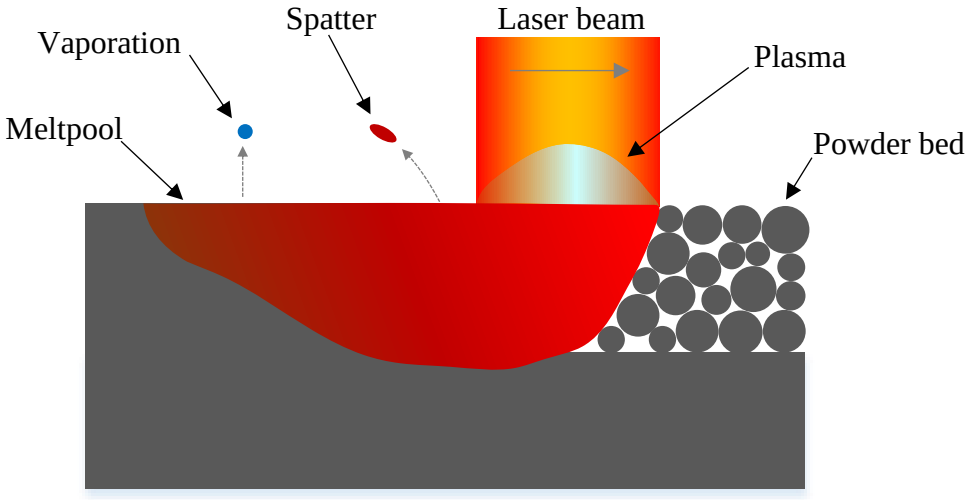


**Figure 2.4** Schematic diagram of laser-material interaction within selective laser melting.

#### 2.4.3.2 Recoil Pressure

The recoil pressure is a laser induced compression of high vapour pressure on the surface of meltpool. Studies have shown that it can enforce wetting of the meltpool and improve part density [222]. However, a recoil pressure greater than the pressure exerted by the surface tension of the melt can blow material away from laser-material interaction zone [223]. Therefore, preventing the formation of recoil pressure by controlling the meltpool temperature to decrease vaporisation can avoid material spattering, in addition to flatten the melt and improve surface quality [224].

#### 2.4.3.3 Spattering

Spattering is a very common phenomenon that occurs mainly due to instability of meltpool in the process. However, it is difficult to accurately define the principle of spattering. Generally, spatter refers to metallic jet, droplet spatter and powder spatter. The spatter appearance is very distinct, hence indicating the existence of various spatter formation mechanisms [225,226]. Unfortunately, any spatter formed during the process is detrimental for the mechanical properties of fabricated parts. This is because the spattered material is one of the major sources of defect creation. The chemical composition in spatter material differs from initial powders [227,228]. Since spatter material is highly sensitive to oxygen, surface oxides enriched is typically encountered in the most volatile elements of the material. A such spatter may adhere to the formed

surface or mix with and contaminate clean powders to affect subsequent structure formation [229,230]. Generally, a high velocity shielding gas flow is used to minimise oxidation and powder bed contamination. However, control or suppression of spatters is more ideal. It was reported that spattering intensity increases with increasing energy densities, and that a complete suppression of spatters may be possible when combining low energy densities with large laser beam spot sizes [231].

#### 2.4.3.4 Solidification

L-PBF is associated with rapid solidification ($10^4$-$10^6$ K/s) phenomena [232]. Temperature gradient within the meltpool governs cooling rates and influences solidification microstructures [233]. The rapid extraction of thermal energy during solidification leads to a substantial deviation from equilibrium, hence allowing for microstructure refinement, extension of solid solubility, increased chemical homogeneity and formation of metastable phases [234,235]. Reactions occurring during rapid solidification can lead to the formation of amorphous, crystalline and polymorphous structures. Figure 2.5 shows the various solidification fronts that may form depending on the local thermal gradient and growth rate. The local thermal gradient and the growth rate dominate the solidification microstructure and their product determines the size of the solidification structure [236,237]. Therefore, it would be advantageous to predict what microstructure would develop under certain processing conditions so that the desired microstructure could be selected based on the appropriate choice of processing parameters.

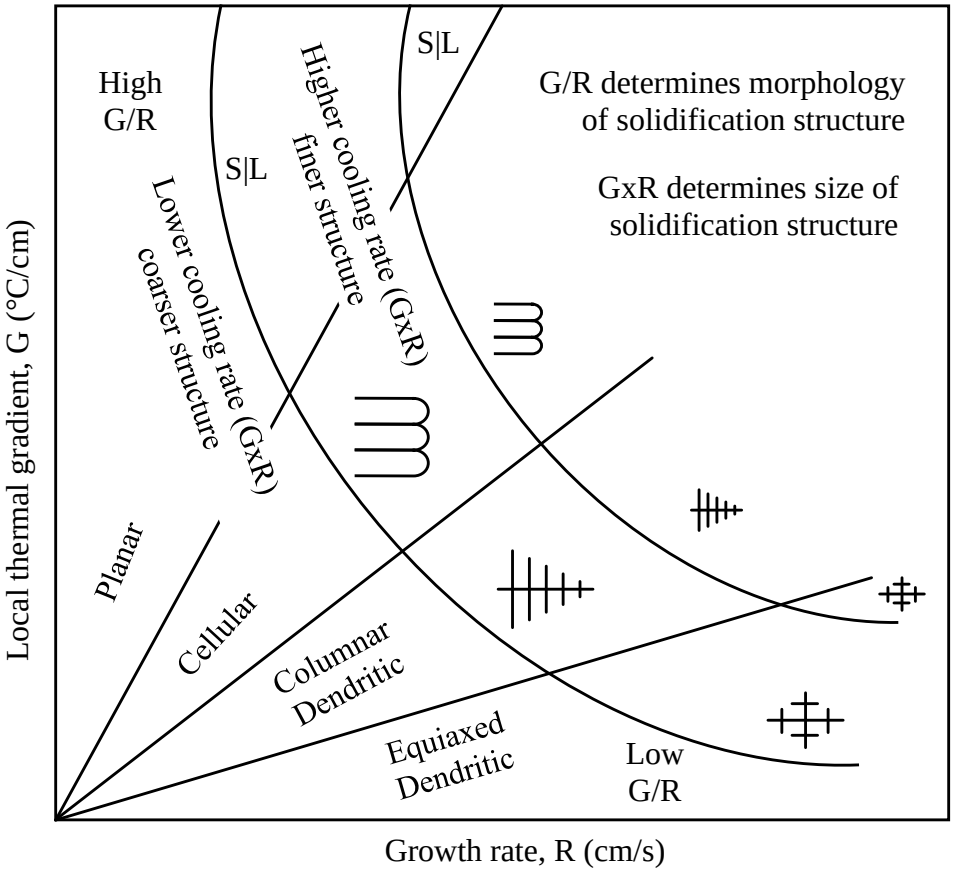


**Figure 2.5** Effect of temperature gradient and growth rare on the size and morphology of solidification structure [238].

### 2.4.4 Typical Defects

Defects formation is a common problem in L-PBF. They are inevitably introduced if any of the parameters are improperly chosen, and in the presence of process disturbances. The presence of defects remains an issue regarding reproducibility, reliability and quality of L-PBF parts.

#### 2.4.4.1 Porosity

Porosities are considered as a critical factor affecting the performance of parts, as such defects degrade fatigue and mechanical properties [239]. Usually, porosity is driven by gas inclusions, lack of melting, solidification and others more complex phenomena such as oxidation and interaction of recoil pressure and Marangoni convection within the meltpool [240,241]. Regarding these, researchers have shown that porosity can be effectively reduced and controlled by adjusting the powder morphologies and process parameters [9,242].

#### 2.4.4.2 Lack of Fusion

Lack of fusion is caused by insufficient energy to melt powder particles. A lack of fusion defect may contain enclosed un-melted particles which may lead to inconsistent and discontinuous tracks, poor interlayer bonding, cracks, delamination and porosities, hence impacting on part quality. The main factor behind lack of fusion defects are the laser and scanning parameters [243,244]. Therefore, their optimisation is key in avoiding insufficient or excessive energy inputs.

#### 2.4.4.3 Balling

Balling is a defect that is very detrimental to the forming quality of L-PBF parts. Its origin may be attributed to local powder arrangement, excessive hatch distance, presence of oxygen in the powder or build chamber, meltpool instabilities and splashing at high scanning speeds, viscosity changes of meltpool and inadequate leaser energy input [245]. Balling can increase surface roughness, form discontinuous tracks, cause porosity and scratch the recoater. Solutions include using higher energy densities (high power and low scanning speed and layer thickness) and adding powder deoxidants [246–248].

#### 2.4.4.4 Roughness

Surface roughness influences the part functional properties such as geometric tolerance, structural integrity, fluid dynamics, heat transfer, mechanical properties and aesthetic [249]. Because of the layered nature of L-PBF and the associated parameters and powder morphology, reduction and control of surface roughness may introduce technical challenges [250]. Compared to continuous wave emission, pulsed wave emission can provide lower surface roughness [251]. However, it increases building times. Surface roughness can also be decreased by using finer powders. Additionally, the various other parameters governing the L-PBF process can also influence on the surface roughness of parts. Commonly, part surface roughness varies depending on the building orientation and direction in which it is measured. The function of contour scanning is also to improve surface quality. However, during the scan the meltpool attaches powders from the sorroundings.

#### 2.4.4.5 Thermal Anomalies

L-PBF is related to high thermal gradients due to fast melting, solidification and cooling, which inherently exist in the process. The outcome of this is thermal stresses, and

consequently delamination, distortions, cracks and shrinkage. Residual stresses caused by thermal cycles is a critical issue since they generate part delamination and distortion [224,252]. High residual stresses in the part increase the risk of delamination and distortion when removing it from the base plate [253]. Distortion is a consequence of thermal gradients in the part and thermal expansion mismatch [254,255]. Proper wetting of the meltpool on the previous consolidated material ensures strong bonding between successive layers and prevents delamination. Material oxidation during the process causes poor interlayer bonding, and when combined with residual stresses it induces delamination [256]. A more homogeneous temperature distribution is obtained when laying the smaller length of the part in the direction of gas flow. Because, this has a less of an influence in the cooling and so results in less thermal stresses [257]. An appropriated energy density and optimal scanning strategy can provide a proper melting and minimise high thermal stresses [258]. Additionally, residual stresses in parts can also be mitigated during processing by preheating, laser shock peening and closed-loop feedback control or relieved with post processes such as heat treatment or machining [259].

A number of different process parameters and physical and thermal phenomena can cause part cracking. Large thermal gradients in the meltpool while solidification is proceeding can generate cracks [260–262]. Also, internal residual stresses in the part can exceed the strength of the material and form cracks [263]. The rapid cooling of the meltpool is also accompanied by a shrinkage in the metal volume, which can distort the part [264,265]. Hence, volume shrinkage is dependent on temperature gradient and temperature distribution [266]. Part shrinkage is generally anisotropic and more intense in the Z-direction dimensional [267]. Fortunately, dimensional compensations can be used to overcome the negative effect of shrinkage behaviour [268]. Shape accuracy can be optimised by avoiding support overhanging structures, and the volumetric shrinkage and dimensional accuracy can be optimised by using appropriated laser and scanning parameters [269,270].

#### 2.4.4.6 Anisotropy

In L-PBF, the heat of meltpools is preferentially dissipated downwards through the part into the build substrate. This assists the formation of thin grains pointing vertically (Z-direction) or horizontally (opposite direction to heat extraction), such as columnar or equiaxed dendritic grains. [271,272]. The effect this has on the mechanical properties of

parts is profound since anisotropy is dependent on their inherent microstructure [273,274]. Anisotropy depends upon the material employed as well as on the laser and scanning parameters, which can cause a substantial change in the grain structure, phases present and their distribution within the microstructure [275,276]. Changes in solidification rate resulting from variations in temperature gradient influences phase stability and results in microstructure anisotropy [277]. Similarly, the atmosphere (oxygen, inert gas and impurities) can also influence on microstructural morphology, cause phase instability and defects [278]. Therefore, contributing to anisotropy in parts.

## 2.5 Laser-Powder Bed Fusion of Metal Matrix Composites

### 2.5.1 Feedstock powder

Feedstock powder preparation is one of the most critical steps in L-PBF of MMCs. Therefore, the four main techniques currently used to prepare powders were compared against each other.

Composite atomisation is that where a molten matrix and dispersed material are atomised to produce composite powders. This process completely satisfies the powder requirements. However, gas atomisers are very expensive and prone to contamination, hence requiring a dedicated atomiser. A such powder preparation technique would be suitable to a well-stablished industrial scale production [279–284].

In particle injection atomisation, atomised molten droplets of the matrix are injected with reinforcing nanoparticles. This technique holds the same advantages and disadvantages to composite atomisation. However, here the atomiser requires an integrated mechanism for particle injection. It is important to note that injected particles, which have higher melting temperature than the matrix, do not undergo melting and hence retain their original morphology [285–288].

Ball mill mixing involves the mixing of powders by a rotating drum, resulting in either a powder mixture or coated particles. This technique is simple, inexpensive, and applicable to small- and large-scale productions. However, care is needed to avoid particle crushing, contamination and oxidation. Unfortunately, it is challenging but possible to obtain a homogeneous powder mixture or uniform coating via ball mill mixing [289–293].

There are various wet synthesis techniques, and they may involve material dissolution, dispersion, treatment/functionalisation, precipitation, blending, stirring, heating, cooling,

filtration, evaporation and drying, and also introduction of agents such as acids, alcohols, salts, gases, lubricants and binders. Wet synthesis are complex multistep techniques applicable for powder preparation. However, powder morphology change, aggregations, contamination and unwanted reactions are typical drawbacks accompanying the wet synthesis techniques [294–302].

From the above comparison, as seen in Figure 2.6, the resulting feedstock powders differ in nature from one technique to another, hence this must also be considered when selecting a powder preparation technique.

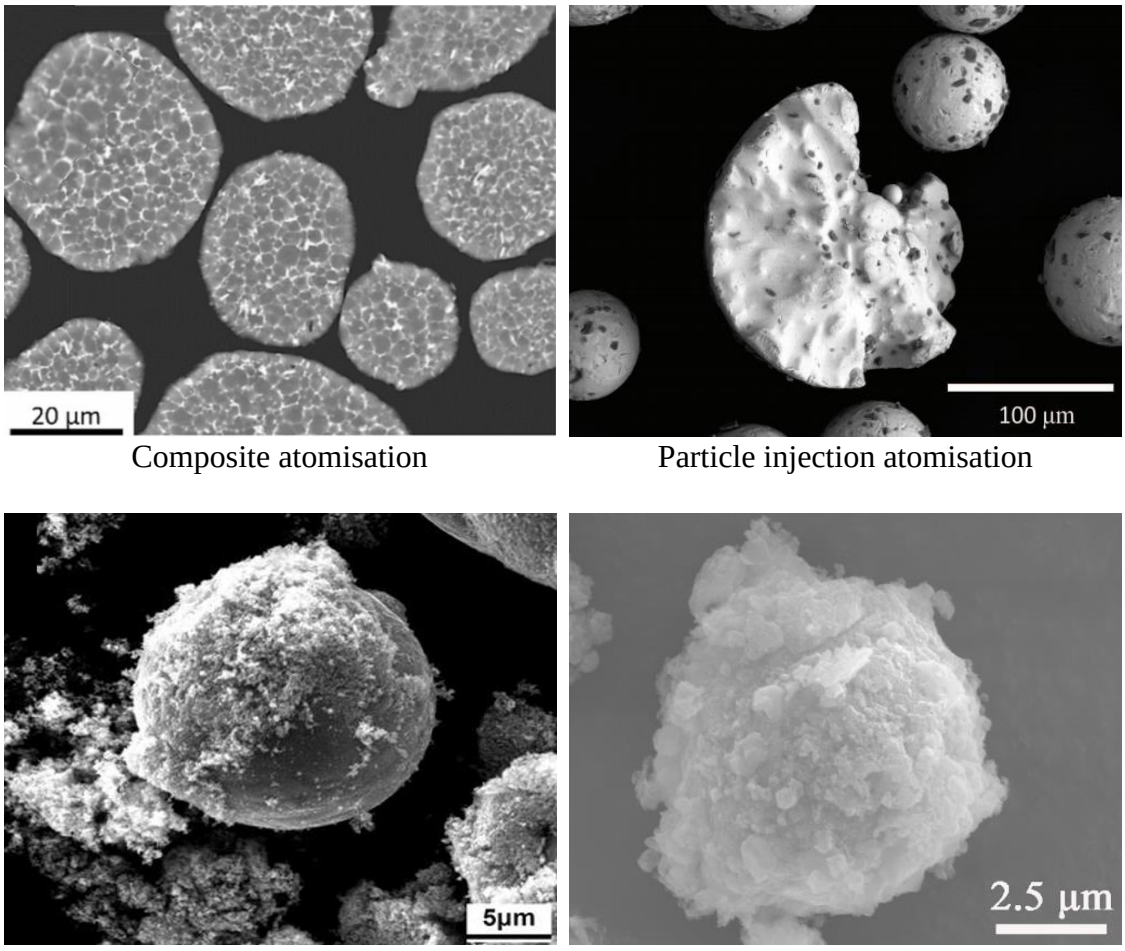


Composite atomisation | Particle injection atomisation

Ball mill mixing | Wet synthesis

**Figure 2.6** Comparison of four main powder preparation techniques applicable for laser-powder bed fusion of metal matrix composites [284,288,291,299].

### 2.5.2 Current Challenges and Issues

#### 2.5.2.1 Metal Matrix Composites

The production of MMCs is faced with numerous challenges, which should be addressed prior to or during the production process in order to be successful in taking advantage of

the superior properties of the reinforcement within the matrix. Based on the assessment of literature, the following points summarise the challenges and issues concerning MMCs.

1. Conventional production processes are not always suitable for manufacturing of complex net shaped composite components [303].
2. The selection of suitable and high quality materials is rather difficult due to lack of data from suppliers on corresponding raw materials [304].
3. Powdered reinforcing materials are prone to segregation and clustering and can sink or float depending on their density relative to the liquid metal [305,306].
4. While the strength and stiffness of MMCs increase with the increase in the volume amount of reinforcement, the ductility of the matrix normally deteriorates [307,308].
5. A non-uniform and non-steady heating and cooling can result into formation of non-equilibrium microstructures within the composite [309].
6. It is difficult to produce porosity free composite and the tendency for porosity increases with increasing volume fraction of reinforcement [310].

#### 2.5.2.2 Laser-Powder Bed Fusion

The typical challenges and difficulties faced during L-PBF of metals and alloys are also applicable to MMCs. The below are specific challenges to L-PBF of MMCs.

1. The spreading of powders into thin layers is a critical step in L-PBF as powder layers are the foundation for part building. Obtaining uniform and consistent powder layers is challenging for monomodal powders and even more challenging for powder mixtures containing nanoparticles [311].
2. Laser energy absorption of two-component powders is affected by several factors such as each powder thermal properties, surface chemistry and size. Therefore, formed powder layers containing non-homogenous mixture of powders result in complex laser absorption behaviour, hence influencing melting stability [312–315].

3. L-PBF opens up potential to manufacture MMCs with new materials combinations free from limitations of conventional production routes and has the potential to combine benefits such as those provided by powder metallurgy and casting. However, these potentials remain as hypothesis, and there is also a need for a proper understanding of the processing, microstructure and property interrelationship [316–319].

### 2.5.3 SiC/316L, WC/316L and TiC/316L Composites

Many have reported production of stainless steels reinforced with SiC, WC and TiC via conventional routes [320–328]. However, to date, there is very little work done on L-PBF of TiC/316L, SiC/316L and WC/316L.Therefore, the L-PBF manufacturing potentials for these composites are yet to be researched.

Zou et al. investigated strength and wear resistance of L-PBF SiC/316L. Samples with 0, 3, 6, 9 and 12 vol% of SiC were successfully fabricated. A fraction of the irregular shaped micro-sized SiC particles were refined to nano-size during the laser irradiation. With increasing SiC content, the wear properties gradually improved. While the wear mechanism of the matrix was severe adhesive and abrasive wear, including oxidation wear, the composite containing 9 vol% of SiC indicated a dominating slight abrasive wear. The reinforcement greatly improved the hardness and ultimate tensile strength of composites, reaching 520 HV and 1.3 GPa on those with 9 vol% SiC. However, the elongation at break was considerably deteriorated, decreasing from 43.3 % (matrix) to 5.1 % (composite with 9 vol% SiC). They also reported that increasing the volume of reinforcement reduced ductility and wettability and increased porosity and crack manifestation and increased residual stresses and induced dislocations in the matrix. In addition to changing the microstructure from equiaxed to dendrites morphology [329].

Al-Mangour et al. conducted a number of studies on L-PBF of TiC/316L. They reported that the composite grain size can be tailored by regulating the applied volumetric energy density. In fact, high volumetric energy densities led to coarser microstructures and intensified crystallography textures. Improvements in microhardness and compressive yield strength obtained at 67 J/mm$^3$ were attributed to grain refinement. However, this volumetric energy density promoted meltpool instabilities which produced a disordered liquid solidification front. While between 100-200 J/mm$^3$ the wear rate was improved, at 300 J/mm$^3$ the dispersion of nano-TiC was homogenised within the matrix. Also, because

of the densification improvements, the microhardness increased in comparison to that of the composite processed at 200 J/mm$^3$. However, porosity and thermal cracking were observed. In comparison with micro, nano-TiC particles showed better liquid-solid wettability and higher enhancements on the composites density, wear performance and microstructure homogeneity. It also revealed significant improvement in mechanical properties moving up the critical temperature to 650 °C, which was achieved with the 15 vol% nano-TiC reinforced 316L [330–334].

Shuming et al. reported that the improvements in composite densification was related to the increasing of both laser power and laser exposure time. The highest density was measured from the 316L samples without reinforcement, and the presence and increase of nano-TiC mass fraction aggravated the spheroidisation effect increasing the composite porosity volume. In this regard, TiC particles contributed to pore formation, and this was evidenced by aggregated TiC particles adhering to inner wall of pores. The highest microhardness was obtained from the composite with 4 wt% TiC (285.2 HV) while the highest ultimate tensile strength from the composite with 2 wt% TiC (748.6 MPa). Their results also revealed the detrimental impact of TiC on the elongation at break and impact toughness of composites [335].

### 2.6 Conclusions

Although enormous research progress has been made in L-PBF, there are still several fundamental knowledge gaps, particularly in understanding powder bed formation and identifying its influencing factors. The complexity of L-PBF reflects its large number of input parameters and its in-process related phenomena. The various phenomena discussed in the literature are prompters to part defects, and these are governed by the input parameters. In order to suppress detrimental phenomena a compromise is required when selecting the parameter levels and this may be possible via a proactive optimisation driven by the sought part characteristics. Evidently, the full understating and control of the L-PBF process is as important for metals and alloys as it is for composites.

MMCs have the potential to provide enhanced mechanical, physical, electrical and thermal properties beyond the established limits of conventional monolithic alloys. By careful selection of type, size and amount of reinforcement, matrix alloy, and the manufacturing route that brings them together, it is possible to tailor such properties to meet specific requirements. However, despite this advantage several existing issues

prevent MMCs expanding their applications. Internal defects control and related ductility and toughness improvements are some of the on-going challenges for MMCs production process development and implementation. A simple and cost-effective production route capable of preserving the dispersed phase original characteristics ensuring uniform distribution and promoting wetting and bonding between phases is required. L-PBF has the potential to eliminate several issues such as the difficulty of process control, non-uniform reinforcement distribution, lack of wettability, undesirable chemical reaction and excessive porosity, which have been reported from traditional processing routes. L-PBF also could provide for the production of integrated, very complex, lightweight structures with competitive cost, and reduced lead times. At the moment, L-PBF is the most promising route to process complex part design MMCs as its layer-by-layer fashion of manufacturing provides freeform fabrication capability. During L-PBF, material melting and solidification is performed in a controlled inert atmosphere and provides the potential for pointwise control of microstructure and mechanical properties which are some of the points that make this process unique compared to traditional MMC processing routes. Additionally, L-PBF will possibly provide a new method for production of tailored MMCs within a single step process.

With this in mind, the proposed approach to this work is:

1. Two aspects of L-PBF lacking in knowledge and that have implications on the MMC part integrity will be studied in-depth:
    a. Location, the print location across the build platform. Assessment of part-properties dependency of on the printing location in L-PBF.
    b. Spreadability, the spreading behaviour of a powder. Assessment of influencing factors and optimal spreading conditions within the L-PBF system.
2. The development of a homogeneous powder mixture, containing tailored micrometre-scale metallic particles and nanometre-scale ceramic dispersed particles, of improved flow properties for the L-PBF of MMCs.
3. The PM production route will be adopted for testing developed powders through the manufacturing of MMCs. Also, the resultant measured part properties will be used as reference for assessing the properties of L-PBF manufactured MMCs.
4. L-PBF of MMCs using the developed powder and the optimised parameters, followed by evaluation of the mechanical, physical and tribological properties of

the resulting composites. Additionally, a novel scanning methodology, different to the current linear laser paths employed within L-PBF, is presented and used within the L-PBF system in an attempt to address ductility issues, as well as to reduce energy consumption and lead times related to L-PBF MMC production.

5. The implementation of a commercial L-PBF printer to work with colloid form of feedstock material as well as powders for the manufacturing of MMCs. A such single step process to manufacture MMCs could for example minimise feedstock material contaminations and health and safety hazards relating to powder handling, while also providing a more versatile method of MMC production.

# Chapter 3

## Assessing Dependency of Part Properties on the Printing Location in Laser-Powder Bed Fusion Metal Additive Manufacturing

**Publication Status:** Published

Mussatto, A., Groarke, R., Vijayaraghavan, R. K., Hughes, C., Obeidi, M. A., Doğu, M. N., Yalçin, M. A., McNally, P. J., Delaure, Y., and Brabazon, D., 2022, "Assessing Dependency of Part Properties on the Printing Location in Laser-Powder Bed Fusion Metal Additive Manufacturing," Materials Today Communications, 30, 103209.

https://doi.org/10.1016/j.mtcomm.2022.103209

## 3.1 Abstract

Despite the accelerated growth of laser-powder bed fusion in recent years, there are still major obstacles to be overcome before the technology enjoys truly widespread adoption. These include inconsistent part quality and repeatability issues linked to variability in the properties of printed parts. Commonly, the print location across the build platform is overlooked and assumed to have little or no effect on the overall part properties. There is a lack of previous systematic studies and a lack of knowledge of the influences of the location parameter on the final part properties. Therefore, to address the existing problem, the current study completely isolated the location parameter to accurately assess any effect of this variable on the microstructure and mechanical properties of laser-powder bed fusion manufactured parts. The results revealed the importance of the build location and showed that there is correlation between the location parameter and part properties as qualitative and quantitative properties of printed parts varied between the selected extremity locations. The findings highlight the importance of considering the location of the part being printed on the build platform and how the location may need to be fixed for multiple builds in order to achieve acceptable repeatability.

## 3.2 Introduction

In recent years, laser-powder bed fusion (L-PBF) has been gaining increasing industrial attention for the production of functional components as it offers a step change in the possibilities of design and manufacturing [336]. L-PBF enables the manufacturing of components exhibiting complex features, innovative shapes and lightweight structures that are difficult or even impossible to manufacture with conventional techniques [337,338]. In this context, ensuring the quality, repeatability and reproducibility of L-PBF manufactured components is fundamental to meet the stringent requirements and certification constraints imposed by leading industries such as aerospace, automotive and medical [339]. Unfortunately, the lack of process robustness, stability and repeatability has been identified as a major barrier for the industrial breakthrough of L-PBF [340,341]. In fact, despite significant technological advances, the defect rates are still too high with respect to conventional techniques.

Achieving high levels of quality, repeatability and reproducibility of L-PBF components is extremely challenging due to a multitude of factors, such as the high number of processing variables and the physics of the underlying phenomena and transformations

that take place during component manufacturing [342]. To overcome some of these challenges substantial work has been carried out on key processing parameters (laser, scanning, recoating and build environment parameters) and powder bed properties. Also, considerable emphasis has recently been placed on process monitoring and feedback control strategies [343]. However, L-PBF has over 100 processing parameters, some of which, along with their interactions have gained little or no attention yet [344].

The location, a processing parameter of L-PBF, refers to the printing location of a part on the build platform [345]. It can cause intra-build variations that occur within one build space and potentially within one part. Recently, the location parameter has been a matter of research as it was suspected to be a contributor to variation in the final microstructure characteristics and mechanical performance of printed parts [346]. It was reported that the location can influence the final surface roughness [347]. In fact, a smoother finishing was achieved in parts located in the area close to the gas inlet and towards the build platform back location [348]. Nevertheless, thin parts having high aspect ratios are more sensitive to critical locations, thus requiring a more careful consideration [349]. It was also reported that the generation of oxidation spots and lack of fusion defects can also arise from the location parameter [350]. In this respect, the presence of oxidation spots was then attributed to the inert gas flow turbulences and so inefficiencies in preventing oxidation due to oxygen exposure. Similarly, the lack of fusion defects was related to laser attenuations due to plumes of fine particles formed from the evaporated material, to which the inert gas flow failed to ensure the laser beam quality and stability of the melting process [350,351]. Laser-spattered powder particles are detrimental for the final properties of building parts. It was reported that parts located along the inert gas flow or nearby the gas outlet are more affected by spatter [352]. Inert gas flow is also identified as one significant factor that induces microporosity during the L-PBF process and this was assumed to be due to non-uniform distribution of gas flow across the powder bed [353]. The location was also reported to have an effect on the tensile properties of parts [354,355]. Fracture critical properties are affected by numerous factors such as defect density and microstructure variation. In L-PBF, lack of fusion, cracks and porosities typically progress together with the build direction [356]. Generally assumed to be influenced by local inhomogeneities of thermal fields within the process, part density was reported to be dependent also on the location [357]. Elliptical distortions (intensity distribution and shape) of the laser spot occur when scanning parts located near the edge

of the build platform and this is due to high scanner deflection angles. Such a beam profile distortion can cause lack of fusion and produce different defects, including poor dimensional accuracies and porosity depending on the building location [358,359]. The location also affects the fatigue behavior of parts [360]. Higher fatigue life was reported on those parts printed near the front of the build platform. The reduction of fine particles and agglomerates improved powder flowability and this was found to reduce location dependency of the fatigue behavior [360]. It is also well documented that powder bed characteristics (segregation and density) varies substantially throughout the build area [361–363]. Additionally, it was reported that variation in terms of build location is also material-dependent. Therefore, some materials may be more or less sensitive to the location in which they are printed on the build platform [364].

Despite the work noted above, much remains to be systematically investigated. To address this problem, the current study isolated the location parameter to accurately assess any effect of this variable on the microstructure and mechanical properties of L-PBF manufactured parts. The outcomes of this investigation are presented and discussed in this article. However, it was not the objective of this study to critically judge any variations promoted by the location parameter for specific applications as these are dictated depending on the related industry sector requirements.

## 3.3 Experimental

### 3.3.1 Material and Sample Preparation

In this study, vacuum inert gas atomised micron size (35-50 µm) stainless steel AISI 316L powder supplied by Mimete S.r.l. was used as the feedstock material. Samples were printed with an Aconity Mini (Aconity GmbH, Germany) equipped with an ytterbium fibre laser from IPG, model YLR-200-WC-Y11, 2011 series. The laser beam spot diameter was tested and calibrated within the recommended time as instructed by the printer's manufacturer. Based on the printer's manufacturer, the laser beam intensity at the outer areas of the build platform becomes lower, but in comparison to the central area this difference in spot size and related intensity is so small that this effect can be neglected. The shape of the Gaussian laser beam was ensured by the manufacturer to be circular at the central area of the build platform. However, at high scanner deflection angles such as those required to scan the outer areas of the build platform, distortions to the laser beam cross-section could be introduced. All prints were performed in an argon

atmosphere using a volume flow rate of 3 l/min, which kept the oxygen level below 100 ppm. This fresh flow of argon entered the processing chamber through inlets located at the bottom of the build cylinder, bottom of the powder reservoir and middle of the processing chamber, while, the argon filtration and re-circulation unit provided a gas volume flow rate of 200 l/min and a gas velocity of 63 mm/s across the build platform. The argon pressure inside the processing chamber was automatically regulated to 50 mbar above the ambient pressure. To completely isolate the location parameter, all the samples were printed using the same conditions. The laser power, scanning speed, layer thickness, laser spot diameter, hatch distance and hatch translation per layer were set as 150 W, 800 mm/s, 50 µm, 50 µm, 50 µm and 25 µm, respectively. To better assess the effect of location, cubes (5x5x5 $mm^3$) and cuboids (60x8x8 $mm^3$) were strategically printed at critical locations on the build platform. These locations are at front, back, argon inlet and argon outlet as shown in Figure 3.1. The powder recoating starts at front and ends at back. Argon flows across the build platform (140 mm diameter) from the inlet to the outlet diffusor. The build direction (BD), scanning direction (SD) and hatching direction (HD) coordination are also shown in Figure 3.1. The experiment was repeated three times, with the four cubes and four cuboids per print.

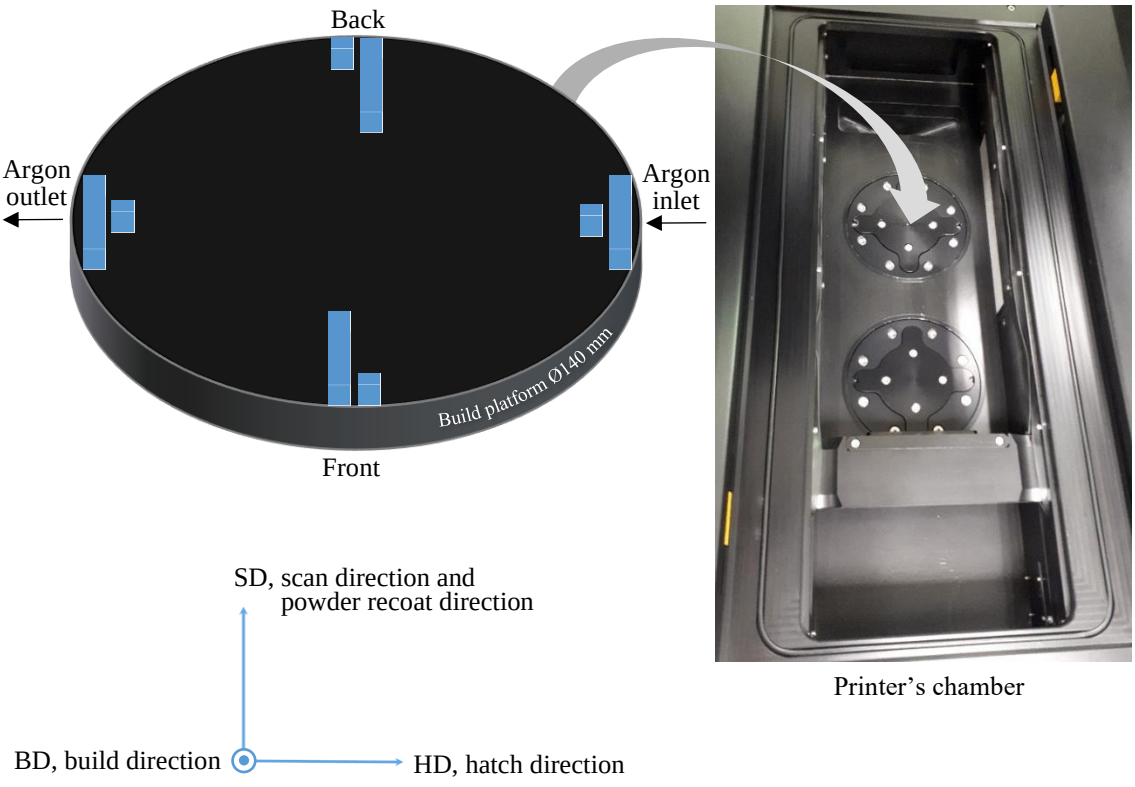


**Figure 3.1** Illustration of built parts at the selected locations on the build platform.

### 3.3.2 Sample Characterisation

The printed cuboids were machined to dimensions according to the ASTM E8 standard and used for the tensile testing [365]. The cubes were used to assess the effect of location on the density, hardness, microstructure and corrosion properties of the samples. Archimedes density testing was performed in accordance with the ASTM standard B962 [366]. The measurements were conducted on a Sartorius YDK01 density determination kit coupled onto an Avery Berkel FA215DT density scale, where, deionised water (at room temperature) was used as the immersion liquid while determining the density. For robustness and cross checking of the measurement, the density of the printed samples was also measure with a Micromeritics AccuPyc 1330 helium pycnometer, where in each run the instrument reported the average density and standard deviation calculated from ten measurements. Prior to the hardness measurements and crystallographic analyses, the samples were ground with abrasive SiC papers and polished with 60 nm silica suspension, followed by ultrasonic cleaning in deionised water and drying with nitrogen gas. The Vickers hardness of the samples was measured using a Leitz microhardness tester and the measurements were performed according to ASTM E92 standard [367]. A nanoindenter (Bruker Hysitron TI Premier, USA) equipped with a standard Berkovich diamond indenter was used for nanohardness measurement of the samples. An array of sixteen nanoindentations was performed in the centre of each metallography sample with a 10 mN load (indentation depth around 300 nm) and intervals of 200 µm between indentations. The tensile test was performed using a Zwick Z050 (Zwick/Roell GmbH, Germany) computer-controlled tensile tester equipped with an Epsilon clip-on extensometer model 3542. A JEOL JSM-IT100 scanning electron microscope and a Keyence VHX2000E optical 3D digital microscope were used to obtain microstructural data. Crystallographic information about the samples was obtained using a triple-axis Jordan Valley Bede D1 high resolution X-ray diffraction system with a copper ($\lambda = 1.5405$ Å) radiation source operated at 45 kV and 40 mA, and a Zeiss Merlin field emission scanning electron microscope equipped with a EDAX/TSL EBSD system and a Hikari EBSD camera.

The electrochemical behaviour of the samples was investigated using a Gamry Reference 1000E potentiostat in a standard three-electrode cell. A saturated calomel electrode (SCE) and a high-density graphite rod were taken as the reference and the counter electrode, respectively, and the sample as the working electrode. Prior to electrochemical testing,

the samples were ground with abrasive SiC papers and polished with 60 nm silica suspension, followed by ultrasonic cleaning in deionised water and drying with nitrogen gas. A surface area of 0.25 $cm^2$ was exposed to the electrolyte solution of 3.5% w/v NaCl $H_2O$ during electrochemical testing. Initially, the working electrode was immersed in the electrolyte solution and kept at open circuit potential (OCP) for up to 2 hours for stabilisation, or until the potential variation was below 0.05 mV/s. Potentiodynamic polarisation behaviour was recorded at a scan rate of 1 mV/s, scanning from -0.5 V (vs. OCP) to an apex potential of 1.5 V (vs. OCP), or until the apex current density of 25 $mA/cm^2$ was measured during anodic polarisation, followed by a reverse scan back to 0.2 V (vs. OCP) at the same scan rate of 1 mV/s. Electrochemical impedance spectroscopy (EIS) was performed at OCP over a frequency ranging from 100 kHz to 10 mHz by applying a small alternating current perturbation of ±5 $mV_{rms}$. All electrochemical measurements were repeated three times. Electrochemical circuit modelling of the EIS data was performed using Gamry Echem Analyst version 7.8.2.

## 3.4 Results and Discussion

### 3.4.1 Effect of Part Location on Part Properties

#### 3.4.1.1 Microstructure

The microstructure was characterised on the plane perpendicular to the build direction. Figure 3.2 shows that the laser meltpools were elongated along the laser scanning direction and that their geometrical features (formed patterns) varied according to their stabilities and surrounding conditions. Laser track meltpool anomalies such as inconsistencies (Figure 3.2c) and discontinuities (Figure 3.2b) could affect the crystallographic textures formed within the built part and the deformation mechanisms active in the deformation process, which could result in different mechanical properties. Porosity, which is a common defect in L-PBF processed 316L [368] was observed for all the samples as highlighted in Figure 3.2d. Here, the existence of porosity could be due to the stability, behaviour, and dimensions of the meltpools and the applied input parameters, in addition to related process phenomena and phase transformations that took place during printing. It was reported that failure of the meltpool to wet the surrounding material resulting from oxides at the side of the meltpool create regions of weakness and porosity [369]. Similarly, incomplete homologous wetting and solidification cause the molten material to have discontinuous propagation down with the previous layer which

can result in spherical or irregular-shaped pores [370]. Porosity may also be formed when gases entrapped in the powder bed and powder particles dissolve in the meltpool and remain after solidification due to the high cooling rate [371]. Also, trapped within the solidified melt region, keyhole pores are formed when high enough energy densities are used. This is because the L-PBF welding regime changes from conduction (shallow and semi-circular meltpool shape) into keyhole mode (deep and narrow meltpool shape). Typically unstable, the keyhole mode can form pores due to metal vapour bubbles entrapped by solidification [372]. Meltpool instabilities appear at low laser scanning speeds in the form of distortions and irregularities, while excessively high laser scanning speeds give rise to the balling phenomenon. Balling, a manifestation of Plateau Rayleigh instability, can occur when the meltpool elongates and becomes unstable, breaking up into small islands [373]. Both balling (small spherical balls) and laser splashed particles (spatter) decorating the lased surface usually lead to the formation of irregular shaped pores.

The origin of defects in L-PBF is often related to the Plateau Raleigh capillary instability, Marangoni effect, vapour recoil pressure, Kelvin-Helmholtz hydrodynamic instability and external influences. The hydrodynamic instability of the meltpool known as the Kelvin Helmholtz hydrodynamic instability can cause humping (periodic occurrence of beadlike protuberances). Humping occurs when the velocity of the liquid metal at the top of the molten pool is lower than the inert gas velocity. This difference in velocities prompts the Kelvin Helmholtz hydrodynamic instability which occurs when the ratio of buoyancy force to shear force (Richardson number) is less than 0.25 [374]. The fluctuations of surface morphology can therefore lead to pore concentrations around the valleys. Resulting typically from the usage of very high laser scanning speeds and high laser powers, humping may greatly deteriorate the mechanical performance of printed components [375]. Similarly, insufficient heat input leads to lack of fusion defects. Figure 3.2b shows a lack of fusion void present in the microstructure of the argon outlet sample. It exhibits a high aspect ratio and preferred alignment with layer boundaries in the laser scanning direction. The formation of lack of fusion at the argon outlet could be related to argon flow separation and turbulences at this location. These could then increase the laser attenuation in response to the inert gas inefficiency in removing spatter and vapour plume emissions [376]. Consequently, reducing the depth and width of meltpools. The microstructure of L-PBF processed 316L is fully austenitic and it has been frequently

reported to consist of columnar grain structure [377,378]. The formation of columnar grains along the build direction is as a result of severe thermal gradient due to the heat sink of the previous layer. It can also be attributed to the formation of wider and shallower meltpools as a result of high laser power and decrease in cooling rate. The sample printed at the front of the build platform also exhibits banded grains grown through and perpendicular to meltpool boundaries, Figure 3.2a. As such the microstructure of elongated, banded grains, are particularly susceptible to intergranular corrosion. The severity of intergranular corrosion will depend on the extent to which grains elongated and banded, in addition to the continuity of the anodic path at grain boundaries [379–381]. On the other hand, the presence of banded grains in the sample can help to reduce brittleness as cracks moving through it may be deflected parallelly to the grains [382]. A recent study which obtained a similar grain structure to this study reported that the achieving of a high strain hardening rate was due to higher crystallographic texture dependent twinning [383]. Therefore, to some extent this finding can be related with the work hardening behaviour of the front location sample.

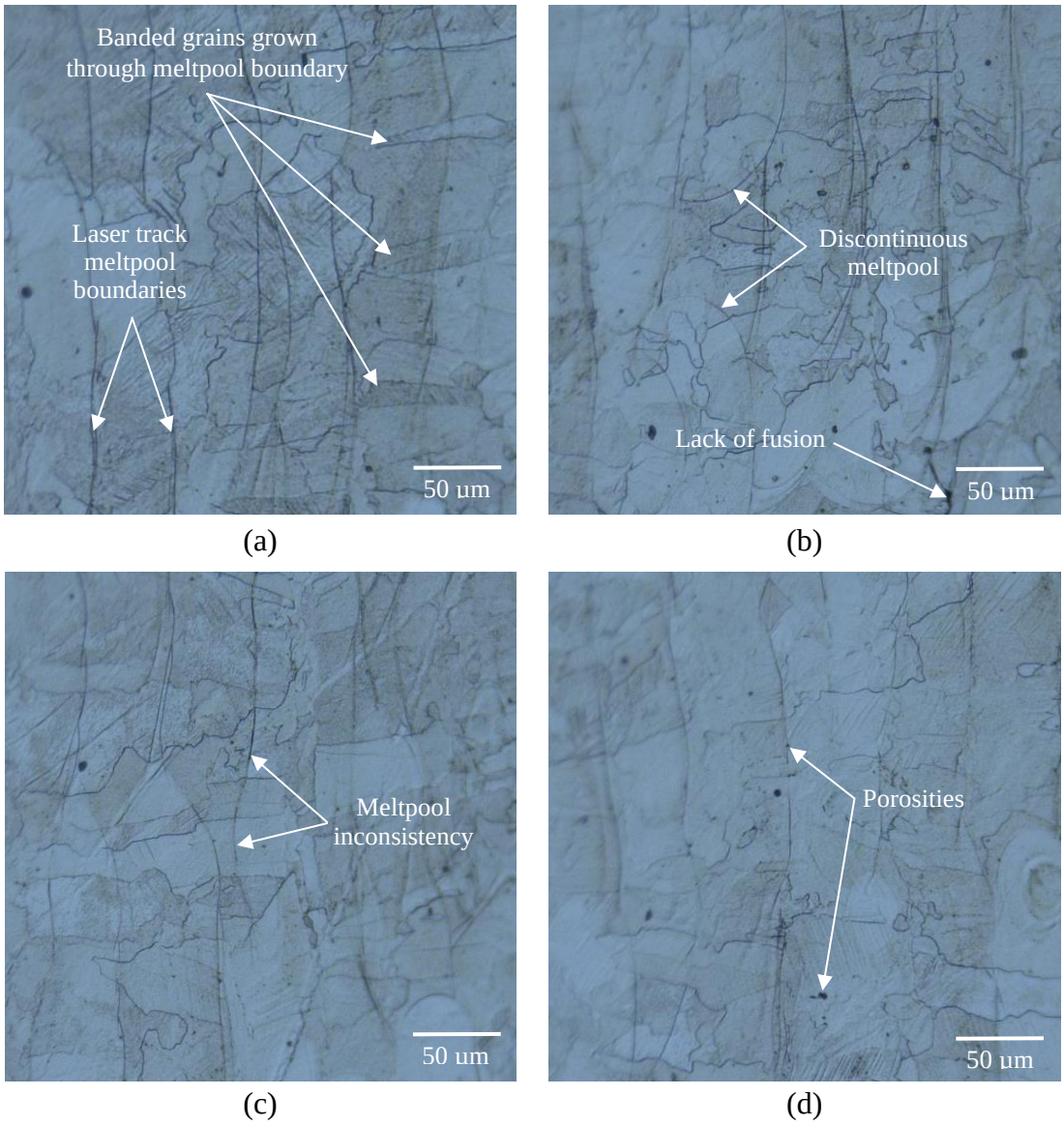


**Figure 3.2** Optical micrographs showing microstructures at the: (a) front, (b) argon outlet, (c) back, and (d) argon inlet locations.

The samples were also investigated via electron scanning microscopy in order to obtain additional information about their microstructure. The common features observed in the samples are shown in Figure 3.3. Porosity defects were observed in all of the samples and this was found to be more pronounced in the argon outlet sample. The appearance of porosity defects was observed to be somewhat random within a given microstructure. Based on the clean nearby microstructure and the solidified molten boundaries around them it could be said that they emerged due to local instabilities in the molten metal track. Porosities with up to 20 µm in diameter were observed in the samples. However, most of the pores were spherical and <10 µm in diameter, suggesting gas entrapment during the solidification process. It is possible that the local instabilities in the molten region induced

the deep or keyhole mode in response to the evaporation of elements. This evaporation could then cause instantaneous volume expansion and produce pressure on the meltpools. Consequently, strong stirring and accelerated flow velocities in the liquid meltpools could have involved and strapped ambient gas. Therefore, when the recoil pressure became high and the surface tension become low, the gas bubbles descended near the bottom of meltpools. During this period, some gas bubbles could have escaped and others coalesced and trapped in the microstructure due to the fast cooling, which is a characteristic of the L-PBF process. Therefore, as the lifetime and depth of the keyhole mode meltpools are larger than that of the conductive mode meltpools, it could be said that the large pores within the microstructure of the samples are related to a local keyhole mode of melting. Interestingly, the back sample was the sample most affected by pores and these were rather elongated. An obvious explanation to this is the contamination of the powder bed in this region from spatter particles. Due to the alignment of the front sample with the back sample in the powder recoating direction, the collapsed spatter particles near the front sample were mixed with the virgin powder during the spreading of consecutive powder layers which then formed contaminated powder beds at the back sample location. In agreement with these results, Karimi et al. [346] reported a 20 % increased level of defects, mainly pores, in those samples printed near the corners of the build platform. To which, the formation of porosity was attributed to an existing higher cooling rate at these locations, accompanied by reduced liquid metal flow and shrinkage due to a lower specific volume of the solidified material than that of the melted material. Obeidi et al. [384] who also reported similar densities and microstructures to this work correlated the poor tensile performance of the samples to the keyhole pores and lack of fusion defects. It was noted in this work that the laser power and scanning speed play an important role in the development of such defects. Here, the fast solidification and cooling also induced the growth of very fine cellular structures within the microstructure of the manufactured samples, with cell widths of apparently only several hundred nanometers. According to the Hall-Petch relationship the strength of the material scales with the cell size [385]. While the elongation of the cells correlates to the progressive and steady strain hardening mechanism provided by the abundant and complicated interactions between dislocations and cells [386–388]. Therefore, the existing cell structures had a positive contribution to the mechanical properties of the samples. This is in agreement with the literature which reports cellular structures led-improvements in yield strength, hardness and fatigue performance [389–391].

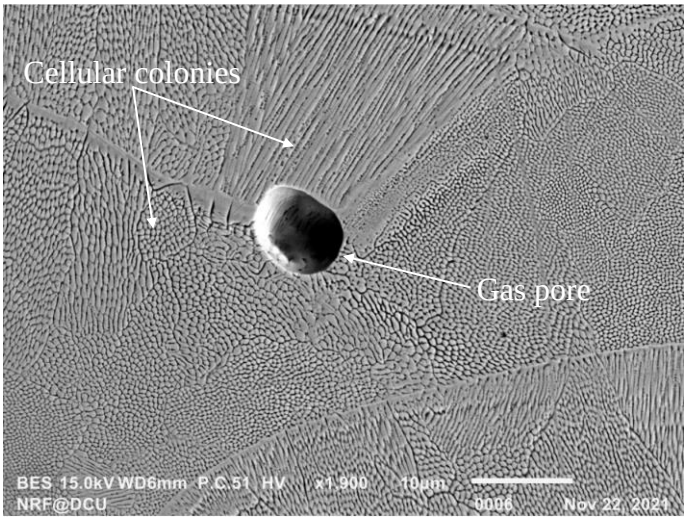


(a)

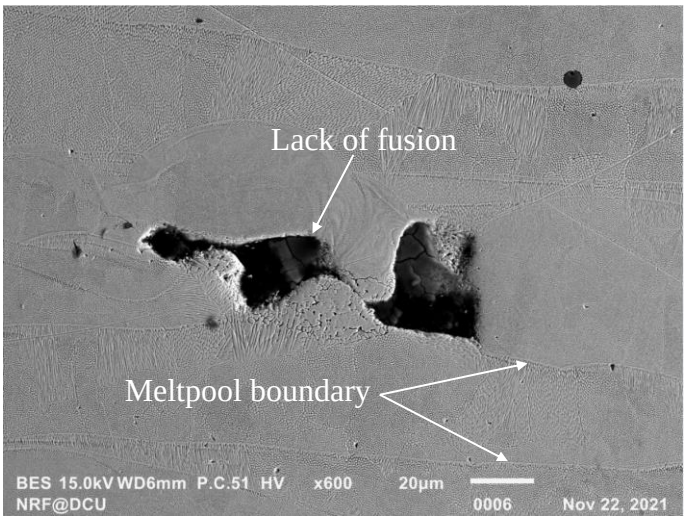


(b)

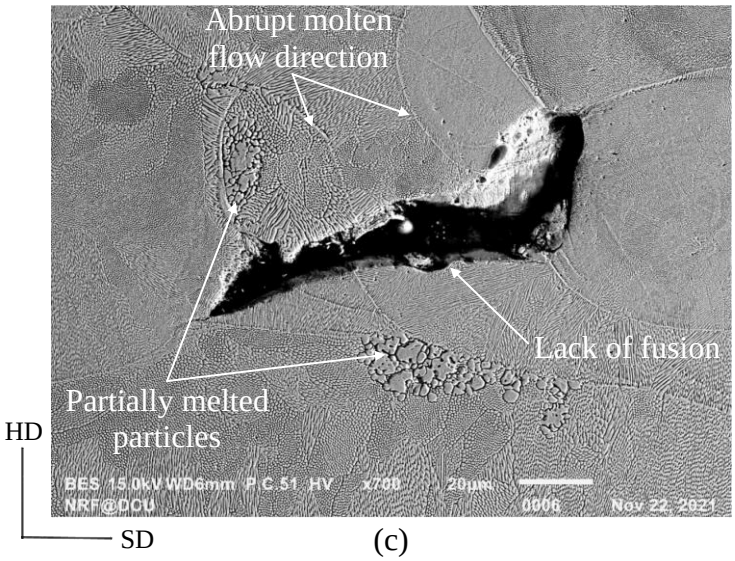


(c)

**Figure 3.3** Backscattered electron micrographs showing the lack of fusion and porosity defects and the existence of subgrain cellular structures in the microstructure of the samples.

#### 3.4.1.2 Grain Size

The effect of the build location parameter on grain size is contrasted in Figure 3.4. The results show a trend in the relationship between the average grain size and the sample print location, in which, two distinct grain size groups exist. The front and back locations led to the growth of several coarse grains (>45 µm). In contrast, the argon outlet and argon inlet locations led to the growth of relatively finer grains. Clearly, the high alignment of the argon outlet and argon inlet samples with the flowing argon stream, see Figure 3.1, resulted in a slightly higher cooling rate. Consequently, grain size became relatively uniform and finer. As all of the four samples were printed in the same build and using the same input processing parameters, one would hypothesise the build location to have no effect on grain size. However, the results showed that the location parameter plays a contributing role to grain refinement. Additionally, despite the observed grain size refinement being only 2 µm, when considering all the resulting microstructure features together, the final mechanical performance of each individual sample can be different.

In the literature, the Hall-Petch equation expresses that the hardness increases as 1/ grain size$^{0.5}$ [392]. This means that smaller grain-sized material is harder. In a harder material, higher applied stresses are required to propagate dislocations through it, which is the case for small grain-sized materials, where the role of the grain boundaries in preventing dislocation propagation becomes progressively pronounced, leading to increased stress concentration at grain boundaries due to dislocation pile up.

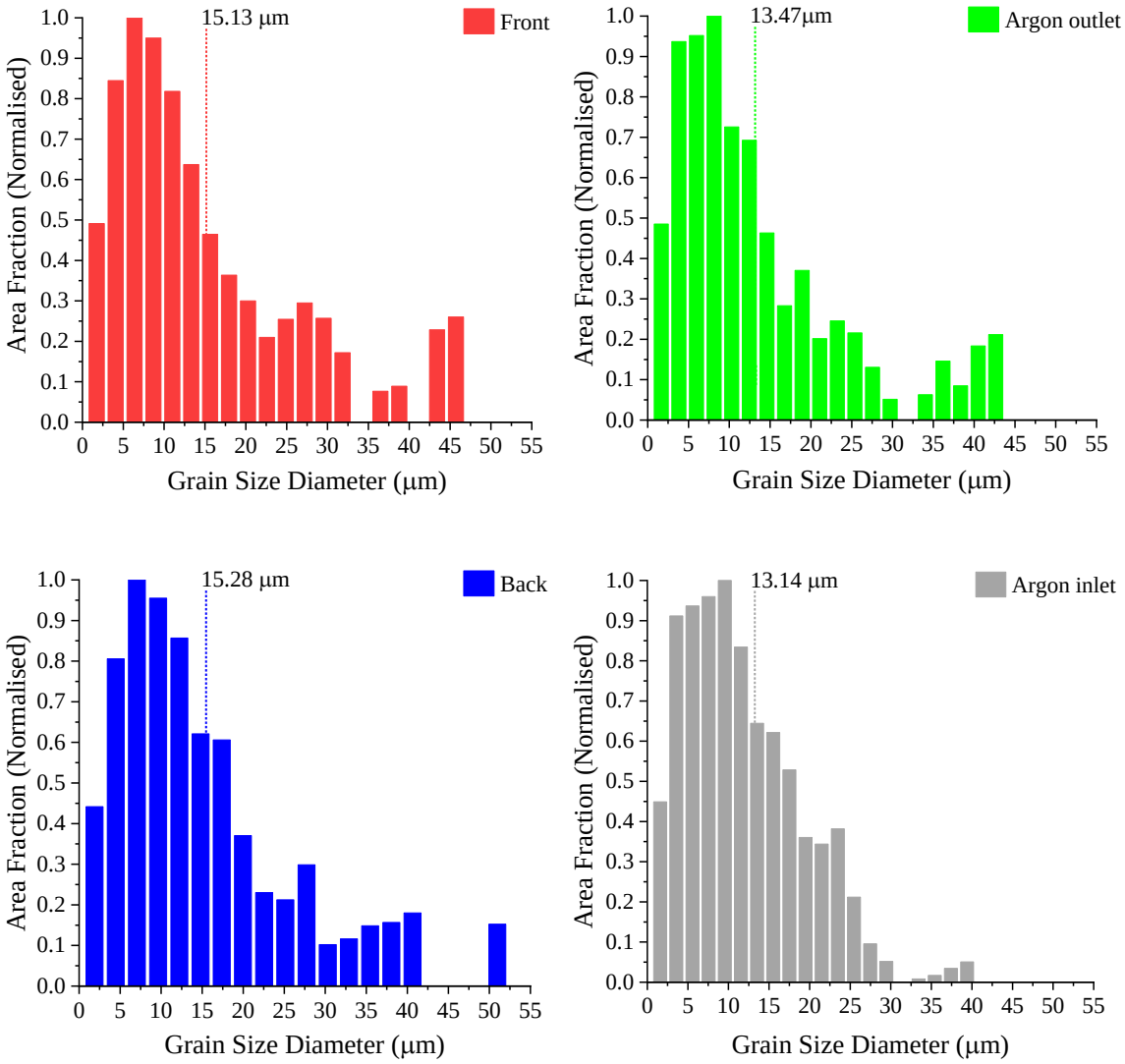


**Figure 3.4** Electron backscatter diffraction quantitatively measured grain size distribution contrasting the effect of sample build location.

### 3.4.1.3 Density

Density is an important physical property influencing the mechanical integrity of parts. Hence, it is used as a measure of part quality [393]. In L-PBF, the density of parts is generally discussed as being influenced by the laser and scanning parameters which can lead to defects in the part such as lack of fusion, voids and pores [394,395]. The study presented here indicates that part density is also influenced by the part build location. In order to properly assess the influence of the build location on part density, the density of the 316L powder used to print the samples was measured via helium pycnometry. The measured powder density of 7.82 g/cm$^3$ was then assumed to be the true density of the 316L. Table 3.1 shows that part density varies substantially throughout the build space.

The highest density was measured for those parts printed at front and the lowest density was measured for those parts located near the argon outlet. There are various contributors to density anisotropy within the build space. However, here, the main contributors were the powder bed packing density and the process by-product known as spatter. Particle size segregation takes place along the powder recoating direction, therefore, from the front to the back location. At the front, finer particles contained in the powder ensures a higher powder bed packing density at this location [361,396]. At the back, there exists a lower packing efficiency due to the lack of fine particles and so voids are left between the coarser particles [361,397]. One of the functions of the argon flow is to prevent in-flight spatter from collapsing onto the build platform. The likelihood that some spatter will collapse onto a building surface located near the argon outlet is much higher than that of the argon inlet. Therefore, the difference in density between the parts located near the argon inlet and argon outlet is predominantly due to a spatter-induced defect within the bulk part. Spatter is detrimental and its formation should be minimised [352]. Furthermore, the results indicated that a higher powder bed packing density is key to achieving higher part densification.

**Table 3.1** The density of the samples with respect to their printing location on the build platform. The uncertainty was estimated with a 95% confidence interval.

| **Sample** | **Archimedes method (g/cm$^3$)** | **Helium pycnometry (g/cm$^3$)** |
|---|---|---|
| Front | $7.48_{\pm 0.034}$ | $7.40_{\pm 0.030}$ |
| Argon outlet | $7.07_{\pm 0.060}$ | $7.00_{\pm 0.035}$ |
| Back | $7.31_{\pm 0.020}$ | $7.30_{\pm 0.018}$ |
| Argon inlet | $7.37_{\pm 0.036}$ | $7.35_{\pm 0.027}$ |

#### 3.4.1.4 Microhardness

It is evident that the location also has an influence on the samples microhardness, see Figure 3.5. Parts printed near the argon outlet are more liable to internal defects. However, as the highest hardness was measured at those parts printed near the argon outlet it is possible that the microstructural characteristics of the samples varies with the location. Therefore, the observed discrepancies in hardness may be attributed to different grain size and texture induced by the location parameter. One big player to this is the

argon flow as it influences the cooling rate and cooling direction depending on the part location.

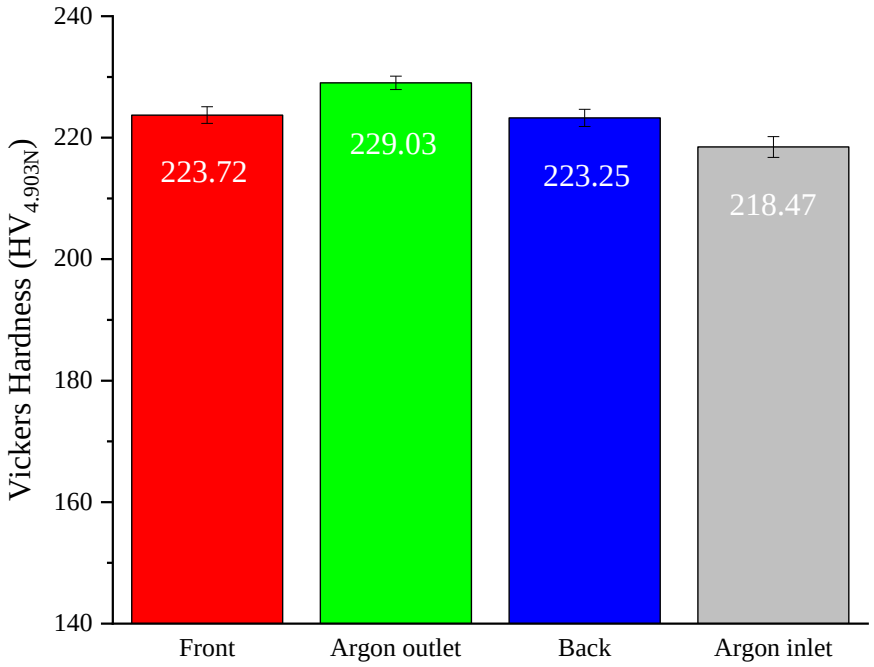


**Figure 3.5** Microhardness of the printed samples with respect to part location on the build platform. The uncertainty was estimated with a 95% confidence interval.

#### 3.4.1.5 Nanohardness

Figure 3.6 shows the nanoindentation load-displacement curve and the measured nanohardness, reduced modulus and the calculated nanoindentation parameters of the printed samples. The load-displacement curves depict an elastic-plastic deformation behaviour. It was observed that the sample located near the argon inlet showed the largest penetration depth. The argon outlet and back samples showed similar load-displacement curves and a higher resistance to plastic deformation, which implies a higher hardness and stiffness. The nanohardness values are aligned with the microhardness results. Both indicate the highest hardness on the sample located near the argon outlet and the lowest hardness on the sample located near the argon inlet. It was reported elsewhere and it is in this case possible that there is a dependence of hardness on crystal orientation [398]. The results of the crystallographic analysis will be presented and discussed in section 3.1.6. The reduced modulus $E_r$ obtained from the nanoindentation test represents the elastic deformation that occurs in both sample and indenter tip [399]. The indentation modulus $E$ is comparable with the Young's modulus of the material and it can be expressed as:

$$E = \frac{(1 - v^2)}{\frac{1}{E_r} - \frac{(1 - v_i^2)}{E_i}}$$

where $v$ is Poisson's ratio for the sample, $E_i$ and $v_i$ are the elastic modulus and Poisson's ratio for the indenter. For the Berkovich diamond indenter, the values of $E_i$ = 1140 GPa and $\nu_i$ = 0.07 are frequently used [400] and the Possion's ratio of L-PBF processed 316L was taken as 0.25 [401]. The calculated Young's modulus for the front, argon outlet, back and argon inlet samples are 220.46, 225.88, 222.43 and 203.79 GPa, respectively. These results indicate that the nanohardness tends to increase with an increase in Young's modulus. The elastic and plastic behaviour of the samples were further assessed from the nanoindentation results by evaluating the elastic recovery index $(W_e/W_t)$ and plasticity index $(W_p/W_t)$. The elastic recovery index provides information about the energy released from the material under mechanical loading, while the plasticity index provides information about the intrinsic plastic behaviour of materials [402,403]. Although material hardness is a crucial parameter controlling wear, other parameters in the nanoscale such as the ability of a material to resist elastic strain $(H/E_r)$ and the material's resistance to plastic deformation in loaded contact $(H^3/E_r^2)$ are also used to understand the wear behaviour of materials [404,405]. The highest elastic recovery index was obtained for the argon outlet sample and the lowest for the argon inlet sample, see Figure 3.6c. Here, a general correlation between hardness and elastic recovery index exists, where elastic recovery index increases with increasing hardness. The argon inlet sample showed the largest intrinsic plasticity, which implies that it experienced the least hindrances to plastic deformation owing to its higher ductility. From the results, it is observed that the argon outlet and back samples depict the highest resistance to elastic strain to failure. This suggests that these samples can allow redistribution of the load over a larger zone and thus lead to a delay in surface failure. Figure 3.6c also shows the effect of printing location on the $(H^3/E_r^2)$ parameter. It indicates that the argon outlet sample has higher wear resistance to wear caused by gradual removal of material driven by plastic deformation. It is observed that the elastic recovery index, resistance to elastic strain and the resistance to plastic deformation of the samples are directly proportional; they also follow the same trend as the nanohardness and reduced modulus. For some metals like stainless steels, the strength of a material is related to its hardness and a material with higher hardness retains a higher strength [406]. From the reported

nanoindentation parameters, it can be said that discrepancies between samples may be ascribed to differences in the microstructure, as a smaller measured grain size is related to a high hardness [407].

(a)

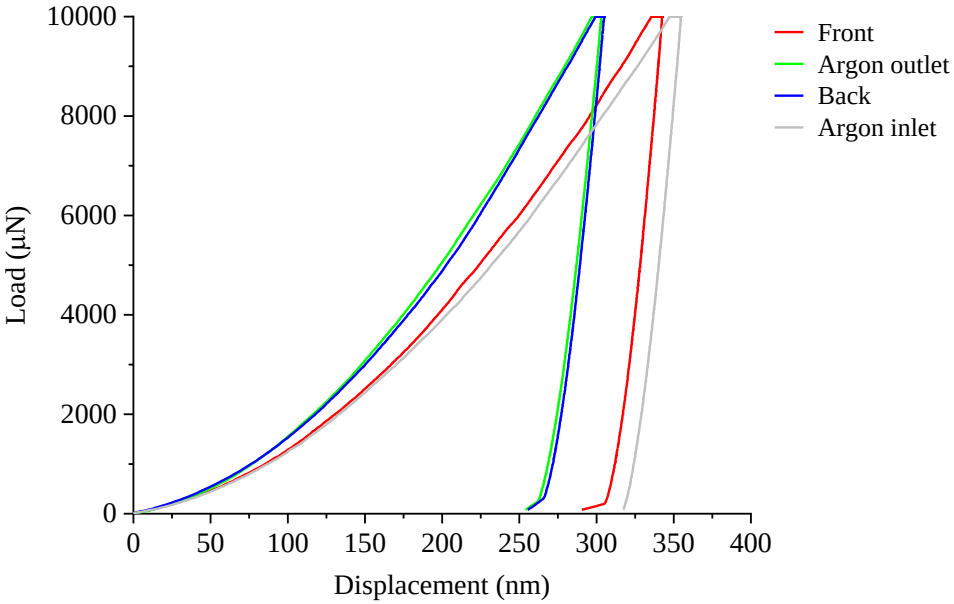


(b)

| Location | Nanohardness (GPa) | Reduced Modulus (GPa) |
|---|---|---|
| Front | $3.42_{\pm 0.14}$ | $195.11_{\pm 4.28}$ |
| Argon outlet | $4.46_{\pm 0.22}$ | $199.07_{\pm 3.26}$ |
| Back | $4.38_{\pm 0.31}$ | $196.55_{\pm 6.08}$ |
| Argon inlet | $3.17_{\pm 0.07}$ | $182.71_{\pm 3.48}$ |

(c)

| Location | $W_e/W_t$ | $W_p/W_t$ | $H/E_r$ | $H^3/E_r^2$ (MPa) |
|---|---|---|---|---|
| Front | 0.121 | 0.879 | 0.018 | 1.05 |
| Argon outlet | 0.153 | 0.847 | 0.022 | 2.24 |
| Back | 0.150 | 0.850 | 0.022 | 2.18 |
| Argon inlet | 0.115 | 0.885 | 0.017 | 0.95 |

$W_e$, $W_p$ and $W_t$ indicate recoverable elastic work, residual plastic work and total work [408,409].

$H$ and $E_r$ indicate nanohardness and reduced modulus, respectively.

**Figure 3.6** Nanoindentation data: (a) load-displacement curve, (b) measured nanohardness and reduced modulus and (c) calculated nanoindentation parameters of the printed samples. The uncertainty was estimated with a 95% confidence interval.

### 3.4.1.6 Tensile Properties

The tensile performance of the samples based on their location is presented in Figure 3.7. Similar tensile properties were obtained from the front, back and argon inlet samples, however, the highest yield strength as well as the highest ductility were both found in the argon inlet sample. It was reported that grain refining increases yield strength while also improving toughness [410–412]. Therefore, in the case of the argon inlet sample, the strengthening occurred through the increase in grain boundary area. This would make crack propagation more difficult, as to go across a fine grained material, a crack would require to be initiated in and cross over many grains. This would require a great amount of energy and consequently raising the energy to fracture. The negative effect of the argon outlet location on the tensile properties is clear from Figure 3.7a and Figure 3.7b. The inferior tensile strength of the argon outlet sample could be due to several factors such as microstructure, crystallographic texture and porosity. It was reported that low elongation to failure could be attributed to a combination of factors such as dislocation pileup at grain boundaries and the presence of irregularly shaped defects like lack of fusion porosity [413]. Poor elongation to failure is most likely attributed to the presence of lack of fusion defects. The presence of such defects having a high aspect ratio oriented perpendicularly to the uniaxial testing direction could act as stress concentrators, therefore leading to a decrease in tensile ductility. The argon outlet location is the location on the build platform most affected by spatter [414]. In L-PBF, spatter residing near or onto a building surface can alter powder redistribution, cause agglomerations, contamination and loss of powder, which are known to contribute to defect formation.

In order to understand the work hardening behaviour of the samples, the instantaneous strain hardening rate was considered. Kocks-Mecking plot illustrating strain hardening rate ($\theta = d\sigma/d\varepsilon$) as a function of net flow stress ($\sigma - \sigma y$) is depicted in Figure 3.7c. In polycrystals, stage I hardening is absent and stage II hardening often degenerates into a low strain limit that is athermal [415,416]. Stage I hardening depends strongly on the crystal orientation and if deformation takes place through multiple slips it might not be observed. Stage II hardening is governed by the interaction of dislocations belonging to the primary slip system with those moving through the intersecting slip system [417]. Both of these stages were missing in the present investigation. The samples exhibited instead a different type of two-stage work hardening behavior, Stage III and IV. This is shown by a distinct sharp decline in strain hardening rate (transient stage) followed by a

gradual nearly linear decrease at high stresses (stage IV hardening). At the elastoplastic transition, Stage III hardening, the strain hardening rate underwent a drastic reduction. While at the dislocation storage process, stage IV hardening, it was observed a nearly constant strain hardening rate [418]. The higher strain hardening rate of the front and argon outlet samples in the early stages of deformation can be attributed to a higher rate of primary twinning formation and twin density. The favorable effect of twinning on strain hardening capacity at stage IV hardening of the argon inlet region could be related to the the dynamic Hall-Petch effect of reduction of the dislocation mean free path, as twin boundaries provide high energy obstacles to dislocation glide. This inferred influence from the results presented herein from the microstructure and the texture has been noted previously [419,420].

(a)

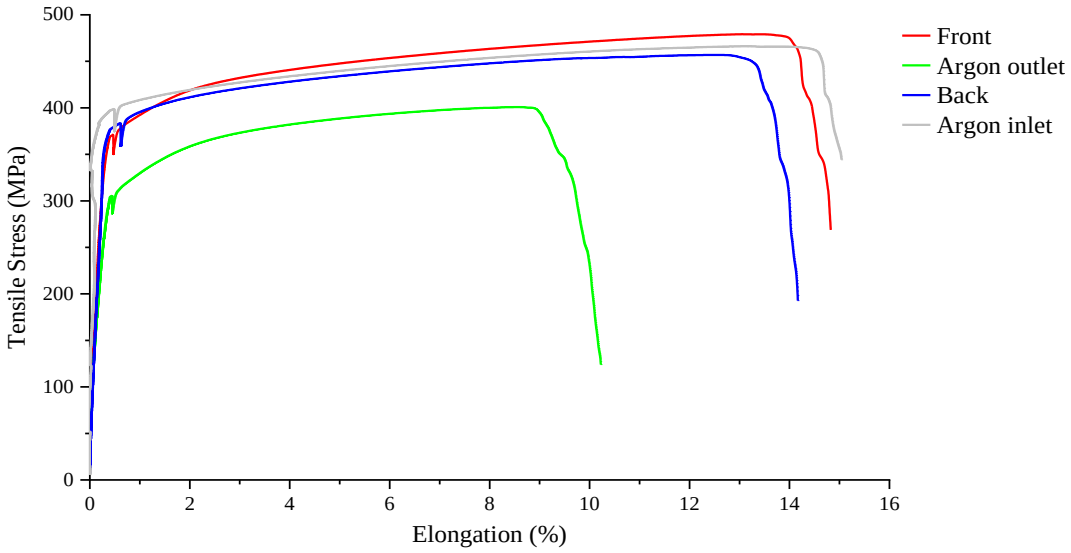


(b)

| Location | Modulus of Elasticity (GPa) | Tensile Strength, Yield (MPa) | Tensile Strength, Ultimate (MPa) |
|---|---|---|---|
| Front | $146.49_{\pm 2.99}$ | $393.89_{\pm 27.57}$ | $475.83_{\pm 21.59}$ |
| Argon outlet | $129.61_{\pm 3.00}$ | $293.42_{\pm 9.29}$ | $344.46_{\pm 41.91}$ |
| Back | $140.21_{\pm 5.22}$ | $381.25_{\pm 39.14}$ | $458.38_{\pm 37.95}$ |
| Argon inlet | $144.77_{\pm 4.32}$ | $403.63_{\pm 6.47}$ | $459.01_{\pm 11.79}$ |

(c)

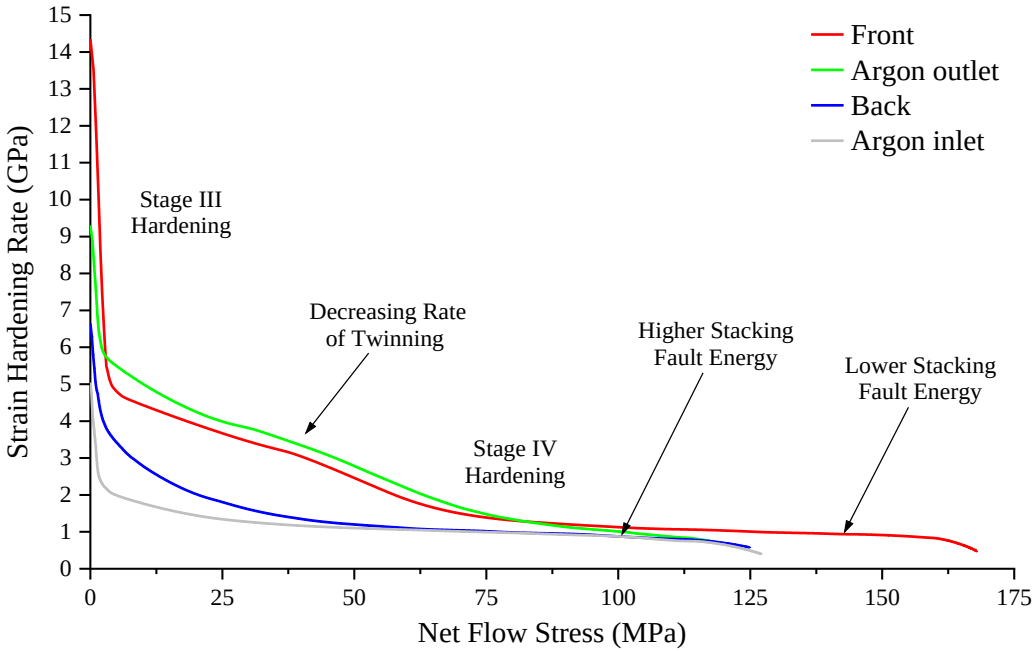


**Figure 3.7** (a) Tensile curve of samples printed at critical locations, (b) their respective tensile properties and (c) Kocks-Mecking analysis of work hardening. The uncertainty was estimated with a 95% confidence interval.

### 3.4.1.7 Crystallography

A comparison of the X-ray diffraction patterns for the samples is shown in Figure 3.8. The face-centered cubic peaks (111), (200), (220) and (311) corresponding to the crystalline austenite phase were identified and agree with previous results in the literature [421,422]. A considerable change in relative intensities was observed in all samples, mainly through the (111) and (200) peak intensity distribution. This suggests the presence of different crystallographic texture effects between samples generated by the location parameter. The X-ray peak broadening could be due to lattice defects such as microstrains, crystallite sizes and process-induced dislocations [423]. Similarly, the diffraction line shifts, noticeable from the 2θ angles listed in Table 3.2, could be a result of stress imbalance at grain boundaries and spatter induced composition changes introducing foreign atoms in the lattice, hence changing the lattice size.

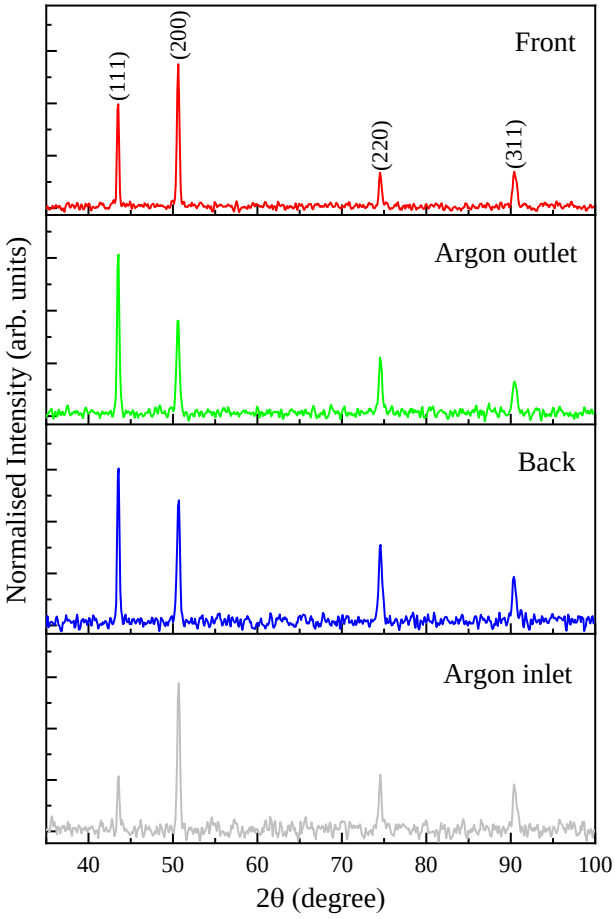


**Figure 3.8** X-ray diffraction spectra of the printed samples in dependence of the part location on the build platform.

The stacking fault energy represents the barrier level for the dissociation of a perfect dislocation into Shockley partial dislocations and the susceptibility for formation of stacking faults [424–426]. Partial dislocations are known to play unique roles in twinning, phase transformations and formation of dislocation barriers. Hence, the stacking fault energy is an important parameter to determine the deformation schemes. Here, the stacking fault probability ($P_{sf}$) and root mean square microstrain ($\langle\varepsilon_{50}^2\rangle_{111}$) were determined by analysing the X-ray diffraction peak profiles as described in reference [427]. Then, the stacking fault energy was calculated using the well-established Reed and Schramm's relationship [428].

$$Stacking\ fault\ energy = \frac{6.6\ a_0}{\pi\sqrt{3}} \left(\frac{2C_{44}}{C_{11} - C_{12}}\right)^{-0.37} \frac{\langle\varepsilon_{50}^2\rangle_{111}}{P_{sf}} \left(\frac{C_{44} + C_{11} - C_{12}}{3}\right)$$

where $a_0$ is the lattice parameter, and the elastic constants $C_{11}$, $C_{12}$ and $C_{44}$ of stainless steel AISI 316L were adopted from reference [429]. The calculated stacking fault energies are shown in Table 3.2 for the respective part locations. All the samples presented similar and relatively low stacking fault energy of ~25 mJ/m$^2$, which favours deformation-induced twinning. In general, it has been known that the stacking fault energy varies depending on temperature, concentration of alloying elements, grain size and strain. In fact, during tensile testing, the stacking fault energy decreases with increasing strain [430–432]. Where this is associated with deformation activity changes from dislocation slip to twinning as straining. Based on this and on the results seen until now and also knowing that low stacking fault energy relates to high strain hardening rate, the higher strain hardening rate of the front sample seen in Figure 3.7c can be attributed to a longer twinning period due to much earlier manifestation of the critical resolved shear stress for twinning, in addition also to possibly larger amounts of stacking faults which increase the stacking fault probability, consequently causing the decrease of the stacking fault energy.

**Table 3.2** X-ray diffraction data, interplanar spacing and stacking fault energy of the printed samples.

| Sample | (hkl) | 2θ (degree) | FWHM (degree) | d-spacing (nm) | Stacking Fault Energy ($mJ/m^2$) |
|---|---|---|---|---|---|
| Front | 111 | 43.493 | 0.140 | 0.208 | 24.833 |
| | 200 | 50.619 | 0.173 | 0.180 | |
| | 220 | 74.552 | 0.189 | 0.127 | |
| | 311 | 90.479 | 0.313 | 0.108 | |
| Argon outlet | 111 | 43.519 | 0.160 | 0.208 | 25.198 |
| | 200 | 50.593 | 0.209 | 0.180 | |
| | 220 | 74.573 | 0.214 | 0.127 | |
| | 311 | 90.471 | 0.330 | 0.108 | |
| Back | 111 | 43.535 | 0.154 | 0.208 | 24.658 |
| | 200 | 50.651 | 0.205 | 0.180 | |
| | 220 | 74.570 | 0.243 | 0.127 | |
| | 311 | 90.396 | 0.248 | 0.109 | |
| Argon inlet | 111 | 43.542 | 0.160 | 0.208 | 24.652 |
| | 200 | 50.672 | 0.183 | 0.180 | |
| | 220 | 74.544 | 0.158 | 0.127 | |
| | 311 | 90.401 | 0.284 | 0.109 | |

During the L-PBF processing of 316L, columnar grain growth is determined by heat flow direction and influenced by the process input parameters. Within the columnar grains, cellular structures tend to grow perpendicularly to the liquid-solid interface regardless of crystal orientation. However, when the growth rate increases then the direction of cell growth diverges towards the preferred crystallographic growth direction. Therefore, it is important to determine the influence of the location parameter on crystallographic texture in order to understand the mechanical behaviour of the printed samples.

Typically, in L-PBF columnar grains grow elongated along the build direction [433]. Therefore, when viewed from the plane normal to the build direction, depending on the applied scanning strategy, grains can exhibit equiaxed, banded and or irregular faceted morphologies [434–436]. Figure 3.9 presents electron backscatter diffraction maps contrasting the effect of sample build location on grain orientation. With reference to the inverse pole figure colour coded map, it can be seen that the crystallographic orientation of the samples is mainly in the <001> orientation. However, the argon outlet and argon inlet samples showed a higher number of grains oriented between <001> and <101> (yellow coloured). As the location of these two samples was perfectly aligned with the

flowing argon stream, they possibly experienced a higher cooling rate and so a higher horizontal cooling gradient. It is also worth mentioning that the formed and seen grain patterns resulted from the applied scanning strategy. Additionally, as it is observed, the applied 50 % hatch translation per layer play a major role in grain downsizing and grain size uniformity.

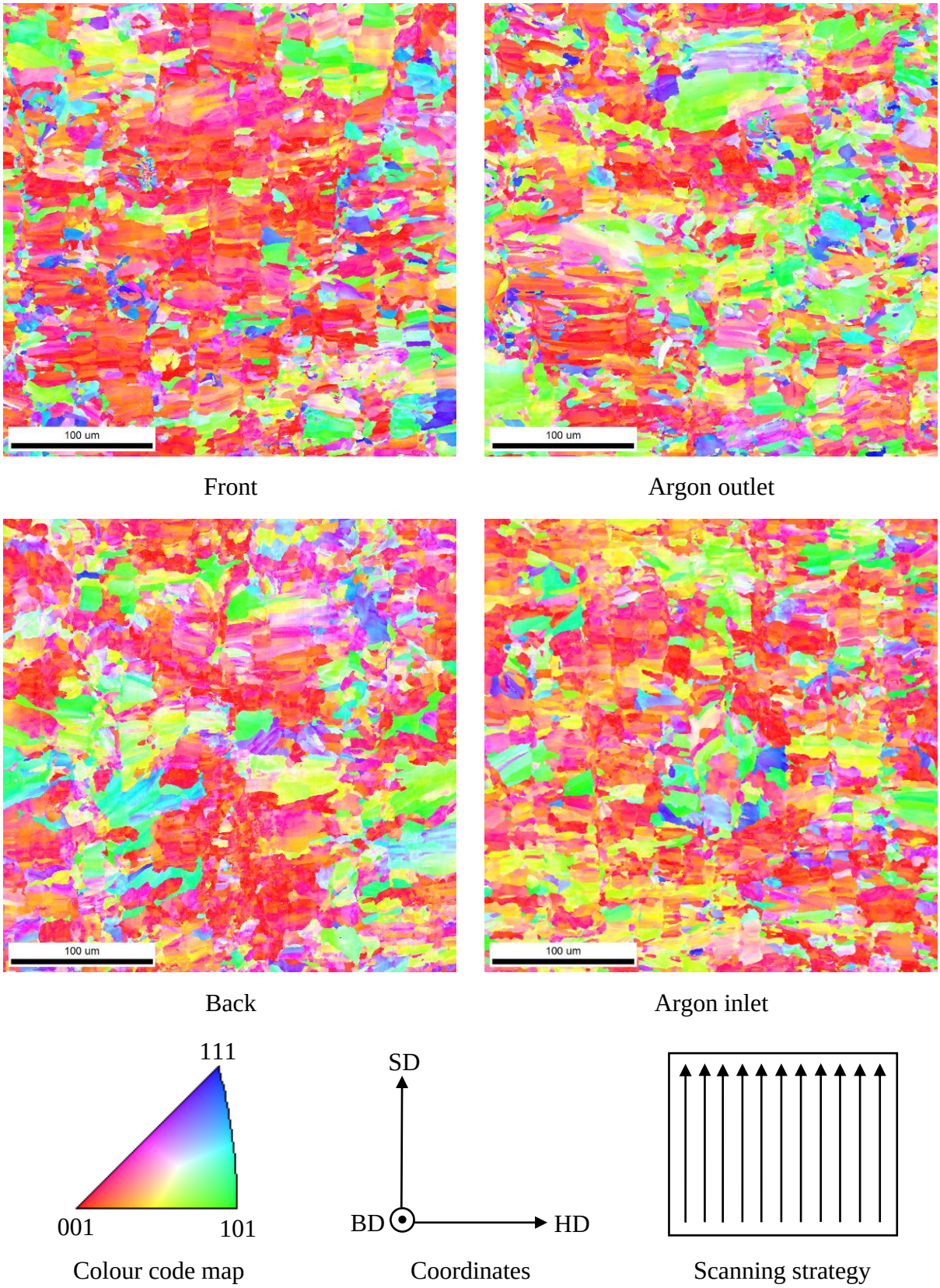


**Figure 3.9** Electron backscatter diffraction maps contrasting the effect of sample build location on grain orientation.

The crystallographic textures resulting from the build location parameter are depicted in Figure 3.10. All four locations exhibited a very sharp <001> cube texture, indicating that many of the grains were aligned with reference to the samples build direction. However, it is worth to note and compare the maximum intensity of the colour scale bars corresponding to the representative pole figure of the samples. Although the texture was qualitatively similar in the four samples, the lower intensity of the argon outlet pole figure indicates that the argon outlet sample had inferior crystallographic anisotropy in comparison for example with the argon inlet sample. Therefore, as the argon outlet sample showed the highest hardness and lowest yield strength and the argon inlet sample the lowest hardness and highest yield strength, it can be concluded that location parameter slightly altered the crystallographic anisotropy, and hence contributed to the seen discrepancies between the samples mechanical performance.

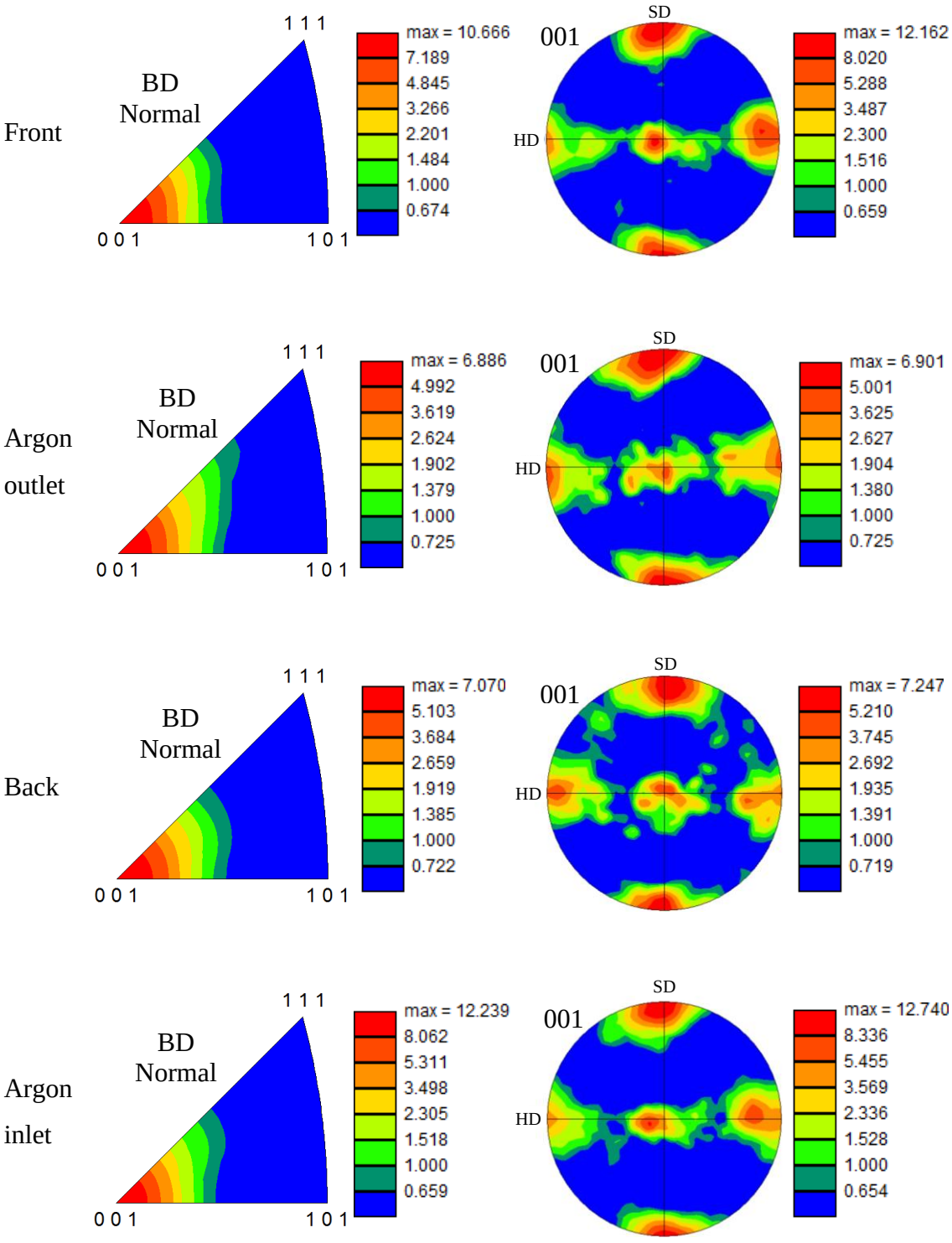


**Figure 3.10** Crystallographic textures resulting from the build location parameter.

Figure 3.11 shows the changes in grain boundary misorientation angle due to the location parameter. The red line represents the low angle grain boundaries (LAGBs) (<10°) and the blue line represents the high angle grain boundaries (HAGBs) (≥10°). Figure 3.11 also tabulates the fraction of LAGBs and HAGBs in the samples. A salient feature of L-

PBF processed 316L is the existence of a large fraction of LAGBs [385]. However, here, it is observed an equal fraction of LAGBs and HAGBs in the argon outlet misorientation map. In contrast, the back sample exhibited a high fraction of LAGBs. It is also worth noting the presence of a large number of LAGBs between the meltpools boundaries, and that the LAGBs and HAGBs are not uniformly distributed in the microstructure of the samples. It appears that these were due to the cyclic local high heating and cooling and the thermal constraint with the previously processed layer, which then developed uneven residual stress in the microstructure [437]. Consequently, grains with large residual stress accommodated the strain and produced local orientation and <2° angle grain boundaries. Considering the results presented in Table 3.1 and Figure 3.7 and knowing that the ductility decreases as a result of defects such as porosity, it can be observed a relationship between the crystallographic misorientations and the mechanical performance of the samples. Samples with large fractions of LAGBs showed higher yield strengths. This was because the LAGBs hindered dislocation motion during the tensile deformation, hence strengthening the samples. However, in comparison to the cellular structures (Figure 3.3), the respective contribution of LAGBs to the yield strength was much lower [385,438]. Additionally, cellular boundaries with high dislocation densities could have acted as HAGBs during the deformation and so resulted in grain boundary strengthening. Conversely, cellular boundaries with low dislocation densities could have enhanced the deformation twinning and contributed to the ductility of the samples. The local variation in misorientation observed through kernel average misorientation maps and distributions was used to evaluate the residual strain and dislocation density in the samples which are presented next.

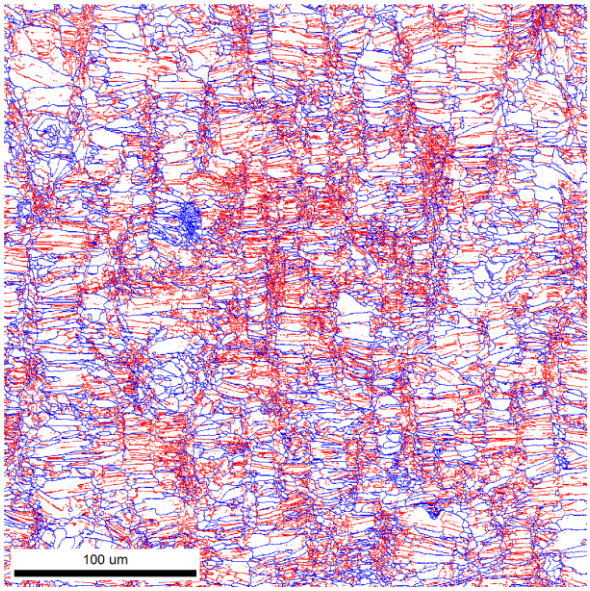


Front

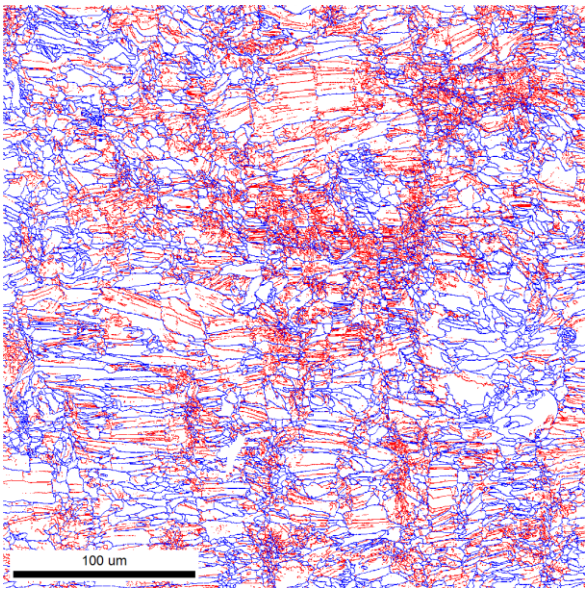


Argon outlet

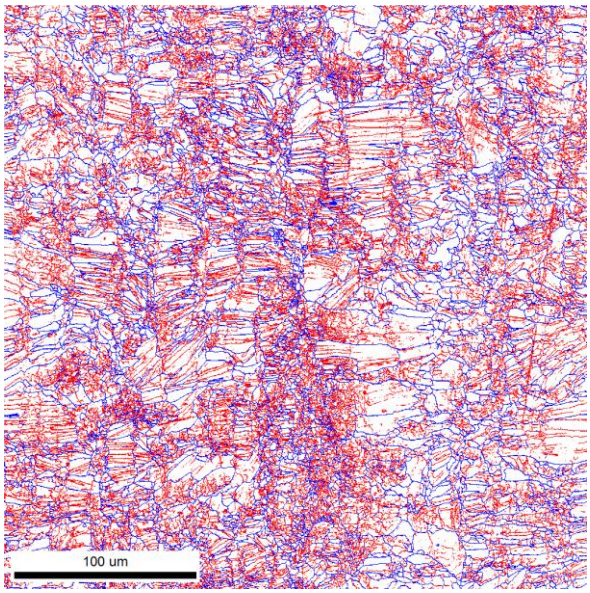


Back

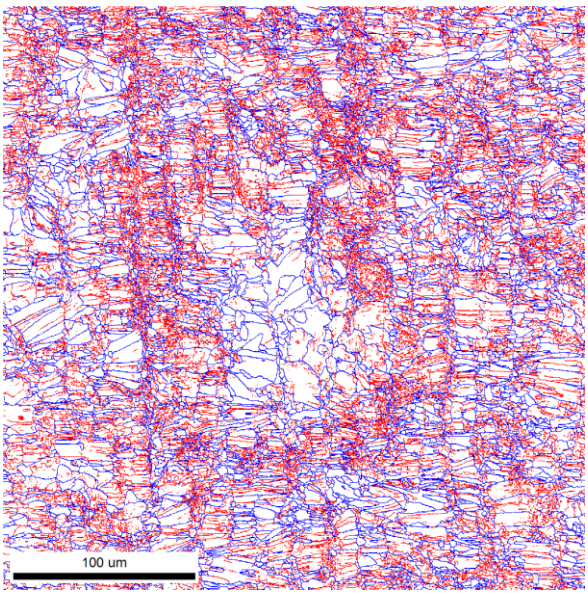


Argon inlet

| Sample | LAGBs (<10°) | HAGBs (≥10°) |
|---|---|---|
| Front | 0.58 | 0.42 |
| Argon outlet | 0.50 | 0.50 |
| Back | 0.64 | 0.36 |
| Argon inlet | 0.59 | 0.41 |

**Figure 3.11** Grain boundary maps obtained by electron backscatter diffraction contrasting the fraction of low angle and high angle grain boundaries in the samples.

The kernel average misorientation of the samples is shown in Figure 3.12. The front, argon outlet and argon inlet samples exhibited similar distributions of kernel average misorientation. However, the back sample developed a relatively high kernel average misorientation, with an average value of 0.84°. An increase in the angle of kernel average misorientation is usually related in the literature to low laser input energies [439–441]. Therefore, contrary to the aforestated, heat accumulation resulting from high laser input energies can lead to an in-situ relaxation heat treatment that reduces the amount of strain and dislocations in the material. Accordingly, it is possible that the observed kernel average misorientation in the back sample resulted from laser attenuations in response to the inert gas flow separation and turbulences at this location, and from local multiple thermal cycles due to meltpool fluctuations. Additionally, the degree of local misorientation seemed also depend on the crystal orientation. This was confirmed in the pole figure of the back sample (Figure 3.10), as in this sample, several grains grew oriented between the scanning and hatching direction. Therefore, the resultant kernel average misorientation in the back sample was driven mainly by the processing conditions at the back location and the local microstructure. Moreover, the results suggested that microstructures having more dominant textures would accumulate lower amounts of kernel average misorientation, therefore increasing the residual stress relaxation effect.

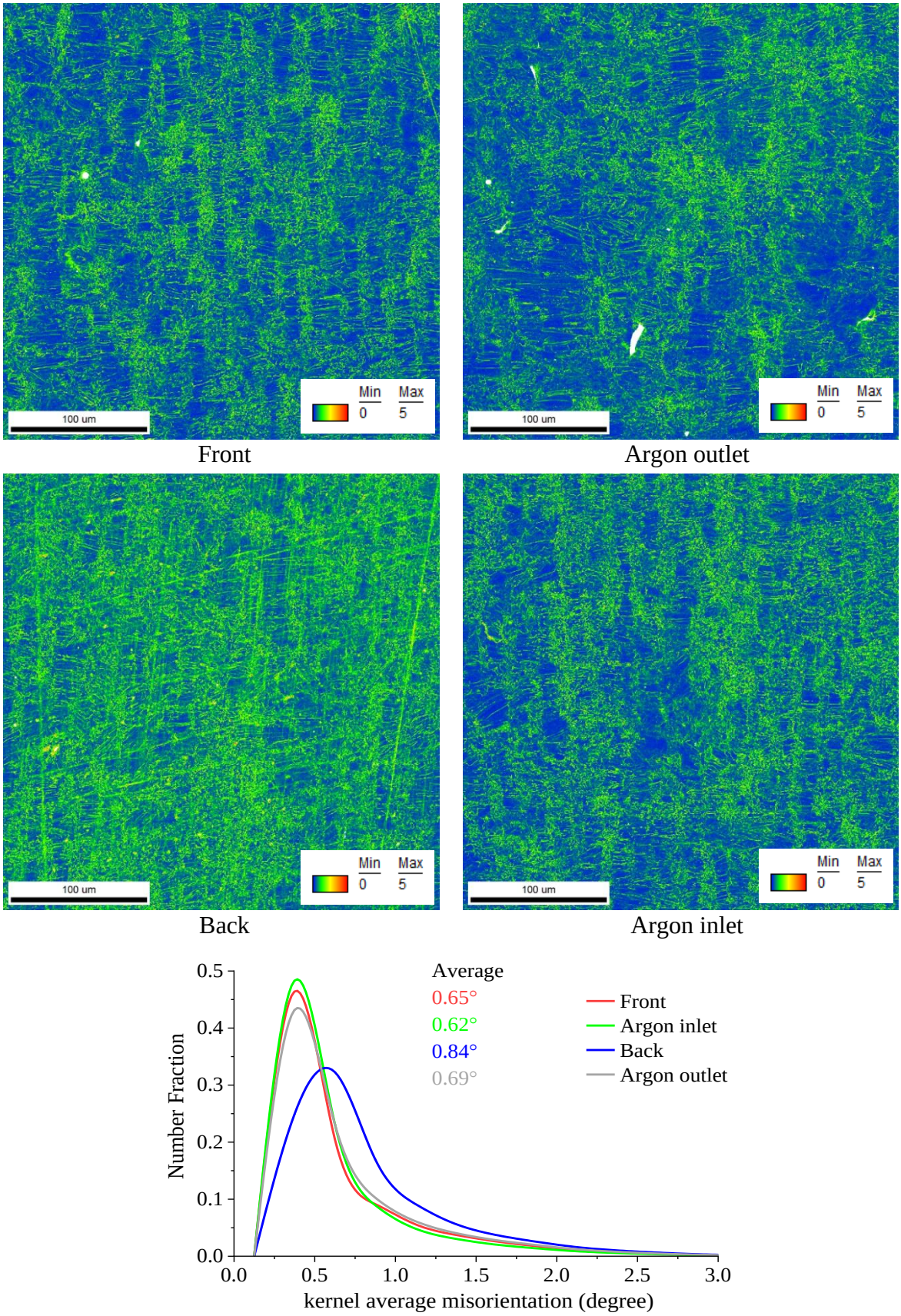


**Figure 3.12** Kernel average misorientation maps and angle distributions corresponding to the 316L samples printed at critical locations on the build platform.

### 3.4.1.8 Corrosion

The dynamic corrosion behaviour of the samples to 3.5% w/v NaCl $H_2O$ (pH = 8.2) electrolyte solution captured by potentiodynamic polarisation is presented in the voltammograms of Figure 3.13a and the relevant parameters extracted from the polarisation curves are presented in Figure 3.13b. The argon outlet and back samples show a passivation-like curve (active-passive behaviour) [442]. Where a distinctly diminished passive span can be observed, revealing that passivation was unstable. The presence of pores in the samples could affect the formation of the protective passive film while polarising. For example, by forming a porous thin or non-uniform film which can be easily penetrated, hence accelerating corrosion. Furthermore, because of the existence of an abnormal film, localised corrosion could manifest as contribute to anodic current via oxidation of the surface within the pores. Additionally, the observed ever increasing current during anodic polarisation is a clear indication of the formation of a defective oxide film. The polarisation curve of these two samples also shows a slightly lower passivation current density for the back sample, suggesting that the passive film is relatively easier to form. As seen in Figure 3.13a, the front and argon inlet samples both exhibited noticeable pseudo passivity, therefore suggesting that stable pitting sites (localised corrosion) were formed during the OCP measurements. The observed pseudo passivation resulted from the formation of a non-protective oxide film. This implies that the surfaces were only partially passivated and that active pitting sites were already initiated at potentials lower than the pseudo passive potential spans. Above the pseudo passive span, the contribution of pitting to the total current becomes significant and resulted in an increasing current density with the increasing potential. The extracted polarisation parameters presented in Figure 3.13b show that the front sample exhibited the noblest corrosion potential (-205.00 mV), followed by the argon inlet sample (-267.33 mV) which then exhibited the lowest corrosion current density (0.48 $\mu A/cm^2$). Therefore, the argon inlet sample demonstrated higher corrosion resistance than the other three samples. Additionally, the argon inlet sample also showed a lower corrosion rate (0.80 mils per year, mpy) (1 mil = 0.0254 mm) [443]. This could be due to dissolution of iron and chromium oxides/hydroxides in the presence of the electrolyte forming stable complexed species already at OCP window prior to anodic polarisation [444].

(a)

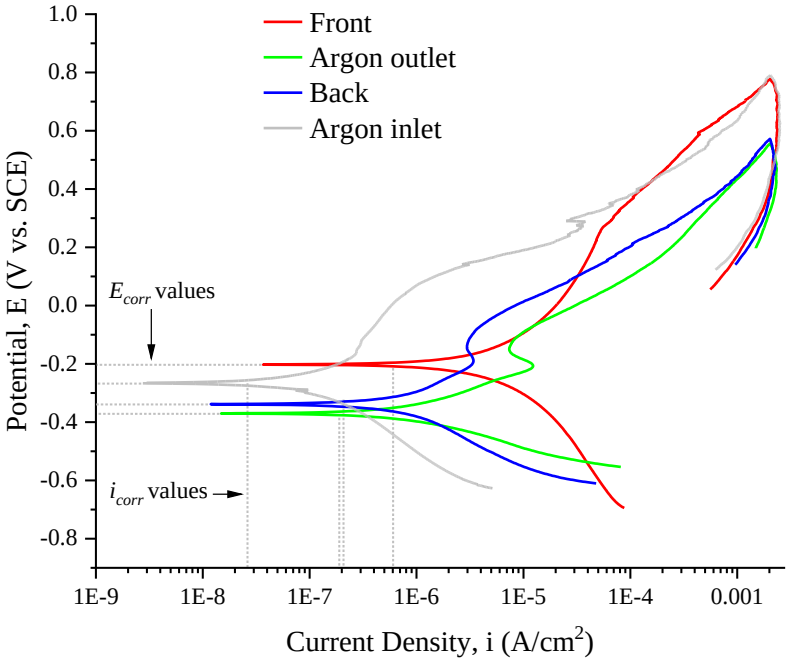


(b)

| Location | $E_{corr}$ (mV) | $i_{corr}$ (µA/cm$^2$) | CR (mpy) |
|---|---|---|---|
| Front | -205.00$_{\pm 8.29}$ | 29.90$_{\pm 1.15}$ | 41.11$_{\pm 1.98}$ |
| Argon outlet | -365.00$_{\pm 13.14}$ | 6.92$_{\pm 0.30}$ | 6.74$\pm$0.31 |
| Back | -348.67$_{\pm 7.93}$ | 7.86$_{\pm 0.20}$ | 7.36$_{\pm 0.21}$ |
| Argon inlet | -267.33$_{\pm 7.41}$ | 0.48$\pm$0.02 | 0.80$_{\pm 0.03}$ |

**Figure 3.13** (a) Potentiodynamic polarisation curve of the samples in 3.5% w/v NaCl H2O solution and (b) their respective corrosion potential, corrosion current density and corrosion rate. The uncertainty was estimated with a 95% confidence interval.

In order to gain insights regarding the interfacial characteristics of the passive film and on prevailing corrosion mechanisms, EIS measurements were performed. Figure 3.14a and Figure 3.14b show the EIS results depicted in the forms of Bode and Nyquist plots. The EIS data was further analysed using equivalent circuit modelling by fitting the data to a modified Randles circuit, Figure 3.14c. In this model, $R_e$ is the uncompensated resistance of the electrolyte between the working and the reference electrode and $R_{ct}$ represents the electrical resistance to the charge movement offered by the electrical double layer formed on the working electrode surface. A constant phase element (CPE) was used to represent the non-ideal capacitive behaviour of the electrical double layer forming at the working electrode-electrolyte interface [445]. The impedance of the constant phase element is defined as:

$$Z_{cpe} = \frac{1}{Y_0(j\omega)^{\alpha}}$$

where $j$ is the imaginary component ($j^2 = -1$) of the impedance, $\omega$ is the angular frequency ($2\pi f$) and $Y_0$ is the admittance of the CPE defined by the ease of alternating current flow into the circuit. The CPE represents an ideal capacitor behaviour when $\alpha = 1$ or intermediate characteristics between a capacitor and resistor when $0 < \alpha < 1$ [446,447]. The parameters of the equivalent electrical circuit obtained from simulation based on the EIS experimental data is shown in Figure 3.14d. In spite of the fact that the CPE element is related to the double layer capacitance, here, it does not behave as a pure capacitor since $\alpha < 1$. Therefore, in order to determine the effective double layer capacitance, the well-established Brug's equation was used [448], as expressed below:

$$C_{dl} = Y_0^{1/\alpha} (R_e^{-1} + R_{ct}^{-1})^{(\alpha-1)/\alpha}$$

According to the Bode plots of Figure 3.14a, the overall electrochemical behaviour of the samples follows the same trend and confirms the assumption of a single time constant, identified from the phase angle. At lower frequencies (i.e. <1 Hz), the polarisation resistance became dominant and these curves departed the higher frequency trend as they formed the low frequency plateau which represented the sum of $R_e$ and $R_{ct}$. While at high frequencies (i.e. >10 kHz) the curve behaviour was related to $R_e$, which was much smaller than the charge transfer resistance, $R_{ct}$. At middle frequency ranges (i.e. 1 Hz to 10 kHz), the phase angle drop represents the capacitive response of the electric double layer and/or passive oxide film. In the low frequency region, there are apparent differences in the impedance modulus. These indicate that the samples exhibited dissimilar barrier properties of the oxide layer. Based on the phase angle, the argon inlet sample passive film is mainly capacitive, as an ideal capacitor has a phase angle of -90° [449]. A higher negative phase angle indicates an increase in the protective nature of the oxide film. The argon outlet peak phase angle shifted the most towards higher frequencies, which shows that the passive film became less stable, hence the risk of corrosion began to increase. The phase angle peak of the argon inlet is relatively flat (wider frequency range) in comparison to the other samples. This implies that its protective oxide layer remained intact over a longer period of time.

The EIS results presented as Nyquist plots are depicted in Figure 3.14b. The lowest $Z_{real}$ value (high frequency) represented the $R_e$ and the highest $Z_{real}$ value represented the sum

of $R_e$ and $R_{ct}$ at low frequencies. According to these plots, typical capacitive semicircles are similar for all samples, but with different radius. The larger the radius of the semicircle is indicative that the passive films formed by potentiodynamic polarisation present higher impedance response and that represents higher resistance to corrosion. As expected, the $R_e$ was low and very similar for all samples. The argon outlet and back location samples showed significantly higher electrochemical reaction rates. This is clear from their lower $R_{ct}$, which is indicative of an enhanced charge transfer of chloride ions through the CPE and hence of a less protective film. The $Y_0$ values also justified the existence of a less uniform and defective oxide film on these samples. Therefore, the lower $R_{ct}$ and larger $Y_0$ suggest the dissolution of oxides and formation of larger concentration of defect sites within the oxide films. It is important to notice the particularly higher $R_{ct}$ of the argon inlet sample (233.25 $\Omega cm^2$), which reflects to a higher stability of oxide film. This higher resistive behaviour could be directly related to its grain structure, lower grain boundary density and less surface defects (i.e. pores). In fact, in stainless steels, it is well-known that grain refinement is an important factor in passive film formation and growth [450–452]. Therefore, a refined grain structure could effectively decrease the diffusion path length for metal atoms to migrate toward the metal-electrolyte interface to form a protective and uniform passive film. In which, as a result, enables the thickening of the passive oxide film. According to the Helmholtz model and the standard expression for parallel plate capacitors, $L_{ss} = \varepsilon\varepsilon_0 A/C_{dl}$, the steady-state film thickness ($L_{ss}$) is inversely proportional to the $C_{dl}$ [453,454]. Therefore, the $C_{dl}$ results of Figure 3.14d help to explain the better corrosion performance of the argon inlet location sample.

(a)

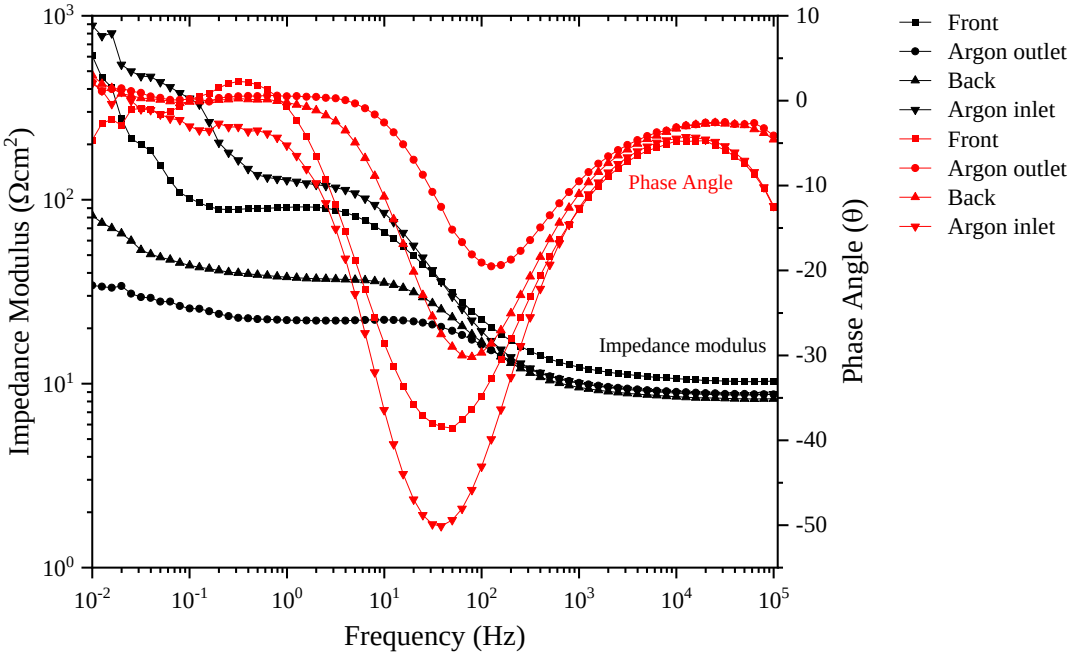


(b)

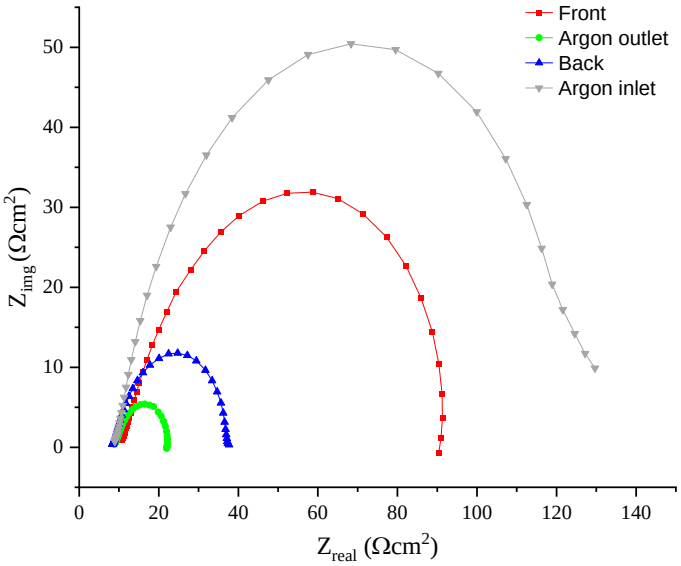


(c)

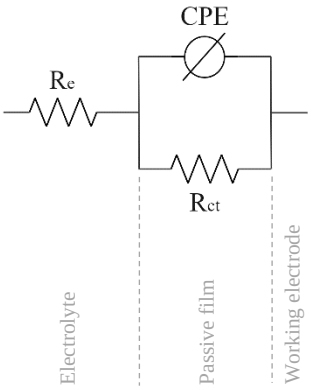


(d)

| Location | $R_e$ (Ωcm$^2$) | $R_{ct}$ (Ωcm$^2$) | $Y_0$ (μΩ$^{-1}$cm$^{-2}$s$^{\alpha}$) | α | $C_{dl}$ (μFcm$^{-2}$) |
|---|---|---|---|---|---|
| Front | $10.49_{\pm 0.05}$ | $109.64_{\pm 4.71}$ | $37.96_{\pm 1.31}$ | 0.75 | 270.89 |
| Argon outlet | $8.84_{\pm 0.05}$ | $16.41_{\pm 0.68}$ | $50.26_{\pm 0.68}$ | 0.75 | 332.20 |
| Back | $8.31_{\pm 0.04}$ | $29.69_{\pm 1.34}$ | $48.54_{\pm 0.67}$ | 0.75 | 330.33 |
| Argon inlet | $8.55_{\pm 0.09}$ | $233.25_{\pm 11.12}$ | $38.84_{\pm 1.65}$ | 0.75 | 265.76 |

**Figure 3.14** Electrochemical impedance spectroscopy data showing (a) the Bode plots and (b) the Nyquist plots recorded for the samples in 3.5% w/v NaCl H2O solution; (c) the equivalent electrical circuit used to model the data and (d) the obtained equivalent electrical circuit parameters. The uncertainty was estimated with a 95% confidence interval.

### 3.4.2 Part Property Repeatability

#### 3.4.2.1 Evidence of Repeatability Issues

The repeatability of the investigated properties based on the location parameter is shown in Figure 3.15. The calculation of the repeatability percentages was based on the classical analysis of coefficient of variation [455,456]. Each value was calculated for each specified sample property as calculated from three samples printed in different builds using the same location and sample production inputs. For easy visualisation of the effect of the location parameter, the repeatability percentages of each property is presented colour ranked from lowest to highest values. A large repeatability span for nanohardness and yield and ultimate tensile strengths was observed, implying that the location parameter had a considerable effect on the repeatability of these properties. On the contrary, the repeatability of density and Vickers hardness were less sensitive to the location parameter. It is clear from Figure 3.15 that none of the critical locations showed better all-around repeatability of the investigated properties. However, overall while having some lower levels of measured physical properties, the argon inlet location presented the best repeatability. The factors responsible for diminishing repeatability could be for example, unique processed-layer defects progressing and worsening through consecutive layers, inconsistent meltpool stabilities, temporal formation of inconsistent and multi-component non-homogeneous microstructures.

| Property | Part Location | | | |
|---|---|---|---|---|
| | Front | Argon outlet | Back | Argon inlet |
| Density | 98.84 | 98.55 | 98.96 | 98.88 |
| Vickers Hardness | 99.46 | 99.57 | 99.44 | 99.31 |
| Modulus of Elasticity | 97.96 | 97.69 | 96.28 | 97.02 |
| Tensile Strength, Yield | 93.00 | 96.83 | 89.73 | 98.40 |
| Tensile Strength, Ultimate | 95.46 | 87.83 | 91.72 | 97.43 |
| Nanohardness | 92.94 | 90.07 | 85.70 | 95.52 |
| Reduced Modulus | 96.12 | 96.66 | 93.69 | 96.36 |
| Contact Stiffness | 96.72 | 97.07 | 97.21 | 97.83 |
| Corrosion Rate | 95.18 | 95.33 | 97.61 | 96.61 |

**Ranking**

Lowest  Highest

**Figure 3.15** Part properties repeatability-dependency on printing location. The repeatability percentages of each property is colour ranked for easy visualisation of the effect of the location parameter.

To assess the significance of the properties variability induced by the location parameter, the probability values (p-values) were calculated. An α level of 0.01 was chosen to set limits of acceptable probability for the role of change in the measured distinctions. Then, statistical significance was proclaimed if the calculations yielded a p-value below α. Table 3.3 shows the summary of test statistics. From the investigated critical locations, statistical differences were identified in yield strength and hardness for samples printed near the argon inlet and argon outlet. An ideal argon condition for printing near the argon inlet location is less likely of efficiently preventing flying spatter powder from collapsing onto the meltpool and powder bed, and removing fumes and condensate at those parts being printed near argon outlet location. Additionally, the laminar argon flow exiting the argon inlet diffusor is likely to undergo a turbulent transition by the time it reaches the argon outlet location [457], as well as an obvious temperature increase as it flows over the hot build platform (powder bed), which is supported by a temperature difference observed between the argon inlet and argon outlet tubing at the argon filtration/cooling unit. Differently, an ideal argon condition for printing near the argon outlet location, which requires a higher argon velocity and flow rate, is typically observed blowing away powder from the powder bed near the argon inlet location. Therefore, it can be said that at the argon outlet and argon inlet printing locations, a slightly different processing

condition exist for a given argon velocity and flow rate. As seen in Figure 3.15, a reasonable repeatability for the corrosion rate was achieved in all of the four critical locations. However, the variability of the corrosion rate between the locations was shown to be statistically significant in Table 3.3. In addition to the discussion in section 3.1.8, it is clear that the integrity, uniformity and morphology of the protective oxide film varies with the print location parameter. One driving force for corrosion is the existence of heterogeneities in the material, ranging from atomic to several microns in scale, arising for example from crystal structure defects, segregation of elements and non-metallic inclusions [458,459]. Therefore, such factors could have contributed to corrosion activation and accelerated corrosion propagation. In conclusion, it can be said that the observed corrosion rate variability was related to the sample metallurgical characteristics developed by its location parameter.

**Table 3.3** Test statistics summary showing the statistical significance of the properties variability based on the location which the sample was printed.

| **Property** | **P-value** | | | |
|---|---|---|---|---|
| | **Front** | **Argon outlet** | **Back** | **Argon inlet** |
| Density | 0.1373 | 0.0475 | 0.2298 | 0.1509 |
| Vickers Hardness | 0.4478 | 0.0053 | 0.3306 | 0.0138 |
| Modulus of Elasticity | 0.0494 | 0.0186 | 0.4923 | 0.1389 |
| Tensile Strength, Yield | 0.1581 | 0.0038 | 0.1949 | 0.0081 |
| Tensile Strength, Ultimate | 0.0566 | 0.0467 | 0.1626 | 0.0491 |
| Nanohardness | 0.0387 | 0.0877 | 0.1676 | 0.0065 |
| Reduced Modulus | 0.3867 | 0.1511 | 0.3645 | 0.0558 |
| Contact Stiffness | 0.0398 | 0.0644 | 0.0523 | 0.0502 |
| Corrosion Rate | 0.0013 | 0.0004 | 0.0003 | 0.0001 |

| **Hypothesis** | **Significance level α = 0.01** | **Colour code** |
|---|---|---|
| $H_0$: μ = $\overline{x}$ | $P - value < \alpha \rightarrow reject\ H_0$ | $P - value < 0.01$ |
| $H_a$: μ ≠ $\overline{x}$ | $P - value \geq \alpha \rightarrow fail\ to\ reject\ H_0$ | $P - value \geq 0.01$ |

### 3.4.2.2 Attributes Impairing Repeatability

Unfortunately, different definitions for repeatability in published work related to additive manufacturing are still used [460–463,456,464–466]. Repeatability is also sometimes

wrongly addressed as replicability (printed in the same or different site, different operator, same experimental setup, different builds) and reproducibility (printed in different site, different operator, different experimental setup, different builds) [467–469]. One of the reasons could be the fact that additive manufacturing technologies are adopted by different scientific disciplines and institutions. As a consequence, each of them may prefer to apply their own definitions and hence introduce confusion to the definition of these terminologies [470]. Recently, the American Society for Testing Materials (ASTM) developed a number of additive manufacturing standards intended to help the implementation of additive manufacturing technologies [471]. Including the ASTM 52900 standard which defines repeatability as the degree of measurable properties between identical parts, printed by the same operator, using the same printer and input parameters, but printed in different builds [472]. At present, there is no certified guideline on how to report property variability between parts printed in the same build. In order to efficiently tackle the repeatability issue in additive manufacturing, the aforementioned issues should be addressed first.

In modern L-PBF processing, between 150 and 200 input parameters exist and have an influence on the ultimate quality of printed components. The total number of input parameters varies depending mainly on the feedstock material (i.e. form and quantity), printing file (number of commands and amount of layer detail) and printer (i.e. model and capability). Since the underlying source of repeatability issues is unclear, it is imperative to look beyond the commonly studied input parameters and focus more on other less or not yet studied input parameters. In-situ real-time monitoring and closed-loop process control should be implemented and used to improve repeatability. Until then, repeatability will continue to be an issue for L-PBF which needs to be well measured and recorded in relation to the process input parameters. As a reference, an acceptable repeatability is the one that fulfils the minimum requirements to serve practical purposes for each specific industry part requirement.

### 3.5 Conclusions

The present study provides a comprehensive insight into the effect of the part location parameter on the properties of components manufactured using L-PBF. The isolation of location from the other input parameters enabled an accurate quantification of part property variability caused by this parameter. In total, four critical locations on a build platform were examined, here named as front, argon outlet, back and argon inlet, which

are locations prone variability in part properties. Hence, these locations were considered to assess the extent of this phenomenon.

Based on this study, the main conclusions are summarised below:

(1) A statistical difference in the part properties was found depending on the location where the part was printed. Therefore, an effect of the printing location on resultant part properties exists and should be considered depending on produced part application requirements.

(2) The repeatability (build-to-build) was found to vary across locations. This was because some of the locations were more susceptible to meltpool instabilities and spatter. The reduction in part-property repeatability was due to variation in microstructure and defects for the same location in successive builds.

(3) The front location promoted enhanced part densification due to a higher powder bed packing resultant from the inevitable particle segregation phenomenon taking place during powder spreading and due to a reduced volume of pores and voids within the part bulk microstructure.

(4) Parts printed near the argon outlet were more liable to internal defects. Nevertheless, superior hardness was measured from the argon outlet parts and related to their crystal orientation and grain size.

(5) Similar tensile performance was obtained for the parts printed at the front, back and argon inlet locations. The poor elongation to failure and inferior tensile strength of the argon outlet parts were ascribed to porosity and lack of fusion defects at this location. Banded grains present in the microstructure of the parts printed in the front location contributed to ductility, while the higher and constant strain hardening rate of these parts was accredited to a stronger crystallographic texture which promoted a longer twinning period and higher twin density.

(6) The influence of the location parameter on the corrosion behaviour of parts was evidenced by the electrochemical measurements. In fact, parts printed at the argon outlet and back locations showed substantially higher electrochemical reactions, dissolution of oxides and formation of defect sites within the oxide films. In contrast, the argon inlet parts formed a much more stable and thicker protective film which remained intact over a longer period of time. The superior corrosion resistance evidenced by the determined lower corrosion rate of the argon inlet parts were attributed to their lower level of porosity and their small grain structures.

# Chapter 4

## Influences of Powder Morphology and Spreading Parameters on the Powder Bed Topography Uniformity in Powder Bed Fusion Metal Additive Manufacturing

**Publication Status:** Published

Mussatto, A., Groarke, R., O'Neill, A., Obeidi, M. A., Delaure, Y., and Brabazon, D., 2021, "Influences of Powder Morphology and Spreading Parameters on the Powder Bed Topography Uniformity in Powder Bed Fusion Metal Additive Manufacturing," Additive Manufacturing, 38, 101807.

https://doi.org/10.1016/j.addma.2020.101807

## 4.1 Abstract

Powder spreading is a crucial step in the powder bed fusion process, which controls the quality of powder bed and consequently affects the quality of printed parts. To date, however, powder spreadability has received very little attention and substantial fundamental work is still needed, largely because of the lack of experimental studies. Therefore, the focus of the present study addresses the influences of powder morphology, spreading velocity and layer thickness on the powder bed topography uniformity. The experiments were conducted with a laser powder bed fusion printer and the powder layers were spread systematically and comprehensively assessed. In summary, it was found that particle sphericity and surface texture dictates the degree of impact that the spreader velocity and the layer thickness exert on the quality of powder bed topography in spread layers. The spreader velocity has substantial influence on powder bed uniformity, such that better uniformity is achieved with low spreading velocities, $\leq 80$ mm/s. Powders with a wide particle distribution and containing large number of fine particles ($< 25$ μm) enabled formation of uniform and dense powder beds, however such powders were found to be more affected by segregation. In addition to these observed effects, for the first time, the major process related challenges to powder spreadability and powder bed quality are reported in this study.

## 4.2 Introduction

Selective laser melting (SLM) is as known as the laser powder bed fusion (L-PBF) technique for metal additive manufacturing (AM) which allows the printing of three dimensional parts by spreading and selectively melting powder in a layer by layer fashion [473]. In comparison with conventional manufacturing techniques, SLM offers near net shape production of complex geometries and capability for pointwise control of microstructure, as well as a high degree of control over the physical and mechanical properties of parts [474,475]. However, the SLM process is very complex and governed by numerous factors and physical mechanisms [476]. For this reason, substantial research has been conducted in recent years in order to gain further understanding of the underlying physical mechanisms which are strongly material and process parameter-dependant, and ultimately optimise the process and properties of fabricated parts [477].

The powder properties and the powder bed quality are key factors governing the numerous physical mechanisms and hence properties of printed parts [478]. Therefore, it

is important to understand how powder is spread across the build area and understand the formation of powder layers, in order to accurately predict powder bed quality [479]. A powder must possess suitable rheology properties in order to form thin, dense and uniform powder layers [480,481]. However, the ability of a powder to flow well is highly influenced by the shape, size, size distribution, surface texture, porosity, chemical composition, moisture content, density, electrostatic charge and stiffness of its particles [482–485]. Therefore, powders having values for these and other characteristics inclined towards optimisation of their flowability are preferable [486]. In terms of spreadability, a powder which has ideal flow characteristics for SLM does not alone ensure the formation of good quality powder layers, as spreadability is also governed by other factors such as spreader speed, spreader pressure, spreader material type and powder temperature. Nonetheless, flowability is an essential powder property towards the achievement of uniformly spread powder layers [487].

The powder spreading process is also governed by the spreader system (roller or blade), spreading parameters, powder supply factor and powder layer thickness [488]. During powder spreading, particles undergo particle-particle and particle-spreader interactions which can lead to electrostatic charging and particle morphological changes, which can prevent the formation of high quality powder layers [489–493]. The spreading of powder onto a non-uniform and unstable layer which was previously spread and a very rough built surface as well as the presence of large spatter particles on the powder bed can be challenging for the formation of uniform consecutive layers. Additionally, the powder bed can also be affected by the inert gas flow system which functions to remove by-products and ensure a safe process atmosphere. An excessive flowrate and velocity of inert gas has been shown to remove particles from spread layers and hence compromise the powder bed quality [494–497].

Recently, it was reported the lack of standard test methods for spreadability that provide guidance for quantitative assessment of powder spreadability [498]. Unfortunately, today measuring and quantifying powder spreadability is identified as a crucial knowledge gap in the SLM process [499]. However, research efforts are now being seen in this area in terms of in situ investigations and simulations. Nevertheless, there exist numerous challenges such as complex part architecture, rough environment inside the building chamber of SLM systems and the lack of physical results against which to validate powder spreading simulations.

The discrete element method has been a useful numerical tool for studying powder flow dynamics in PBF AM [500]. Recently, it has been also exploited by a number of researchers to study powder spreading dynamics. A recent study reported that a small amount (vol%, 1.5) of fine particles (20 μm < d < 40 μm) added to the baseline powder (45 μm < d < 150 μm) can slightly improve the quality of the powder bed in terms of packing density and surface roughness. However, the spreadability increased and then decreased with adding fines [501]. It was also reported that powders with mean diameter ≤ 17 μm are highly influenced by cohesive forces such that it dominates the gravity forces. The use of such powders resulted in the formation of powder layers of poor quality [502]. Chen et al. concluded from their study that the influence of Van der Waals force rises and dominates with increasing fine particle content. This also resulted in poor powder flowability and in turn powder spreadability. On the other hand, powders with particle radius > 21.8 μm were more favourable for powder flowability and presented lower particle friction coefficients, resulting in a denser and more uniform powder bed layer [503]. In terms of spreaders, Haeri utilised discrete element method simulations to optimise the geometry of blade spreaders while assuming a super elliptic edge profile and varying its height, width and overall shape. The results showed that the optimised blade can generate a bed with packing density very close to roller systems and can translate to higher production rate (velocity) than the non-optimised blade with limited impact on the powder bed quality [504]. However, to fully demonstrate the effectiveness of the optimised blade design, it should be tested on an actual PBF system. In a different study, the spreading of non-spherical particles was also simulated using the discrete element method [505]. The results suggested that larger particle aspect ratios or higher spreader translational velocities resulted in smaller packing density and higher surface roughness of spread layers. Therefore, this study highlights the importance of particle sphericity and spreader velocity on the quality of powder bed. Nan et al. investigated the effect of layer thickness on transient particle jamming using discrete element method simulations [506]. They found that small layer thicknesses are influenced by powder segregation and can form empty patches on spread powder layers due to particle jamming. The collapse of jammed particles during spreading was then reported in some instances to lead to the particle burst into the spreading layer, deteriorating even further spread layers.

Other studies focused purely on the experimental side of powder spreadability. Snow et al. developed a powder spreadability test rig to assess powder spreadability. They

reported that the angle of repose is one of the most influential input factors in powder spreadability. Powders with lower angle of repose were more flowable and provided higher deposition rate, whereas powders with high angle of repose formed a poor powder coverage and powder aggregates. Increasing the spreader velocity from 50 to 150 mm/s increased the powder deposition rate. However, those powders with angle of repose > 40° exhibited poor flowability for high spreading velocities and based on the rate of change of the avalanching angle were unable to improve spreadability [499]. Another study investigating the effect of powder moisture on spreadability reported that powder morphology had a large influence on moisture absorption and flow behaviour. From the investigated powders, Aluminium alloys were found to be extremely sensitive to oxygen and moisture uptake in comparison to Inconel and titanium alloys. The spreading of moisture-containing powders showed their tendency for agglomeration formation and segregation of particles during the spreading. Additionally, the authors also reported that the spreading of such powders was characterised by scratches on the powder bed [507]. Lerma et al. concluded from their study that powders with morphological characteristics towards sphericity and surficial smoothness led to an almost 50% increase in packing density. In addition, they also reported particle segregation during the powder spreading. Large particles segregated near the beginning of spreading while smaller particles segregated towards the end of the build platform [508]. However, another study reported the opposite segregation behaviour and found higher packing densities near the beginning of spreading and a decline of the packing density near the end of the build platform [509].

The reviewed literature demonstrates the importance of powder spreadability for PBF systems and the influence of various powder characteristics, spreading parameters and intrinsic mechanisms on the powder bed quality. To date, powder spreadability has received very little attention, with conflicting observations. Therefore, substantial fundamental work on this topic is still needed. Hence, experimental approaches are the best way forward to thoroughly understand spreadability and validate numerical models. The focus of the present study addresses the influences of powder morphology, spreading velocity and layer thickness on the powder bed topology uniformity. Briefly, the powder samples underwent a series of investigations to enable the correlation of their characteristics to their observed spreadability. A three-level full factorial design was employed in order to obtain a comprehensive understanding of the influence of each of the three factors and their levels on the powder bed topographical quality. Uniformity,

profile height and profile void volume were studied from the powder bed topography. Additionally, particle segregation and process inherent challenges were examined and are presented in order to expand the understanding of powder spreadability and its implications to part quality.

## 4.3 Materials and Methods

### 4.3.1 Powder Characterization

Three AISI 316L stainless steel powders obtained from Alfa Aesar (powder A), not supplied for metal AM, and from Castolin Eutectic (powder B) and Carpenter Additive (powder C), which were designed for metal AM. The powders physical characteristics were analysed using a scanning electron microscope (SEM) Zeiss EVO LS-15 and a Malvern Mastersizer 3000 particle size analyser. A Micromeritics AccuPyc 1330 Helium Pycnometer was used to assess the density of the powders, and the flow properties of the powders were investigated using a Freeman FT4 powder rheometer. The powders angle of avalanche was measured using the in-house developed system based on the Revolution Powder Analyzer and the angle of repose was measured using the Hall Flowmeter funnel set up as recommended by the ASTM F3049 standard [510,511].

### 4.3.2 Powder Spreading and Experimental Design

In order to ensure the relevance of the spreadability test to the actual laser PBF process, the experiments were conducted inside the laser PBF build chamber of an Aconity Mini (Aconity3D, Germany). To minimise the electrostatic charging of the powder during the spreading process, the powder spreader system of the printer was fitted with an anti-static carbon fibre brush. A powder supply factor typical of metal AM processing on the Aconity of two was employed which means that twice the amount of powder required for the set layer thickness was spread. This was to ensure that there is enough powder to cover the printing area while avoiding excessive and unnecessary use of powder. The experiments were conducted using extreme parameter levels as well as levels that are typically used in powder bed metal printing (as per the design illustrated in Table 4.1) in order to understand the effect of the various powder morphologies, rheological characteristics and spreading parameters on the spreading of uniform powder beds. A 20 mm by 20 mm by 5 mm depth container was placed within the powder bed to capture the powder bed samples. This was filled with powder while embedded within the powder bed. When filled, a further five layers of powder were spread according to the automated

spreader operation. The sample container was then carefully extracted in order to not disturb the powder surface before surface profile measurement.

**Table 4.1** Experimental design.

| Sample | Run | Layer Thickness (µm) | Spreader Velocity (mm/s) | Powder |
|---|---|---|---|---|
| 1 | 17 | 70 | 160 | C |
| 2 | 22 | 50 | 160 | C |
| 3 | 4 | 30 | 160 | C |
| 4 | 12 | 70 | 80 | C |
| 5 | 6 | 50 | 80 | C |
| 6 | 14 | 30 | 80 | C |
| 7 | 16 | 70 | 10 | C |
| 8 | 25 | 50 | 10 | C |
| 9 | 18 | 30 | 10 | C |
| 10 | 13 | 70 | 160 | B |
| 11 | 21 | 50 | 160 | B |
| 12 | 27 | 30 | 160 | B |
| 13 | 11 | 70 | 80 | B |
| 14 | 24 | 50 | 80 | B |
| 15 | 8 | 30 | 80 | B |
| 16 | 26 | 70 | 10 | B |
| 17 | 1 | 50 | 10 | B |
| 18 | 10 | 30 | 10 | B |
| 19 | 20 | 70 | 160 | A |
| 20 | 9 | 50 | 160 | A |
| 21 | 23 | 30 | 160 | A |
| 22 | 3 | 70 | 80 | A |
| 23 | 15 | 50 | 80 | A |
| 24 | 5 | 30 | 80 | A |
| 25 | 2 | 70 | 10 | A |
| 26 | 19 | 50 | 10 | A |
| 27 | 7 | 30 | 10 | A |

### 4.3.3 Powder Bed Topography Assessment

Precise measurement of the spread powder topographies was conducted using a Keyence VHX2000E optical 3D digital microscope. A magnification of 300x was found to be suitable for this analysis as it enabled a good balance between area of coverage and degree of detail visible. The set-up for a depth resolution of 1µm was employed in order to

accurately capture and report the topographical characteristics of powder bed samples such as peaks, pores and agglomerations. Eight profile measurements within this area of 800 µm by 1102.3 µm were taken for each powder sample, which was based on the sample original area. This was to measure powder bed topography variations to allow to draw a more precise conclusion about the investigated parameters. The sample size, n, was chosen based on the profile void volume and profile height responses as per equation $n = (1.96\,\sigma/e)^2$, where $\sigma$ is the standard deviation and $e$ is the sampling error.

### 4.3.4 Particle Segregation Evaluation

Powder C was used in this study as it has better all-around properties (physical and flow) and because it performed better than powder A and B in the spreadability studies. 100 layers each having 50µm thickness were spread with a powder supply factor of two using a spreader velocity of 80mm/s. The powder samples were then collected from the begin, middle and end of the build platform and assessed using the Malvern Mastersizer 3000 particle size analyser.

### 4.3.5 Morphologies Challenging Powder Spreadability

Four 5 x 5 x 5 mm cubes were printed using the parameters of sample five, Table 4.1. The Aconity Mini (Aconity3D, Germany) laser PBF machine was used to print these samples. The hatch spacing was held constant at 60 µm and the focus diameter was set to 80 µm. The parts were exposed with a laser power of 140 W at a scanning speed of 800 mm/s. Argon was used as protective gas and the oxygen content inside the chamber was kept below 50 ppm. The morphology of the powder bed with the printed samples were then investigated using a Keyence VHX2000E optical 3D digital microscope.

## 4.4. Results and Discussion

### 4.4.1 Powders morphology and flow characteristics

The three powders investigated in this study are shown in the images in Figure 4.1. Powder A is deemed morphologically unsuitable for selective laser melting. The reason for using this powder was to help to assess the spreadability of the other two powders. This powder consists of nonspherical and elongated irregularly shaped particles. On the contrary, powder B has a good particle sphericity and a small number of elongated particles. However, its particles present a consistent surface texture. Powder C has a higher degree of sphericity. However, irregular, fines and satellite particles are present.

The optical images to the right handside of the micrographs show the pouring characteristics of each of the powders. Powder A presented poor flowability for PBF applications mainly due to substantial particle mechanical interlocking. The flowability of powder C also seems to have some degree of restriction due to particle mechanical interlocking. However, powder B apparent to be a free flowing powder.

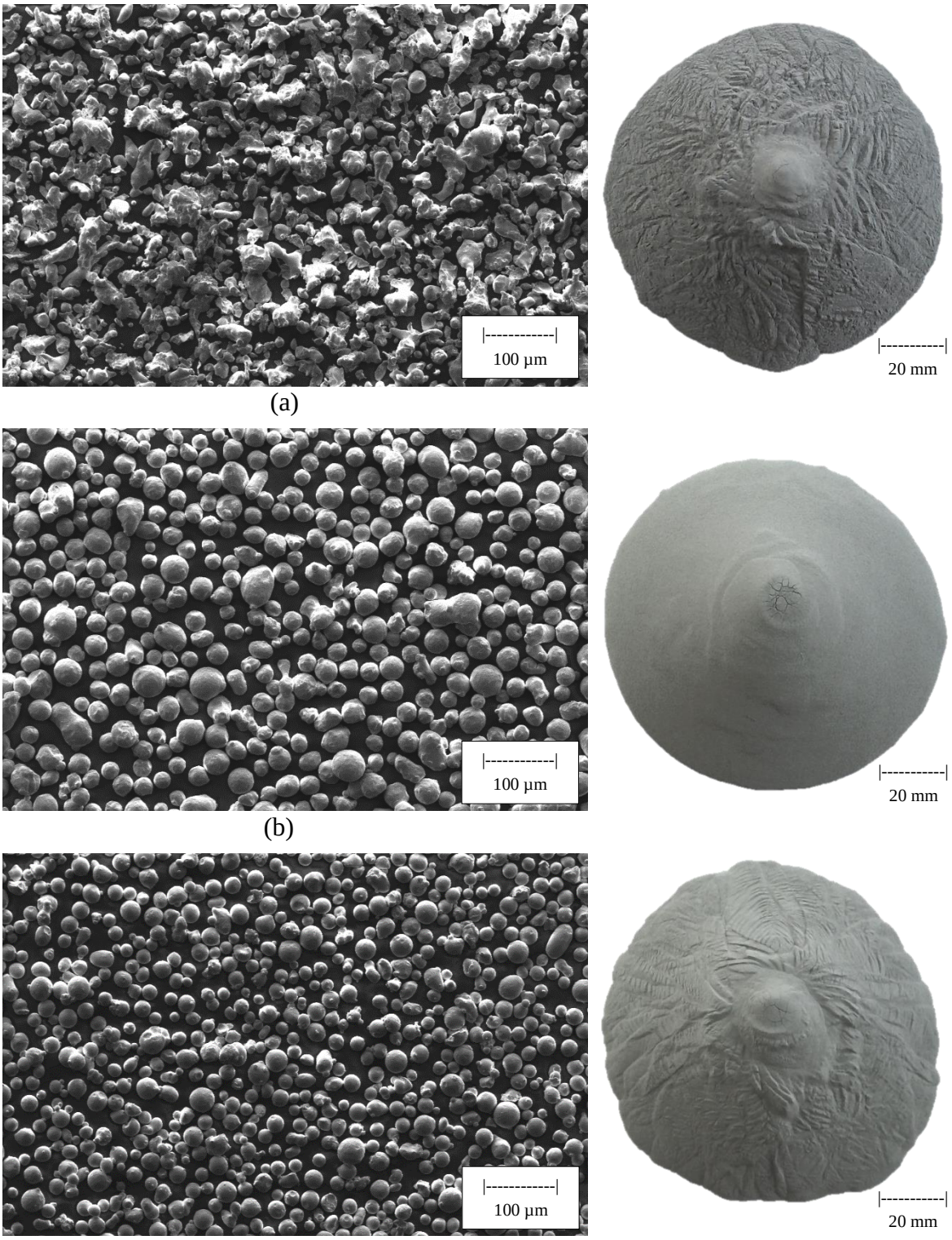


**Figure 4.1** SEM micrographs of the 316L stainless steel powder (a) A, (b) B and (c) C. The optical images on the right hand side compares the pouring characteristics of the powders.

The particle size distributions of the powders under investigation are shown in Figure 4. 2. As expected, powder A has the wider particle size distribution. It is comprised of very

large particles (≈100µm) and a considerable number of fines. Powder B presented a Gaussian type of distribution which is generally considered optimal for the SLM process. A similar distribution is seen in powder C. However, the distribution is shifted to the left and approximately half of the particles contained in this powder is sized below 30µm. Fine particles (< 20µm) are known to have a tendency for agglomeration and high level of cohesiveness therefore impacting on its powder flowability.

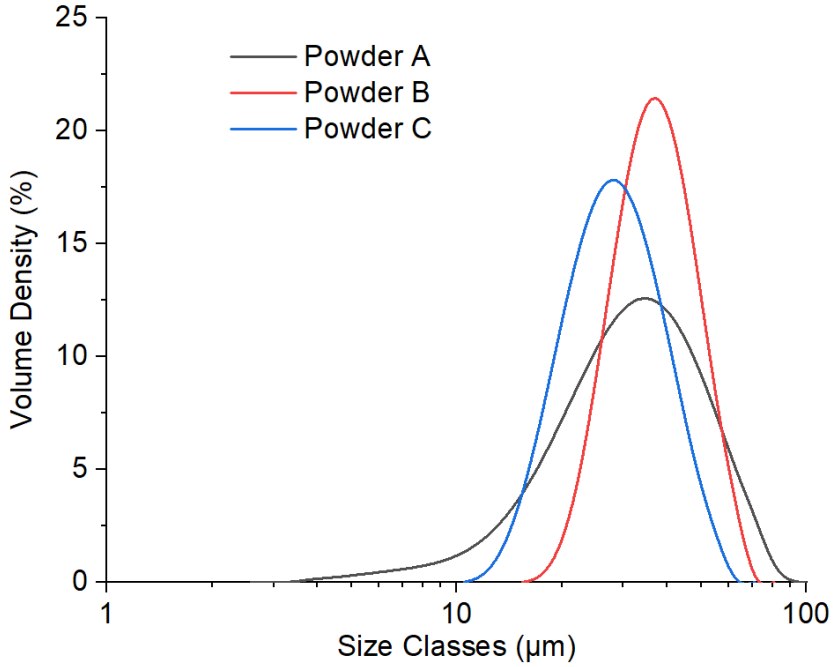


**Figure 4. 2** Particle size distribution of the powders, as measured by laser diffraction.

Table 4.2 compares the morphological, physical and rheological characteristics of the powders that are fundamental for understanding their spreadability. The up and down arrow directions seen in the table indicate the favourable trend to maximise spreadability. Powder B and C presented similar circularity (circularity is a measure of the particles sphericity). However, Powder C presented 10% higher sphericity than powder B and this can be considered an advantage towards a better flowability. In addition, powder C also presented the best length to width relationship (aspect ratio). This is also seen in the micrographs of Figure 4.1. The effect of particle morphology on the bulk density of the powders is seen in Table 4.2. As shown by the bulk density measurements, powder A presented a large void volume fraction of packed powder, whereas the spherical powders B and C were seen to achieve a more efficient packing. The avalanche and repose angle results suggest that the flowability of powder A is largely restricted by its irregular particles morphologies. Therefore, this powder lacks in a vital requirement for achieving

good powder spreadability. On the other hand, both powder B and C presented very similar angles to those powders suitable for PBF [512]. The specific energy measurements which were obtained assuming flow in a low stress environment identified powder B as having the lowest cohesion in comparison to the other two powders. This is mainly because of its superior physical properties such as particle size, shape and texture. All the three powders presented low flow rate sensitivity. However, powder B presented the lowest sensitivity to flow rate and there is enough evidence to suggest that this is related to its free flowing behaviour and to the fact that its particles are slightly coarser. Furthermore, identifiable from the powder particle micrographs, the particle surface smoothness of powder B particles was key in determining this powder flowability.

**Table 4.2** Comparison of the important morphological, physical and rheological characteristics of the powders for spreadability.

| **Measurement** | **Powder A** | **Powder B** | **Powder C** | **Instrument** |
|---|---|---|---|---|
| Size, $Dv_{90}$ | 55.5 µm | 61.6 µm | 42.4 µm | |
| Size, $Dv_{50}$ | 31.8 µm | 36.7 µm | 28.0 µm | Malvern Particle Sizer |
| Size, $Dv_{10}$ | 15.6 µm | 25.7 µm | 18.3 µm | |
| Circularity, ↑ | 0.37 | 0.76 | 0.87 | SEM/ |
| Elongation, ↓ | 0.40 | 0.22 | 0.09 | ImageJ |
| Helium Density | 7.77 g/cm$^3$ | 7.81 g/cm$^3$ | 7.83 g/cm$^3$ | Pycnometry |
| Bulk Density | 2.85 g/cm$^3$ | 4.36 g/cm$^3$ | 4.56 g/cm$^3$ | FT4 Powder |
| Specific Energy, ↓ | 3.10 mJ/g | 1.86 mJ/g | 2.51 mJ/g | Rheometer |
| Flow Rate Index, ↓ | 1.09 | 1.05 | 1.18 | |
| Avalanche Angle, ↓ | 54.6 ° | 36.1 ° | 38.5 ° | Rotating Drum |
| Repose Angle, ↓ | 48.2 ° | 30.3 ° | 28.2 ° | Hall Flowmeter |
| | ↑: index to maximise, ↓: index to minimise | | | |

### 4.4.2 Powder Bed Topography

#### 4.4.2.1 Profile Height

The profile height measured from the powder bed topography quantified the difference between the lowest valley to the highest peak of powder. Hence, it is an indication of the non-uniformity of a powder layer height which due to lack (valleys) and excess (peaks) of powder. When present in excess these defects are typically found in large quantities

and randomly dispersed over the powder bed area. A powder bed having a high profile height would certainly lead to problems such as discontinuous and variable meltpool volumes and defects due to lack of fusion. Therefore, to avoid these and other resulting problems the profile height should be as close to 0 µm as possible. The profile height measured from the various powder beds, which were generated using the conditions of Table 4.1 is shown in Figure 4.3. Samples 19 to 27 correspond to Powder A. The effect of this powder's morphology on the profile height is clear. Therefore, based on the results found for powder B and C, it can be said that particle sphericity and smoothness are significant factors in powder flowability and thus they enabled the formation of more uniform powder layers. However, this is more evident for those samples of powder C, namely samples 3, 4, 5 and 9. The results from these samples suggest that the layer thickness and spreader velocity have a large influence on the profile height. Therefore, it can be said that these two parameters are very relevant for powders with high flowability.

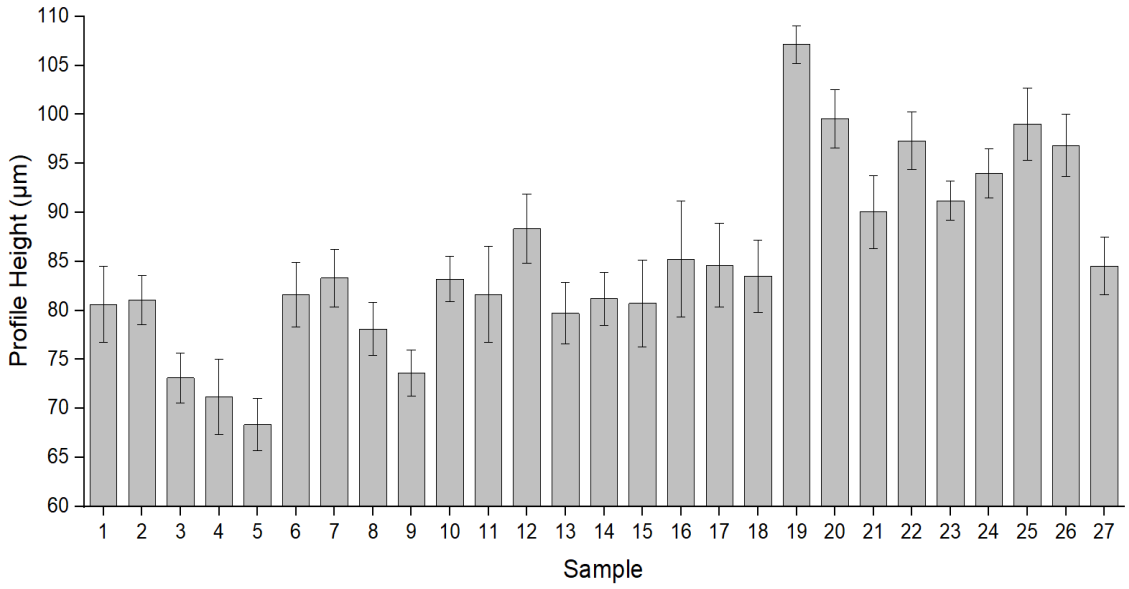


**Figure 4.3** The maximum profile height measured (from the lowest valley to the highest peak of powder) from the powder bed topography, n=8.

#### 4.4.2.2 Profile Void Volume

The profile void volume measured from the powder bed topography was defined in this study as the volume required to fill out the valleys up to the highest peak of the powder profile. Figure 4.4 shows the profile void volume measured from the investigated area (800 x 1102.3 µm) of the powder bed samples. The high profile void volume obtained from the samples of powder A can be correlated to its particles shape and roughness

which caused substantial mechanical interlocking and interparticle friction during the spreading. When particle morphology is more spherical (powders B and C), mechanical interlocking is less influential as particles are more likely to glance past one another during spreading. However, their net interaction is still influenced by mechanisms such as friction and static charges, which one are also highly influenced by the spreading conditions. In contrast, the below powder samples 4, 5, 8 and 9 presented the lowest profile void volume and this is mainly because Powder C has better all-around characteristics (sphericity, size distribution, texture, etc.) for spreadability and consequently reduced net interaction.

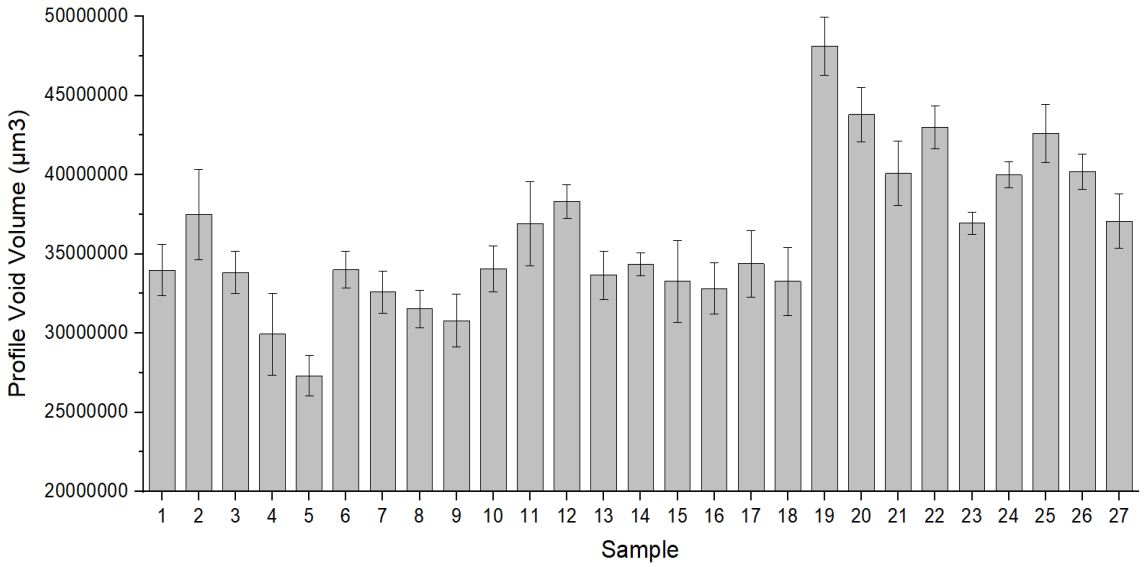


**Figure 4.4** The profile void volume measured from the powder bed topography (the volume of powder required to fill out valleys with powder up to the highest peak of powder), n=8.

Analysis of variance (ANOVA) was used to assist in understanding the fundamentals of powder spreadability, to evaluate the influence of the parameters on the profile void volume and to find a way to further reduce the profile void volume within the powder bed topography. The analysis was performed using the commercial Design-Expert software v11. Table 4.3 shows the summary of the ANOVA. The F-value of 10.98 implies the model is significant. There is only a 0.01% chance that an F-value this large could occur due to noise. P-values less than 0.05 indicate model terms are significant. The Predicted $R^2$ is in reasonable agreement with the Adjusted $R^2$, the difference is less than 0.2. The Adequate Precision measures the signal to noise ratio, and a ratio greater than 4 is desirable. The obtained ratio of 11.312 indicates an adequate signal.

**Table 4.3** ANOVA for 2FI model of the profile void volume.

| Source | Sum of Squares | df | Mean Square | F-value | P-value | |
|---|---|---|---|---|---|---|
| Model | 4.99E+14 | 9 | 5.55E+13 | 10.98455 | 1.74E-05 | significant |
| A-Layer Thickness | 5.77E+12 | 1 | 5.77E+12 | 1.142889 | 0.299988 | |
| B-Spreader Velocity | 5.74E+13 | 1 | 5.74E+13 | 11.37335 | 0.003617 | |
| C-Powder | 3.9E+14 | 2 | 1.95E+14 | 38.65011 | 4.74E-07 | |
| AB | 6.13E+11 | 1 | 6.13E+11 | 0.121444 | 0.731753 | |
| AC | 4.41E+13 | 2 | 2.2E+13 | 4.365363 | 0.02951 | |
| BC | 9.71E+11 | 2 | 4.86E+11 | 0.096154 | 0.908814 | |
| Residual | 8.58E+13 | 17 | 5.05E+12 | | | |
| Cor Total | 5.85E+14 | 26 | | | | |

| Fit Statistics | Value |
|---|---|
| $R^2$ | 0.853272 |
| Adjusted $R^2$ | 0.775593 |
| Predicted $R^2$ | 0.701581 |
| Adequate Precision | 11.31158 |

Figure 4.5 (a) shows the impact on the profile void volume when spreading with an irregular shaped powder. The plot suggests that lower layer thickness and spreading velocities favour profile void volume reduction. However, a such trend only exists because of three factors; low layer thicknesses (< $D_{50}$ size of the powder) restrict the spread of large particles, lower spreading velocities aid the spread of the powder's fine particles first and the fact that the spreader transported twice the volume of powder that is actually required to form the layer. Powder B and C, due to their greater sphericity, showed substantial reduction in profile void volume on their powder bed topographies. When correlating the results presented in Figure 4.1 and Table 4.2 with the results of Figure 4.5 (b-c), the following can be said. Powder B displayed superior rheological performance. However, Powder C enabled the spreading of layers with lower profile void

volume. This is due to its wider particle size distribution and higher number of fine particles. However, it is seen that as the amount of fine particles increases the effect of layer thickness on spreadability decrease. Furthermore, the results suggest that the spreading velocity has substantial influence on the profile void volume, where low spreading velocities (≤80mm/s) resulted in profile void volume reduction.

(a)

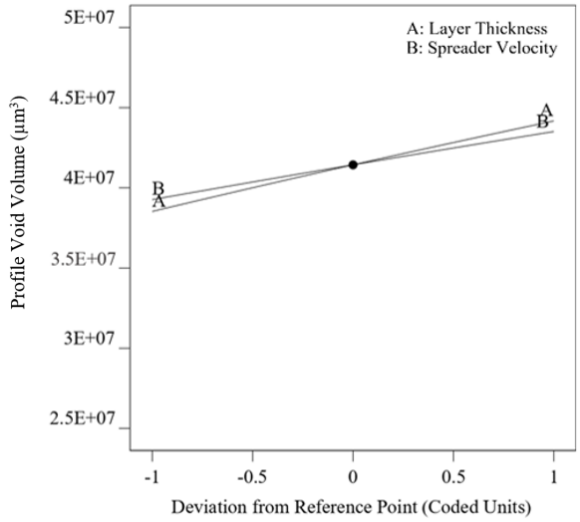


(b)

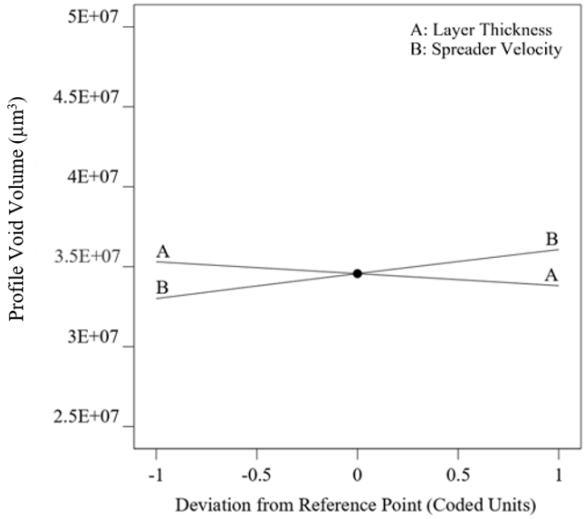


(c)

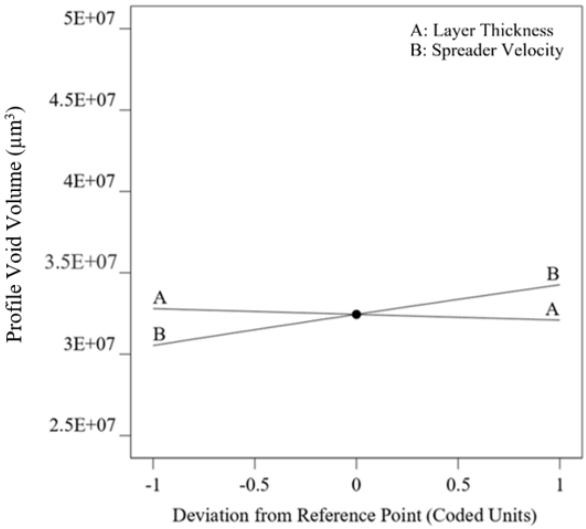


**Figure 4.5** Summary of the analysis of variance showing the effect of each factor on the profile void volume of the powder bed topography for powder (a) A, (b) B and (c) C.

#### 4.4.2.3 Layer Uniformity

This particular study focused on providing an understanding of the powder spreadability process step which is difficult to quantitatively analyse. The uniformity of the powder bed topographies was determined by assessing the ratios between powder peaks and valleys and their dispersion on the powder bed. The images of the powder bed samples can be found in the supplementary document. Figure 4.6 shows the results of this study. There is no clear evidence of interrelation of the parameters at any of the three levels. It can be said that the three powders appear to be similarly influenced by interparticle forces. Furthermore, the powders arrangement behaviour is also influenced by the particle size and particle morphology. Therefore, from the three powders, powder C appears to be slightly less influenced, potentially due to its better all-around morphological properties. Nevertheless, to better comprehend such behaviour of particles when forming powder layers, further studies enveloping a broad range of influencing factors is required.

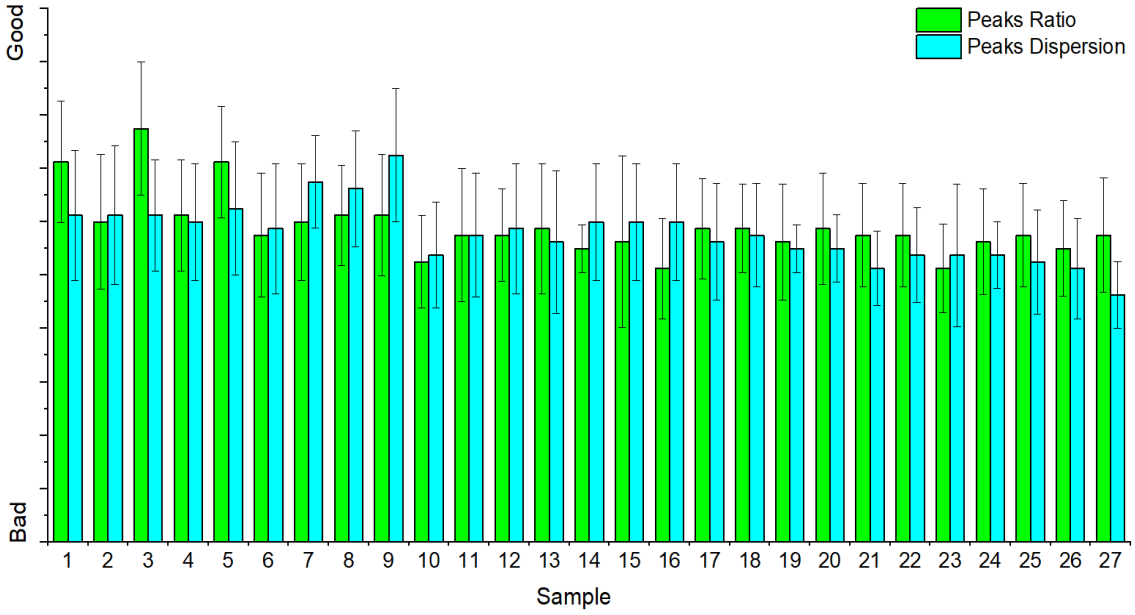


**Figure 4.6** Ratio between peaks and valleys and their dispersion in the powder bed topography, n=8. Peak ratio is the ratio between peak count and valley count. A good peak ratio has equal count of powder peaks and valleys. Peak dispersion refers to the dispersion of powder peaks. A good peak dispersion is when peaks and valleys are dispersed uniformly.

#### 4.4.2.4 Factors Affecting the Results

The three commercial powders used in this study were supplied having the same particle size distribution. Still, prior to carrying out the experimental work, these powders underwent sieving to remove the variable of different particle size distribution to enable an accurate study of the investigated factors and correlation between their physical and flow characteristics. However, as seen in Figure 4. 2 there was still exist a small difference between the powders particle size distributions and their volume densities. As can be seen, it is difficult to remove these two variables completely when comparing powders. Nevertheless, their influence on the responses can be minimised via sieving as addressed in this study.

An anti-static carbon fibre brush was used in the spreading of the powders to minimise any static charge within the spreading mechanism from being transferred to the powder particles. However, almost all of the PBF machines and the one used in this study have their chamber and spreading mechanism protected with an anti-static coating material. The carbon fibre type of brush is often used and for very specific applications and in this study it was chosen and used to reinforce the anti-static barrier from the spreading mechanism to the spreading particles. Therefore, the results presented here are also applicable to other blade materials such as rubber lip.

At the magnification used in this work the microscope provided a repeatability of 1 μm. Investigations into the ability of the microscope to reproduce the same measurement revealed a coefficient of variation (standard deviation/mean) of 0.031 for the profile height and 0.026 for the profile void volume. In summary, the measurement error introduced by the microscope is very small having no significant impact in the reported measurements.

The careful and gentle sample removal from the test bed to the microscope did not show any sign of powder bed disturbance or particles rearrangement. A recommendation for an alternative way of assessing the powder bed topography is the optimisation and incorporation of a system within PBF machine right above the printing area such as an ultrahigh accuracy 3D laser profilometer. For example, the hyperspectral interferometry technique has the potential of covering features small as 0.025 μm and real-time surface inspections [513,514]. Other non-contact techniques such as ultrasonic and capacitive are also useful for specifying surface parameters [515,516].

### 4.4.3 Particle Segregation

In order to characterize the uniformity of the spread powder layer, particle segregation resulting from the powder spreading process was also investigated in this study. Figure 4.7 shows the particle segregation across the length of the powder bed build platform area. Small particles were deposited preferentially at the start of the build platform (as measured from where the powder spreader crosses into the build area) while larger particles were deposited towards the end of the build platform. In fact, the degree of fine particle segregation and deposition was higher at the beginning than when the spreader reached the middle of the build platform, thereby not leaving as many fine particles within the spreading powder toward the end of the build platform. The points X, Y and Z indicated in Figure 4.7 show clearly the preference of the fine particles contained in the powder deposited initially. The effect of such segregation behaviour resulted in a new particle size distribution in the powder bed length between 70 and 140 mm, where the D-values for this region differ from the D-values of the same powder before its spreading. A powder size density ratio between the original and the powder from this last region of the deposition of close to 3:2 resulted as it seen from $Dv_{10}$ to $Dv_{50}$ and $Dv_{50}$ to $Dv_{90}$. This is mainly due to percolation segregation occurring within the dynamic powder avalanching during spreading. While small particles move downwards through the mass filling spaces between the large particles and at the same time the larger particles move upwards due to the Brazil Nut effect [517,518]. It was previously reported that the main contributors to segregation are particle size, particle size distribution, concentration of fines, particle shape and density [519]. However, the layer thickness and the spreading velocity are also considerable contributors to particle segregation [520,521]. In addition, the results here showed that particle segregation also occurs to those powders with narrow particle size distribution. Therefore, a convenient approach to minimise segregation would be to optimise the spreading parameters and layer thickness as well as strategically position parts on the build platform in areas less affected by segregation. Particle segregation within a powder bed should be avoided as it produces local variations of the powder bed density and can cause process instabilities in terms of meltpool signature [522,523].

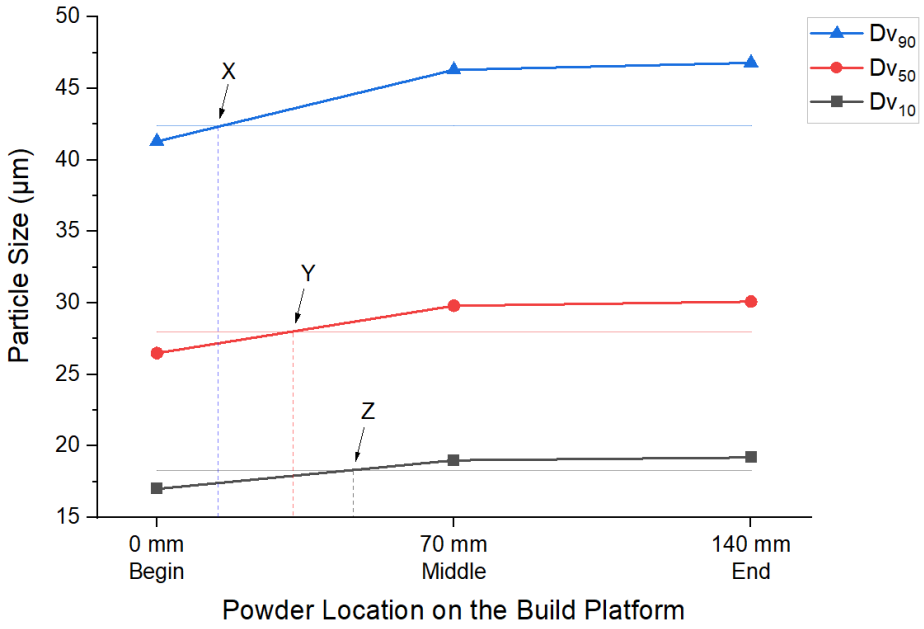


**Figure 4.7** Particle segregation for powder C in the powder bed measured from the begin to end length of the build platform. The highlighted points X, Y and Z shows the distance from the begin of the build platform where the D-values of the spread powder equal those of the same powder before the spreading, n=3.

### 4.4.4 Characteristics of Laser Scanned Layers

In selective laser melting, the spreading of powder layers is much more complex than simply spreading one new layer of powder on top of another. Laser processed two-dimensional geometries have very unique textures and laser scanned powder bed layers contain unwanted micro structures inherited from the interaction of the laser with the powder, in addition to other process intrinsic defects. Figure 4.8 (a) shows spatter particles ejected from the meltpool that fell onto the powder bed. Such spatter particles are likely to become fused with particles from the powder bed. Therefore, when spreading consecutive layers these fused particles can either cause flow separation, be pushed by the spreader scratching the powder bed or cause particle jamming resulting in particles which then collapse and burst into the spreading layer. Figure 4.8 (b) shows the topography of the powder bed, heat affected particles and the scanned geometry. The spreading of homogeneous consecutive layers in this case is challenging as the volume of powder required to fill the consecutive layer would be different in each of the three zones. In addition, the spreading of powder onto the scanned geometry would certainly led to localised segregation in the powder bed due to its greater depth. Also, it should be understood that the scanned geometry is fixed to the build platform while particles are

loose and the powder bed is compressible. Figure 4.8 (c) shows the presence of defects on the topography of the scanned geometry. The observed swelling, warping and balling features are common defects in PBF processing geometries. These and similar defects challenge the spreading of subsequent quality layers. The problem with such defects intensifies further when the structures resulting from them pass above the consecutive layer thickness. This is because the contact of the spreader blade with such structures cause localised wear in the blade resulting in non-uniform powder distribution over the powder beds [524]. Defects onto the built surface such as those encountered and reported here can be mitigated by optimisation of the processing parameters such as laser power, scanning speed and hatch spacing as well as using high quality powders [525].

(a)

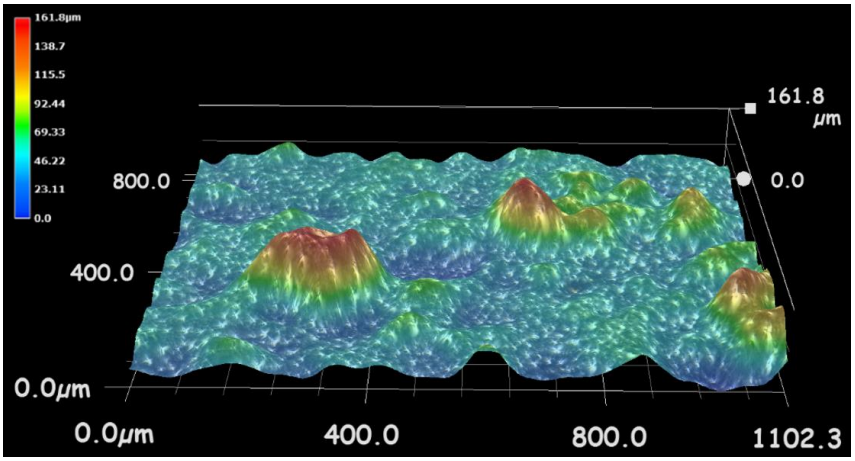


(b)

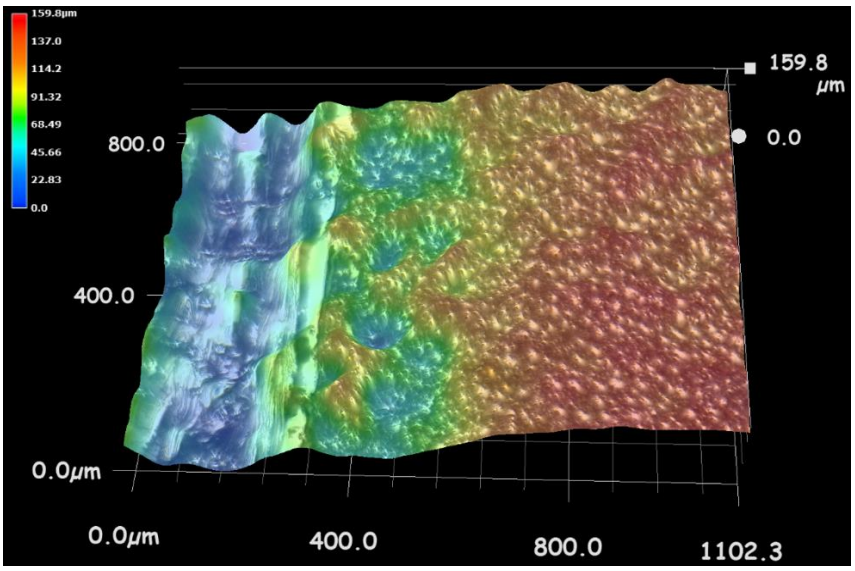


(c)

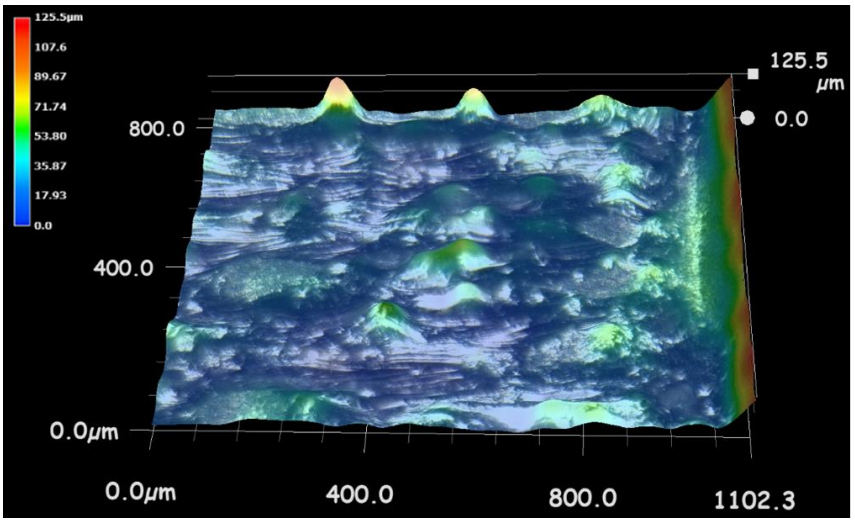


**Figure 4.8** Morphologies challenging powder spreadability in consecutive layers. Large spatters fused with particles of the powder bed profiling above the layer height (a), Height differences at the interface between the scanned two-dimensional geometry and its powder bed (b) and warping, balling and swelling defects in scanned geometries compromise powder spreadability and the life of powder spreading blades (c).

### 4.5 Conclusions

In this work, the spreadability of metal powders was experimentally investigated using a commercial PBF printer. The effect of powder morphology and the role of the spreading parameters on the quality of powder layer topography is demonstrated in this contribution. To thoroughly understand the influence of the spreading parameters on powder spreadability, a three-level full factorial design was employed. Particle segregation is also reported in this work as well as the major process related challenges to powder spreadability. The main conclusions from the presented work are summarised as follows:

(1) The flowability of the highly spherical powder (powder C) containing satellites were slightly lower compared to the less spherical and smoother powder (powder B). This was because of the higher mechanical interlocking of satellite particles, hence naturally resisting to flow. Powders containing large number of fine particles (< 25 µm) presented higher specific energy and higher flow rate sensitivity due to the cohesive forces.

(2) The profile height of the powder bed topography is primarily based on the powder flow characteristics, and in this study the profile height was further reduced by optimising the layer thickness and the spreader velocity. Therefore, it can be concluded that these two parameters are very important for powders with high flowability, and deserve careful consideration.

(3) The profile void volume of the powder bed topography is influenced by the powder morphology, spreading conditions and the interaction of the particles. Powder B exhibited higher rheological performance. However, Powder C enabled the spreading of layers with lower profile void volume due to its wider particle size distribution and higher fine particle content. However, as the amount of fine particles increase the effect of layer thickness on spreadability decreases. Furthermore, the results suggest that the spreading velocity has substantial influence on the profile void volume. Where low spreading velocities ($\leq$ 80 mm/s) resulted in profile void volume reduction. In conclusion, the best uniformity of the powder bed topography was achieved with powder C when spread at 80 mm/s in a layer thickness of 50 µm. Based on this, it can also be concluded that the largest particles (D90, and those above it) dictate the minimum layer thickness.

(4) Particle segregation is unavoidable when spreading powders with wide particle size distribution using a spreading blade system. Mitigation of this problem is possible by using tailored powder characteristics (such as particle size distribution, concentration of fines and particle shape) and optimisation of the spreading parameters and layer thickness. Strategically positioning parts on the build platform in areas less affected by segregation also helps to mitigate this problem.

(5) Laser processed two-dimensional geometries have very unique textures and laser scanned powder bed layers contain unwanted microstructures inherited from the interaction of the laser with the powder, in addition to other process intrinsic defects. Therefore, the uniformity and homogeneity of consecutive layers is very complicated to predict well. For this, the relationship of the in-printing characteristics, including scanned geometry, to powder spreadability need to be considered.

The results presented herein are suitable for validating numerical models and they extend beyond the fundamentals of powder spreadability, providing guidelines and recommendations to PBF operators. An accurate prediction of the quality of each spread layer is possible and achievable via powder spreadability simulation coupled with process monitoring. However, for this to come into existence, substantial work is still required around modelling powder dynamics during spreading and a substantial amount of experimental results are needed to validate powder spreading simulations.

The experimental approach used in this work may be referred to as deep powder bed studies (a powder layer spreader onto existing powder layers). Deep powder beds are relevant when printing typically produced parts which contain supports, overhangs, bridges and/or angled facets. The other aspect of powder bed, yet to be researched, is thin powder layer powder spreading (i.e. the spreading of powder layers onto built surfaces). A challenge to this is that every single built surface will have its own characteristics i.e. roughness and geometry. However, comprehensive studies into both, deep powder bed and thin powder layer will be required in order to acquire powder spreadability data for validating numerical models developed for this process.

# Chapter 5

## Evaluation via Powder Metallurgy of Nano-Reinforced Iron Powders Developed for Selective Laser Melting Applications

**Publication Status:** Published

Mussatto, A., Groarke, R., A-Hameed, A., Ahad, I. U. I., Vijayaraghavan, R. K., O'Neill, A., McNally, P., Delaure, Y., and Brabazon, D., 2019, "Evaluation via Powder Metallurgy of Nano-Reinforced Iron Powders Developed for Selective Laser Melting Applications," Materials & Design, 182, 108046.

https://doi.org/10.1016/j.matdes.2019.108046

## 5.1 Abstract

In this work, a gas atomised stainless steel AISI 316L powder was used as metal matrix and SiC was employed as a nano reinforcement. The powders were experimentally characterised to determine the effect of the morphology, size, and levels of reinforcement on the powder flowability. The powder was developed via the powder metallurgy route and the effect of material, process conditions and various levels of reinforcement were investigated through the microhardness of the sintered samples. Sintered samples produced from the 316L+SiC+PVA powder mixes presented improved hardness. Analysis of the Energy Dispersive X-ray measurements detected high intensity levels of carbon and silicon on the surface of the reinforced 316L particles. In terms of measured powder rheology, the 6 wt. % SiC coated 316L provided the highest flowability of the prepared SiC coated 316L powders and a much higher flowability than the as received 316L powder. All prepared SiC coated 316L powders showed good flowability and highly repeatable powder rheology. The high degree of flowability was attributed to the particle spherical morphology, the narrow range of particle size distribution and also the coating of nano SiC particles on the 316L particles which were found to act in this case as a solid lubricant. A successful homogeneous and uniform reinforcement of SiC onto the surface particles was resultant from the established mixing technique. While the nano-SiC improved the powder fluidity, the obtained improvement in hardness was also due to the nano-SiC dissolution and resultant precipitates formed during the thermal treatment.

## 5.2 Introduction

In recent years, metal matrix composites (MMCs) reinforced with nano-particles reached a degree of maturity, with promising properties suitable for numerous structural and functional applications. These composites consist of one or more reinforcement materials, embedded into and featuring mechanical and physical properties very different from those of the metal matrix [526]. Nano-reinforcements can improve the base material in terms of mechanical strength and wear resistance, and retain composite properties at elevated temperatures [527]. Powder metallurgy (PM) routes are extensively used for new composite composition investigation. Besides being inexpensive and simple, the PM process is suitable for the synthesis of micro- and nano-ceramic reinforced MMCs, in addition to the resulting lower extent of material usage and waste generation [528–532].

The properties of the powders have a major impact on the packing ability and spreading performance of the consolidation method applied. In fact, it is well known that particle size, size distribution, shape and surface texture influence flowability and packability of powders, and that chemical composition, entrapped gas and oxidation influence their processability, energy input requirements and reactions [23,533,534]. The homogeneous mixing of reinforcement with matrix powders is a critical step to process MMCs, as it can have a significant influence on mechanical properties and production of defects [535,536]. Achieving a homogeneous distribution of the reinforcement in the matrix can be difficult. However, it has been reported that low energy milling enables fine reinforcement particles to adhere onto the surface of large matrix particles [537,538]. To date, several researchers attempted to obtain homogeneous blend of powders [539–544]. However, a processing route to obtain consistently good homogenous mixtures, still remains elusive, due for example to reinforcement particles clustering and reinforcement falling from the surface of matrix particles due to lack of adherence.

The rheological properties of metal powders are very important for both PM and selective laser melting (SLM) processes. In PM, a powder with poor flow characteristics may result in uneven compactions which can cause sample distortion, porosity and density anisotropy and stress concentrations [545,546]. Similarly, powder flow characteristics are key for the powder bed system to form uniform and consistent layers of powder [547,548]. Powder flow can be improved by particle surface smoothing, uniform particles size, reduced cohesion and increasing particle density and rounding. Powder flow can be influenced by particles with high friction, high mechanical interlocking, temperature, high moisture content, electrostatic charge, consolidation, process related variables and aeration of cohesive and non-cohesive powders [549]. It is recently further reported that fine powders, those below 30 μm, often exhibit poor flow and tendency to agglomeration as a result of higher Van der Waals forces [550]. The effect of particle size distribution studied by Ashcroft et al. showed that powders with narrower width of particle size distribution provided better flowability and produced parts with higher hardness and tensile strength [551]. Therefore , it was suggested that a better all-around combination of properties is obtained with an average particle size in the range of 30-45 μm [552].

A considerable amount of research has been performed in attempting to characterise the rheological behaviour of powders [553–558]. However, they concentrate on a single material type of powder, and to date there is no rheological records related to flow

behaviour of nano-SiC reinforced steel powder mixtures. Therefore, this study was completed in order to have this information to better develop feedstock powders for processes like SLM and PM for the production of MMCs with improved properties. While most commercial metal matrix composites are aluminium based, steel-based metal matrix composites are can be used in a variety of applications. For example, 316 reinforced by SiC can offer corrosion resistance with increased stiffness as may be required in marine, fuel processing or vehicle fuel line, aerospace or food processing applications. Other applications could include armour plating and vehicle mechanisms where higher stiffness and/or wear resistance are required compared to what can be achieved with aluminium matrix composites. It is worth noting that moving mechanical components with higher stiffness can provide an important efficiency of energy transfer and hence energy saving.

In this work, an iron-based powder was used as metal matrix and nano SiC was added as reinforcement. In order to assess the potential for these powders to be used within the SLM and PM process, they were first experimentally characterised to determine the effect of the morphology, size, and nano reinforcement on the powder flowability. Then the powders were assessed via the PM route and the effect of various levels of reinforcement were investigated through the microhardness and microstructure of the sintered samples.

## 5.3 Experimental Work

### 5.3.1 Powders

In this study, a gas atomised micron size stainless steel AISI 316L powder supplied by Castolin Eutectic was used as metal matrix iron-based material. Its chemical composition was 0.02 C, 1.47 Mn, 0.75 Si, 18.36 Cr, 12.20 Ni, 2.04 Mo, 0.04 P, 0.02 S, 0.10 N and Fe in balance (in wt.%). Nano size SiC powder (purity > 99 %) was obtained from US Research Nanomaterials Inc. and used as reinforcement. Polyvinyl alcohol (PVA) in powder form (> 99 % hydrolysed, Mw 98000) was obtained from Sigma-Aldrich and used as binding material.

#### 5.3.1.1 Powder Sieving

The sieving was performed with an Endecotts Octagon 200CL sieve shaker and two woven wire mesh sieves of mesh sizes of 38 µm and 50 µm. Seven batches of 200 grams

of the as received 316L powder were sieved. Each batch was sieved for 30 minutes in an amplitude of 3 mm.

#### 5.3.1.2 Powder Quality Assessment

The particle size distribution of the 316L and PVA powders were obtained by laser diffraction measurements using a Malvern Mastersizer 3000. Both, the 316L and PVA particles were analysed in powder form. Additionally, the SiC powder was dispersed in de-ionised water and ultrasound was used to assist on the dispersion and break up of agglomerated particles. After two hours of sonication, the particle size of the SiC powder was measured by a Microtrac Nano-Flex 180° dynamic light scattering (DLS) system. Microstructural and morphological characterisation of the powders particles were conducted via scanning electron microscopy (SEM) using a Zeiss EVO LS-15 microscope.

### 5.3.2 Development of Powder

#### 5.3.2.1 Powder Development process

The powder samples were prepared in terms of weight percent. The mixing of the powder samples was performed in a Pascal ball mill using a drum of 100 mm internal length and 90 mm internal diameter. Four 20 mm diameter spherical milling balls were used as mixing media and the rotation speed of the drum was set to 150 rpm.

#### 5.3.2.2 Powder Flowability Analysis

Four batches of 100 grams of powder, each composed of sieved 316L + SiC 6 wt. % were prepared for mixing. The ball mill was set up as described previously and each batch of powders were mixed for four hours and then the four batches of powders were combined and mixed for another hour. For comparison, the flowability of the as received and sieved 316L powders were also investigated.

The stability, variable flow rate, aeration, compressibility and permeability characteristics of the three powders were investigated using a Freeman FT4 powder rheometer. The standard procedure of each test can be summarised to the following: The powders to be tested were placed inside cylindrical glass vessels of known volume. The stability test involved eight identical repeated tests with blade tip speed of 100 mm/s. Whereas for the variable flow rate test the blade tip speed was gradually reduced in steps

(100, 70, 40 to 10 mm/s) in the remaining four tests. In between each test a conditioning cycle was performed, where the blade passed through the powder eliminating any packing history. The various flow terms were then calculated from the work done in moving the blade through the powder from the top to the bottom of the vessel. The aeration test was conducted in a vessel mounted on a base with an air inlet port. During the test, the blade travelled downward helical path through the powder bulk. Between each of the different air flow rates (0, 2, 4, 6, 8 and 10 mm/s) the powder underwent a conditioning cycle. The incorporation of air into the powder was used to assess whether the powder flow properties change. The aeration measurements were then based on the reduction in flow energy. Prior the compressibility test, the powder samples were submitted to three conditioning cycles. Then, the blade was replaced by a vented piston which slowly consolidated the powder by applying a normal load in small increments between 1 to 15 kPa. The compressibility was then computed based on the percentage change in powder volume. The permeability test was run similarly to the compressibility test except by using a vessel base with an air inlet port. While the air velocity across the powder bed was maintained constant at 2 mm/s, the permeability of the powder was quantified by measuring the pressure drop across the powder bed whilst the applied normal pressure was gradually increased. The various flow terms and their definitions are given in Table 5.1.

**Table 5.1** Flow terms and their definitions available for the FT4 Powder Rheometer.

| Term | Definition |
|---|---|
| Basic Flowability Energy (BFE) | The energy needed to displace a conditioned powder sample during downwards testing. |
| Stability Index (SI) | The factor by which the measured flow energy changes during repeated testing or processing. |
| Flow Rate Index (FRI) | The factor by which the flow energy is changed when the flow rate (tip speed) is reduced by a factor of 10. |
| Specific Energy (SE) | The energy per gram needed to displace conditioned powder during upwards testing using a negative 5º helix (lifting to produce shear and no consolidation). |
| Conditioned Bulk Density (CBD) | Bulk density of a conditioned powder sample. |
| Aeration Ratio ($AR_{10}$) | The factor by which the BFE is reduced when the sample is retested whilst being aerated at 10 mm/s of air velocity. |
| Aerated Energy ($AE_{10}$) | The energy needed to displace an aerated powder sample whilst being aerated at 10 mm/s. |
| Compressibility ($CPS_{15kPa}$ %) | Percentage by which the bulk density has increased with an applied normal stress of 15 kPa. |
| Pressure Drop ($PD_{15kPa}$) | The decreased pressure while passing air through the powder at a speed of 2 mm/s while apply a normal stress of 15 kPa to powder. |

#### 5.3.2.3 Energy Dispersive X-ray Analysis

Energy Dispersive X-ray (EDX) analysis was mainly used to characterise the chemical composition present on the surface of the developed SiC coated 316L particles, but also to investigate if any trace of moisture, contamination and oxidation were present on them. The EDX analysis was performed on a sample of sieved 316L + SiC 6 wt. % powder, from the powder flowability analysis, using a SEM-EDX Hitachi S5500.

### 5.3.3 Fabrication of Composites

#### 5.3.3.1 Composite Fabrication Process

The powder samples were prepared as mentioned previously in the powder development process. Sieved 316L was mixed with SiC (0, 1, 2, 3, 4, 5 and 6 wt. %) and 2 wt. % PVA, where each of the 15 grams of sample powder was mixed for four hours.

Powder compaction was performed using a Specac Atlas™ Autotouch 40T hydraulic press and a 20 mm in diameter pellet die. Before each compaction the die elements were lubricated with a thin layer of boron nitride powder. Three grams of powder was used per compaction which led to 1.5 mm thick and 20 mm diameter coin shaped green compacts. A compaction pressure of 500 MPa was held for three minutes and then slowly released. The green compacts were placed onto alumina rectangular crucibles and then kept in a desiccator filled with silica gel until the next day when sintering was performed.

The sintering process was performed using a Lenton horizontal tube furnace, model LTF. The green compacts were sintered in argon atmosphere using a gas flow rate of one litre per minute. The green samples were heated up and cooled down at a rate of 5 °C per minute. When the temperature inside of the furnace reached 250 °C, a dwell period of 30 minutes was applied. This allowed smooth initiation of thermal degradation of the PVA material within the samples. After this, the samples were heated up to 1200 °C and held at this temperature for three hours to enhance particle bonding and sample densification. Once the dwell time elapsed the temperature of the furnace was brought back down to room temperature at the rate previously mentioned.

#### 5.3.3.2 Metallographic Sample Preparation

A Buehler Simplimet 2000 mounting press was used for the encapsulation of the samples in Bakelite. After this the samples were ground using SiC grinding papers of 240, 400, 800 and 1200 grit, and then pre-polished with Nylap cloths and 6 and 1 µm diamond suspensions, followed by a final polishing with a PSA polishing cloth and colloidal silica suspension of 50 nm, in a Grinder-Polisher Metken Forcipol 2V. The polished samples were etched with a solution composed of glycerol 20 %, nitric acid 20 % and hydrochloric acid 60 %.

#### 5.3.3.3 Sintered samples Analysis

The hardness of the sintered samples was measured using a Leitz microhardness tester and the measurements were performed according to ASTM E92 standard, with 10 random indentations in each sample, indentations at the same direction as the load applied during compaction.

Microstructural analysis of the 316L (sieved) + SiC 6 wt. % composite was carried out using a triple-axis Jordan Valley Bede D1 high resolution X-ray diffraction (XRD) system with a copper ($\lambda$=1.5405 Å) radiation source operated at 45 kV and 40 mA, and on a Zeiss SUPRA 40 field emission scanning electron microscope (FESEM) equipped with a Bruker Electron backscatter diffraction (EBSD) detector.

## 5.4 Results and Discussion

### 5.4.1 Powder Characterisation

#### 5.4.1.1 As received powders

Ideally, for selective laser melting, powders with a Gaussian type of distribution are preferable. A powder with this type of distribution generally has good symmetric agreement about the mean particle diameter, $D_{50}$. This is normally the case for powders with narrow size distributions.

The as received 316L powder used in this study presented a negative skewed distribution which means that the powder contained a proportion of fine particles. These fine particles are better observable in the micrograph, see Figure 5.1 (a). From this type of particle size distribution, one would expect that this powder could provide a dense packing of the spread powder layer. However, a powder with a narrower width of particle size should provide a better powder flowability and enable production of parts with improved mechanical properties. Additionally, it can be seen from the micrograph that most of the particles had good sphericity. However, a small amount of the particles contained satellites. These sort of irregularity with the particles are not desired as they affect the flowability and packing ability of the powder.

The result of the particle size distribution analysis performed on the PVA powder showed that this powder contained a portion of particles from 10 to 50 µm. However, this powder contained a wide distribution, including some very large particles, see Figure 5.1 (b). The micrograph of the PVA powder showed that the particles were reasonably spherical and

composed of several globular structures. These globular structures are common in these polymeric powders, as during the formation of the particles, macromolecules (long chain molecules) coil into globules.

Figure 5.1 (c) shows the particle size distribution of the SiC spherical powder. The plot indicates that the powder had a narrow distribution and a median particle size of 41 nm. It can be seen from the micrograph that the SiC particles tend to cluster, which is probably due to cohesive and electrostatic forces between the particles. The high degree of clustering of SiC particles may impose some difficulties on obtaining a homogeneous distribution of this material in the matrix powder. Local inhomogeneity and clustering of reinforcement particles influences the mechanical properties of the MMC, as clustered regions promote interface debonding and crack initiation and have a negative effect on toughness and fatigue and tensile strength of the composite. To overcome this problem and to obtain a uniform dispersion of reinforcement in the MMC, a good mixing technique is required.

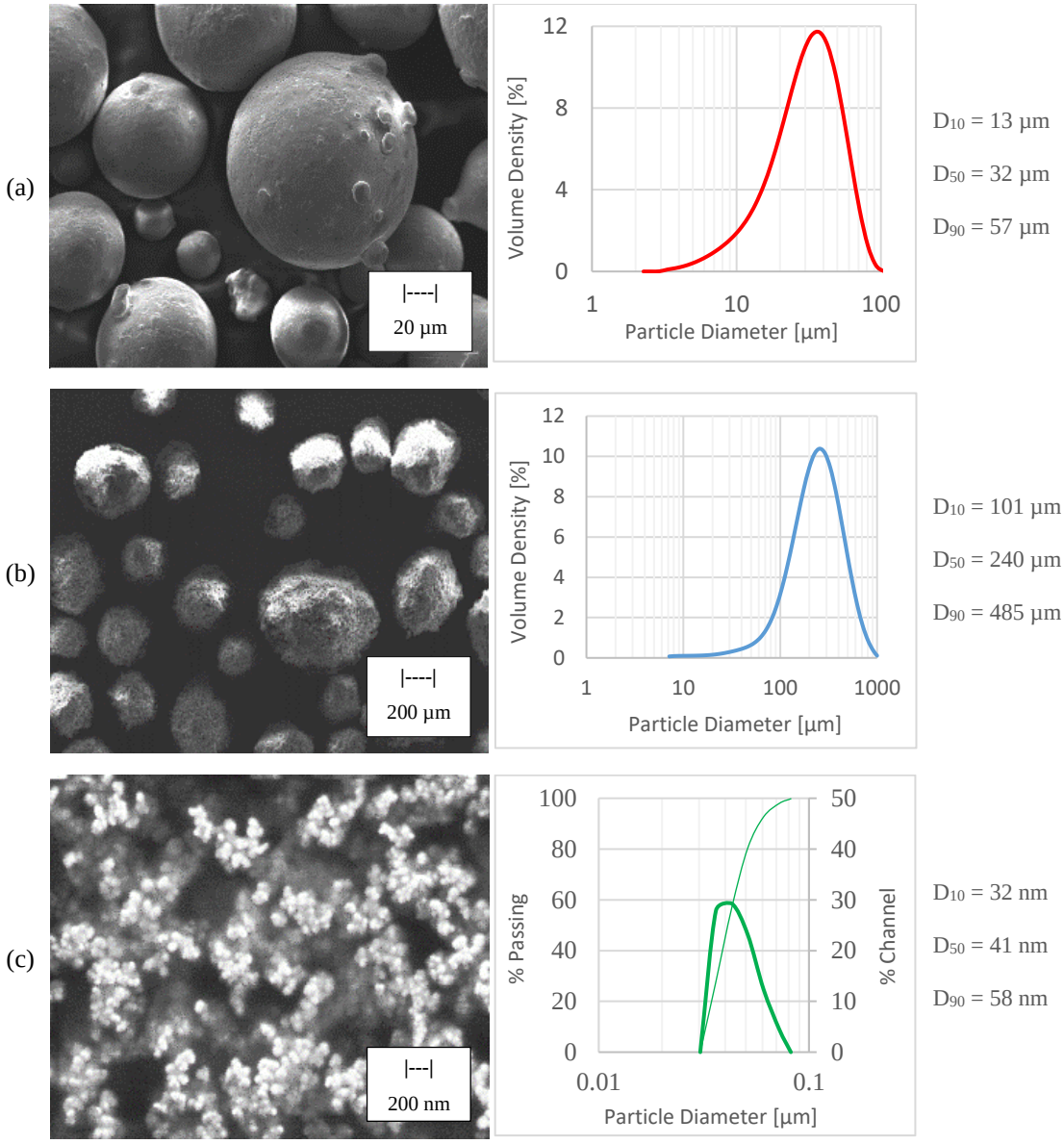


**Figure 5.1** SEM micrographs and particle size distribution of the as received powders; (a) 316L, (b) PVA and (c) SiC.

### 5.4.1.2 Sieved 316L Powder

Sieving of the 316L powder was conducted in order to obtain a narrow particle size distribution and to remove very small particles and large irregular shaped particles. Particles smaller than 30 µm tend to agglomerate easily, present high level of cohesiveness and strongly vary packing fractions, thus affecting powder layer quality. Larger particles require a higher energy density for processing, affect the packing densification and thermal conductivity and could contribute to larger void sizes in printed parts reducing mechanical strength [559]. Therefore, sieving has the potential of improving powder flowability, which is very important for a powder bed system to form

uniform and consistent layers of powder. Sieving to a discrete size range can also lead to a more consistent produced part porosity size in manufactured parts, thus facilitating their control and reduction through the optimisation of the processing parameters.

The resultant powder mass obtained from the sieved powder within 38 µm and 50 µm was approximately 40 % of the as received powder mass. The collected sieved powder was analysed in terms of particle size distribution and compared with the as received powder, see Figure 5.2. When analysing the particle size distribution given by the sieved powder it is seen that the $D_{90}$ is slightly above 50 µm and that $D_{10}$ is slightly below 38 µm. This is expected as some large irregular and elongated particles may have passed through the 50 µm mesh. On the other hand, particles that are smaller than 38 µm rarely remain in the 38 µm mesh. But in this case, some particles sized slightly smaller than the sieve mesh remained in the sieve. This could be due to the shape of these particles and due to too short sieving time. However, it can be said for this powder characteristics that the sieving time was performed near optimum conditions as equally - 5 µm for the small sieve mesh and + 5 µm for the large sieve mesh deviated from the expected particle size distribution. A longer sieving time would possibly allow more irregular shaped particles to pass through the 50 µm mesh and this would later impact on the powder bed quality. It is seen from the plot that volume density of the sieved powder increased, this was simply because the volume occupied by particles that were of the size $D_{50}$ or close to the size $D_{50}$ increased in comparison to the size $D_{50}$ given by the as received powder. Additionally, it can also be said that powder size control with sieving is maximised as particles sphericity increases and topographic roughness smooths.

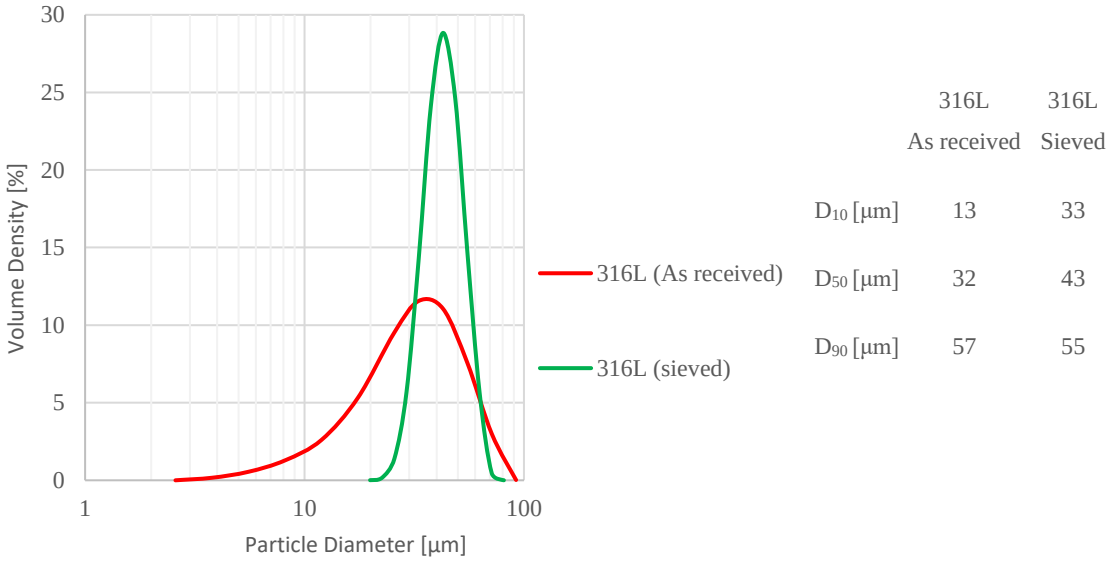


**Figure 5.2** Particle size distribution of the sieved 316L powder.

### 5.4.2 Developed Powder Characterisation

#### 5.4.2.1 Powder Flowability Assessment

The measured stability, variable flow rate, aeration, compressibility and permeability properties of the 316L as received, 316L sieved and 316L sieved + SiC 6 wt. % powders are shown in Figure 5.3 and Table 5.2.

The relatively low basic flowability energy (BFE) measured from the three powders are characteristics found in powders with good flow properties, and this is due to many physical properties of the particles such as size, shape and surface texture. The specific energy (SE) measured from the powders indicated that they had low cohesion. A powder with low BFE and low SE is easy to displace due to the ease with which the particles move over each other, and this powder is more likely to have low conditioned bulk density (CBD). The CBD of the as received 316L powder is slightly higher than the other two powders because of its morphology and particle size and distribution. The stability index (SI) indicated that the powders were robust materials of good flow stability, and the flow rate index (FRI) suggested that the reinforced powder was much less sensitive to flow rate, such that it could be considered a flow rate insensitive powder. The superior reproducibility of the developed powder (316L sieved + SiC 6 wt. %) in comparison to the other tested powders is indicated by the calculated margin of error presented margin of error in Table 5.2. In addition, the change in the variable flow rate measured for this powder is lower than that recorded for the other powders. This indicates that this powder

would be less sensitive to variations in process speed across various SLM or PM processing systems. In brief, the stability and variable flow rate results of the powders showed that the developed powder provided higher levels of repeatability and a very stable rheology.

The aeration results show that the powders were very sensitive to even very low air velocities, presenting a rapid rate of total energy reduction. With slightly increase in air velocity it is noted that the fluidisation state of the powders occurred, as the flow energies reduced to nearly zero. The higher value of the aeration energy ($AE_{10}$) measured from the as received 316L powder may be attributed to agglomeration and adhesion among its small sized particles. All the tested powders presented very high aeration ratios ($AR_{10}$) strongly suggesting that the powders were very sensitive to aeration and prone to fluidization, where this was even more pronounced with the sieved and reinforced 316L powders.

The compressibility test does not provide a direct measure of the flowability. However, it was used in this work to understand the behaviours of the powders such as during the roller or blade spreading of powder in SLM systems. The compressibility results indicate that the powders had moderate sensitivity to compression. However, the powders without the reinforcement had less change in volume even at high normal stresses. The slightly higher compressibility of the reinforced powder is explained by its nano coating of SiC which acted as a lubricant and thus impelling this powder to a higher compressibility. This is also visualised in the compressibility plot for this powder, as a sharp increase in compressibility. In such a case, like of the reinforced powder, compressibility may not be a good and true indicator for powder cohesiveness.

The permeability results show that compression has minimal or no effect on the permeability of the powders. The reinforced powder generated higher pressure drop across the powder bed than the other two powders, indicating either very small or limited number of channels between the particles. At this stage it is not known if the permeability level found in each of the powders influence the SLM process. A certain level of permeability is desirable to move a powder from one position to another, this allows gas to replace space vacated by the particles more easily. This case is analogous to the powder spreading process. A permeable powder has the capacity of retaining unwanted gas and

release it during its processing. Such a powder then can have a detrimental effect on the SLM process and on the quality of its printed products.

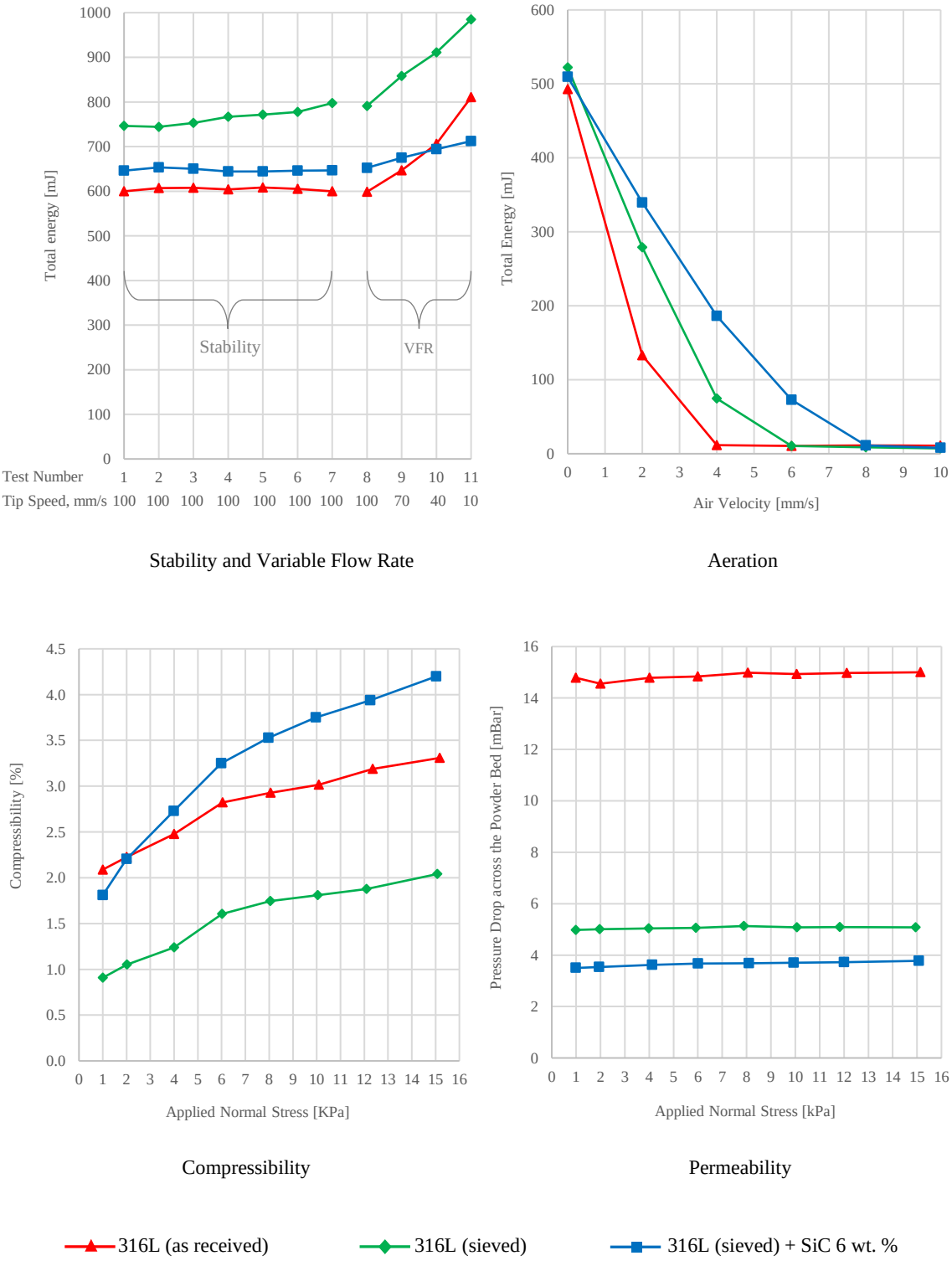


**Figure 5.3** Dynamic flow properties (stability, variable flow rate and aeration) and bulk properties (compressibility and permeability) of the powders (316L as received, 316L sieved and 316L sieved + SiC 6 wt. %).

**Table 5.2** Flowability characteristics of the powder samples.

| Stability and Variable Flow Rate, n=3 | | | | | |
|---|---|---|---|---|---|
| Series Name | BFE [mJ] | SI | FRI | SE [mJ/g] | CBD [g/ml] |
| 316L (as received) | 599.90 | 1.00 | 1.35 | 1.74 | 5.15 |
| *Margin of error (95% C.I.)* | 118.51 | 0.05 | 0.03 | 0.27 | 0.04 |
| 316L (sieved) | 797.39 | 1.07 | 1.25 | 1.88 | 4.85 |
| *Margin of error (95% C.I.)* | 142.28 | 0.11 | 0.09 | 0.21 | 0.05 |
| 316L (sieved) + SiC 6 wt. % | 646.80 | 1.00 | 1.09 | 2.96 | 3.46 |
| *Margin of error (95% C.I.)* | 32.75 | 0.08 | 0.04 | 0.14 | 0.16 |

| Aeration, n=1 | | | |
|---|---|---|---|
| Series Name | BFE [mJ] | AE_10 [mJ] | AR_10 |
| 316L (as received) | 493.00 | 10.84 | 45.46 |
| 316L (sieved) | 522.21 | 7.20 | 72.58 |
| 316L (sieved) + SiC 6 wt. % | 509.35 | 7.89 | 64.53 |

| Compressibility, n=1 | | |
|---|---|---|
| Series Name | CBD [g/ml] | $CPS_{15kPa}$ [%] |
| 316L (as received) | 5.21 | 3.31 |
| 316L (sieved) | 4.85 | 2.04 |
| 316L (sieved) + SiC 6 wt. % | 3.48 | 4.20 |

| Permeability, n=1 | | |
|---|---|---|
| Series Name | CBD [g/ml] | $PD_{15kPa}$ [mBar] |
| 316L (as received) | 5.35 | 15.00 |
| 316L (sieved) | 5.08 | 5.08 |
| 316L (sieved) + SiC 6 wt. % | 3.65 | 3.78 |

### 5.4.2.2 Powder Topography and Chemical Analysis

Figure 5.4 (a) and (b) compares the topography of a 316L particle with a 6 wt. % SiC coated 316L particle. The porous coat of SiC onto the particle seen in Figure 5.4 (b), which is better seen in (c), was estimated to be 470 nm. Monte Carlo simulation (CASINO V2.51) was used to find the EDX settings for an ideal depth of interaction volume for the particle shown in Figure 5.4 (b). Figure 5.4 (d) illustrates the simulated scattering paths of electrons from the particle shown in Figure 5.4 (b). The path represented by the red colour are backscattered electrons and the path represented by the blue colour are secondary electrons (absorbed electrons). Based on the simulation, it is seen that majority of the chemical information was extracted from the SiC layer. However, energetic electrons could have penetrated the SiC layer and backscattered electrons having chemical information about the 316L. Figure 5.4 (e) shows the chemical composition measured from the surface of particle shown in Figure 5.4 (b). As expected, very high concentrations of Silicon and Carbon were observed. Additionally, Iron, Nickel, Chromium, Manganese and Molybdenum were identified, indicating the main elements composing the 316L. The presence of these elements can be explained along with the presence of Silicon and Carbon. A significant amount of the Silicon and Carbon were from the applied coat, and the other elements were most likely satellites detached from the 316L particles crushed during the powder mixing process that adhered to the surface of 316L particles together with the SiC particles. It was found that 6.45 wt. % of Oxygen was present on the SiC 316L surface. Oxygen could negatively affect the SLM process and the printed product quality. Figure 5.4 (e) presents the surface chemical composition. It should be noted that EDX is not able to accurately quantify absolute elemental concentration for carbon and oxygen due to their low atomic weight but can be used to indicate relative difference between sample for these elements.

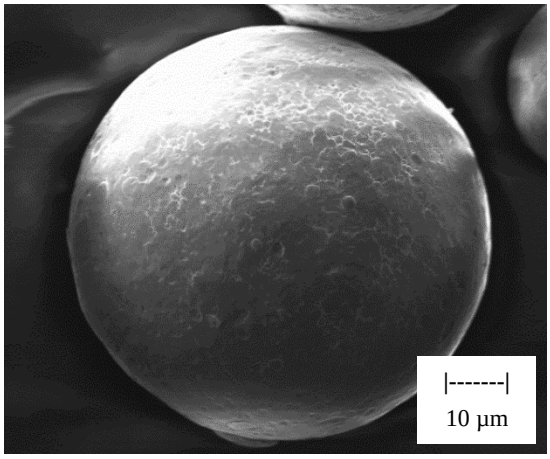


(a)

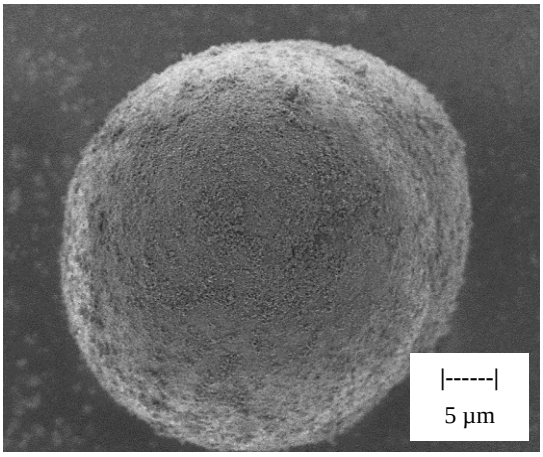


(b)

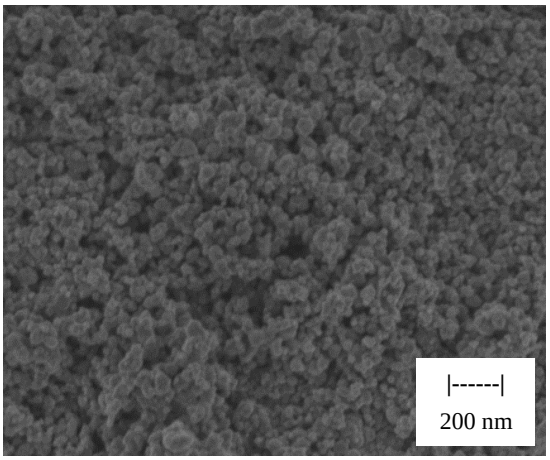


(c)

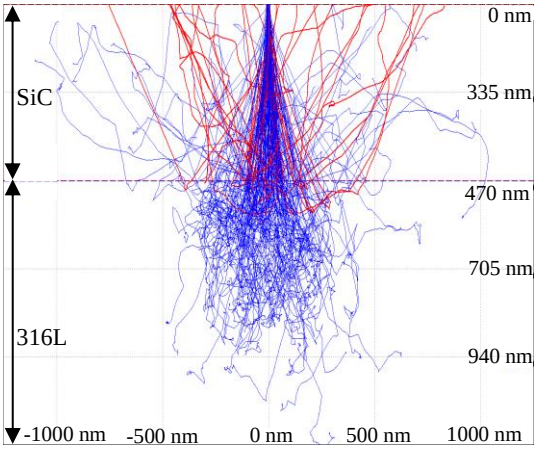


(d)

| C | Si | Fe | Cr | O | Ni | Mn | Mo | Al |
|---|---|---|---|---|---|---|---|---|
| 40.89 % | 12.44 % | 27.30 % | 7.40 % | 6.45 % | 3.42 % | 0.88 % | 0.86 % | 0.36 % |

(e)

**Figure 5.4** SEM micrographs comparing the topography of a 316L particle with a 6 wt. % SiC coated 316L particle, and the elemental composition obtained from the surface of the SiC coated 316L particle. (a) 316L particle, (b) 6 wt. % SiC coated 316L particle, (c) close-up view of the SiC nanoparticles coating the 316L particle, (d) Monte Carlo simulation displaying electron trajectories from the surface of the SiC coated 316L particle during the EDX analysis and (e) the measured chemical composition in terms of weight percent.

### 5.4.3 Sintered Samples Evaluation

#### 5.4.3.1 Composite Microhardness

The Vickers hardness measure from the sintered samples is shown in Figure 5.5. Clearly, the addition of SiC to stainless steel 316L has improved the hardness remarkably. It is seen a nearly exponential relationship between the amount of reinforcement and hardness. The hardness results obtained in this experiment showed that small amount of SiC can significantly improve the hardness of stainless steel 316L. It is expected that this is importantly due to carbide segregation at grain boundary which restricts grain growth, hence further contributing towards enhancement of the hardness. Further hardness increase could potentially be achieved through further detailed investigation of the processing parameters. In general, these measurements give a good indication of what hardness to expect from the developed powders when processed via SLM.

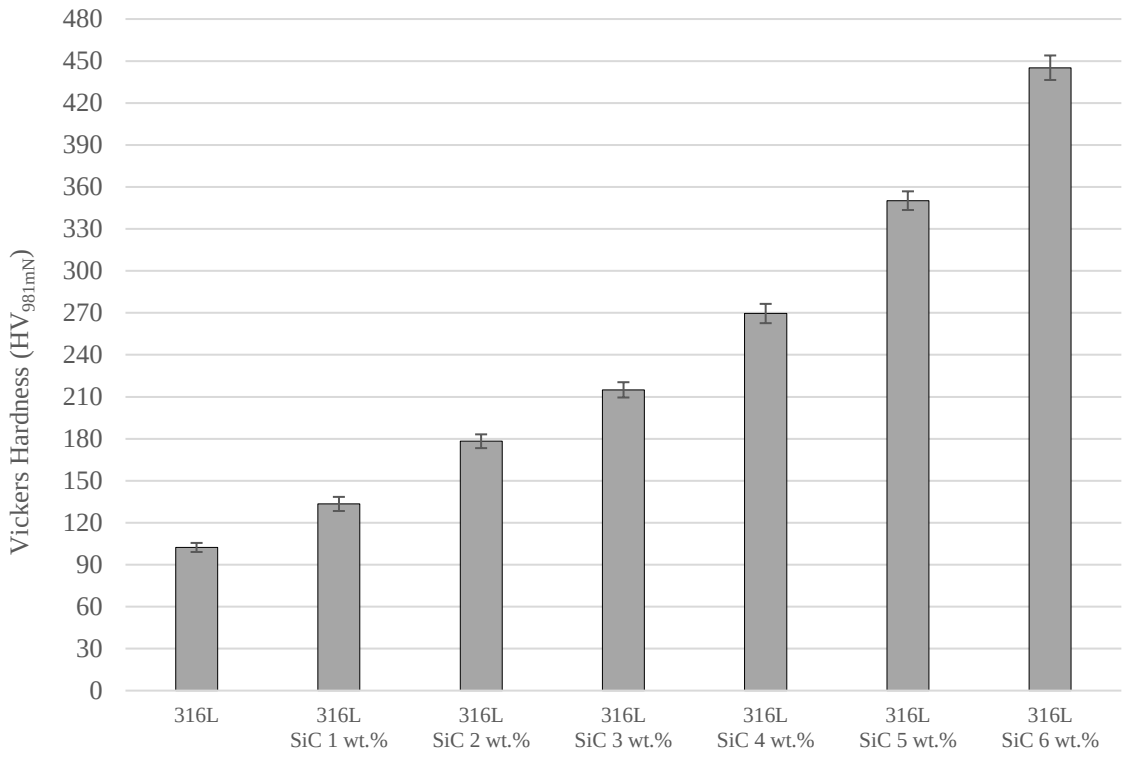


**Figure 5.5** Vickers hardness results obtained from the sintered samples, n=3.

#### 5.4.3.2 Composite Microstructure

The microstructures of the 316L samples prepared with different amounts of nano-SiC are shown in Figure 5.6 (a-g). The effect of adding SiC into the 316L matrix is clear on the presented micrographs. According to these micrographs, secondary phases were

introduced by precipitation reactions involving the reinforcement and matrix elements. The numerous particle boundaries and angular pores seen in Figure 5.6 (a) are indicative of either not a sufficient temperature or not a sufficient period of time for sintering, termed here as undersintering. Those particles lacking on contact points prevented the diffusion mechanism, which is responsible for particle bonding, hence leading to porosity. On the other hand, a well sintered microstructure with low level of porosity and small rounded pores is seen in Figure 5.6 (g). The relative density $\rho_{relative}$ of the samples was determined by $\rho_{relative} = \rho_{measured\ /\ }\rho_{theoretical}$ using the method mentioned in our previous work [560]. The relationship between relative density and weight percent of SiC is presented in Figure 5.6 (h). It is seen that the relative density increases almost linearly with increasing of SiC content. Therefore, confirming the influence of nano SiC on sample densification. Differently, it was reported that the addition of reinforcement reduces the density of composites due to low reaction between the carbide and stainless steel particles [561,562] which was not found to be the case in this study.

The relative density of sintered samples is influenced by the volume of the porosities in the green samples. In this study, the volume of the porosities was reduced by the SiC nanoparticles filling effect during the compaction. Potentially, the SiC nanoparticles also assisted on forming contact points between the matrix particles. Therefore, maximising particle bonding and porosity reduction. The oxide layer on the surface of 316L particles has the capacity of inhibiting formation of sintering bridges, whereas internal oxides are known to be particularly detrimental to the microstructure as they may result in unwanted reactions. Elements such as carbon and silicon have been widely used for reduction of oxides. In principle, these reducing agents diffuse into the particles to form a new phase, either a solid or a gas. It was reported the silicon has the potential of impairing the oxidation in the early stage of sintering (low temperatures) and that carbon is more efficient at higher temperatures [563–565]. Therefore, as both of these elements were present in the reinforcing material, this could also be a factor behind the composite densification. It is well known that nano-scale particles exhibit a melting temperature which depends on the particle size [566–570]. This is because atoms near the surface have fewer bonds and neighbouring atoms, hence less energy is needed for them to leave the surface [571,572]. Here, the melting point depression of the SiC particles was calculated using the classical Gibbs-Thomson equation [573]. The theoretical relationship between melting temperature and particle size of SiC nanoparticles is shown

in Figure 5.6 (i). It indicates that at the sintering temperature (1200°C), nanoparticles as large as 12 nm melt. Therefore, suggesting that the SiC addition could have the lowered the melting point of the powder mixtures. Moreover, it could have acted as a fluxing agent facilitating particle diffusion. Hence, reducing microstructural porosity and enhancing composite densification.

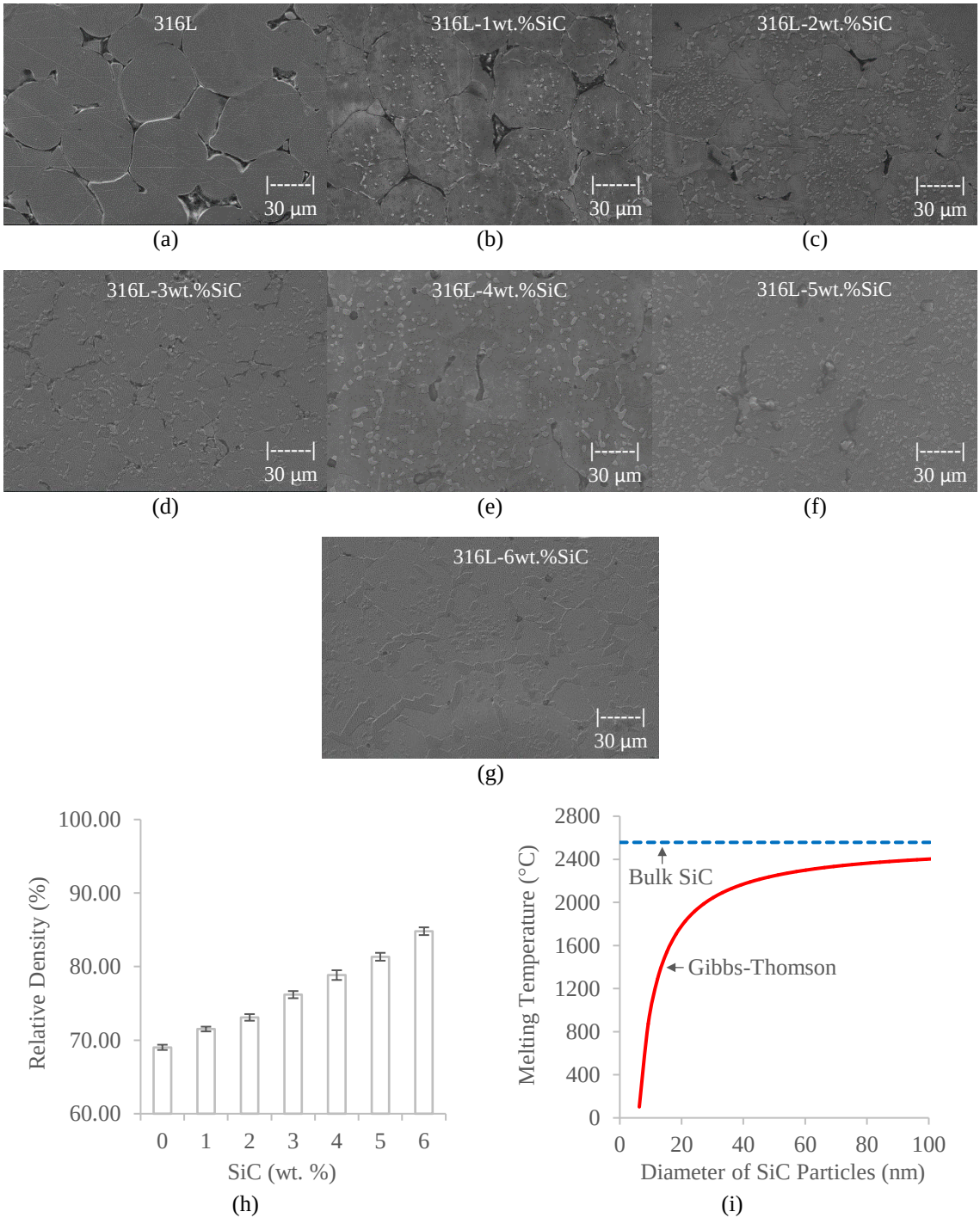


**Figure 5.6** Scanning electron micrographs of the sintered composites (a-g), the composites relative density as a function of reinforcement percentage (h) and the

theoretical relationship between melting temperature and particle size of Silicon Carbide nanoparticles (i).

Figure 5.7 shows x-ray diffractograms comparing the 316L and 316L-6wt.%SiC sintered samples. As seen in the diffractogram of the 316L sample, the effect of slow cooling induced the precipitation of $Fe_2Si$ at the austenite grain boundary. The presence of austenite, iron silicide and chromium carbides phases were identified in the composite sample. However, SiC phases were absent in the composite. It is known that SiC undergoes significant change in thermal character at about 1200 °C and that it can decompose at this temperature when in contact with iron [574–576]. This is the case here, where the decomposition of SiC led to the formation of silicon and carbon atoms at high temperatures. During the solidification, the silicon and carbon atoms dissolved into the austenite, leading to precipitations of the silicon rich phase $Fe_2Si$ and the complex carbides $Cr_3C_2$ and $Cr_7C_3$. $Fe_2Si$ is a ferromagnetic brittle phase of reduced corrosion resistance [577]. In general, chromium carbides have high abrasive resistance, but $Cr_3C_2$ has the highest oxidation and corrosion resistance and hardness of all [578,579]. However, chromium carbide precipitations are normally undesired since its presence is associated with decreased ductility and toughness. Nevertheless, they exhibit good resistance against shear deformation [580]. The increase in hardness in the analysed composite is attributed to the formed precipitates and grain refinement.

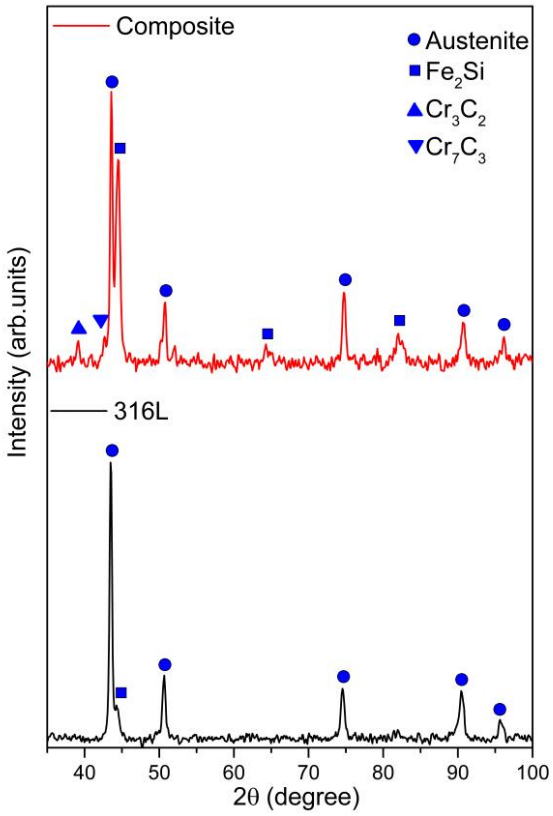


**Figure 5.7** XRD diffractogram comparing the sintered 316L and 316L-6wt.%SiC composite.

The microstructural crystallographic characteristics of the 316L-6wt.%SiC composite was investigated via EBSD analysis. Figure 5.8 (a) shows the inverse pole figure map for the normal direction and (b) its respective index maps. There is no clear evolution of the austenite texture. On the other hand, the iron silicide phase revealed a preferential grain growth to the (001) and (120) crystallographic alignment. With the preferred grain growth being along the (001) direction distinctly. Conversely, the chromium carbides presented a relative weak (001) texture. Essentially, the (001) texture reflects vertical oriented grains, and this could be related to the solidification direction, as the top surface of the sample was under continuous argon flow and the bottom was in contact with the crucible. Therefore, the directional of growth occurred due to the induced sintering high temperature gradient and low solidification rate. The phase analysis revealed the presence of austenite, iron silicide and chromium carbides, see Figure 5.8 (c). Thus, agreeing with the XRD data. Austenite phase of average size of 18.3 μm exhibited a fine surrounding boundary of iron silicide (average grain size 1.6 μm) surrounded in turn by chromium carbides (average size 5.8 μm). These precipitates were also present dispersed in the centre of austenite phase. These resulted as due to the slow cooling iron silicide and

chromium carbides nucleated and formed at the austenite grain boundaries and in the interior of the austenite grains. However, the precipitates formed in the interior of the austenite grains were oriented short-needle-like crystals. The formation of precipitates around the austenite grain boundaries prevented grain growth. Thus, resulting in fine austenite grains. Figure 5.8 (d) shows the morphology of the precipitated irregular columnar grains. The presence of strain in the crystal lattice is supported by the changes observed in the EBSD Kikuchi diffraction patterns and by the shift in the XRD peaks observed from the composite and matrix diffractogram comparison. In this composite, the strain could have been induced as a result of the precipitations and mismatch in the coefficient of thermal expansion of the various phases.

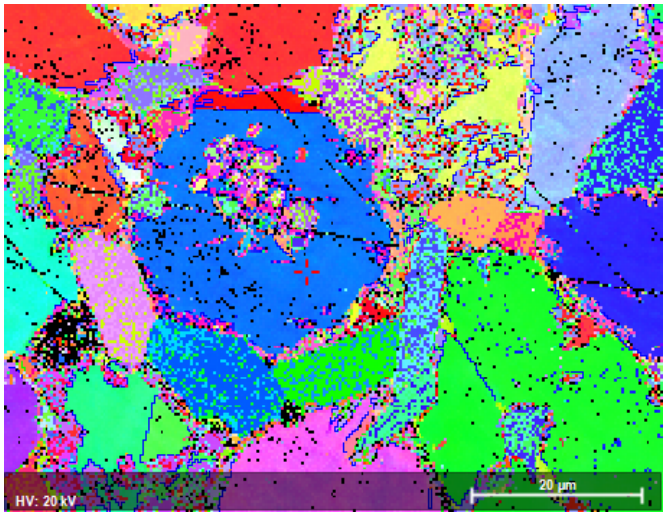


(a)

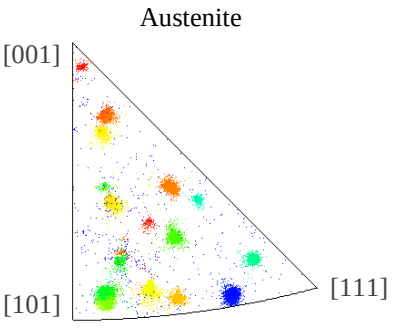


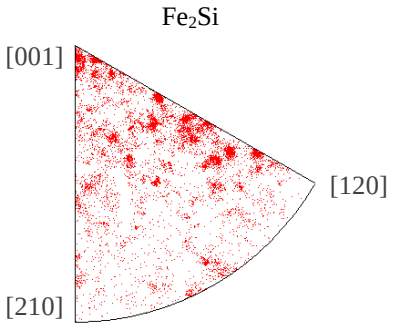


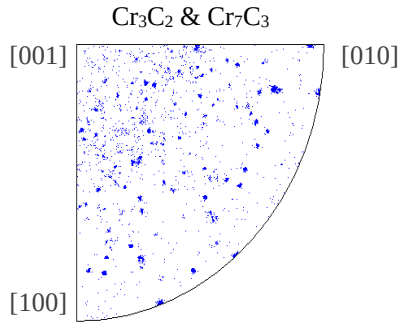


(b)

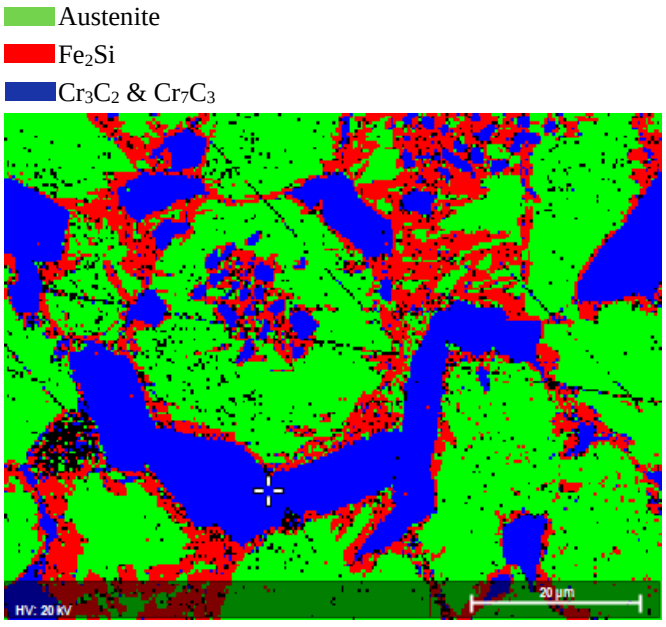


(c)

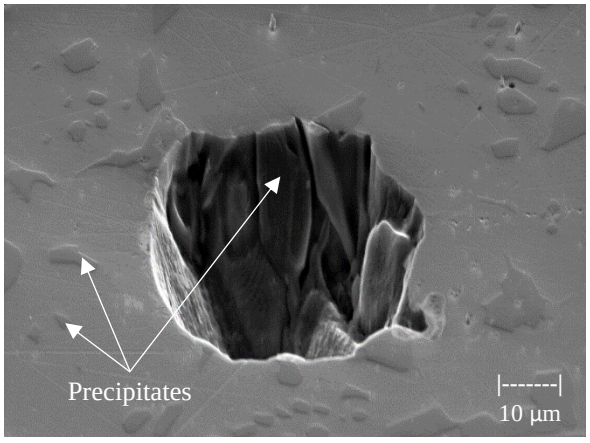


(d)

**Figure 5.8** Microstructure of the 316L-6wt.%SiC composite. (a) EBSD inverse pole map for the normal direction and (b) its respective index maps, (c) phase map and (d) SEM micrograph of plasma etched surface showing irregular columnar precipitates.

## 5.5 Conclusions

Incorporation of nano SiC particles into 316L matrix was investigated. The powder mixing time was found to be an important influencing parameter for obtaining homogenous mixtures. Sintered samples produced from 316L+SiC+PVA powder mixes presented improved hardness. However, it is recommended for future optimisation that the hardness of the sintered samples could be further improved by increasing the compaction pressure and by optimising the heating profile of the furnace for example. The effect of the reinforcement on the tensile, corrosion and wear properties of these composites are important and will be considered in the future studies.

Both reinforced and non-reinforced powders presented similar flow properties such as cohesive levels. However, the reinforced powder provided higher levels of repeatability and a very stable rheology and is relatively flow rate insensitive. This is considered to be due to the fact that the reinforced powder particles lost some of their satellites during the mixing process and also because of the coating of SiC which could act as a solid lubricant.

The development of the powder via the powder metallurgy route gave a good insight of the powders characteristics effects on the developed powder flow behaviour, and it allowed the study and consideration of numerous other factors affecting the powder development process. It is interesting therefore to investigate further the oxidation of the 316L powder and its effect on obtaining samples with improved sintered density and mechanical properties. The technique developed herein, and the optimised results obtained are promising for its implementation for the production of nano-particle reinforced MMCs via the SLM and PM processing routes.

# Chapter 6

## Laser-Powder Bed Fusion of Silicon Carbide Reinforced 316L Stainless Steel Using a Sinusoidal Laser Scanning Strategy

**Publication Status:** Published

Mussatto, A., Groarke, R., Vijayaraghavan, R. K., Obeidi, M. A., McNally, P. J., Nicolosi, V., Delaure, Y., and Brabazon, D., 2022, "Laser-powder bed fusion of silicon carbide reinforced 316L stainless steel using a sinusoidal laser scanning strategy", Journal of Materials Research and Technology, 18, pp. 2672-2698.

https://doi.org/10.1016/j.jmrt.2022.03.170

## 6.1 Abstract

Laser-powder bed fusion has been identified as a promising technique for manufacturing metal matrix composites. However, over a decade later, little progress has been made in addressing the persisting issues hindering the wider exploitation of the L-PBF production and industrial usage of metal matrix composites. Therefore, the present study proposes the implementation of a feasible solution to accomplish advancements in L-PBF metal matrix composites. Accordingly, the issues concerning their performance and cost have driven this study towards the development of a novel scanning strategy. A hatching system based on a sine wave was successfully developed and employed in the printing of metal matrix composites. Composites printed using the sinusoidal hatching exhibited an enhanced yield strength and ductility owing to the resultant grain refinement and texture. The dabber mode formation of material tracks promoted the growth of highly oriented intragranular cellular structures. Apart from playing an important role in improving hardness, this control over the cellular growth could also be used towards improving composite toughness. Additionally, besides improving composite performance, the sinusoidal hatching strategy was also effective in reducing manufacturing lead time and process energy consumption in response to its natural high scanning speed and low laser power requirements.

## 6.2 Introduction

In many modern technological applications, components are very often required to have properties which are only possible by combining different materials, as opposed to the monolithic options individually [581]. Metal matrix composites (MMCs) are considered advanced materials due to the growing interest in them over the past decades in various high-performance applications such as those in the automotive and aerospace sectors [582,583]. Although MMCs have been used and are excellent candidate materials for advanced engineering systems, several aspects are hindering their further applications [583]. To which two of the mechanical properties which could be improved for composites are the ductility and toughness which tend to be reduced with an increasing amount of reinforcement [584]. Technical challenges including inhomogeneous reinforcement dispersion, low wettability, deleterious interfacial reaction, weak interfacial bonding, porosity and micro defects are well known to have a major impact on the properties of MMCs [585–591]. Another challenge associated to MMCs is the availability of a suitable processing technique to extract the maximum benefits from

reinforcements [592]. Ease of processing, adequate economic efficiency, low energy consumption and complex net-shape ability are process related aspects to be considered [583,593–595]. Even though substantial research is still needed, in specific applications, the MMCs property-profiles are distinguished from metals and alloys by offering a gain in performance. Yet, as far as industries are concerned, the viability of MMCs depends on the balance between their performance and cost [596].

As aforementioned, the production of MMCs via conventional manufacturing techniques faces several challenges and limitations. Rapidly becoming more and more popular, laser-powder bed fusion (L-PBF), which is suitable for obtaining ultrafine, gradient and pointwise-controlled microstructure, has been used for the production of both in-situ and ex-situ MMCs [593,583,597]. L-PBF offers an exceptional flexibility for producing functional, geometrically complex dense composites, besides allowing for unprecedented freedom of design and customisation [598]. It provides also an opportunity for producing MMCs with a homogeneous dispersion of reinforcement and material pairings free from limitations, which is extremely important when developing new materials [599,600]. Recently, L-PBF was identified as the most promising technique to process MMCs as it has the potential of addressing several of the current issues concerning MMC production, including the better control of manufacturing costs, waste and lead time [601,602]. However, while there are promises, and the fact that L-PBF is still in its infancy means, its true and full potential for MMC production is yet to be discovered.

To date, little research into L-PBF of silicon carbide (SiC) reinforced 316L composites exists. From these, it was reported that SiC additions affect microstructural morphology and texture, and improve the composite strength due to the grain boundary, Orowan, dislocation and load transfer strengthening mechanisms. However, densification was reported to be affected by the SiC addition as a result of increased porosity. High residual stresses due to coefficient of thermal expansion mismatch between phases caused micro cracks, hence reduced the ductility in composites. The decomposition of SiC encouraged the formation of iron and chromium silicide phases, and these resulted in a decrease in mechanical strength of MMCs [603,604].

In L-PBF, the spatial moving pattern of the energy beam is regarded as scanning strategy. This parameter is known to have an influence on the building time and properties of printed components [605–607]. The most common, not necessarily commercially

available, filling patterns are stripes, islands (i.e. based on stripes, hexagons and chessboard), grid zigzag, square spiral and contour offset [608–611]. Additionally, despite their limitations, fractal patterns such as the Hilbert and Peano-Gosper have been used as a method of reducing thermal gradients and residual stresses [612,613]. Unfortunately, all these aforementioned infill patterns have one thing in common and this is the fact that their resulting scanning paths are linear. The generation of nature inspired and custom scanning strategies which may be required in order to avoid printing defects, or to achieve a desirable component property value, are not explicitly supported in current commercial slicer software packages. Bo et al. developed a helix scanning strategy based on the Voronoi diagram of the model slice and the recursive generation of a toolpath algorithm for an engine impeller aiming to reduce the shape deformation magnitude and residual stress profiles [614]. Similarly, the equidistant scanning algorithm was claimed to improve processing efficiency and component quality [615]. In fact, several other path generation algorithms that might be suitable for developing new scanning strategies can be found in the literature [611,616–620].

In this work, a specially developed powder mixture having a high flowability and spreadability performance was used for L-PBF of MMCs. A novel scanning strategy, here named sinusoidal hatching, was developed and used during the printing process in an attempt to improve the composites tensile properties and control crystallographic texture. Additionally, this scanning strategy was also explored as a feasible solution to some of the aforementioned issues faced by MMCs.

## 6.3 Experimental

### 6.3.1 Material and Sample Preparation

The characteristics and performance of the powder mixture developed for this work is presented in previous studies [621,622]. The powder mixture is composed of a free-flowing gas atomised (35-50 μm) stainless steel 316L powder and a high purity (45-65 nm) SiC powder, obtained from Mimete S.r.l and US Research Nanomaterials Inc. Figure 6A1 of Appendix A shows the powder mixture (316L + SiC 1 wt.%) which is characterised by the cohesive SiC nanoparticles adhering and evenly decorating the surface of 316L particles.

The scanning strategies used in this work are illustrated in Figure 6A2 of Appendix A. For generating the stripe hatching, models of the specimens were designed using

SolidWorks and then the hatching was generated using a commercially available slicing tool, Netfabb Autodesk. For the sinusoidal hatching, the three-dimensional design of the specimens and slicing were generated using a sine function, Excel Macro and JavaScript, then converted into the Common Layer Interface file format.

Using an Aconity Mini (Aconity GmbH, Germany), cuboids and pins were printed based on the following design: 316L stripe hatching, 316L sinusoidal hatching, 316L-SiC stripe hatching and 316L-SiC sinusoidal hatching. The prints were repeated three times to enable verification of the results and to estimate the experimental variability. To avoid property variations caused by the location parameter, specimens were only printed in the centre of the build platform [623]. The laser power and scanning speed for each individual hatching were established from a processing window obtained from single track experiments. Categorised by the hatching system, the processing parameters used during the printing of the specimens are listed in Table 6.1.

**Table 6.1** Processing parameters used for the stripe and sinusoidal hatching scan strategies.

| **Parameter** | **Stripe Hatching** | **Sinusoidal Hatching** |
|---|---|---|
| Laser power (W) | 180 | 50 |
| Scanning speed (mm/s) | 600 | 10000 |
| Laser beam diameter (µm) | 50 | 50 |
| Layer thickness (µm) | 50 | 50 |
| Hatch spacing (µm) | 75 | 75 |
| Hatch translation per layer (µm) | 37.5 | 37.5 |
| Amplitude (µm) | - | 50 |
| Period (µm) | - | 200 |

### 6.3.2 Sample Characterisation

The density of the specimens was determined by means of densimetry based on Archimedes' principle (density scale Avery Berkel FA215DT and Sartorius YDK01 Density Determination Kit). Deionised water (at room temperature) was used as the immersion liquid while determining the density. The Vickers hardness was measured using a Leitz microhardness tester and the measurements were performed according to ASTM E92 standard [624]. A nanoindenter (Bruker Hysitron TI Premier, USA) equipped

with a standard Berkovich diamond indenter was used for nanohardness measurement of the specimens. An array of 6x14 nanoindentations was performed with 10 mN load and intervals of 30 μm between indentations. The tensile test was performed using a Zwick Z050 (Zwick/Roell GmbH, Germany) computer-controlled tensile tester equipped with an Epsilon clip-on extensometer model 3542. Nanoscratch tests were performed in a Bruker Dimension Icon atomic force microscope equipped with a NanoScope V controller, and using a single crystal diamond tip (AD-40-SS) from Adama Innovations. A micrograph of the tip is shown in Figure 6A3, Appendix A. First, the probe's deflection sensitivity of 60.47 nm/V and its cantilever spring constant of 54.13 N/m were determined by the thermal tune method. Then, single pass scratches were performed in contact mode with an applied normal force of 1 μN and tip lateral velocity of 1 μm/s. A Zeiss Evo LS15 and a JEOL JSM-IT100 scanning electron microscope were used to obtain microstructural data. The microstructure was also investigated using a triple-axis Jordan Valley Bede D1 high resolution X-ray diffraction system with a copper ($\lambda = 1.5405$ Å) radiation source operated at 45 kV and 40 mA, and a Zeiss Supra 40 field emission scanning electron microscope equipped with a Bruker e-FlashHR electron backscatter diffraction detector.

## 6.4 Results

### 6.4.1 Density

The density of the printed specimens is presented in Figure 6.1. In order to properly assess the specimen's densities, the density of the virgin powders was also measured. Using a Micromeritics AccuPyc 1330 Helium pycnometer, densities of 7.75 and 3.16 g/cm$^3$ were confirmed for the 316L and SiC powder. Based on this it would be expected that a 100% dense unreinforced and reinforced specimen would have densities of 7.75 and 7.70 g/cm$^3$ respectively. However, the densities reported in Figure 6.1 suggest the presence of some internal porosity in the specimens. It is clear that, independently of the hatching system, the presence of nano SiC particles have promoted specimen densification. It is also seen that in comparison with the stripe hatching, those specimens printed using sinusoidal hatching showed a reduction in density.

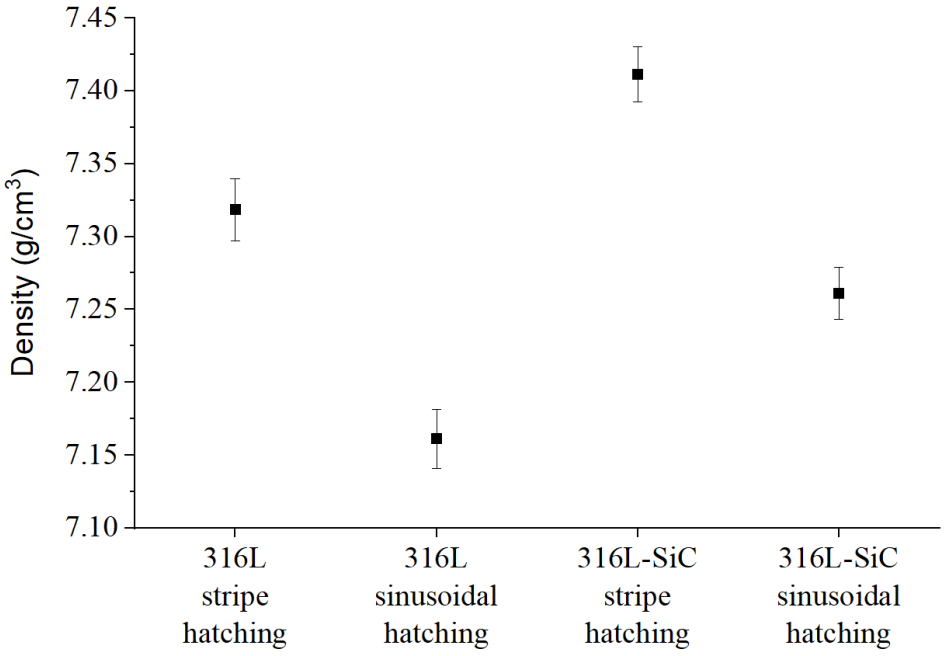


**Figure 6.1** Comparison of the densities measured from the printed specimens.

### 6.4.2 Hardness

The hardness of the specimens measured from the plane perpendicular to the build direction is presented in Figure 6.2. The lower penetration depth, in the load-depth plot, corresponds to higher hardness, Figure 6.2a. It is worth noting that the micro and nanohardness showed a similar trend. The hardness of the 316L sinusoidal hatched specimen is slightly higher than that of the stripe hatched specimen. Regardless of this, based on previous studies, here both the micro [625,626] and nanohardness [627,628] show a degree of improvement. The addition of 1 wt. % SiC has improved the hardness of the base material by approximately 30 %. A similar study also reporting the L-PBF of 316L-SiC claimed 347 HV for their 1.278 wt. % reinforced composite [603]. Therefore, despite using less reinforcement, the composites here printed presented higher hardness. The hardness of the specimens can be related to their yield strength and elastic modulus. Their reduced modulus was also found to increase with increasing hardness, see Figure 6.2c. Factors such as grain size and the presence of residual stresses associated to the L-PBF process could be contributing to the observed hardness improvements.

(a)

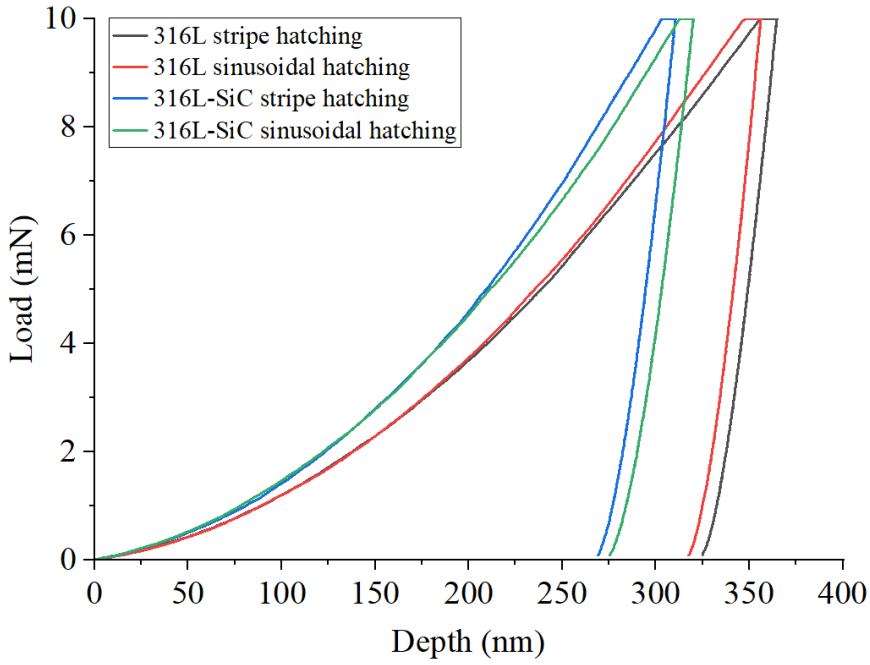


(b)

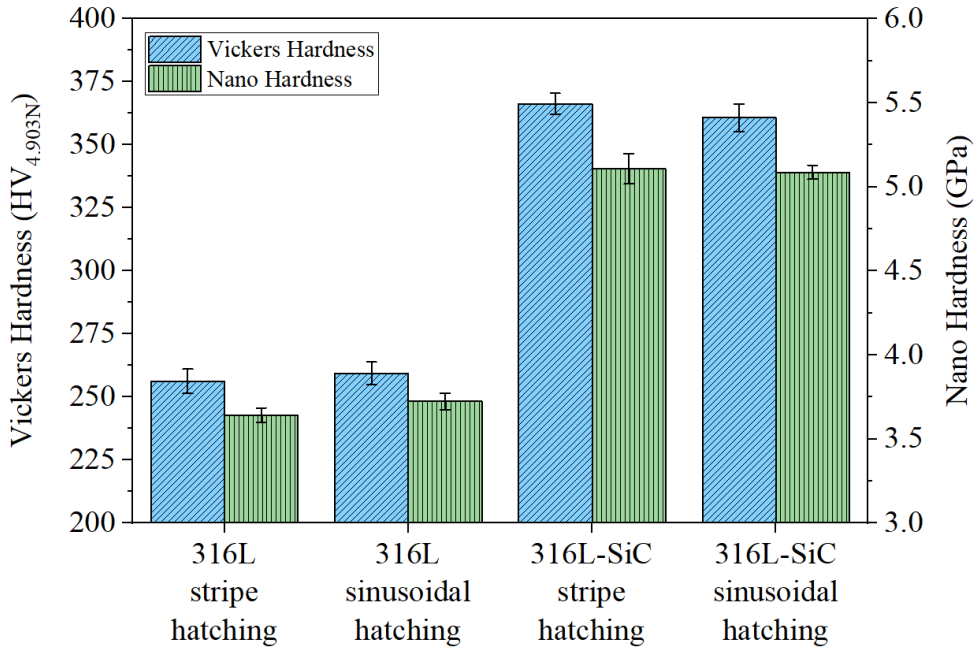


(c)

| Specimen | Reduced Modulus (GPa) |
|---|---|
| 316L stripe hatching | $194.05_{\pm 1.81}$ |
| 316L sinusoidal hatching | $195.07_{\pm 2.45}$ |
| 316L-SiC stripe hatching | $206.91_{\pm 1.44}$ |
| 316L-SiC sinusoidal hatching | $204.81_{\pm 2.03}$ |

**Figure 6.2** Measured Vickers and nanoindentation data: (a) nanoindentation load-displacement curves, (b) micro and nanohardness and (c) reduced modulus.

### 6.4.3 Tensile Properties

The horizontally printed pins were machined to dimensions according to the ASTM E8 standard [365] and used for tensile testing. The tensile properties extracted from the specimens while applying tension along the hatching direction are shown in Figure 6.3. Figure 6.3a shows that the 316L specimen printed using the stripe hatching exhibited the higher elongation and strength at fracture in comparison to 316L specimen produced with the sinusoidal hatching, see Figure 6.3b. The addition of SiC led to an increase in yield strength, ultimate tensile strength and elastic modulus of the base material. However, the enhancement of these properties was accompanied by a loss of ductility. Notably, the sinusoidal hatching system provided a positive effect on the tensile properties of the composite. In contrast with the composite printed using the stripe hatching, the composite produced with the sinusoidal hatching presented superior tensile strength and ductility.

(a)

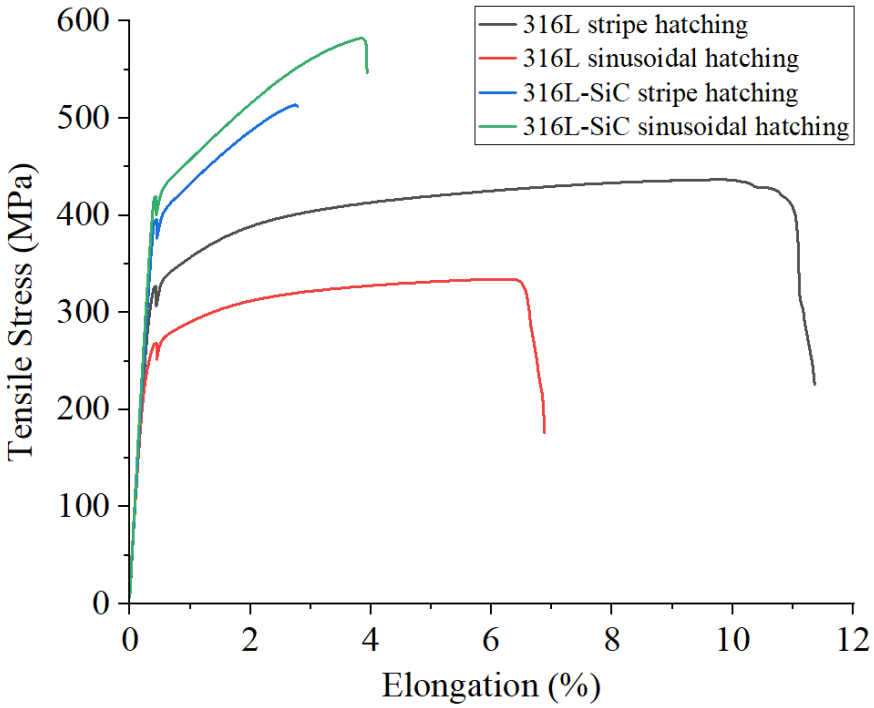


(b)

| Specimen | UTS (MPa) | YS (MPa) | E (GPa) |
|---|---|---|---|
| 316L stripe hatching | $431.82_{\pm 3.68}$ | $343.37_{\pm 4.80}$ | $131.93_{\pm 2.36}$ |
| 316L sinusoidal hatching | $330.17_{\pm 7.87}$ | $278.78_{\pm 2.67}$ | $126.86_{\pm 2.04}$ |
| 316L-SiC stripe hatching | $514.48_{\pm 3.26}$ | $414.25_{\pm 2.73}$ | $137.08_{\pm 2.51}$ |
| 316L-SiC sinusoidal hatching | $561.01_{\pm 15.86}$ | $445.79_{\pm 4.05}$ | $147.67_{\pm 2.79}$ |

**Figure 6.3** Tensile performance of the specimens: (a) tensile stress versus percent elongation curves and (b) ultimate tensile strength, yield strength and elastic modulus.

Fractography analysis was conducted on the specimens using the scanning electron microscopy, with resulting surface images shown in Figure 6.4. The existing porosities were considered as a particularly adverse factor for the tensile performance of the specimens as they contributed to and accelerated void growth and crack propagation causing premature fractures and failure under the tensile loads. The specimen of Figure 6.4a shows a ductile fracture in the presence of shear lips, whereas the specimen of Figure 6.4b shows almost no necking and a slanted fracture path indicating failure by ductility tearing from void coalescence induced microcracks [629]. Both of these specimens exhibited relatively uniform dimpled fracture surfaces, with small dimples (around 1 µm in diameter) visible throughout the surfaces. Therefore, this suggests the existence of a

subgrain structure which affected the nucleation and growth of microvoids. The fracture morphologies of the composite specimens are shown in Figure 6.4c and d. The cleavage facets seen indicate that a brittle fracture process was developed during the failure due to the presence of the reinforcing brittle second phases. Despite the presence of brittle second phases, the composite of Figure 6.4d printed using the sinusoidal hatching also shows the presence of dimple patches, hence both brittle and ductile fracture characteristics were observed in this composite. Therefore, this resulted in the consumption of more plastic deformation, which is also reflected in the maximum elongation before failure for the composite specimens between the two hatching systems as seen in Figure 6.3.

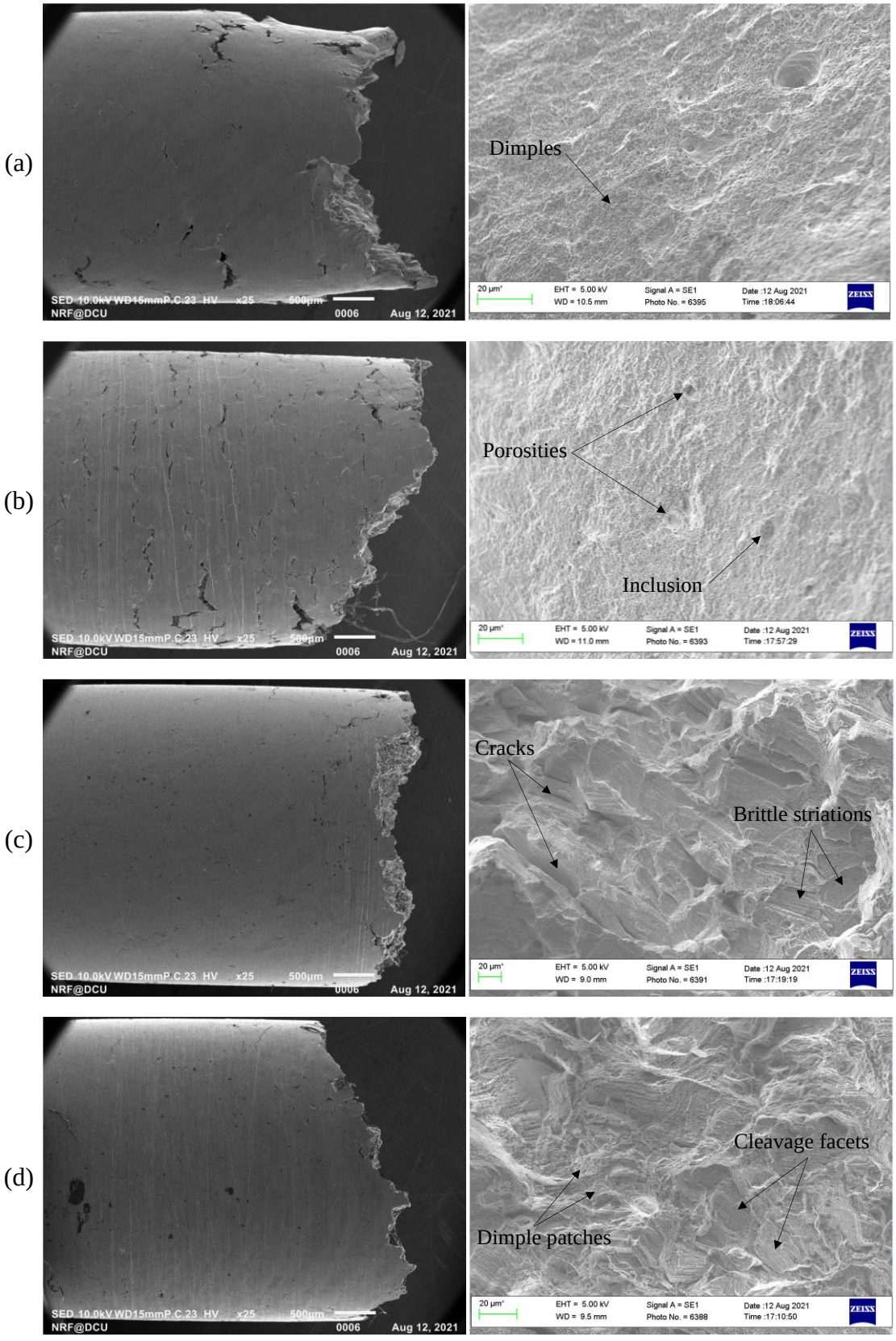


**Figure 6.4** Tensile fracture characteristics of the specimen (a) 316L stripe hatching, (b) 316L sinusoidal hatching, (c) 316L-SiC stripe hatching and (d) 316L-SiC sinusoidal hatching.

### 6.4.4 Microstructure

Figure 6.5 shows the microstructure of the specimens with reference to the build plane which was revealed after electrolytic etching for 30 s at 0.3 A/cm$^2$ with a 50 % $HNO_3$ solution. The etching also revealed the meltpools and their behaviour, but only in the unreinforced 316L specimens. Fine columnar grain bands observed from the specimen of Figure 6.5a were abruptly terminated at meltpool boundaries. Hence, it is possible that they have grown oriented towards the build direction. On the other hand, specimens of Figure 6.5a-c contained more complex columnar structures. Internal structure of columnar grains consists of colonies of cells [630]. In which, depending on growth direction, cells were either equiaxed or elongated [631]. This cellular structure is better observed in the high magnification micrographs of Figure 6.5, and they were formed as a result of complex heat transfer and large temperature gradients in the meltpool inherited from the ultrafast melting and solidification rates during laser processing. The highest temperature gradient is located on the bottom surface of concave shaped meltpools where solidification of cellular structures starts perpendicular from the boundaries towards the centre of meltpools. Hence, cells are most likely to be oriented with its longitudinal direction parallel to the build direction whereas cells formed near the top of the meltpool boundaries can grow horizontally in response to the maximum heat flux direction. However, typically the structures formed on the top of meltpools are remelted during the fusion of the consecutive layer. Fluid dynamics of the meltpool driven by gas expansion and material evaporation resulting from the recoil pressure [632] and the Marangoni flow effect on heat and mass transfer [633] can alter the heat flux direction, and this is one of the reasons for the observed horizontal and arbitrary oriented colonies of cells. An example of a such complex growth behaviour was also observed on discontinuous meltpools, Figure 6.5a. Interestingly, colonies near the meltpool tip are oriented radially perpendicular to the tip planar boundary. A similar growth behaviour was also observed in the Pham et al. single track study [634]. Therefore, it can be confirmed that the cells growth axis is closely perpendicular to the solid-liquid interface due to higher local thermal gradients and the maximum heat flux [635,636].

As illustrated in Figure 6.5b, the rapid rastering of the laser beam through the sinusoidal path led to the formation of meltpools which have a “stack of dimes” type of look resembling weave bead patterns as sometimes seen in metal welding [637–639], where each semicircle corresponds to a dab of filler formed during the welding [640]. The seen

overlapping dabs resulted therefore from a dabber mode formation of material tracks. Factors such as laser, scanning and layer parameters and physical properties of the molten material such as surface tension and viscosity contribute to the spacing of the dabs. In contrast with the continuous mode, this interrupted action allowed for a faster cooling causing grain refinement and strong vertical texture. However, some grains persisted to go through multiple dabs, implying that the dabber mode does not completely prevent grains from elongating. Nevertheless, the colonies seen in this specimen are several orders of magnitude smaller than those of Figure 6.5a. The nonhomogeneous size of the refined structures seen in Figure 6.5c and Figure 6.5d resulted from the addition of SiC to 316L. The degree of constitutional undercooling set by the composite composition, the distribution of SiC and thermal profiles in the liquid were associated with this phenomenon [641–643]. Therefore, based on the unreinforced specimens, here, those colonies decorated with slightly large structures correspond to a reinforcing phase. The observed porosity is probably associated with typical L-PBF defects, as well as 316L and SiC contaminants [644,645]. Therefore, the causes of porosity formation were either from entrapped gases (or absorption of surrounding gases), evaporation of certain elements, meltpool instabilities, shrinkage during solidification or other influencing factors such as powder humidity and oxygen content in the processing chamber. It is worth noting that pores were only found between grains, and where they resided there was a lack of grain boundary. Generally, solidification cracks occur along the grain boundaries and precipitated phases, aided by existing internal defects. Here, the presence of porosities made the specimens less ductile and offered an alternative pathway for cracks to propagate, as cracking along cellular boundary is convoluted and should consume more energy. In accordance with a previous study [646], fewer cracks were observed when using a relative high scanning speed. The 10,000 mm/s scanning speed reduced the solidification time which constrained aggregation of nano SiC particles and consequently reduced the degree of cracking. However, based on the density results of Figure 6.1, the increase in scanning speed correlated with an increase in porosity. Nevertheless, the tensile results of Figure 6.3 confirmed that higher scanning speed provided improvements in the composite tensile strength and ductility.

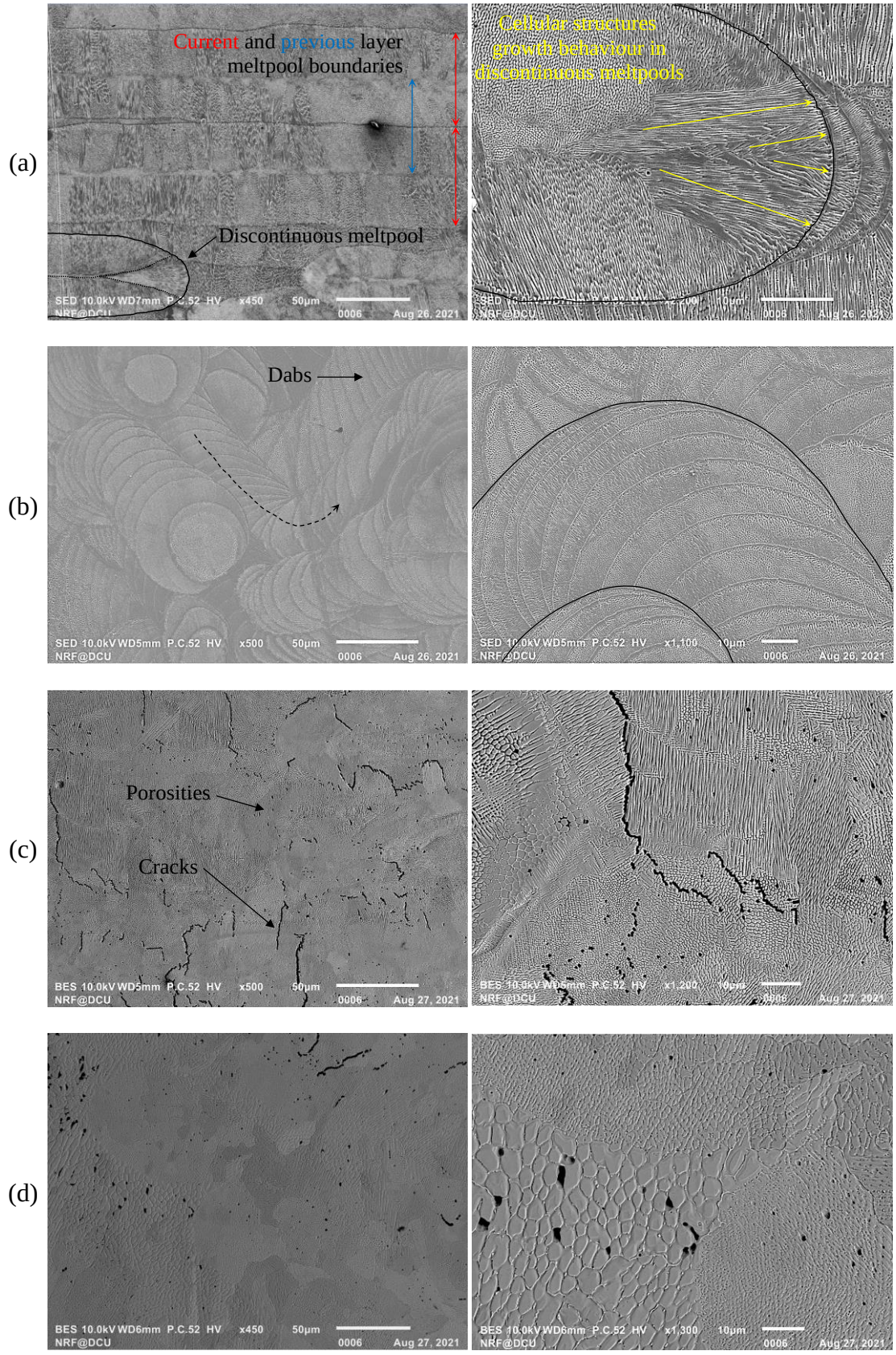


**Figure 6.5** Microstructure of the specimen (a) 316L stripe hatching, (b) 316L sinusoidal hatching, (c) 316L-SiC stripe hatching and (d) 316L-SiC sinusoidal hatching.

### 6.4.5 Nanotribological Properties

The performance of metal matrix composite components such as engine pistons, valves and gas turbine blades also depends on the asperities, friction, wear, corrosion and lubricant properties of their exposed or contact surfaces with other metals, fluids and gases [647,648]. The surface of stainless steel is chemically reactive forming oxide layers in air and in other environments (i.e. chlorides, sulphides and nitrides). Some oxides are very tenacious, and the surface become passivated with no further oxidation. However, others like $Fe_2O_3$ can continue to grow in a humid air environment. Typically, the oxide layer ranges from 1 to 10 nm which is established within a few minutes of exposure of an atomically clean surface. Tribological oxidation is said to reduce the shear strength of the interface which reduces wear and lowers friction, and may effectively separate two contact surfaces [649]. However, at a high load and temperature, the oxide film may be penetrated and then transition to a high friction and wear occurs. Therefore, in order to develop fundamental understanding of the friction and wear properties of the naturally formed oxide films on the surface of the specimens, the nanoscratch testing technique was used.

In the process of nanoscratch testing, vertical and tangential forces are involved in the deformation of surfaces. As the relationship between these two forces is not governed by the Coulomb law of friction, other influencing factors must also be considered. Bowden and Tabor proposed that friction resulted from the sum of two components: a physical component which is the adhesion force required to shear the contacting junctions for sliding to occur and the mechanical component due to the plastic deformation of the contacting surface arising from the ploughing [650]. According to the Hertzian elastic contact theory [651] and the Bowden and Tabor model of adhesive friction force, the adhesive friction coefficient becomes

$$\mu_a = \tau_s \,.\, \pi \,.\, \left(\frac{3r}{4E_r}\right)^{\frac{2}{3}} \,.\, F_n^{\frac{-1}{3}} \qquad (1)$$

where $r$ is the tip radius, $E_r$ the reduced modulus $F_n$ the normal force and $\tau_s$ the interfacial shear strength [650]. Bowden and Tabor, and Goddard and Wilman [652] proposed expressions for the ploughing friction coefficient. However, both expressions assumed that the contact area is a half disc, and their expressions were not corrected for elastic-plastic or viscoelastic contact [653–656]. Subsequently, Lafaye et al. incorporated into

the Goddard and Wilman expression a term which takes into account elastic recovery, assuming a real tip that is conical and truncated by a spherical cap at the extremity [657]. Therefore, the equation which allows to evaluate the ploughing friction coefficient is

$$\mu_p = \frac{2}{a^2} \frac{\beta^2 \sin^{-1}\left(\frac{a\cos w}{\beta}\right) - a\cos w\sqrt{r^2 - a^2}}{\pi + 2w + \sin 2w} \quad (2)$$

where $h$ is the scratch depth and $H$ the specimen hardness. The contact radius $a$, a fictive radius of the tip $\beta$ and the angle made by the contact at the back of the sliding tip $\omega$ were calculated according to the geometrical expressions of (3) [658,659].

$$\begin{cases} a = \sqrt{2hr - h^2} \\ \beta = \sqrt{r^2 - a^2 \sin^2 w} \\ w = \sin^{-1}\sqrt{\frac{2H(r-h)}{aE_r}} \end{cases} \quad (3)$$

The nanoscratch topography and cross-section profile of the specimens are respectively shown in Figure 6.6. Higher penetration depths were achieved on the unreinforced specimens. Minimal, but noticeable variations in depths resulted from the scanning strategy and its respective process parameters (compare: Figure 6.6a against Figure 6.6b and Figure 6.6c against Figure 6.6d). The scratch cross-section profile of the composite specimens is v-shaped and perfectly symmetrical mirroring the profile of the tip. In conjunction with their lower penetration depths, this suggests that the existing films are possibly of low plasticity. Conversely, the apparent smaller widths and the convex walls from the depth cross-section profile of the unreinforced specimens are evidence of elastic recovery (occurring behind the scratch-tip) on the films.

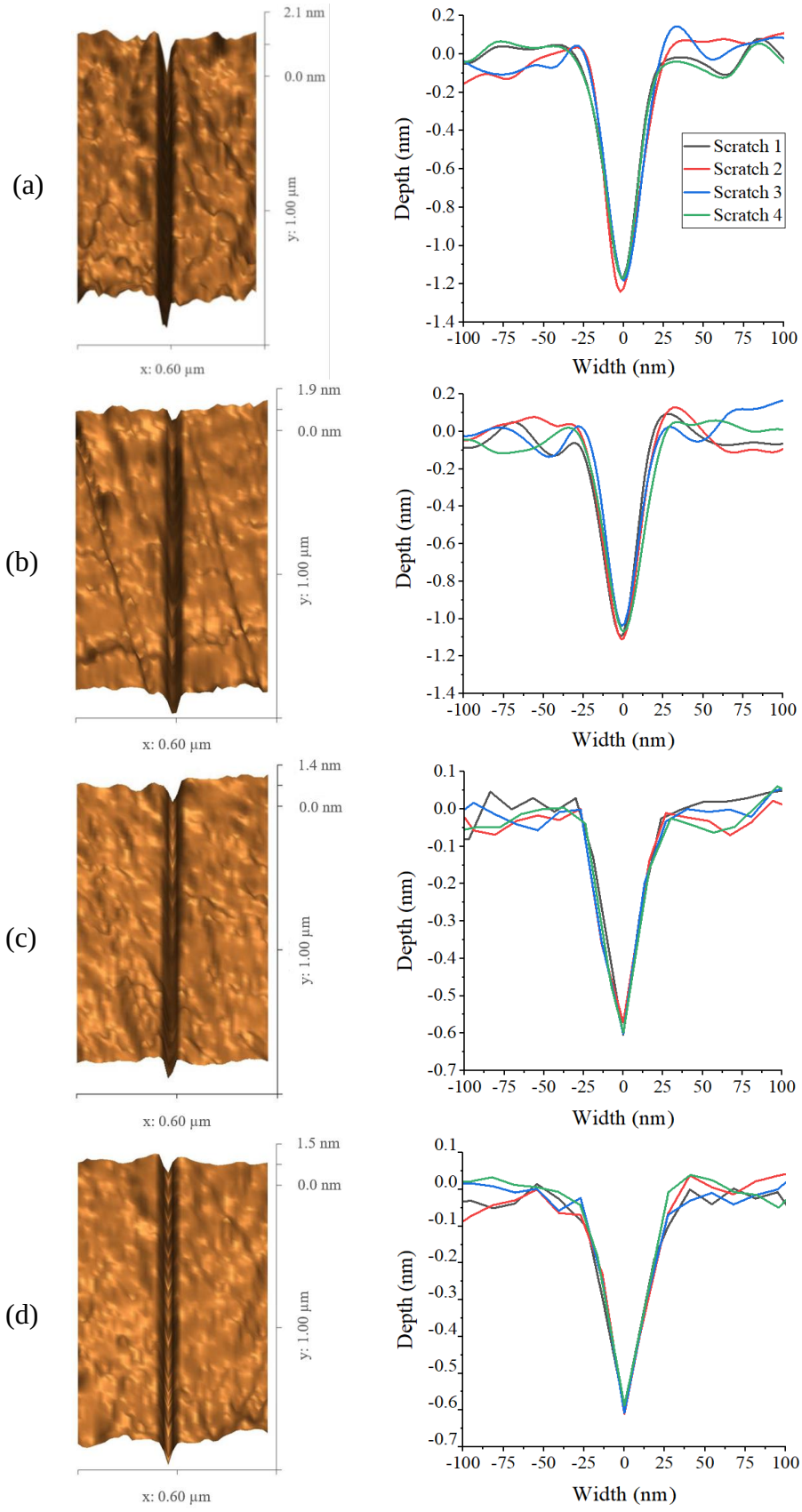


**Figure 6.6** Atomic force microscopy scratches and the scratches cross-section profiles of the specimen (a) 316L stripe hatching, (b) 316L sinusoidal hatching, (c) 316L-SiC stripe hatching and (d) 316L-SiC sinusoidal hatching.

The friction coefficient and specific wear rate of the specimens (wear volume per unit applied normal force per unit scratching distance) obtained from the nanoscratched surfaces are listed in Table 6.2. It is of interest to note the interrelationship of friction with wear, especially the disparities in friction coefficient and specific wear rate between the unreinforced and reinforced specimens. This suggests that their films differ in physical and mechanical properties as well as chemistry. It is well known that 316L is a high corrosion resistant alloy due to its naturally formed protective passive film. Species of Fe (i.e. $FeO_2$ and $Fe_3O_4$), Cr (i.e. $Cr_2O_3$ and $CrO_2$), Mo (i.e. $MoO_2$ and $MoO_3$) and Ni (i.e. $Ni(OH)_2$ and $NiO_2$) formed from reactions with intrinsic elements (i.e. O, H, C, N), other metallic elements and impurities (i.e. sulphides and phosphides) are typically found within oxide films [660–667]. In fact, an oxide film formed on the surface of 316L can be composed of three layers: an inner layer of metallic nickel at trace amount (if present), an intermediate layer of Fe species (existence of Cr species is also possible) and an outer layer of Fe and Mo species [667–671]. Unfortunately, if the oxide film exceeds a critical thickness, it can act as an abrasive during its contact with other surfaces, but if the thickness is less than a critical limit, then the oxide acts as a protective tribological film [672,673]. Additionally, when the hardness of the oxide is close to that of the bulk material and the oxide film thickness is of the order of 10 nm, the film will adhere well to the surface below and hence acts as a solid lubricant [674]. However, oxide films are susceptible to fretting as mechanical friction may destroy them more rapidly than they can grow [675,676], therefore introducing a depassivation environment will have a direct impact on corrosion, wear and friction.

**Table 6.2** Nanoscratch friction coefficient and specific wear rate of the specimens.

| **Specimen** | **Friction Coefficient** | **Specific Wear Rate x$10^{-12}$ ($m^3$/N.m)** |
|---|---|---|
| 316L stripe hatching | $0.239_{\pm 0.0074}$ | $30.28_{\pm 0.85}$ |
| 316L sinusoidal hatching | $0.224_{\pm 0.0084}$ | $26.35_{\pm 0.81}$ |
| 316L-SiC stripe hatching | $0.149_{\pm 0.0063}$ | $15.39_{\pm 0.71}$ |
| 316L-SiC sinusoidal hatching | $0.150_{\pm 0.0064}$ | $16.49_{\pm 0.53}$ |

To gain further understanding on the formed oxide films, deconvolution of their mechanical properties was investigated via in-situ nanoindentation. Graphs illustrating

the evolution of nanohardness and reduced modulus within the oxide films are available in 6.7.2 Appendix B

. At 2 nm depth into the oxide films, both the nanohardness and reduced modulus were found to be much higher in the composites than in the unreinforced specimens. Also, it is worth noting that at this depth the nanohardness follows an expected trend reflecting on the specific wear rate values of Table 6.2. The depth into the oxide film at which the nanohardness was closely related to the intrinsic nanohardness of the bulk material was: 20 nm for the 316L sinusoidal hatching, 30 nm for the 316L stripe hatching and 70 nm for the composite specimens. Therefore, this suggests the existence of a thicker oxide film on the composite specimens. Here, both the nanohardness and the reduced modulus of the films increased with increasing indentation depth. In fact, such a trend is characteristic of many oxides [677–679]. Since a more in-depth investigation is beyond the scope of this study, it can be speculated that variations among the reported properties of oxide films are reasonably explained by the various growth environments.

### 6.4.6 Crystallography

The crystalline phase composition present in the specimens was evaluated by means of x-ray diffraction. Figure 6.7 confirms a fully austenitic structure on the 316L specimen printed using the stripe hatching. Apparently, the sinusoidal hatching led to a different heating and cooling rate in the meltpool, which failed to fully prevent the suppression of solute redistribution and resulted in a portion of the austenitic phase transforming into $Fe_2Si$ and CrSi as confirmed by the JCPDS cards 83-1259 and 65-3298. An evident diffraction peak of SiC was observed in the composites spectrum and confirmed by the JCPDS card 89-1396. The presence of SiC in the microstructure suggests that complete dissolution of SiC particles was avoided under the used set of processing parameters and inherent rapid cooling rates of L-PBF. However, at a temperature of 883 K decomposition of SiC into Si and C atoms began, and according to the Fe-Si binary phase diagram, the phase transformation temperature decreases with increasing content of Si [680–682]. Therefore, Si atoms could have diffused into the lattice of molten Fe and consequently de-stabilised the austenite phase. In this regard, it is clear that displaced Si from SiC reacted with the matrix and contributed to the precipitation of silicide phases.

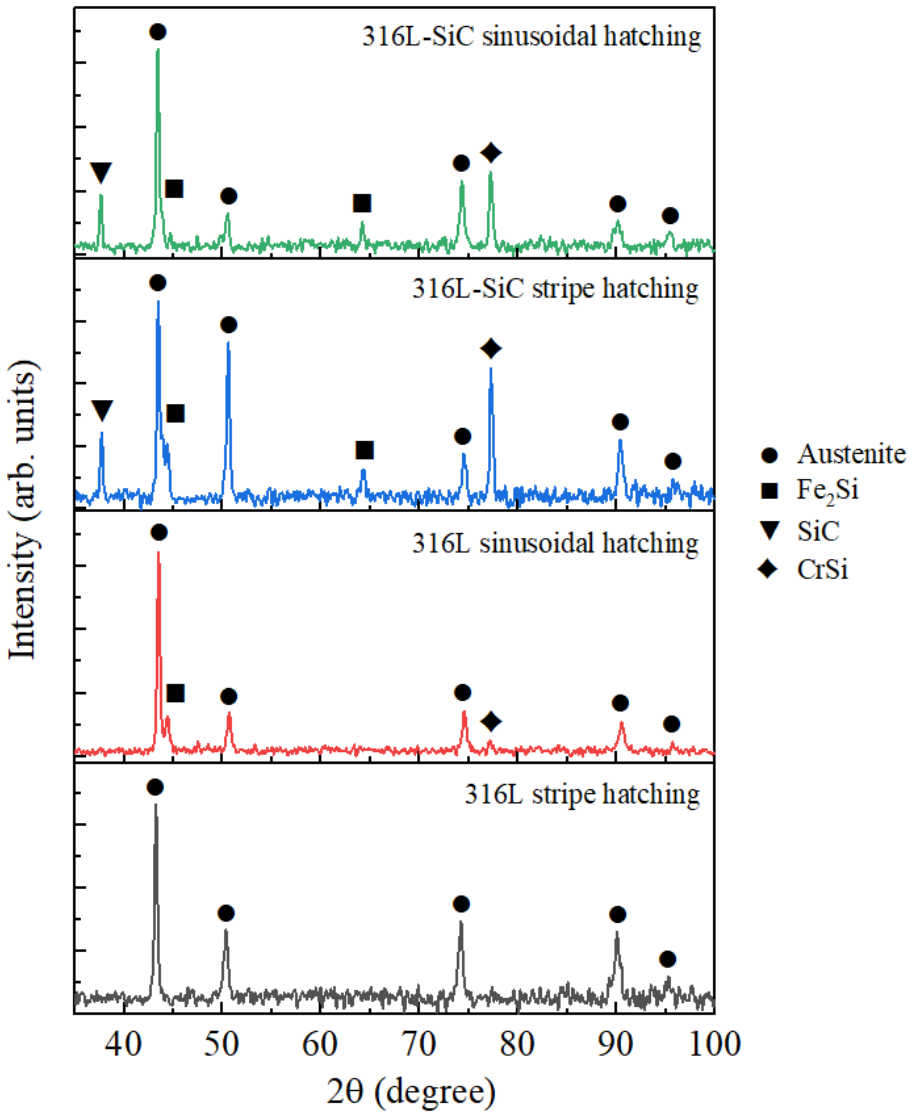


**Figure 6.7** X-ray diffraction patterns of the printed specimens.

Electron backscatter diffraction grain orientation maps normal to the build direction and corresponding discrete pole figures of the austenitic phase are presented in Figure 6.8. It is observed that the specimens printed in this study are characterised by different crystallographic texture. A moderate {100} and {111} texture with preferable [101] and [001] grain growth was revealed in the pristine (unreinforced) 316L stripe hatching. In contrast, both of the composite specimens showed similar but a less strong texture, spread rather towards the {100} crystallographic family of planes. Nevertheless, the 316L-SiC sinusoidal hatching specimen presented a distinct fraction of [001] oriented grains. SiC and precipitated silicide phases had a weak contribution to the specimen's crystallographic texture. It was observed for SiC and CrSi a texture incline to the {100} pole, especially for SiC with orientation parallel to the hatching direction. In both of the

printed composites, it is also observed that SiC grains were preferably oriented between [001] and [101]. On the other hand, grains of $Fe_2Si$ were predominantly [210] and [120] oriented in the specimen 316L sinusoidal hatching, while the $Fe_2Si$ phase present in the composites showed no clear contribution to texture. Supplementary pole figures are available in Figure 6C1 of Appendix C.

The electron backscatter diffraction analysis also showed that the total contribution of silicide phases to each specimen (316L sinusoidal hatching, 316L-SiC stripe hatching and 316L-SiC sinusoidal hatching) was less than 1 % (from this, approximately ¼ being of CrSi). As expected, most of these precipitated silicides ($Fe_2Si$ and CrSi) were distributed along the grain boundaries of the austenite phase. This is because at the grain boundaries, the concentration of vacancies tends to be high, thus permitting easy diffusion of atoms. Additionally, as grain boundaries are potent nucleation sites, precipitating particles may have removed sufficient solute from the adjacent matrix such that the region in the proximity of the grain boundary remained free of precipitates [683–685].

There is clear evidence that both the addition of SiC and the used sinusoidal hatching promoted grain refinement. Large austenite grains underwent approximately 10 µm reduction in response to the sinusoidal hatching, bringing the largest size down to 55 µm in the unreinforced specimen and down to 36 µm in the composite specimen. The sinusoidal hatching system also impacted on the size distribution range of the remaining grains, for example in the unreinforced specimens it was reduced from a range of 1 to 43 µm to a range of 2 to 27 µm. The 316L-SiC sinusoidal hatching presented the most refined microstructure of the four specimens, and this is supported by its low average 20 µm grain size, narrower grain size distribution, and lower as well as more homogeneous area fraction grain size. Electron backscatter diffraction grain maps and grain size distribution plots are available in Figure 6C2 of Appendix C.

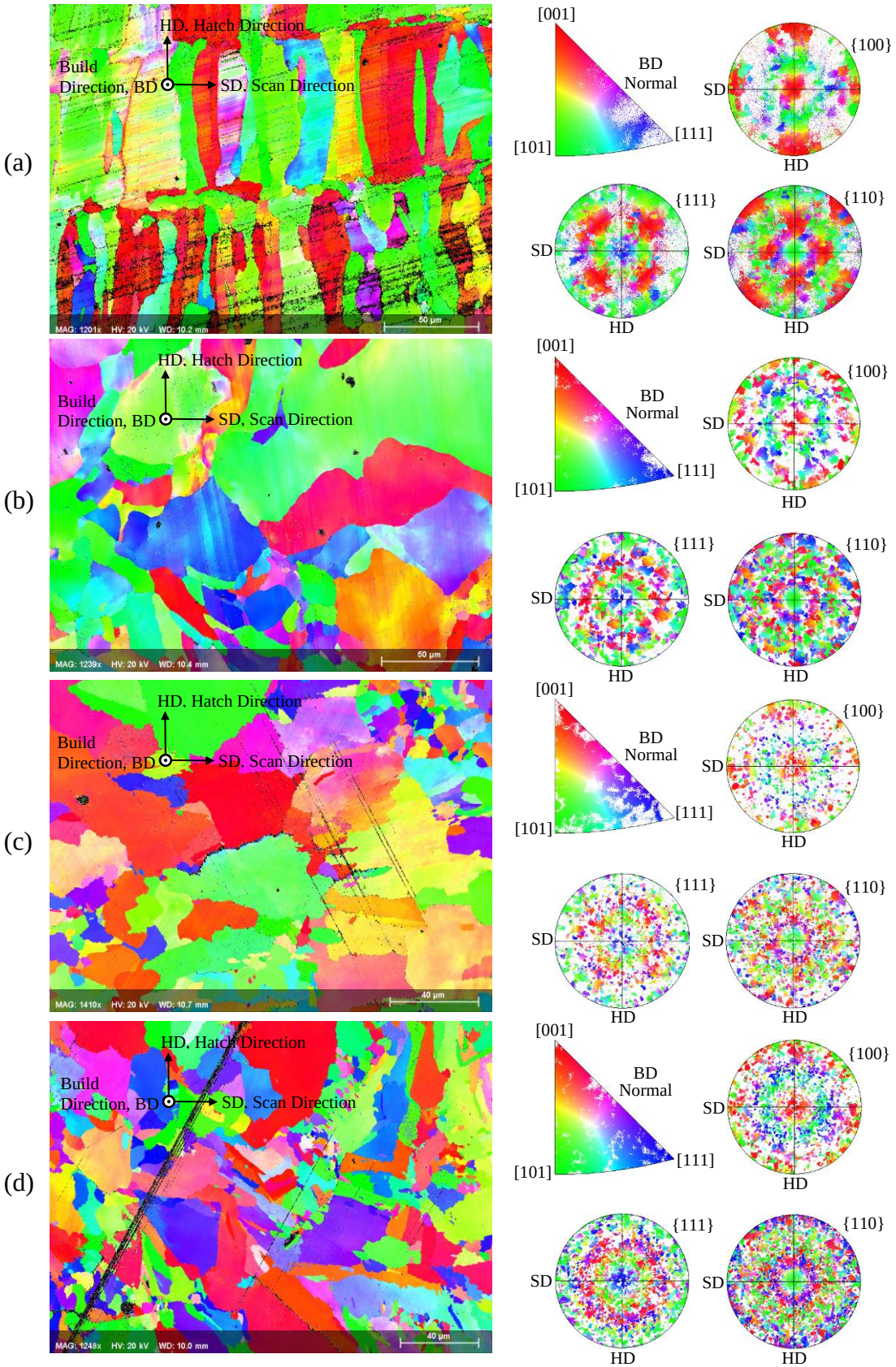


**Figure 6.8** Electron backscatter diffraction discrete pole figures and inverse pole figures for (a) 316L stripe hatching, (b) 316L sinusoidal hatching, (c) 316L-SiC stripe hatching and (d) 316L-SiC sinusoidal hatching.

## 6.5 Discussion

### 6.5.1 Physical and Mechanical Properties of the Specimens

According to the density results, all the specimens possessed a relative low density. Yet, microstructural micrographs showed no evidence of lack of fusion defects, hence the possibility of the observed low densities resulting from the usage of insufficient volumetric energy densities can be disregarded. However, the micrographs do reveal the existence of severe porosity (pores smaller than 5 μm in diameter) within the specimen's microstructure, and these were located particularly at grain boundaries. In this case, its typically said that the presence of moisture and entrapped gas from the feedstock powder, inappropriate shielding gas flow rate/velocity and excessive turbulence in the meltpool are the frequent causes of porosity [686–689]. However, it is most likely that instead, as also supported by the observed spattering from the meltpools, the high energy density process input was a factor. In this case, the melting mechanism was dominated by either a transition or keyhole mode. The keyhole mode represents a highly unstable regime due to typical local temporal fluctuations of evaporation and flow imbalances along the wall of the keyhole cavity [690]. Therefore, it has a large potential of forming small gas bubbles that can get trapped within their meltpool during its rapid solidification. Nevertheless, the keyhole instability can be controlled [691–694]. The reason for this study not using the conductive mode of melting was linked to its productivity limitations, and in fact the keyhole mode is appreciated in industrial applications [695].

It is well known that lower porosity and higher densification are prerequisites for obtaining higher hardness levels [696,697]. Despite their density and porosity, specimens printed in this study showed outstanding hardness. It is therefore clear that addressing these two issues additional hardness improvements are possible. A more detrimental impact of porosity was evidenced from the tensile results. The pores as crack initiation sites, drove the specimens to a premature failure resulting in reduced yield and tensile strength. During solidification, molted metal shrinks due to thermal contraction and in L-PBF this is impeded by the previously solidified layers underneath, which then forms strong compressive stresses at the interface layer. Similarly, the cyclic thermal stress could result in cracks relieving this residual stress. Yet, the inherited residual stresses were not sufficiently high enough to generate cracks in the unreinforced specimens due to the high toughness and ductility of the 316L alloy. However, in the composite specimens, the coefficient of thermal expansion mismatch between the SiC and 316L led

to the generation of thermal stress in the SiC phase, and along with the accumulated residual stresses, this was the driving force of crack formation. Here, crack propagation followed the networks of grain boundaries, where resistance was weakened by the presence of pores and silicides. In the printing of composites with high scanning speeds such as that used for the sinusoidal hatching system, very high heating and cooling rates exists. Despite the fact that cracks were present in the composites printed with both low and high scanning speeds, it could be expected that the high scanning speed would introduce higher thermal gradients, thermal gradient rates and stress, which would then promote and accelerate crack initiation and propagation. However, this was not confirmed in this study. Here, a promising solution for inhibiting the initiation and propagation of crack is to attain further grain refinement to increase the microstructural barriers. Additionally, the preheating (at an optimal temperature) of the build substrate could reduce the temperature gradient and cooling rates and reduce the magnitude of shrinkage stress. Therefore, this could be an effective means of mitigating residual stress and solidification cracking.

### 6.5.2 Tribological and Mechanical Properties of the Naturally Formed Oxide Films

In MMCs, understanding the nanotribology occurring at the interface of two contacting surfaces during their relative motion is necessary in order to develop fundamental understanding to many technological problems, including wear, friction and lubrication occurring at the nanoscale. Also, the importance of this is that it can lead to understanding tribology on the microscale. Considering the discussions accompanying the results, it is observed that despite having a much thicker oxide film, the composite specimens showed almost twofold reduction in friction coefficient and specific wear rate. In fact, the in-situ nanoindentation support this result with its reported nanohardness and reduced modulus. However, it should be noted that this is specifically for the 2 nm depth into the oxide film. The analysis made on the evolution of nanohardness and reduced modulus suggested that further into the oxide film, at a specific depth, different trends for friction and wear to that of Table 6.2 could exist. Ultimately, the influence of the naturally formed oxide films on the nanotribological response was quite different. Mechanically softer oxide layers exhibited an elastoplastic deformation behavior, eventually leading to higher wear. In contrast, harder and stiffer oxide layers led to a reduction in wear and friction. The broad implication of the presented study is that tuning the properties and characteristics of oxide

films can therefore be beneficial for many applications in order to improve tribological performance.

### 6.5.3 Resulting Crystallographic Textures

Typically, the highest temperature gradient is located at the bottom of the meltpool and decreases nonlinearly towards the meltpool upper surface. Therefore, in response to the maximum heat flow, columnar grains grow predominantly parallel to the build direction. However, the results suggested that several grains also grew closely aligned with the hatching direction in the 316L stripe hatching specimen and in the remaining specimens rather closely aligned with the scanning direction. This is most likely consequential to the adopted keyhole mode of melting as high meltpool temperatures can lead to less aligned crystal growth with the build direction [698] due to the keyhole's meltpool promotion of multidirectional heat dissipation in response to the presence of irregular meltpool boundary morphologies. Therefore, the aforementioned along with the processing parameters used explain the absence of strong crystallographic textures.

The stripe hatching is the simplest and most commonly used hatching system in L-PBF. Additionally, several authors have reported it to develop strong <001> columnar grain alignments parallel to the build direction [632,699–702]. Instead, complex hatching systems such as islands [703–709] and fractals [612] have a more profound influence on grain morphologies and development of crystallographic textures. Accordingly, it was demonstrated in [634] [710] [711] that it is possible to control grain orientation as per hatching patterns. Therefore, this suggests that it is possible to grow grains with the sinusoidal hatching system which form sinusoidal patterns. With a such achievement, it would be interesting to verify the implications of sinusoidally oriented grains on the ductility of MMCs when applying tension along the hatching.

The existence of intragranular cellular structures in L-PBF 316L has been reported in a number of studies [712–721]. From these, it is worth noting that neighboring cellular colonies typically are misoriented with each other. As a matter of fact, the resulting misorientation obtained with the stripe hatching was consistent with these reports. However, the sinusoidal hatching system led to the development of cellular colonies highly oriented with the build direction. As contrasted in Figure 6.9, the rastering of the laser at 10,000 mm/s along the sinusoidal path caused periodic oscillation of the molten along the scanning vector hence resulting in the solidification of short spaced overlapping

dabs which influenced the orientation of cellular structures. In this respect, observations confirmed that the temperature gradient more controlling the local cellular growth direction was the vertical temperature gradient, and this being consistent between colonies. A colony of cells is considered as a group of cellular structures with the same morphological orientation and cell spacing.

One of the implications of having misoriented rather than highly oriented colonies of cellular structures is on the tensile performance of specimens. As shown by [721], tension perpendicular to the cells axis caused less deformation in response to accumulation of nano voids in the cellular microstructure, and additional stress then enlarged the nano void sizes breaking cellular boundaries. Under the same conditions, cells which tension was applied along their long axis were void free and the stress was relieved by cell deformation. In both scenarios, cells could only deform to a certain limit until the high tensile stress teared them apart. Therefore, based on these findings and as seen from the comparison of the tensile performance between the composites, the sinusoidal hatching can be used as a mean of collectively improving tensile strength and ductility. Additionally, the cellular microstructure resulting from the sinusoidal hatching could be used towards increasing composites toughness by deviating crack direction to longer paths. Even though both composites showed similar outstanding hardnesses, owing mainly to the barriers of dislocation motions imposed by cellular structures, it was observed that the 316L-SiC stripe hatching composite had a slightly higher hardness. Clearly, this is most likely to be related to the randomisation of the cellular colonies orientations which could potentially induce higher densities of entanglement dislocations. However, the colonies in the 316L-SiC sinusoidal hatching specimen were highly oriented and the reported hardness for this specimen was measured from the transversal axis of the cellular structures. This denotes that the hardness of this specimen with reference to the longitudinal axis of the cellular structures could be different.

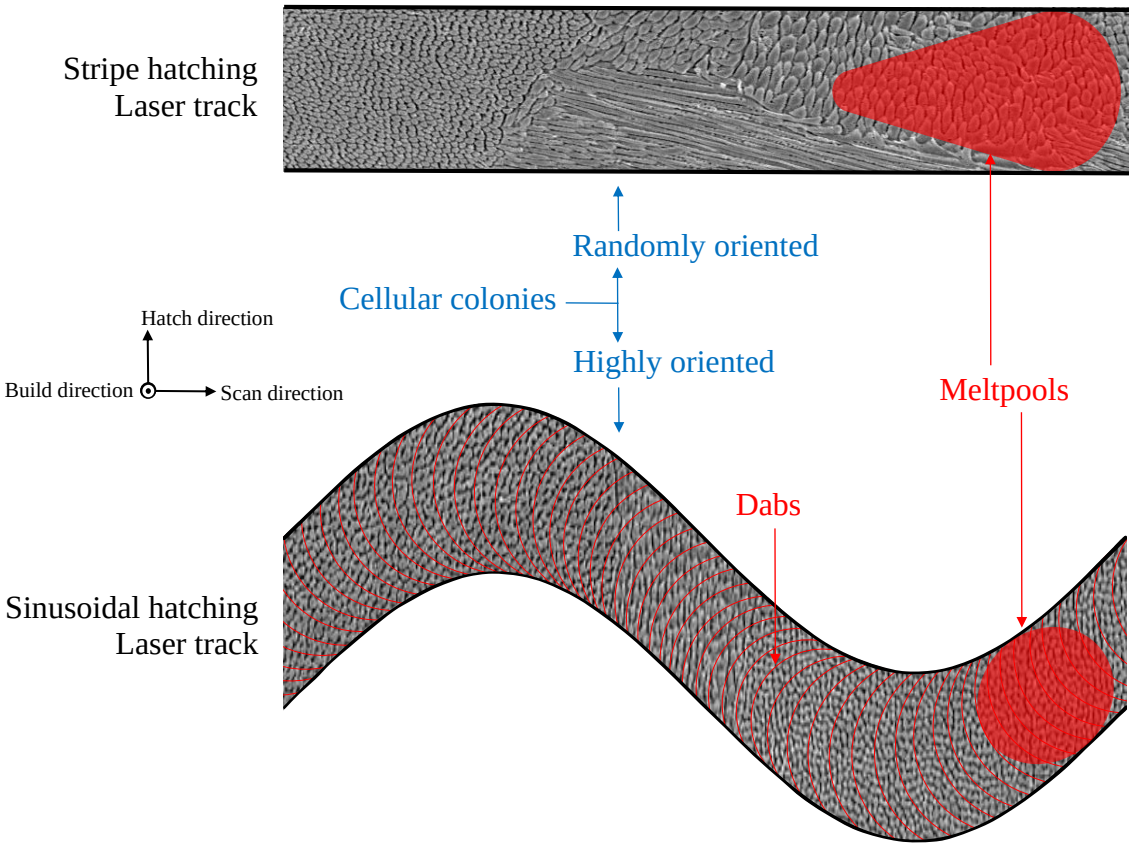


**Figure 6.9** Schematic representation of the hatching systems and their resultant cellular structures.

### 6.5.4 Assessment of the Sinusoidal Hatching System

The sinusoidal hatching emerged as an important hatching system for L-PBF of MMCs. It proved to be capable of contributing to improvements in hardness, strength and ductility in composites. However, the existing gas porosity and solidification cracking within the composite microstructure prevented the exploitation of its full potential, therefore further research is recommended. Contrasting with the stripe hatching, over sixteen-fold increase in scanning speed and over threefold reduction in laser power was successfully implemented in the sinusoidal hatching. Therefore, besides improving performance of composites, the sinusoidal hatching also helps to address the manufacturing lead time and process energy consumption issues concerning the L-PBF process [722,583].

The mechanisms which capacitated the sinusoidal hatching to promote suitable melting with such low laser power and extremely high scanning speed is speculated below. With the used scanning speed, the scanning of consecutive neighboring hatching paths was

ultrafast. Therefore, the rate of heat flowing way from solidified zones as a result of argon flow convection and thermal radiation was reduced. Additionally, the sinusoidal profile of the laser paths is liked to have trapped pockets of hot argon and so reduced the efficiency of the gas flow as a cooling provider. Despite not using preheating, it was observed at the end of the printing job that the build substrate was approximately at 100 °C. Apparently, this temperature stabilised during the printing of the support structures in response to the argon flow and heat dissipation and transfer to the printer components. Therefore, it is clear that a much higher temperature than this in solidified neighboring hatching paths existed. In this respect, the stored thermal energy is well with the applied laser power. Another observation is the reduction of the meltpool width in contrast with the stripe hatching. Nonetheless, the width was very consistent along the sinusoidal paths and no evidence of lack of fusion related defects was found.

### 6.6 Conclusions

A novel hatching strategy here named sinusoidal hatching was developed for L-PBF of MMCs. The presented investigational results provide a detail description regarding the effect of the sinusoidal hatching on the microstructure and mechanical properties. Comparison with the conventional stripe hatched composite shows that an increase in yield strength and ductility can be achieved by implementing the sinusoidal hatching. The tensile properties of the composites were compromised by the existing porosities and cracks which caused premature fractures and failure under the tensile loads. Their existence was attributed to trapped gas bubbles resulting from an unstable keyhole mode of melting and thermal expansion mismatch between the matrix and reinforcement along with accumulated residual stresses. Fortunately, these defects have been shown to be less detrimental to the hardness. Confirmed by reference to the literature, both composites showed an outstanding hardness. Yet, a slightly higher hardness was measured from the stripe hatched produced composite which was attributed to the randomised directional growth of cellular structures.

Friction and wear properties of the naturally formed oxide films and deconvolution of their mechanical properties were also investigated in this study. At approximately 1 nm depth into the oxide film, the composites already presented low plasticity, in contrast, elastic recovery was evidenced in the matrix specimens. As a matter of fact, these deformation responses were consistent with the films nanohardness and reduced modulus, which also correlate with the twofold reduction in friction coefficient and

specific wear rate measured from the composites. However, the depth into the oxide film whose nanohardness closely related to the intrinsic nanohardness of the bulk material was 70 nm for the composites and 20 nm and 30 nm for the unreinforced stripe and sinusoidal hatched specimens. Additionally, the evolution of nanohardness and reduced modulus showed that further into the oxide film, at a specific depth, different trends for friction and wear to that reported could exist. Ultimately, mechanically softer oxide layers exhibited an elastoplastic deformation behavior, eventually leading to higher wear. In contrast, harder and stiffer oxide layers led to a reduction in wear and friction. The broad implication of this study is that tuning the properties and characteristics of oxide films can therefore be beneficial for many applications in order to improve tribological performance.

The sinusoidal hatched composite exhibited a highly refined columnar microstructure having a moderate {100} texture as most of the grains solidified preferentially in the <001> direction with respect to the build direction. A unique molten flow and solidification condition was established by the sinusoidal hatching, as periodic oscillations of the laser molten material along the laser scanning vector resulted in the solidification of short spaced overlapping dabs which formed small colonies of intragranular cellular structures with cells highly oriented with the build direction. The implications of this reflected on the obtained improvements in yield strength and ductility seen from the sinusoidal hatched composite. It is speculated that, apart from tailoring hardness, the sinusoidal hatching could be used towards increasing composites toughness by deviating crack direction to longer paths. Besides improving composite performance, the sinusoidal hatching also reduced manufacturing lead time and process energy consumption in response to its natural high scanning speed and low laser power requirements.

The bulk mechanical properties of the composites were negatively affected by the existing porosities and cracks. Future research should therefore identify the source of theses defects and apply mitigation measures to eradicate them from the composite's microstructure. In-situ process monitoring of temperature and melt flow as well as build substrate preheating for mitigation of crack formation and residual stress are recommended.

The current study helps to pave the path towards addressing several endemic issues concerning mechanical performance and cost effectiveness of MMCs. As there is an increasing demand for materials with supernormal performance, the sinusoidal hatching is worthy of further research.

## 6.7 Supplementary Results

### 6.7.1 Appendix A

As seen in Figure 6A1, the satelliting of SiC nanoparticles onto the surface of the 316L particles notably enhanced the material dispersion, which is evident from the even decoration.

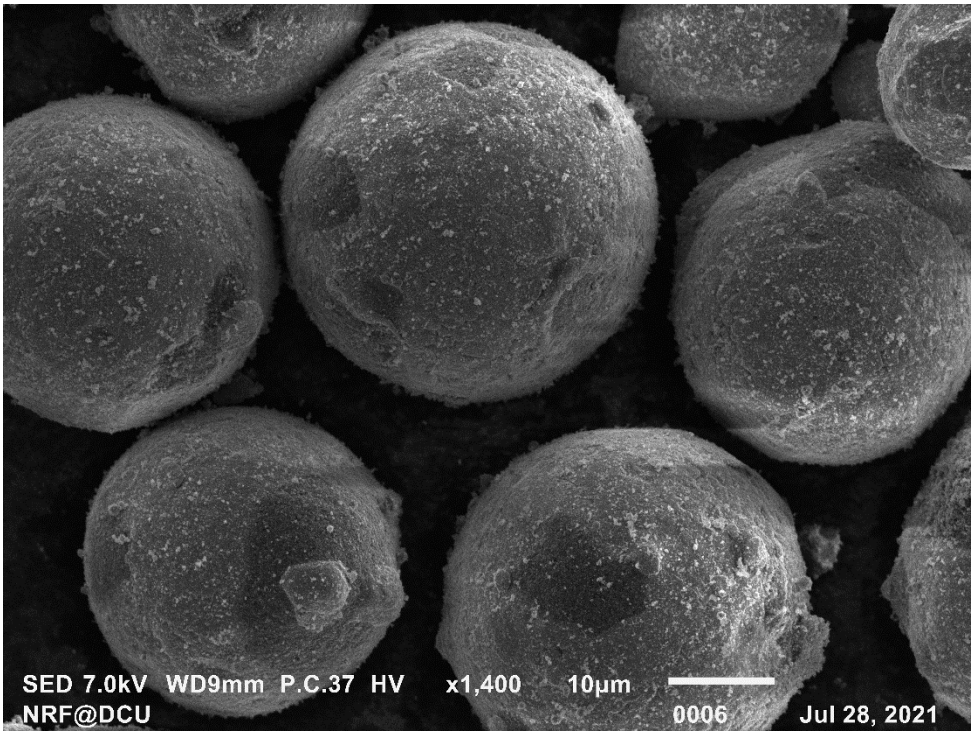


**Figure 6A1** Micrograph of the prepared feedstock powder with 1% SiC.

The two hatching systems used in this work are illustrated in Figure 6A2 and their parameters were given in Table 6.1. The inert gas (argon) flow was set perpendicular to hatching. Additionally, in order to reduce heat concentration zones, unidirectional scanning of the laser paths was considered.

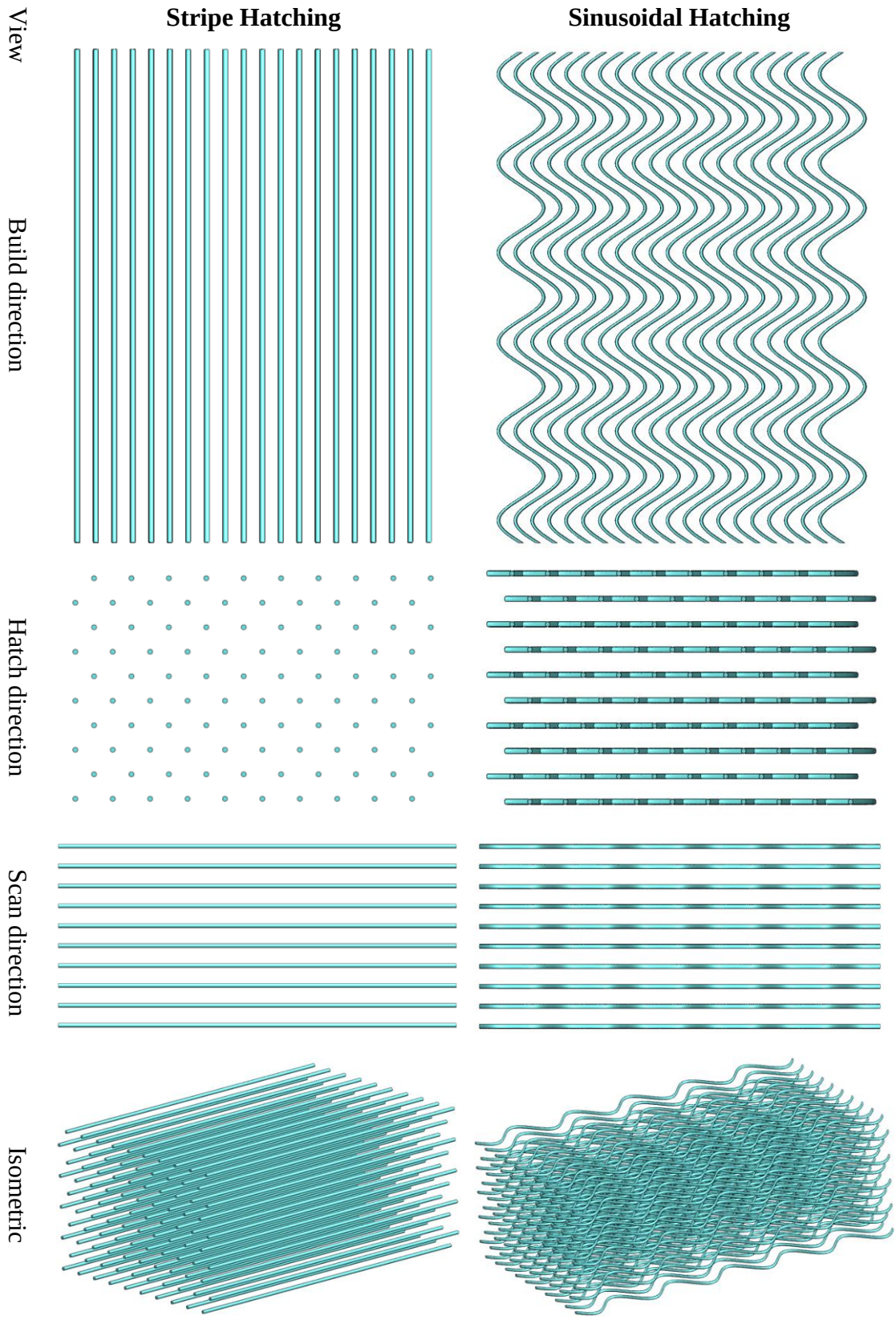


**Figure 6A2** Illustration of the hatching systems used in this work.

Figure 6A3 shows the probe used in the nanoscratch testing. Its deflection sensitivity of 60.47 nm/V and its cantilever spring constant of 54.13 N/m were acquired by the thermal tune method, and used in the atomic force microscope software during the nanoscratch testing.

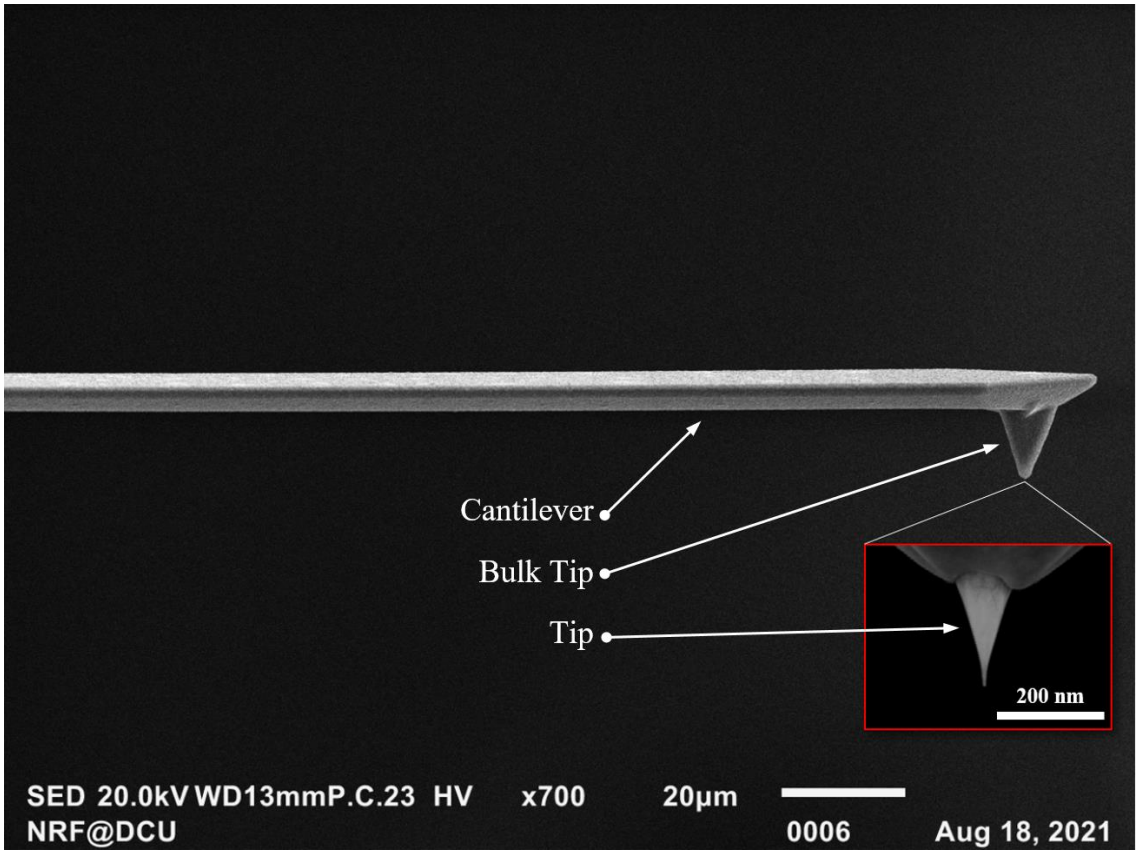


**Figure 6A3** Single crystal diamond atomic force microscopy probe.

### 6.7.2 Appendix B

Nanoindentation on the oxide film of the specimens was performed to support the nanoscratch study, and to measure the depth into the oxide film which the nanohardness is closely related to the nanohardness of the bulk material. The existence of surface defects, grain boundaries and phases affect the oxide film physical characteristics and chemistry. Here, each presented result is the average of six indents (2x3 matrix, 30µm spacing) obtained for the applied nanoindentation experimental design. The tip (a Berkovich diamond indenter) geometry and radius were calibrated with a fused quartz standard of known properties by running a series of tests that spans the load range of the instrument for area function determination and establishment of the compliance correction factor, both to be later utilised by the instrument software. Then, in-situ indentation mode of operation was chosen as it offered drift compensation capabilities

for maximum accuracy. Prior performing each indent, a drift settle time of 300 s was applied while the tip waited on the specimen's surface in feedback prior to begin the drift correction procedure. This was to allow time for the motors and piezos to settle down. Then, the indentation procedures only began when the overall drift rate including thermal drift was within ±0.05 nm/s. All indentations were performed at room temperature. Figure 6B1 shows the evolution of the nanohardness within the oxide film and Figure 6B2 shows the evolution of the reduced modulus within the oxide film. The nanoindentation load-unload behavior of the 2, 10, 20, 30, 40, 50, 60, 70 nm depths into the oxide film is illustrated in Figure 6B3 and Figure 6B4.

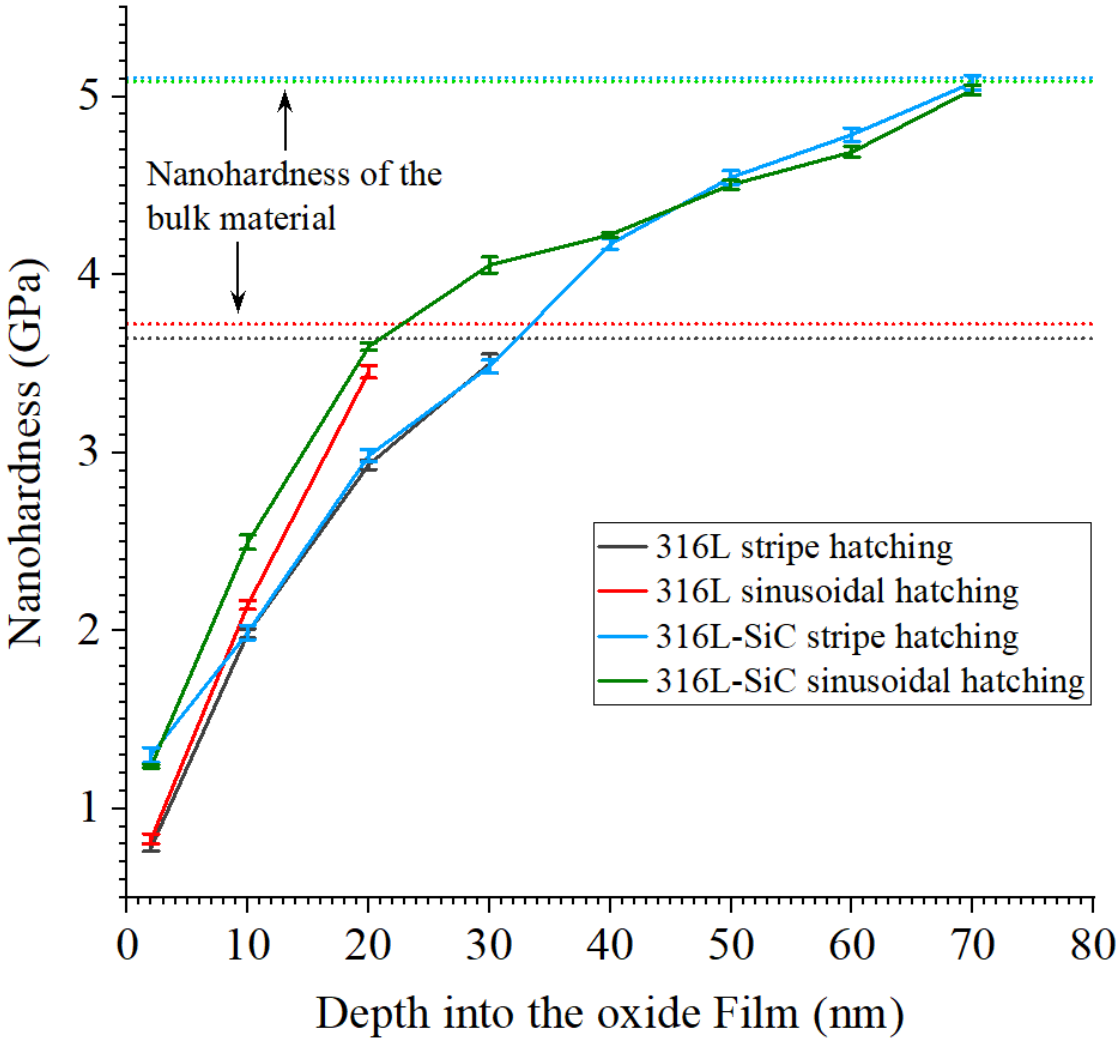


**Figure 6B1** Evolution of the nanohardness within the oxide film.

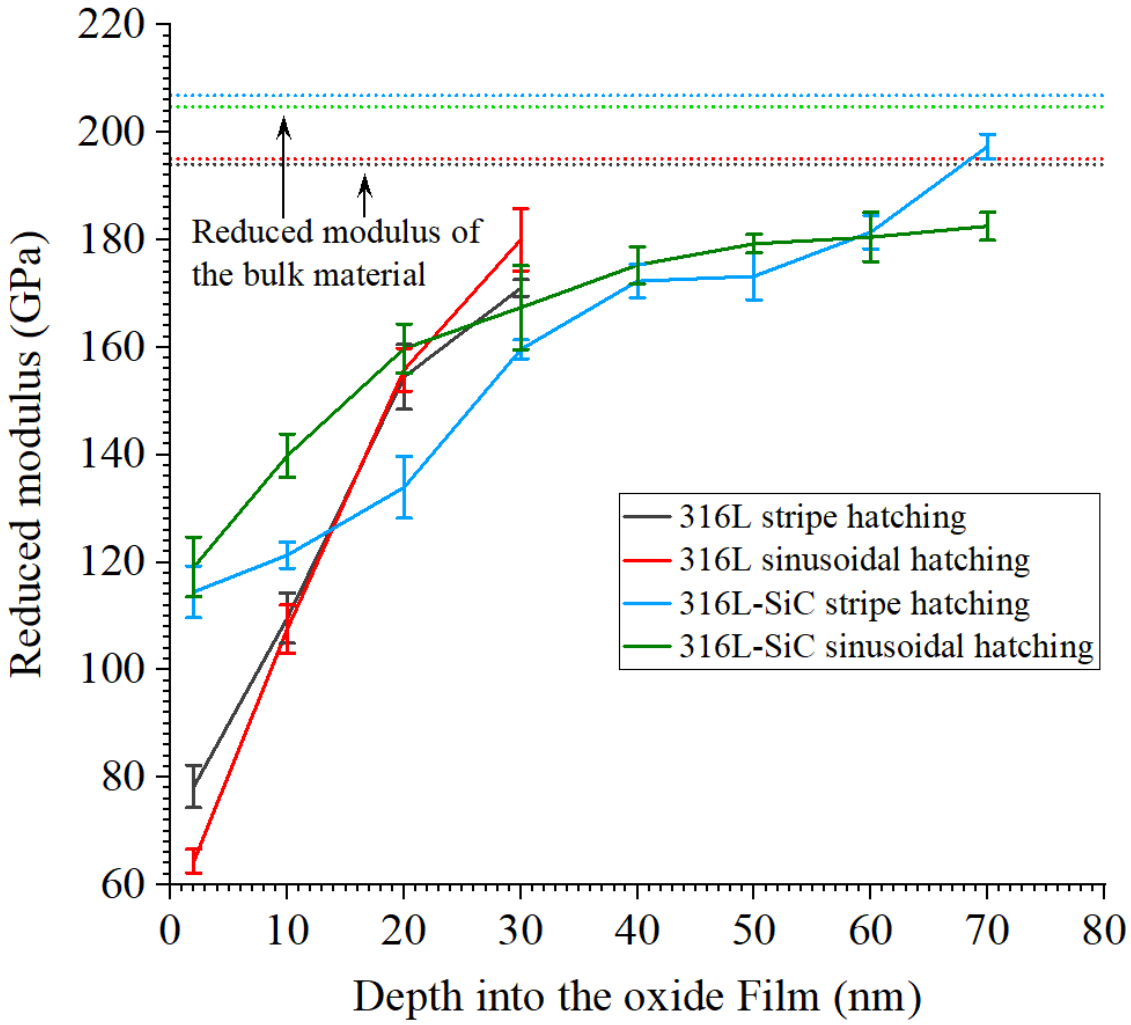


**Figure 6B2** Evolution of the reduced modulus within the oxide film.

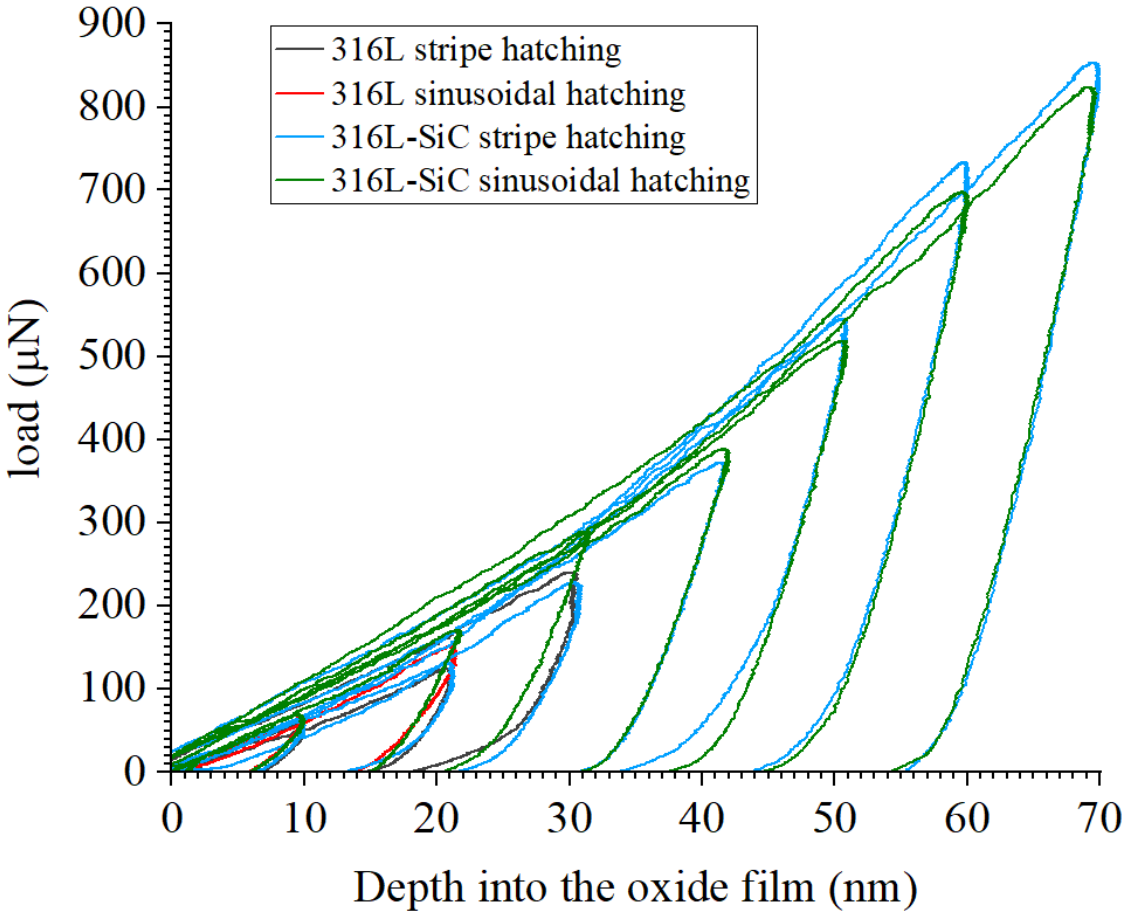


**Figure 6B3** Nanoindentation load-unload behaviour of the 2, 10, 20, 30, 40, 50, 60, 70 nm depths into the oxide film.

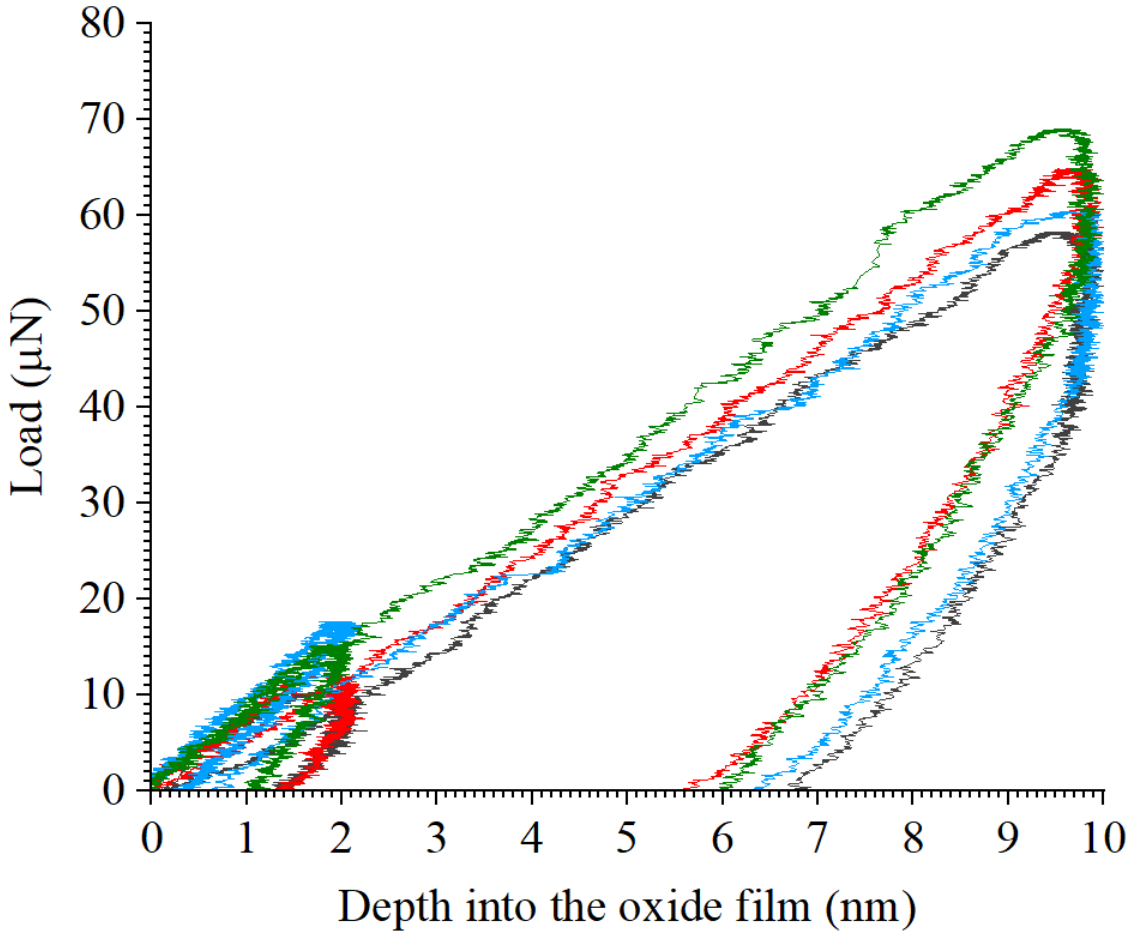


**Figure 6B4** Supporting plot for Figure 6B3.

### 6.7.3 Appendix C

Inverse pole figures and pole figures of the precipitated silicides ($Fe_2Si$ and CrSi) and SiC phase are available in Figure 6C1.

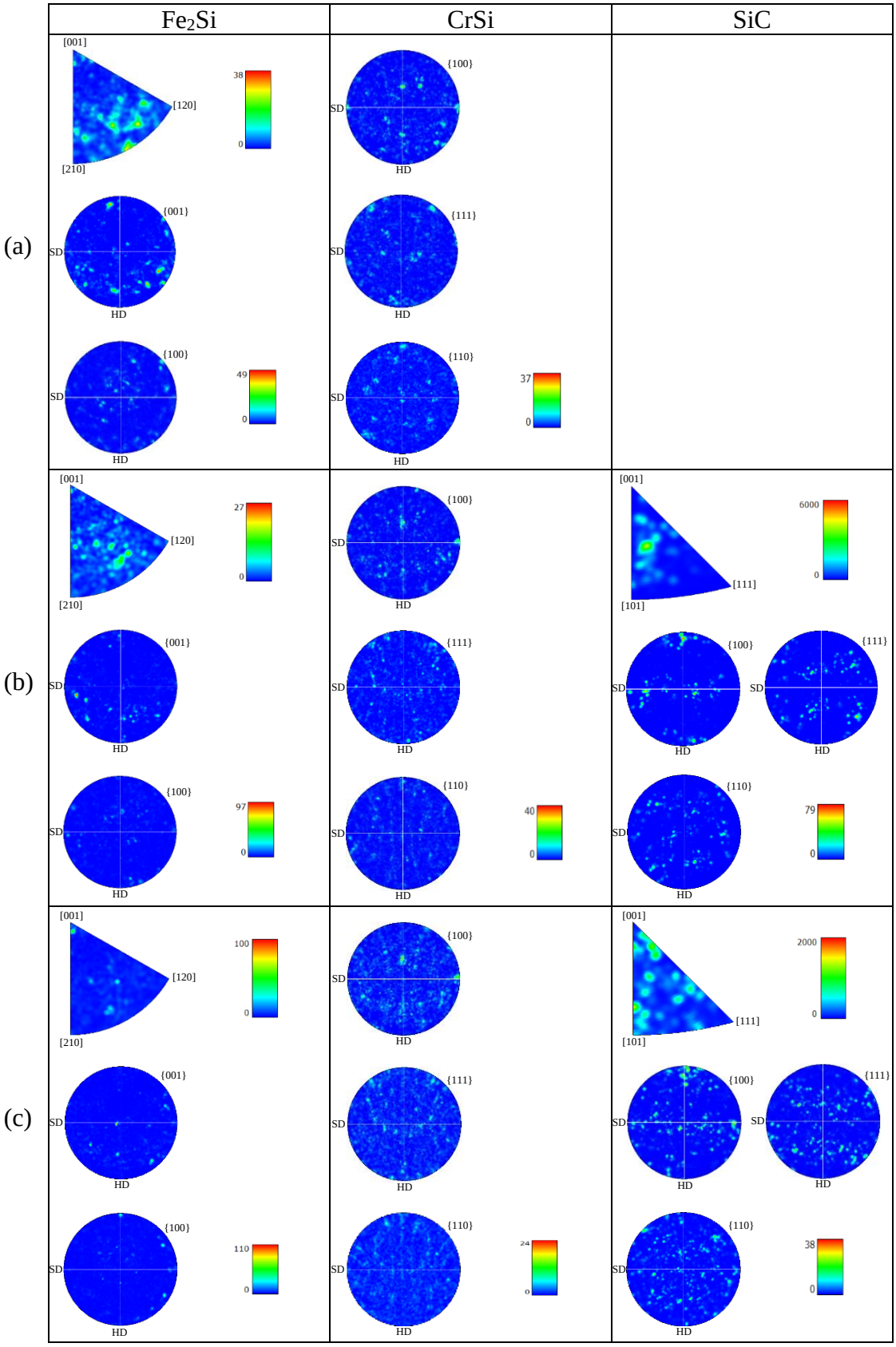


**Figure 6C1** Additional electron backscatter diffraction build direction inverse pole figures and pole figures for (a) 316L sinusoidal hatching, (b) 316L-SiC stripe hatching and (c) 316L-SiC sinusoidal hatching.

Electron backscatter diffraction grain map and grain size distribution plot for the printed specimens are given in Figure 6C2.

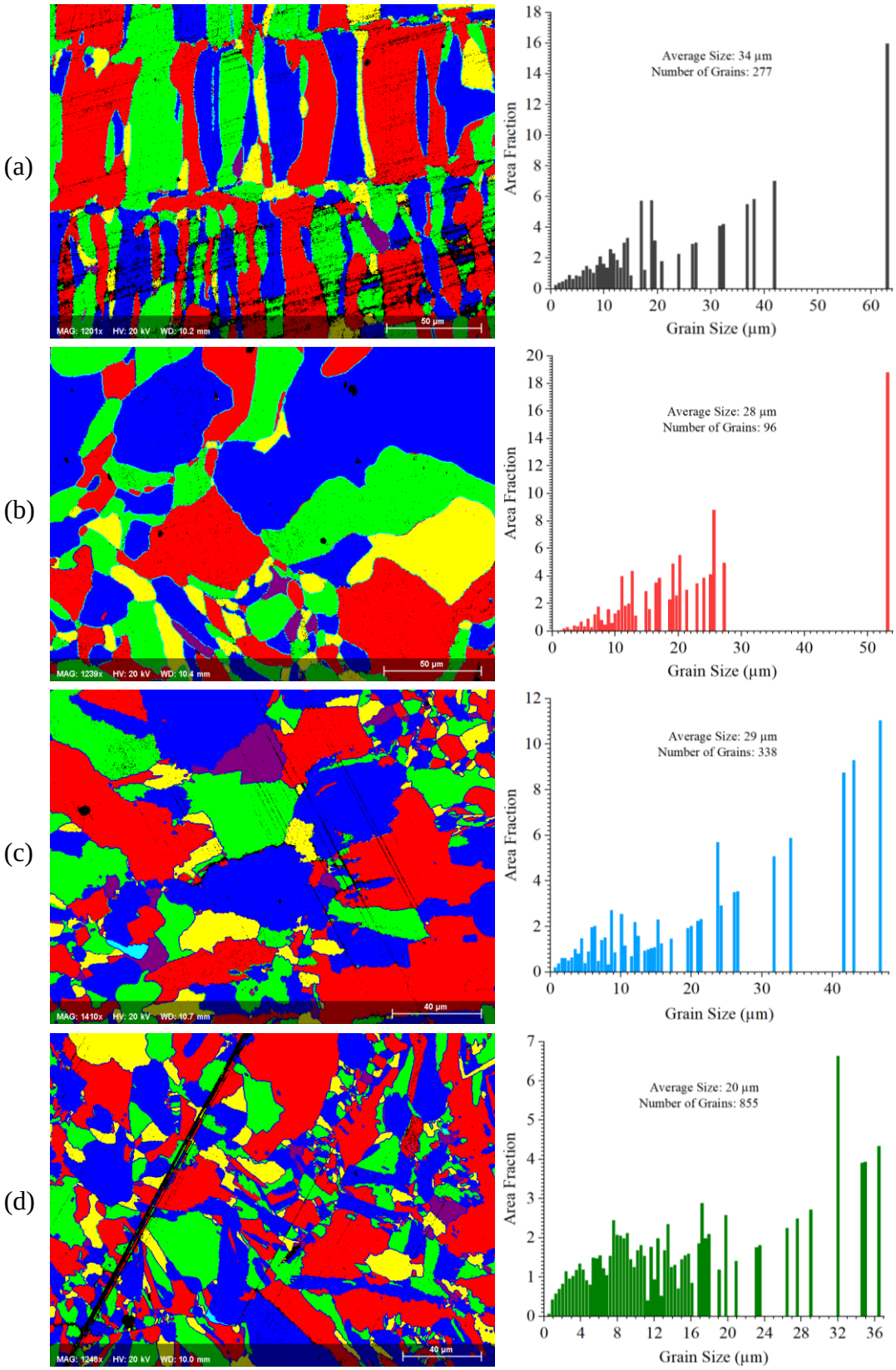


**Figure 6C2** Electron backscatter diffraction grain map and grain size distribution plot for (a) 316L stripe hatching, (b) 316L sinusoidal hatching, (c) 316L-SiC stripe hatching and (d) 316L-SiC sinusoidal hatching.

# Chapter 7

## Laser-Powder Bed Fusion In-Process Dispersion of Reinforcing Ceramic Nanoparticles onto Powder Beds Via Colloid Nebulisation

**Publication Status:** Published

Mussatto, A., Groarke, R., Vijayaraghavan, R. K., Obeidi, M. A., MacLoughlin, R., McNally, P. J., Nicolosi, V., Delaure, Y., and Brabazon, D., 2022, "Laser-powder bed fusion in-process dispersion of reinforcing ceramic nanoparticles onto powder beds via colloid nebulisation", Materials Chemistry and Physics, 126245.

https://doi.org/10.1016/j.matchemphys.2022.126245

## 7.1 Abstract

Functionally grading material composition in laser-powder bed fusion grants the potential for manufacturing complex components with tailored properties. The challenge in achieving this is that the current laser-powder bed fusion machine technology is designed to process only powdered feedstock materials. This study presents a multi-feedstock material printing methodology for laser-powder bed fusion. Utilising colloid nebulisation, tungsten carbide nanoparticles were successfully deposited onto powder beds of stainless steel 316L during the laser-powder bed fusion process. By this means, a controlled volume of tungsten carbide nanoparticles was uniformly dispersed onto powder beds under the inert processing chamber atmosphere. As a result, specimens printed with this methodology showed an increase in strength. Similarly, the colloid medium played an important role in the resulting microstructures. It led to the formation of consistent and stable meltpools and a strong crystallographic texture. Recommendations are given for the successful dispersion of higher volumes of nanoparticles. Additionally, insights into application prospects for material nebulisation in laser-powder bed fusion are presented and discussed.

## 7.2 Introduction

Laser-powder bed fusion (L-PBF) has revolutionised the manufacturing world through its personalised customisation and geometrically intricate capabilities, and through the distinctive resulting microstructures from its rapid cooling and solidification cycles [723]. This reflects on the continuously growing academic research and countless aerospace, automotive and medical industries adopting this technique [724]. Through this revolution a widespread innovation with single-material usage was established [725]. However, the manufacturing world is constantly evolving and today several L-PBF printers have the capability of manufacturing multi-material systems [726].

Multi-material L-PBF enables combining the physical characteristics of different materials into one system to derive a special function that is difficult to achieve through single-material L-PBF or conventional manufacturing methods [727]. Ultimately, multi-material L-PBF can provide solutions to problems associated with fusing dissimilar materials and address inefficiencies in manufacturing by reducing the number of production steps [728,729]. Moreover, multi-material L-PBF entails extensive changes

in regard to the design potential by allowing to change the material properties across a single component and thus locally adjust the material to set criteria [730].

Despite Aerosint SA [731] introducing a commercial dual-powder recoating system for L-PBF, the implementation of multi-material processing in L-PBF is still relatively new. Therefore, only limited research exists on this implementation approach in the field of architecture and construction.

The development of multi-material components with sharp and gradient material transitions has been reported in the literature [732–737]. A sharp transition between two dissimilar materials tends to lead to high stress concentration at the interfaces and can even cause delamination under complex loading conditions [738]. Nevertheless, this can be suppressed by a smooth material gradient transition or remediated by heat treatment [739]. A disadvantage of this multi-material approach is that it provides difficulties with controlling contamination between each powder [740]. Still, several multi-material system such as 316L/CuSn10 [741], IN718/GRCop-42 [742] and AlSi10Mg/C18400 [743] have been successfully developed.

Multi-material L-PBF processing of a feedstock mixture composed of two or more materials typically requires an additional process to blend the powders together [744]. Similar to the in-situ powder deposition [745], the major challenge with this is to ensure that the mixture is homogeneous within a layer and consistent between layers [746,747]. As an alternative, feedstocks of atomised powder blends [748,749] or coated powders [750,751] could be used at the expense of additional processing steps and cost. The capability of L-PBF to process powder mixtures has created exciting material research opportunities in the field of composites [752]. Derived from this, L-PBF of powder mixtures has also been explored for alloy development applications [737]. This in-situ alloying strategy has shown a potential for rapid design and verification of new alloys.

As can be seen from the current state of art, multi-material L-PBF has opened up a broad spectrum of possibilities for more complexity and functionality to new applications. At present, L-PBF systems and its research are restricted to powdered feedstocks. Therefore, the form of feedstock barrier needs to be overcome in order to achieve further advancements in multi-material L-PBF. To address this issue, this work introduces a method for laser-powder bed fusing multiple forms of feedstock materials. In summary, a colloid feedstock of tungsten carbide (WC) is nebulised onto powder beds of 316L

during the laser-powder bed fusion process. To assess this methodology, the printed specimens are characterised at microstructural level and contrasted with traditionally printed specimens. Discussions are then launched to illustrate the research advancements coming from this methodology. Additionally, insights into application prospects for material nebulisation in laser-powder bed fusion are presented.

## 7.3 Experimental

### 7.3.1 Materials and Methods

Vacuum melted argon gas atomised stainless steel AISI 316L powder (35-50 μm) supplied by Mimete S.r.l. and nanometre sized (30-100 nm) hexagonal WC powder supplied by US Research Nanomaterials Inc. were used in this study. The morphology of these powders is shown in Figure 7.1.

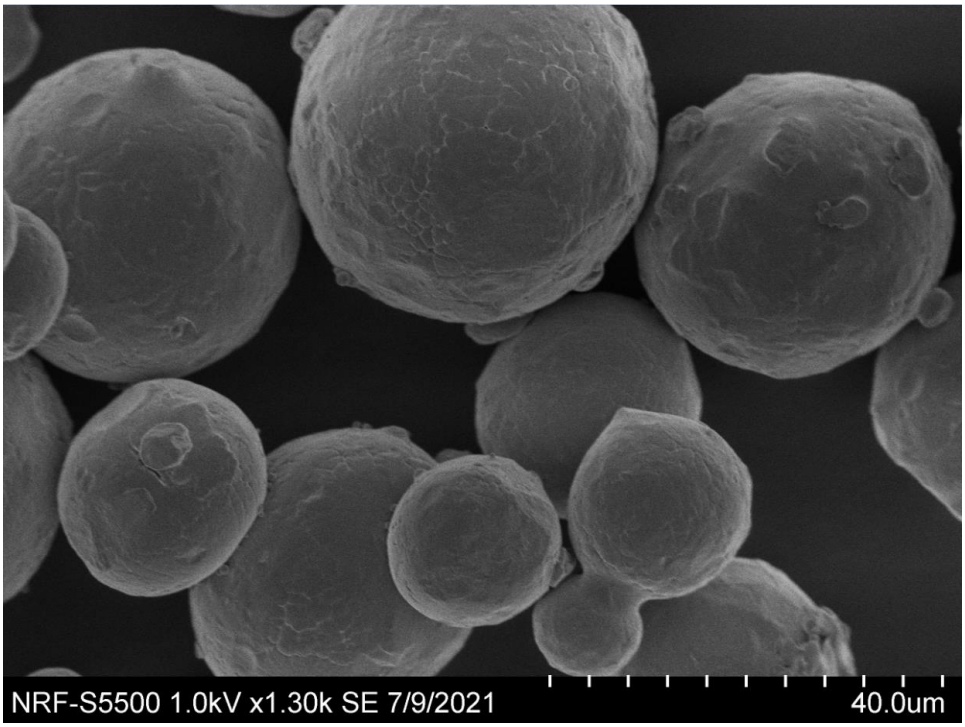


(a)

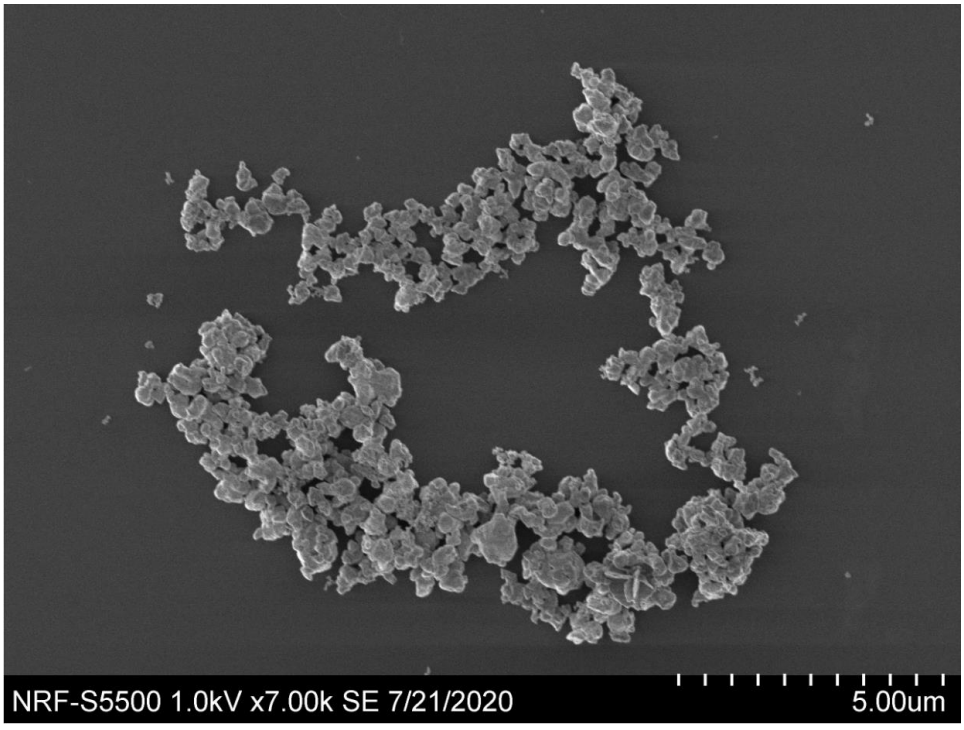


(b)

**Figure 7.1** Scanning electron micrographs of (a) 316L and (b) WC powder.

A colloid consisting of WC 2wt. % in deionised water was prepared. Then, a homogeneous nanoparticle dispersion was obtained using an in-house developed system

based on the THINKY PR-1 mixer. The dynamic viscosity of the prepared colloid (vial labelled WC2 in Figure 7.2) was determined on an Anton Paar MCR 301 rotational rheometer equipped with a stainless steel cone plate (CP50-2, Anton Paar) of 50 mm in diameter and 2° angle. The plate gap was set to 208 µm and the temperature was controlled at 20±0.1 °C using a Peltier element during the measurement.

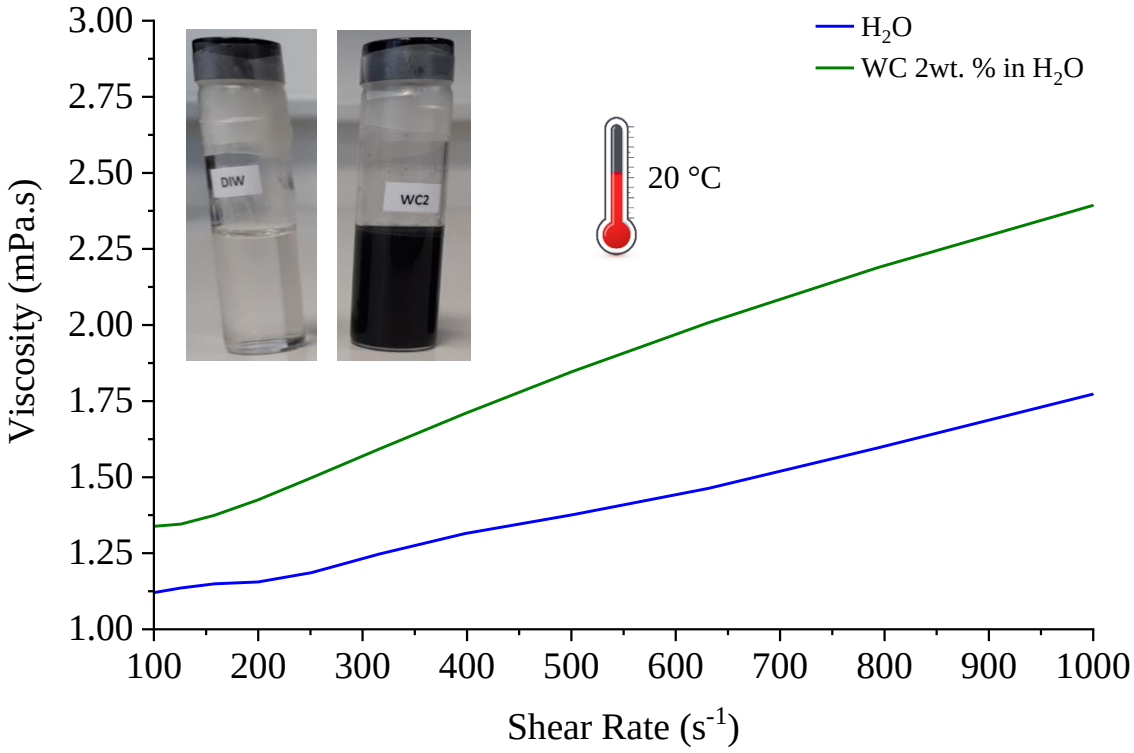


**Figure 7.2** Rheological performance of the colloidal system prepared in this study.

The deposition of this colloid onto powder beds during the printing process was achieved using a vibrating mesh Aerogen© Pro nebuliser. The aerosol jet was projected onto a circular area of 50 mm diameter of the powder bed. Approximately, 0.5 ml of the prepared WC colloid was deposited in each powder layer. Based on the preliminary studies, the evaporation of deposited colloid droplets on the powder was approximately 20 seconds. During printing, the evaporated water was automatically vented out from the printer's processing chamber by the constant 2 l/min argon flow, and any remaining evaporation/condensation was then extracted by the argon circulation/filtration system at its active stages.

4x4x4 $mm^3$ cuboids were printed using an Aconity Mini (Aconity GmbH, Germany) as per coordinates shown in Figure 7.3. The prints were repeated three times for the 316L and WC-316L builds. All prints were performed in an argon atmosphere with the oxygen

level kept below 100 ppm. The laser power, scanning speed, layer thickness, laser spot diameter, hatch distance and hatch translation per layer were set as 160 W, 600 mm/s, 50 µm, 50 µm, 40 µm and 20 µm, respectively. The scanning strategy was based on the unidirectional stripe hatching system. In summary, layer printing cycles consisted of: powder spreading, nanoparticle nebulisation onto powder bed and powder bed selective lasing. This process is illustrated in Figure 7.4.

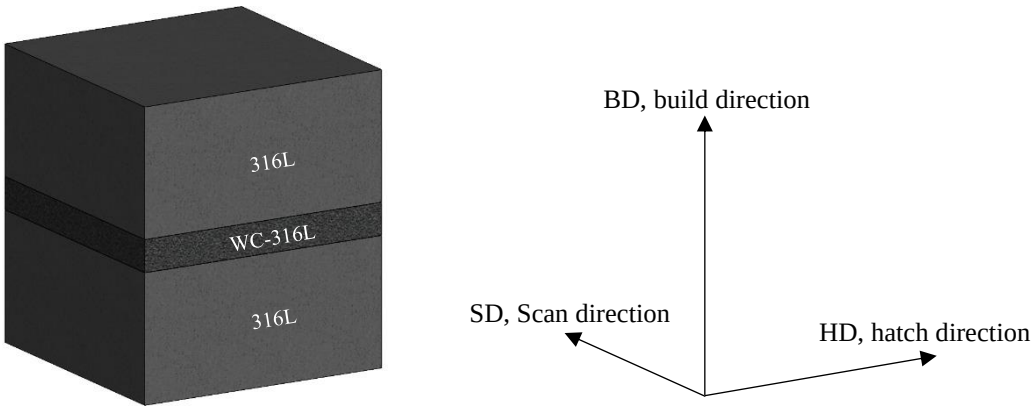


**Figure 7.3** Coordinates of the 4x4x4 mm3 cuboid printed specimens.

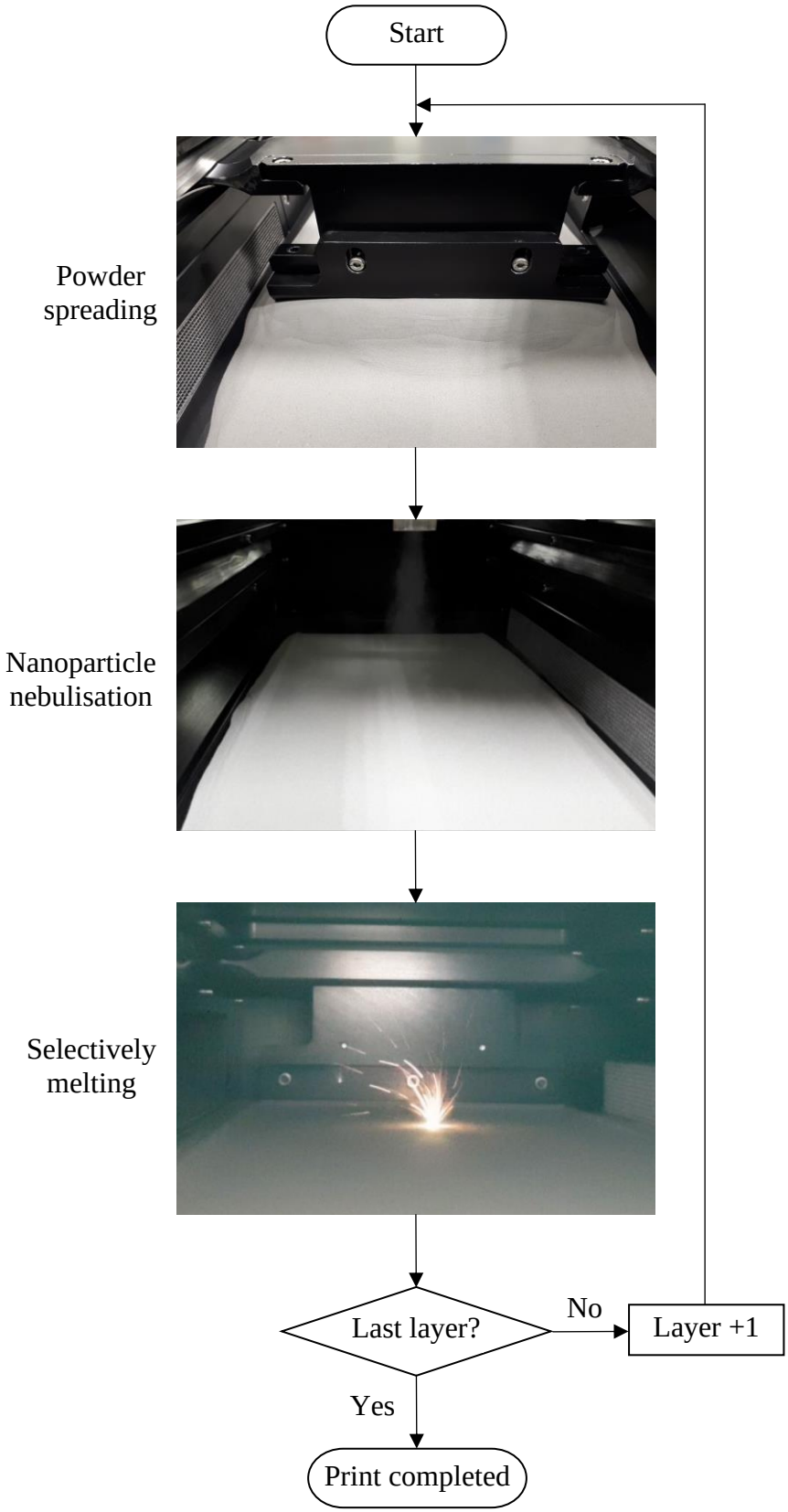


**Figure 7.4** Illustration of the layer printing cycle employed for the manufacturing of WC-316L specimens.

### 7.3.2 Characterisation

The density of the printed specimens was measured with a Micromeritics AccuPyc 1330 helium pycnometer. The mechanical properties were measured via nanoindentation using a Bruker Hysitron TI Premier USA equipped with a standard Berkovich diamond indenter. An array of 10x3 indentations was performed with 10 mN load and intervals of 30 µm. The chemical composition of the specimens was investigated using an energy dispersive x-ray detector coupled into a Hitachi S5500 field emission scanning electron microscope. A JEOL JSM-IT100 scanning electron microscope was used to obtain microstructural images. Phase constituents and crystallographic texture of the specimen were investigated using a triple-axis Jordan Valley Bede D1 high resolution x-ray diffraction system with a copper ($\lambda = 1.5405$ Å) radiation source operated at 45 kV and 40 mA, and a Zeiss Supra 40 field emission scanning electron microscope equipped with a Bruker e-FlashHR electron backscatter diffraction detector. The above characterisations were performed in the plane of the specimens normal to the hatching direction.

## 7.4 Results and Discussion

### 7.4.1 Microstructure

The scanning electron micrographs in Figure 7.5 contrast the microstructure of the specimens. It is worth noting that the resultant solidified microstructures are very similar. The solidification structure is that of columnar grains containing colonies of submicrometric cells separated by low angle grain boundaries. These columnar grains arose due to partial remelting of the previous consolidated layers, as they allowed epitaxial growth. Therefore, this epitaxial growth from the parent grains encouraged the elongation of the columnar grains, which then resulted in a highly textured columnar microstructure, as confirmed later by the electron backscatter diffraction analysis. From the shown plane of view, microstructural features of periodically layer bands are common in L-PBF specimens [753–758]. Accordingly, the behaviour of the layer bands observed in Figure 7.5 resulted from reheat and remelt influence by the consecutive layer deposition. In summary, these layer bands were weak barriers to prevent columnar grain size growth. However, as observed from the high magnification inset micrographs in Figure 7.5, layer bands did effectively break the cellular structures into small colonies. Consequently, neighbouring colonies of cells grew rather misoriented to each other in response to the influence of the layer bands to the local maximum heat flux direction.

Therefore, this randomised orientation of the colonies contrasted with the columnar grains anisotropy. The benefit of this is that such subgrain features could result in strengthening and toughening effects by impeding dislocation movement and altering the course of fracture and propagation paths.

(a)

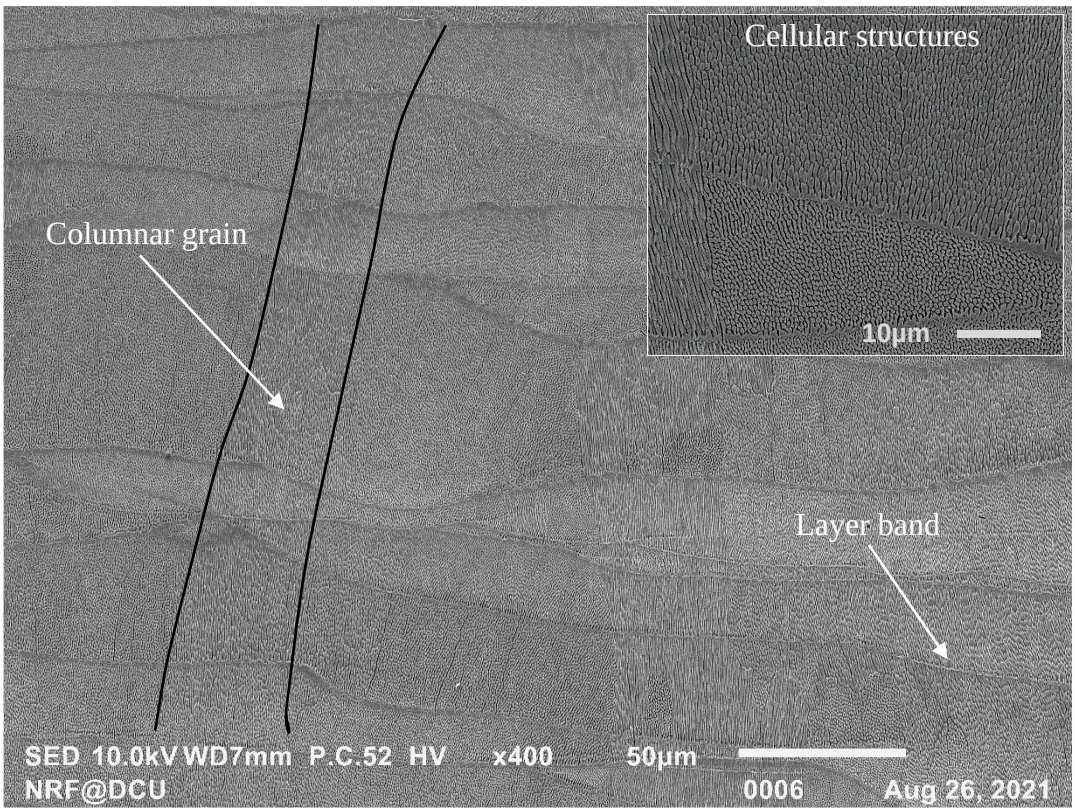


(b)

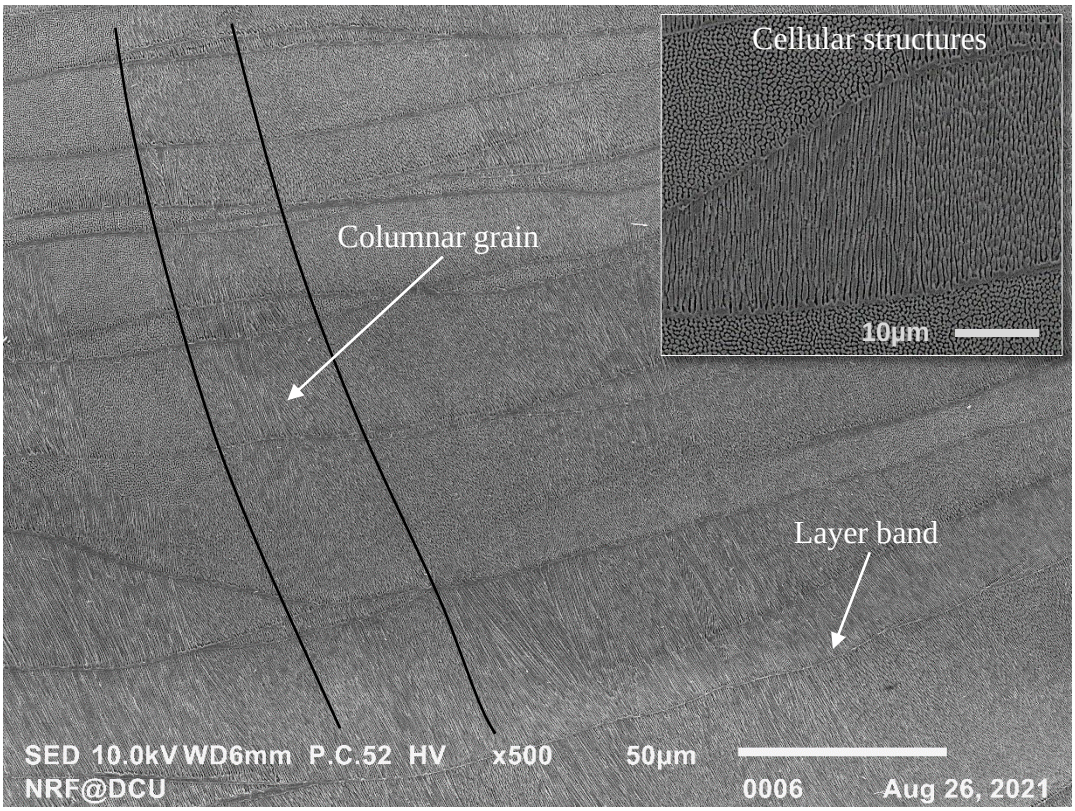


**Figure 7.5** Microstructure viewed from the plane normal to the hatching direction of (a) 316L and (b) WC-316L.

### 7.4.2 Density

The densities of the printed specimens obtained via helium pycnometry are shown in Table 7.1. Based on the true density of 316L, 7.98 g/cm$^3$ [759], it can be concluded that near fully dense specimens were printed in this study. During the printing of the WC-316L specimen, in response to the nebulised material, it is possible that some of the evaporated water molecules got trapped in the molten pools causing hydrogen porosity in the solidified microstructure. However, the difference in density between the specimens was very small, hence this effect could be neglected. Additionally, Figure 7.5 shows no evidence of microstructural porosity or lack of fusion defects in the specimens, and this observation is consistent with the density results of Table 7.1. Therefore, the experimental conditions and input processing parameters used were suitable for printing dense specimens. Such high density values are desired in order to be more effective in improving the properties of materials. Therefore, the printing of a near fully dense WC-316L specimen could enable a significant increase in strength while maintaining the good ductility of the matrix 316L alloy.

**Table 7.1** Density measurement results, n=10.

| Specimen | Density (g/cm$^3$) |
|---|---|
| 316L | 7.95±0.024 |
| WC-316L | 7.92±0.021 |

### 7.4.3 Nanohardness

The mechanical behaviour of the printed specimens was characterised by nanoindentation with a maximum load of 10 mN. The load-depth curves of Figure 7.6(a) shows that the nebulised WC colloid strengthened the 316L matrix, as observed from the reduced indentation depth and steeper unloading slope. This can be ascribed to the existence of a brittle and mechanically hard intermetallic phase. The nanoindentation hardness and modulus measurements are presented in Figure 7.6(b). Typically, the nanohardness of L-PBF 316L is about 3 GPa [760–762]. Therefore, the obtained 3.21 GPa is in relatively good agreement with the literature. The variation in hardness may be attributed to the processing conditions, resultant residuals stress, grain size and crystallographic texture promotion of high dislocation density and formation of a dense network of slip bands. The difference in hardness between the specimens indicates different elastic-plastic

deformation characteristics. Therefore, according to the measured hardnesses, the WC-316L specimen produced less plastic deformation during the nanoindentation testing. This was because the hard WC nanoparticles limited localised plastic deformation. The reduced modulus correlated with the hardness, showing an increase of nearly 12 GPa in the WC-316L specimen, which can be related to the stiffening effect introduced by the WC nanoparticles. In summary, one should note that the overall mechanical improvements were very small. Nevertheless, they do correlate well with the amount of nebulised WC.

(a)

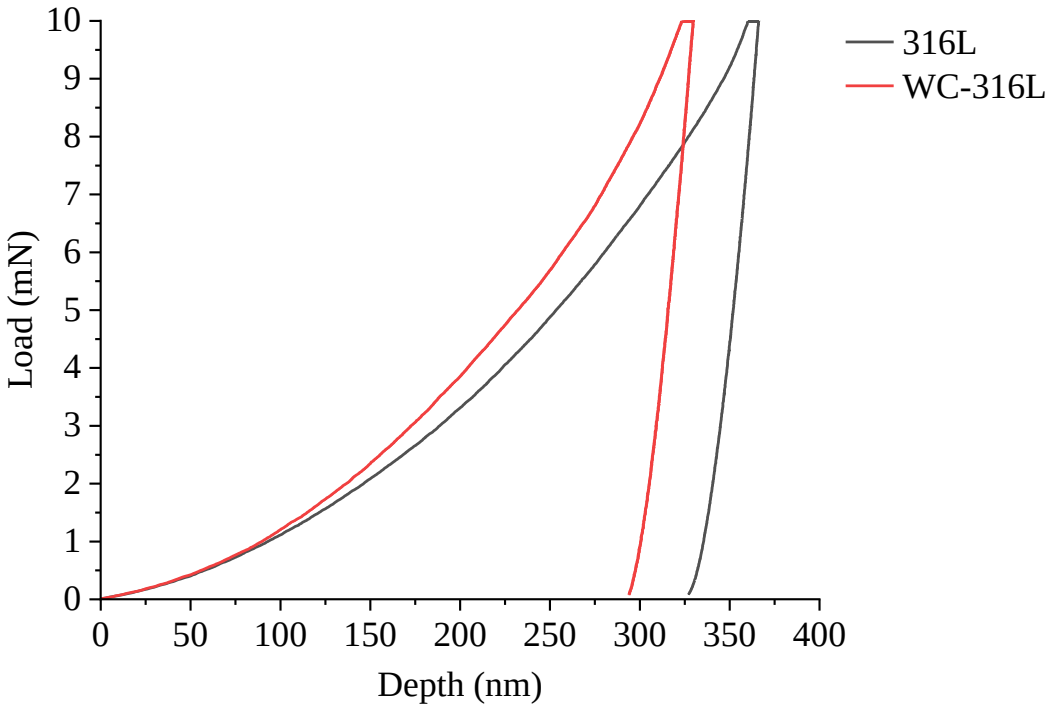


(b)

| Specimen | Nanohardness (GPa) | Reduced Modulus (GPa) |
|---|---|---|
| 316L | $3.21_{\pm 0.12}$ | $195.37_{\pm 2.98}$ |
| WC-316L | $3.51_{\pm 0.08}$ | $207.20_{\pm 5.27}$ |

**Figure 7.6** Mechanical properties of the printed specimens: (a) nanoindentation load-depth curves and (b) nanohardness and reduced modulus; n=30.

### 7.4.4 Chemical Analysis

The results of the elemental analysis performed on the printed specimens are shown in Figure 7.7. Unfortunately, Figure 7.7(a) and (c) reveal tungsten contamination in the 316L composition. After investigations, it was concluded that the supplied powder was contaminated possibly during its atomisation. However, the amount of contamination was

small and the elemental composition of the 316L is now known, therefore it can be contrasted with the elemental composition of the WC-316L specimen. Figure 7.7(b) shows the contribution of the nebulised colloid to the elemental composition of 316L. It is worth noting the increased distribution of tungsten within the analysed area of the WC-316L specimen, which also verifies that a uniform dispersion of WC was achieved via nebulisation. A shortcoming of many conventional manufacturing processes is the high tendency of reinforcing nanoparticles for agglomeration and clustering and the challenge in achieving a uniform dispersion of reinforcement in metal matrix composites [763,764]. Therefore, in-situ nebulisation of reinforcing nanoparticles within the L-PBF process proved to be an alternative solution to these problems.

(a)

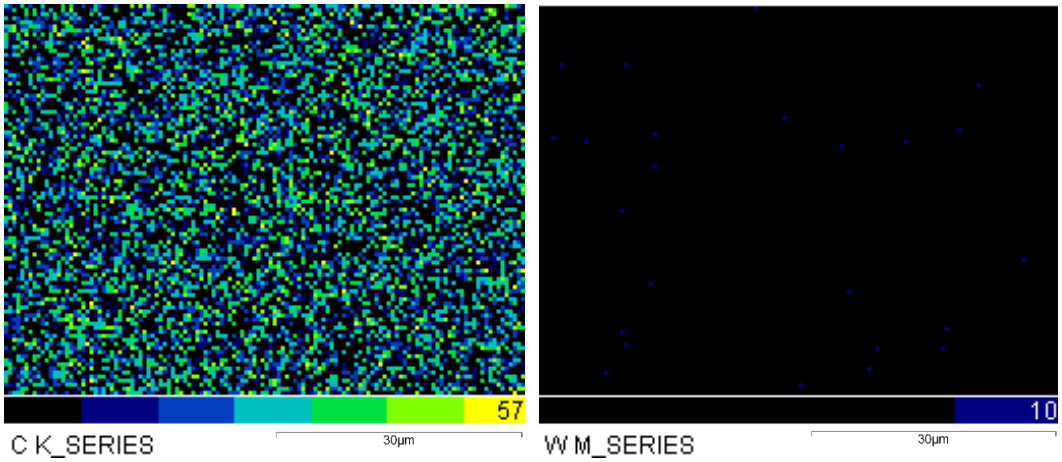


(b)

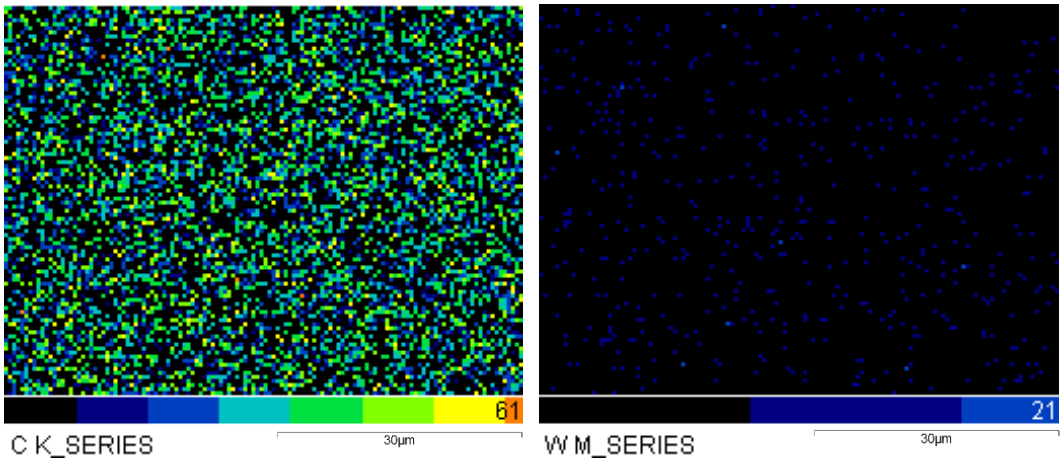


(c)

| Element | 316L | WC-316L |
|---|---|---|
| C (wt. %) | 5.5 | 5.59 |
| W (wt. %) | 0.22 | 0.38 |
| Fe (wt. %) | 64.75 | 63.05 |
| Cr (wt. %) | 15.85 | 16.73 |
| Ni (wt. %) | 10.66 | 11.18 |
| Mo (wt. %) | 2.06 | 1.96 |
| Mn (wt. %) | 0.96 | 1.11 |

**Figure 7.7** Chemical composition of the specimens with mapping of carbon and tungsten for (a) 316L and (b) WC-316L, and (c) quantified results.

### 7.4.5 Crystallography

#### 7.4.5.1 Phase

Constituent phase identification using X-ray diffraction revealed an intricate multiphase mixture in the specimens, see Figure 7.8. Conventionally and additively processed austenitic stainless steels are very often reported as being influenced by precipitation reactions [744,765,766]. The formation of austenite in 316L depends on cooling rate and chemical composition, and if the Cr/Ni ratio is low then the possibility of iron-silicon precipitation is suppressed [767]. The precipitated hard $Fe_2Si$ phase plays a crucial role in determining the material response. However, while improving hardness and wear, corrosion, fatigue and fracture resistance of the specimens could be compromised by the brittle intermetallic $Fe_2Si$ precipitates [768–770]. An evident diffraction peak of SiC was observed in the specimens' spectrum and confirmed by the JCPDS card 89-1396. It is therefore clear that the energy applied to fuse the 316L powder also triggered an exothermic chemical reaction which produced new chemical compounds and also possibly generated enough thermal energy for the propagation of more chemical reactions. Therefore, it is most likely that the formation of SiC was achieved via a solution-precipitation mechanism from the silicon and carbon atoms in the 316L melt. In-situ formed reinforcements are thermodynamically stable at the matrix, leading to less degradation in elevated temperature applications. Additionally, the grains are finer in size and their distribution in the matrix is more uniform yielding better mechanical properties and the matrix-reinforcement interfaces are clean, resulting in a strong interfacial bonding [729]. The existence of WC was confirmed in both specimens, hence it could be concluded that the tungsten contamination in the 316L powder reacted with carbon during the L-PBF process and formed WC precipitates. Also, there is no evidence that the nebulised WC colloid dissolved and formed other tungsten compounds with the matrix elements. Therefore, the x-ray diffraction analysis revealed $Fe_2Si$, SiC and WC reinforcing phases in the specimens. This then implies that discrepancies in mechanical properties between specimens resulted from the nebulised tungsten nanoparticles.

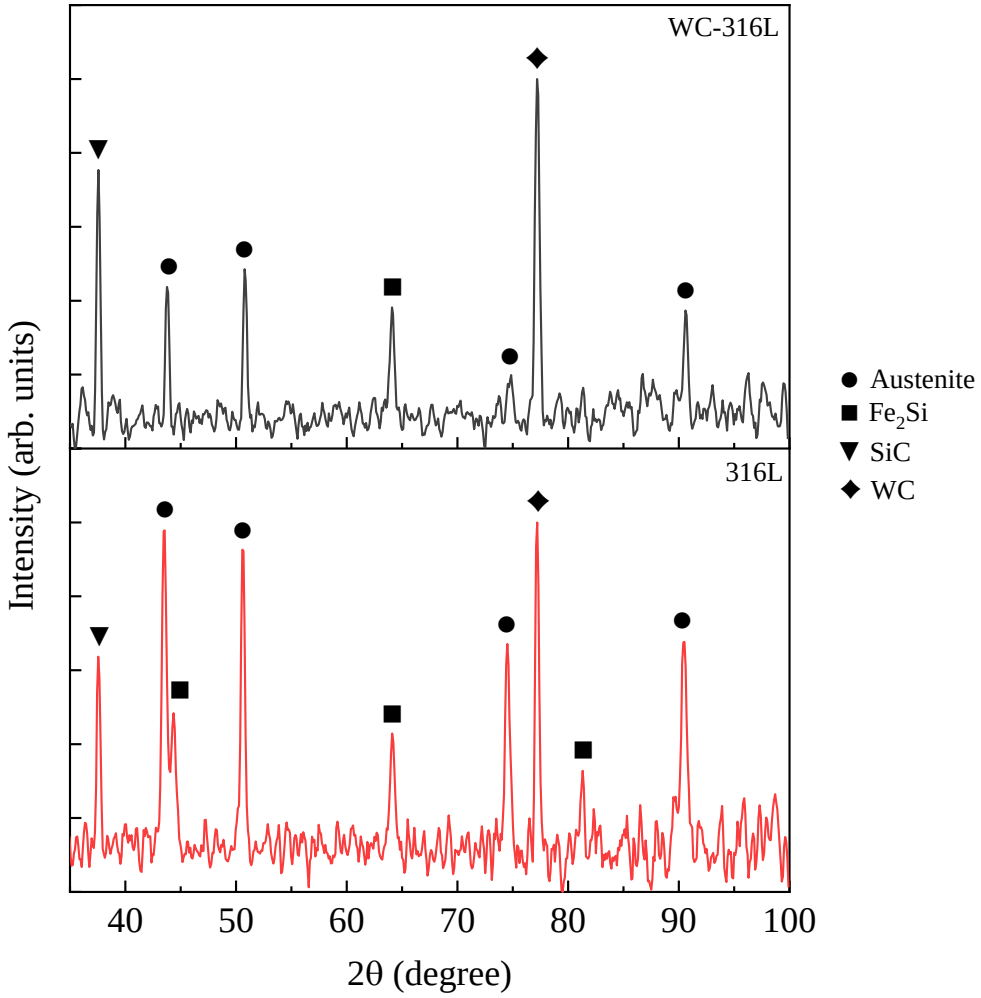


**Figure 7.8** X-ray diffraction patterns of the printed specimens.

#### 7.4.5.2 Texture

Representative electron backscatter diffraction orientation map, pole figure and inverse pole figure of the 316L and WC-316L specimens are shown in Figure 7.9. Large irregular columnar grains going through several powder layers are visible, which indicate that the solidification occurred by epitaxial growth. The 316L specimen exhibited a rotated {100} cube texture component with a combination of <001> and <101> orientation aligned nearly parallel to the build and scan directions. This may be visualised in the grain map of Figure 7.9a where most of the grains appear to be inclined about -30° with respect to the build direction. In contrast, it was confirmed the development of a strong {100} <001> cube texture in the WC-316L specimen. In fact, it is worth noting the high intensity in <001> in the respective inverse pole figure which reflects on the observed grains in Figure 7.9b. Therefore, in this regard, the growth of highly oriented columnar grain

structures in the build direction corresponded to the existence of a highly uniform maximum temperature gradient within the meltpools of the specimen WC-316L.

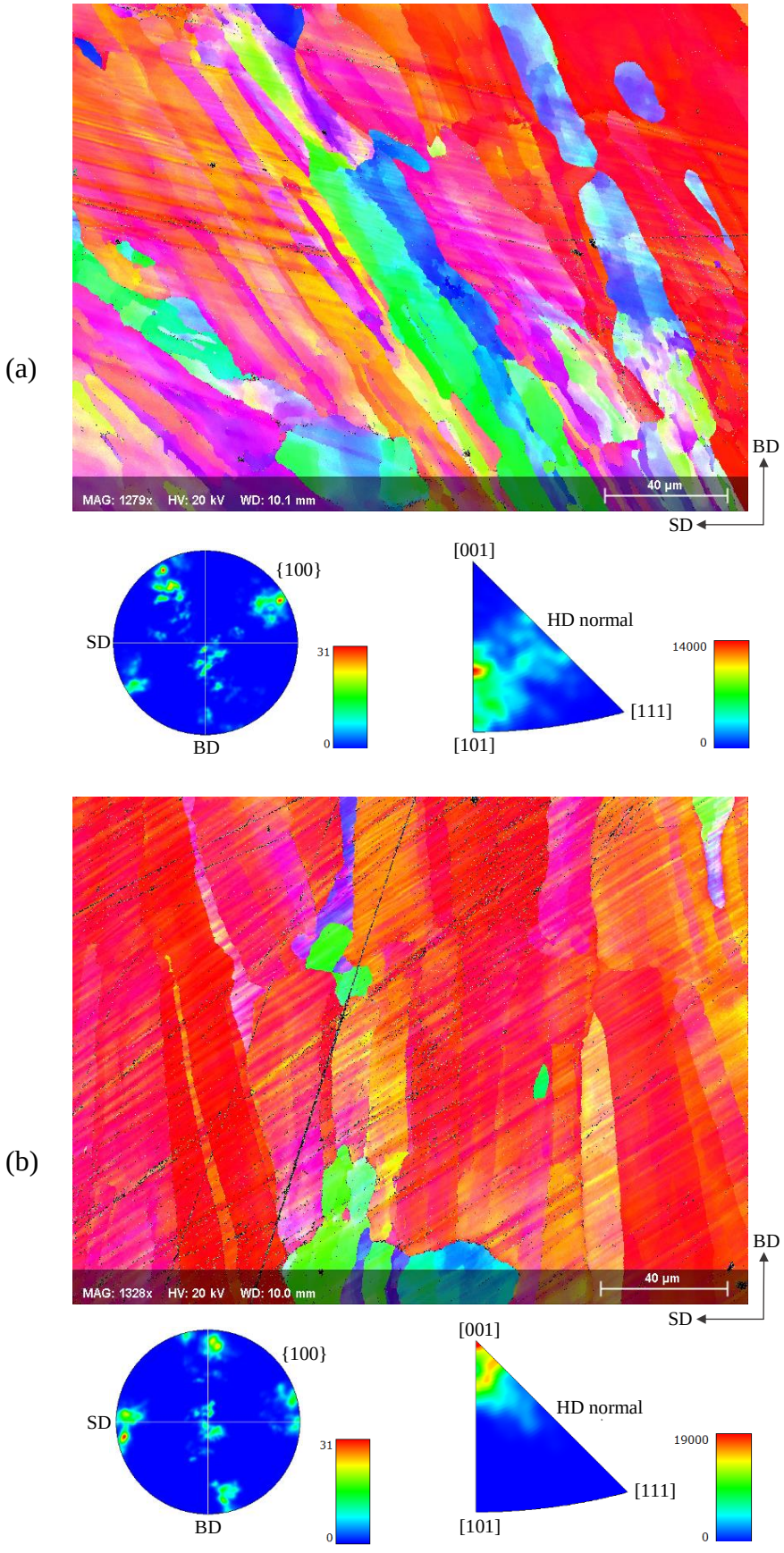


**Figure 7.9** Grain map and texture of (a) 316L and (b) WC-316L.

To understand the reasons for the observed discrepancies in the crystallographic textures, single track scanning experiments were carried out. Figure 7.10 contrasts the effect of colloid nebulisation on single track formation. During the printing of the WC-316L specimens, it is possible that the native porosity within the 316L powder beds trapped colloid droplets preventing the full evaporation of the colloid medium (deionised water). Therefore, residual water molecules could have interacted with the laser beam and also ended up being mixed with the molten metal, and consequently altered the meltpool cross-sectional profile in relation to those of the 316L specimens. The literature suggests that increasing the laser input energy or the efficiency of the photonic absorption by the irradiated material reduces the contact angle and increases the depth and width of solidified tracks [771–773]. It is also known that residual water molecules and water vapour can cause radiation attenuation of the laser beam [774–776]. Additionally, the upward speed of the ejected plume flux is intensified as water vapour is merged with the existing metal vapour. This then introduces a low pressure zone near the melpool and thereupon the Bernoulli effect-driven gas flow. Consequently, several powder particles from the powder bed are entrained in the convective gas flow and draw into and become consolidated with the meltpool [777,778]. Therefore, it was concluded that the shallowing of the meltpool shown in Figure 7.10b was due to the laser beam intensity attenuation resulting from residual water molecules, and the seen larger width was due to the addition of material consolidation to the meltpool. In agreement with the presented study, it was reported elsewhere that shallow and wide meltpools promote the formation of <001> texture [779]. Additionally, both of the tracks showed normal meltpool geometries dominated by a conductive mode of heat transfer [780]. In this regard, the conductive mode characterised stable meltpools with low depth to width ratios which resulted in minimal porosity defects in the microstructure of the specimens.

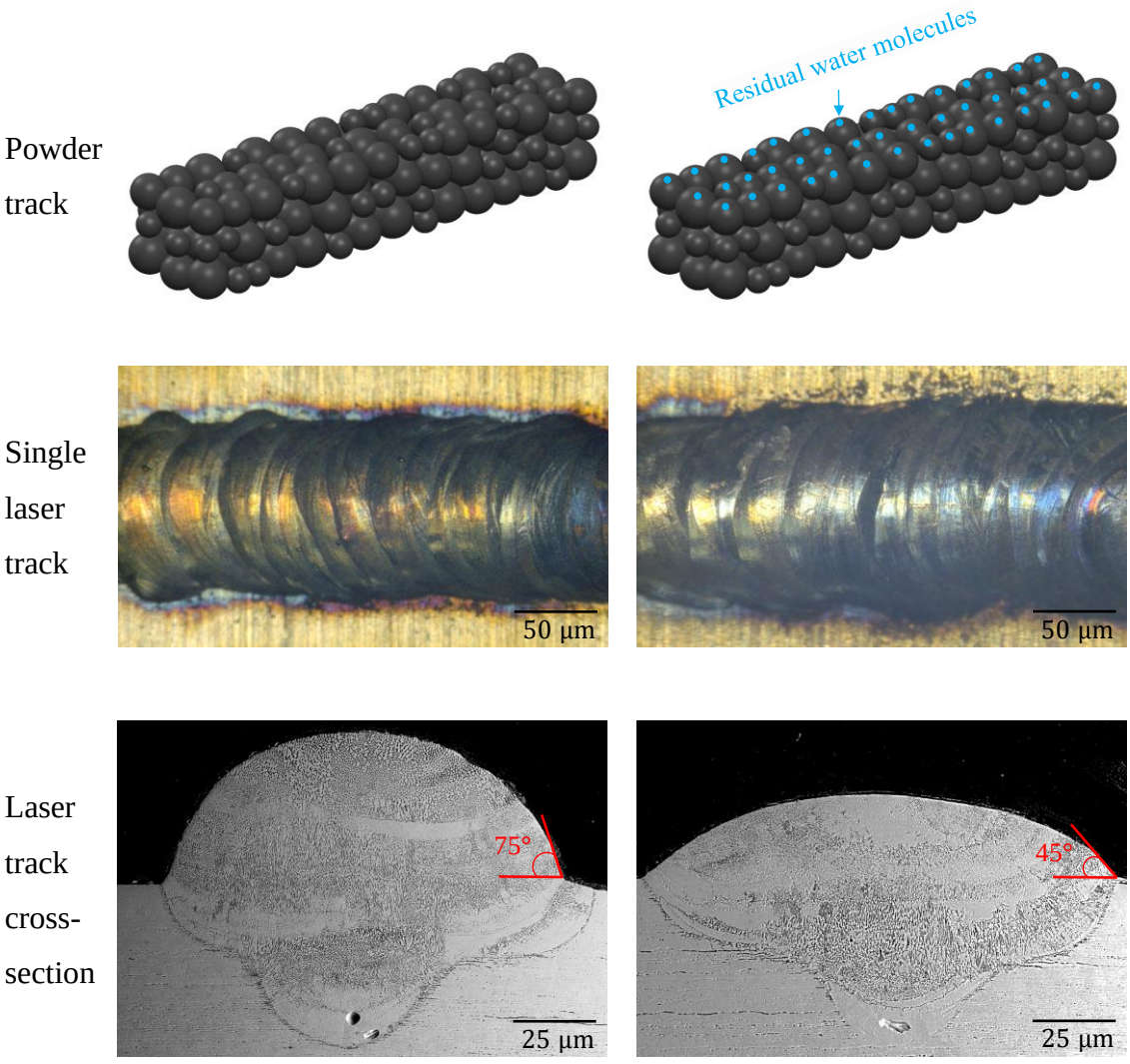


**Figure 7.10** Cross-section of single tracks formed (a) without and (b) with colloid nebulisation.

## 7.5 Discussion

### 7.5.1 Current Achievements

This study successfully deposited colloidal feedstock of WC onto powder beds during the laser-powder bed fusion of 316L. The results presented in the previous section demonstrated that the incorporation of material nebulisation to laser-powder bed fusion is a promising method for tailoring and improving the properties of printed specimens. Additionally, this new method has shown a clear potential for the development of metal matrix composites within a single step production process.

Here, all the specimens presented a nearly full dense microstructure with values close to the true density of 316L. The higher hardness and modulus of the WC-316L specimen resulted from the Orowan strengthening mechanism. In this regard, the presence of the reinforcing particles promoted deformation resistance by preventing dislocation motion and propagation. The difference in meltpool shapes was the origin for developing different crystallographic textures. In response to its shallowed and widened meltpools, grains in the WC-316L specimen grew highly parallel to the build direction and the resulting texture was then strong in the <001> direction. Therefore, as the formation of a strong texture is an effective way of improving strength [781], the mechanical improvements found were ascribed to the presence of the reinforcing particles and the resultant crystallographic texture.

### 7.5.2 Methodological Limitations

One of the limitations of using the nebulisation route was its low volume nanoparticle deposition capability. The 2wt. % colloid concentration employed was the highest concentration capable of maintaining a stable and high throughput rate of droplets. Colloids prepared with higher concentrations were observed to be unstable on account of nanoparticle aggregation and sedimentation. Additionally, the use of stabilisers was found unfeasible for the given application as these altered the viscosity of the colloid, which the nebuliser was sensitive to. Also, it was found that the nebulisation of a higher volume of colloid per layer than that used in this study would inhibit the formation of quality powder beds, see Figure 7.11. This was because the powder bed became saturated with the colloid medium and hence increased the cohesive and adhesive forces between particles. Then, as a result, the forming of the consecutive powder bed layer removed patches of powder from the previous powder bed layer. It is also worth noting that the quality of the powder bed near the consolidated powder was unaffected. Since this area is at higher temperature, a more efficient evaporation of the colloid medium was here achieved. Based on the aforementioned limitations and challenges, future work should use stable and highly concentrated colloids (> 5 wt. %) synthesised from low density ceramics such as silicon carbide, boron carbide, aluminium oxide and titanium carbide. Additionally, it is recommended the use of a printer which is equipped with a counter-rotating roller spreading system as the compaction of powder could in this case result in higher powder bed qualities.

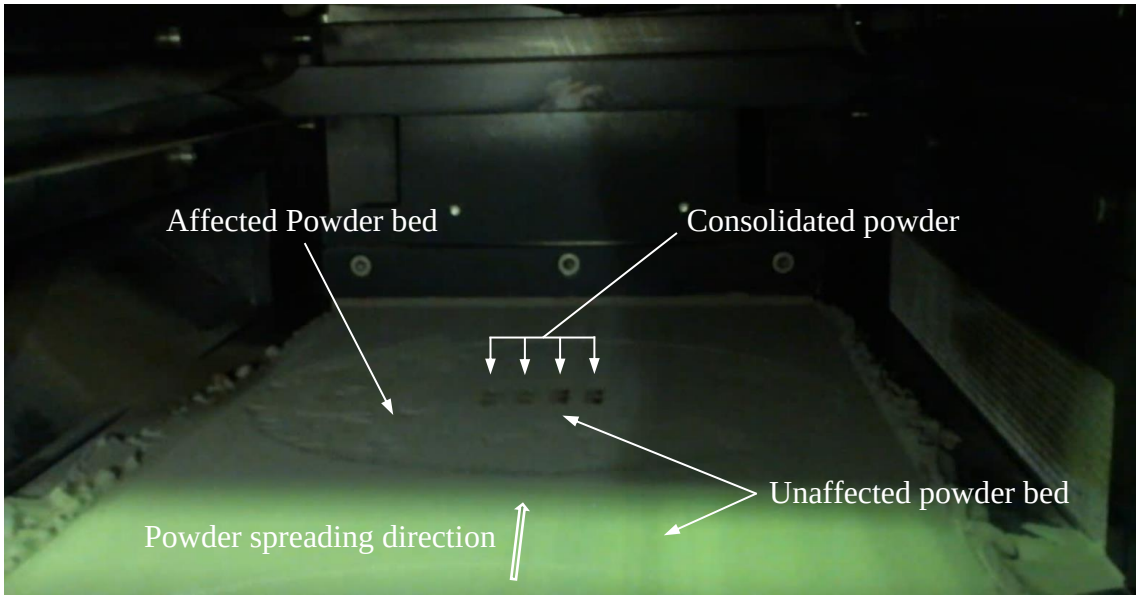


**Figure 7.11** Picture of the detrimental effect on the powder bed when an excessive volume of colloid is deposited per layer.

### 7.5.3 Application Prospects of Material Nebulisation in Laser-Powder Bed Fusion

To date only powdered forms of feedstock materials have been used within the laser-powder bed fusion process. In order to open a window for the development of new technological materials, the nebulisation of colloid feedstock onto powder beds emerged as a potential solution for improving and tailoring the properties of laser-powder bed fused components. The presented multi-feedstock material printing methodology proved to be capable of uniformly dispensing nanoparticles onto powder beds and controlling crystallographic texture. This methodology also showed a unique approach to metal matrix composite fabrication which advantages should be further explored.

The following are examples of what else material nebulisation in laser-powder bed fusion could be used for.

(1) The nebulisation of deionised water could be used for the nucleation and growth of hydrogen gas bubbles which then can be trapped by the process solidification front [782]. This could be particularly useful for printing functional graded porous structures such as for orthopaedic implants.

(2) Grain fining agents such as colloids of $Fe_{0.35}C_{0.15}Ti_{0.25}Nb_{0.25}$ could be nebulised onto metallic powder beds during the laser-powder bed fusion process [783–785].

As there is a growing demand for materials with strengths greater than those found in currently available alloys [786,787], the aforementioned should be considered.

(3) Colloids such as those of graphene, silver and copper could be nebulised onto powder beds to increase the electrical and thermal conductivity of laser-powder bed fused components [788–791]. With the recent electric vehicle revolution, this could be advantageous towards improving the current efficiency of electric vehicles.

(4) When laser-powder bed fusing dissimilar materials for example metals and ceramics where wetting may be an issue or when the melting temperature needs to be lowered in order to preserve the processing material properties, then a colloid intermediary bonding layer containing for example aluminium, copper, silver, nickel or tin compounds could be nebulised onto the powder beds [792–795].

(5) Silver, copper and aluminium are the most challenging materials for laser-powder bed fusion due to their low optical absorption in the near infrared [796,797]. Based on the literature, the nebulisation of carbon and iron colloids could be used to increase the interactions between the laser beam and powder bed particles [798–801].

(6) Laser-powder bed fusion has also recently been considered for repairing high value components such as damaged or worn gas turbine blades and high performance tools [802–805]. However, the strength at the repaired zone depends on the interfacial integrity between the component and the new added material. Therefore, in-situ nebulisation of flux to dissolve oxides from the surface to be repaired and the nebulisation of chemical compounds to purify meltpools should be implemented in the laser-powder bed fusion repair applications [806,807].

### 7.6 Conclusions

This article presents a multi-feedstock material printing methodology for the established laser-powder bed fusion manufacturing technique. In summary, tungsten carbide nanoparticles were uniformly dispersed onto powder beds of stainless steel 316L via colloids nebulisation during the laser-powder bed fusion process.

Nearly full dense microstructures with values close to the true density of 316L were obtained. The nebulised tungsten carbide nanoparticles strengthened the 316L matrix which increased the nanohardness and modulus of the specimens. Overall, the achieved mechanical improvements were small, but they do correspond with the small amount of nebulised tungsten carbide colloid.

Surprisingly, the colloid medium promoted positive effects on the resulting microstructures. This was evidenced by the stable meltpools which were dominated by the conductive mode of heat transfer. The consistent low depth to width ratio of the meltpools played an important role in the resulting microstructure. The most interesting fact was that it led to the growth of grains highly parallel to the build direction and so the resulting texture was very strong in the <001> direction.

To conclude, this study proved that it is feasible to deposit nanoparticles onto powder beds via colloid nebulisation. Additionally, this methodology showed a clear potential for the development of metal matrix composites with a single step production process. Other possible applications of material nebulisation in laser-powder bed fusion together with recommendations can be found within this article.

# Chapter 8

# Concluding Remarks

## 8.1 Conclusions

In achieving the listed research aims and objectives, several detailed investigations were executed to gain a comprehensive understanding and to accomplish advancements in the L-PBF of MMCs. The original contributions to the existing literature which resulted from this PhD project are summarised as follows:

I. The location parameter was identified as being a contributor to the lack of repeatability that has been reported for the L-PBF manufacturing process. The variation in part-property repeatability was due to variations in microstructure and defects induced for example from particle size segregation and spatter. Therefore, the location of the part being printed on the build platform may need to be fixed for multiple builds in order to achieve acceptable repeatability. Additionally, as variation in the final microstructure characteristics and mechanical performance of printed parts within a build also exists due to the location parameter, the location is a parameter that could be exploited when tailoring the final microstructure characteristics and maximising mechanical performance of printed parts.

II. The technique employed for developing the SiC/316L powder was successfully optimised. The resultant homogeneous powder mixture was composed of a uniform and consistent layer of nano-sized SiC particles decorating the micro-sized 316L particles. The flowability of this powder was characterised by high levels of repeatability, a very stable rheology and a relative low flow rate sensitivity. The particles spherical morphology, the narrow range of particle size distribution and also the coating of SiC particles on the 316L particles were found to act in this case as a solid lubricant providing for the powder a high degree of flowability.

III. Powder spreading is a crucial step in the L-PBF, which controls the quality of powder bed and consequently affects the quality of printed parts. Powder bed topography is influenced by the powder morphology, spreading conditions and the particles net interaction. Low powder spreading velocities favour powder bed uniformity, and this is maximised with increasing particle sphericity and

smoothness. Powders with a wide particle distribution containing large number of fine particles enabled formation of uniform and dense powder beds, however such powders were found to be more affected by segregation, which is a source of part property variability. The uniformity and homogeneity of consecutive layers is very complicated to predict well. For this, the relationship of the in-printing characteristics, including scanned geometry, to powder spreadability needs to be considered.

IV. A hatching system based on a sine wave was successfully developed and employed in the printing of MMCs. The samples printed using the sinusoidal hatching exhibited an enhanced yield strength and ductility owing to the resultant grain refinement and texture. The dabber mode formation of material tracks promoted the growth of highly oriented intragranular cellular structures. Apart from playing an important role in improving hardness, this control over the cellular growth could also be used towards improving composite toughness. Additionally, besides improving composite performance, the sinusoidal hatching strategy was also effective in reducing manufacturing lead time and process energy consumption in response to its natural high scanning speed and low laser power requirements.

V. A multi-feedstock material printing methodology for L-PBF of MMCs was implemented. Utilising colloid nebulisation, WC nanoparticles were successfully deposited onto powder beds of stainless steel 316L during the L-PBF process. By this means, a controlled volume of WC nanoparticles was uniformly dispersed onto powder beds under the inert processing chamber atmosphere. As a result, specimens printed with this methodology showed an increase in strength. Similarly, the colloid medium played an important role in the resulting microstructures. It led to the formation of consistent and stable meltpools and a strong crystallographic texture.

The flow diagram of Figure 8.1 provides a graphical visualisation of the evolution of this PhD work and how each chapter fits together and was integrated to impact the state of the art of MMCs production.

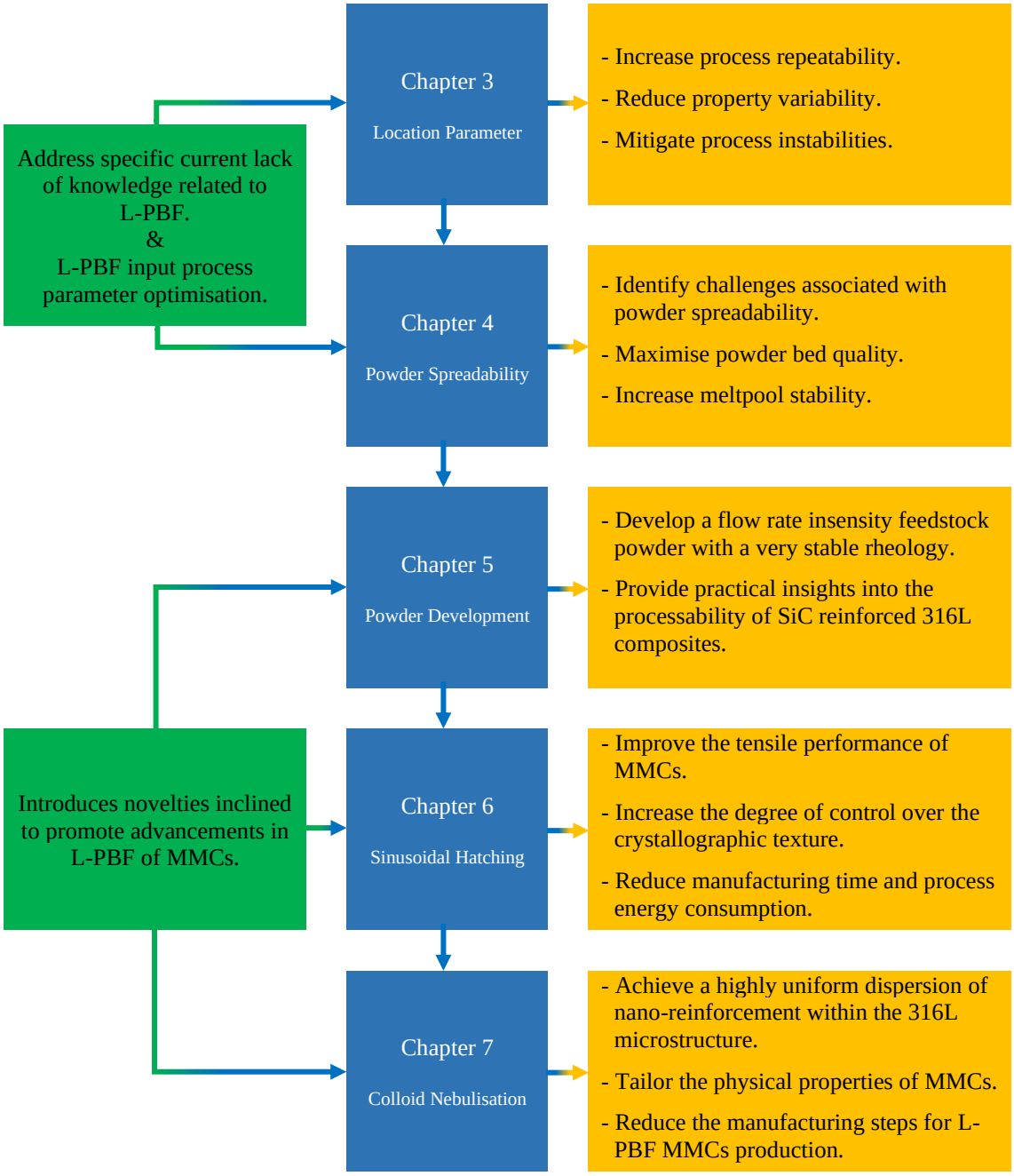


**Figure 8.1** Illustration of this PhD work evolution and how each chapter was integrated to impact the state of the art of MMCs production.

## 8.2 Significance and Impact of the Research

This thesis is expected to greatly enhance the understanding of powder feedstock requirements for L-PBF of MMCs. With an end goal focused on the mitigation of part defects, various aspects of powder flowability and powder spreadability concerning the maximisation of powder bed qualities were investigated. Therefore, the resulting findings

will contribute significantly to the exiting knowledge of L-PBF of MMCs and other materials.

Commonly overlooked and assumed to have little or no effect on the overall part properties, the effect of the location parameter on the final part properties was herein systematically studied. The importance of considering the location parameter in the experimental design was examined in order to achieve acceptable repeatability. Additionally, the results suggested that part variability within a build is unavoidable based on the location parameter. These therefore imply that batch printing may be challenging depending on the related industry sector requirements. The results presented on part location in this thesis help to build a basic knowledge of the source of variability in L-PBF and thus can provide valuable information when designing printing jobs.

For the first time, a sinusoidal hatching system was introduced to the L-PBF technology. This scanning methodology was specifically developed to help advancement in the production of MMCs via L-PBF. The developed method was proven to be capable of contributing to improvements in the hardness, strength and ductility of the produced composites. Apart from improving the orientation control over the cellular growth, the sinusoidal scanning also showed a clear potential to reduce manufacturing energy consumption and time to market. For this reason, the sinusoidal hatching system is viewed as a feasible solution capable of addressing several of the current limitations of L-PBF and in the production of MMCs.

A methodology for dispersing colloidal nanoparticles onto powder beds was introduced. Collectively, the results demonstrated that the incorporation of material nebulisation into L-PBF is a promising method for tailoring and improving the properties of printed parts. Additionally, this methodology showed a clear potential for the development of MMCs within a single step production process. This is also a particularly important advancement as it reduces potential health and environment hazards associated with the handling of nanomaterials for L-PBF of MMCs.

The research studies presented in this thesis help to pave the path towards addressing several endemic issues concerning mechanical performance and cost effectiveness of MMCs. As there is an increasing demand for materials with superior performance, the reported novelties are worthy of further research.

### 8.3 Recommendations for Further Research

Although the body of work presented shows important advancements in the L-PBF of MMCs, there still remain critical areas that have not been addressed through these studies. Therefore, the following recommendations are proposed for future research.

- The mechanical properties of the MMCs printed using the sinusoidal hatching system were negatively affected by porosities and cracks. Future research should therefore identify the source of theses defects and apply mitigation measures to eradicate them from the composites microstructure. In-situ process monitoring of temperature and melt flow as well as build substrate preheating for mitigation of crack formation and residual stress are recommended. Additionally, the literature demonstrated that it is possible to control grain orientation as per hatching patterns. Therefore, it would be interesting to examine the implications of sinusoidally oriented grains on the ductility of MMCs.

- The volume of nanoparticles deposited per layer was limited by the nebuliser capability and colloid stability. Therefore, the use of a higher throughput nebuliser is recommended. Also, the deposition of highly stable and concentrated colloids (> 5 wt. %) synthesised from low density ceramics such as silicon carbide, boron carbide, aluminium oxide and titanium carbide should be exploited. A printer equipped with a counter-rotating roller spreading system could be advantageous, as the compaction of powder could in this case result in more uniform powder bed qualities [808]. Preheating the build substrate to 100 °C should be expected to accelerate the evaporation of the colloid medium and make the entire printing process more efficient; thus making this an interesting route also for future studies.

## References


[1] Davim, J. P., 2014, *Metal Matrix Composites: Materials, Manufacturing and Engineering*, Walter de Gruyter GmbH & Co KG.

[2] Clyne, T. W., and Withers, P. J., 1995, *An Introduction to Metal Matrix Composites*, Cambridge University Press.

[3] Campbell, F. C., and ASM International, 2010, *Structural Composite Materials*, A S M International, Materials Park, United States.

[4] Taya, M., and Richard J., A., 2016, *Metal Matrix Composites: Thermomechanical Behaviour*, Elsevier.

[5] Qian, M., and Froes, F. H., 2015, *Titanium Powder Metallurgy: Science, Technology and Applications*, Butterworth-Heinemann.

[6] El-Eskandarany, M. S., 2015, *Mechanical Alloying: Nanotechnology, Materials Science and Powder Metallurgy*, Elsevier.

[7] Chang, I., and Zhao, Y., 2013, *Advances in Powder Metallurgy: Properties, Processing and Applications*, Elsevier.

[8] Upadhyaya, G. S., 1997, *Powder Metallurgy Technology*, Cambridge International Science Publishing.

[9] Jeon, T. J., Hwang, T. W., Yun, H. J., VanTyne, C. J., and Moon, Y. H., 2018, "Control of Porosity in Parts Produced by a Direct Laser Melting Process," Appl. Sci., 8(12).

[10] Gibson, I., Rosen, D., and Stucker, B., 2014, *Additive Manufacturing Technologies: 3D Printing, Rapid Prototyping, and Direct Digital Manufacturing*, Springer.

[11] Brandt, M., 2017, *Laser Additive Manufacturing: Materials, Design, Technologies, and Applications*, Woodhead Publishing.

[12] Gunenthiram, V., Peyre, P., Schneider, M., Dal, M., Coste, F., and Fabbro, R., 2017, "Analysis of Laser Melt Pool Powder Bed Interaction during the Selective Laser Melting of a Stainless Steel," J. Laser Appl., 29(2), p. Article number 022303.

[13] Yang, Y., Gu, D., Dai, D., and Ma, C., 2018, "Laser Energy Absorption Behavior of Powder Particles Using Ray Tracing Method during Selective Laser Melting Additive Manufacturing of Aluminum Alloy," Mater. Des., 143, pp. 12–19.

[14] Persson, F., Eliasson, A., and Jönsson, P., 2012, "Prediction of Particle Size for Water Atomised Metal Powders: Parameter Study," Powder Metall., 55(1), pp. 45–53.

[15] Boisvert, M., Christopherson, D., Beaulieu, P., and L'Espérance, G., 2017, "Treatment of Ferrous Melts for the Improvement of the Sphericity of Water Atomized Powders," Mater. Des., 116, pp. 644–655.

[16] Popovich, A., and Sufiiarov, V., 2016, "Metal Powder Additive Manufacturing," *New Trends in 3D Printing*, IntechOpen, Croatia, pp. 215–236.

[17] Dawes, J., Bowerman, R., and Trepleton, R., 2015, "Introduction to the Additive Manufacturing Powder Metallurgy Supply Chain," Johns. Matthey, 59(3), pp. 243–256.

[18] Rausch, A. M., Küng, V. E., Pobel, C., Markl, M., and Körner, C., 2017, "Predictive Simulation of Process Windows for Powder Bed Fusion Additive Manufacturing: Influence of the Powder Bulk Density," Materials, 10(10).

[19] Rausch, A. M., Markl, M., and Körner, C., 2018, "Predictive Simulation of Process Windows for Powder Bed Fusion Additive Manufacturing: Influence of the Powder Size Distribution," Comput. Math. Appl.

[20] Spierings, A. B., and Levy, G., 2009, "Comparison of Density of Stainless Steel 316L Parts Produced with Selective Laser Melting Using Different Powder Grades," *Solid Freeform Fabrication Proceedings*, University of Texas, Austin, pp. 342–353.
[21] Simchi, A., 2004, "The Role of Particle Size on the Laser Sintering of Iron Powder," Metall. Mater. Trans. B, 35(5), pp. 937–948.
[22] Ganeriwala, R. K., 2015, "Multiphysics Modeling of Selective Laser Sintering/Melting," PhD thesis, University of California.
[23] Riou, A., Aumund, C., and Erasteel, O., 2015, "Introduction to Additive Manufacturing Technology: A Guide for Designers and Engineers," Eur. Powder Metall. Assoc., 1st Edition, pp. 01–44.
[24] Gurtler, J., Karg, M., Dobler, M., Tzivilsky, I., and schmidt, M., 2014, "Influence of Powder Distribution on Process Stability in Laser Beam Melting: Analysis of Melt Pool Dynamics by Numerical Simulations," *25th, Annual International Solid Freeform Fabrication Symposium*, Solid Freeform Fabrication, Austin, pp. 1099–1117.
[25] Han, Q., Setchi, R., and Evans, S. L., 2016, "Synthesis and Characterisation of Advanced Ball-Milled Al-Al2O3 Nanocomposites for Selective Laser Melting," Powder Technol., 297, pp. 183–192.
[26] Džugan, J., and Nový, Z., 2017, "Powder Application in Additive Manufacturing of Metallic Parts," Powder Metall. - Fundam. Case Stud., pp. 182–198.
[27] Jacob, G., Donmez, A., Slotwinski, J., and Moylan, S., 2016, "Measurement of Powder Bed Density in Powder Bed Fusion Additive Manufacturing Processes," Meas. Sci. Technol., 27(11).
[28] Cacace, S., Demir, A. G., and Semeraro, Q., 2017, "Densification Mechanism for Different Types of Stainless Steel Powders in Selective Laser Melting," Procedia CIRP, 62, pp. 475–480.
[29] Gu, D., Xia, M., and Dai, D., 2019, "On the Role of Powder Flow Behavior in Fluid Thermodynamics and Laser Processability of Ni-Based Composites by Selective Laser Melting," Int. J. Mach. Tools Manuf., 137, pp. 67–78.
[30] Vock, S., Klöden, B., Kirchner, A., Weißgärber, T., and Kieback, B., 2019, "Powders for Powder Bed Fusion: A Review," Prog. Addit. Manuf.
[31] Groarke, R., Danilenkoff, C., Karam, S., McCarthy, E., Michel, B., Mussatto, A., Sloane, J., O' Neill, A., Raghavendra, R., and Brabazon, D., 2020, "316L Stainless Steel Powders for Additive Manufacturing: Relationships of Powder Rheology, Size, Size Distribution to Part Properties," Materials, 13(23).
[32] Prescott, J., and Barnum, R. A., 2000, "On Powder Flowability," Pharm. Technol., 24, pp. 60–84.
[33] Steen, W., 1991, *Laser Material Processing*, Springer-Verlag, London.
[34] Brown, M. S., and Arnold, C. B., 2010, "Fundamentals of Laser-Material Interaction and Application to Multiscale Surface Modification," *Laser Precision Microfabrication*, K. Sugioka, M. Meunier, and A. Piqué, eds., Springer Berlin Heidelberg, Berlin, Heidelberg, pp. 91–120.
[35] Kruth, J.-P., Levy, G., Klocke, F., and Childs, T. H. C., 2007, "Consolidation Phenomena in Laser and Powder-Bed Based Layered Manufacturing," CIRP Ann., 56(2), pp. 730–759.
[36] Bergström, D., Powell, J., and Kaplan, A. F. H., 2007, "The Absorptance of Steels to Nd:YLF and Nd:YAG Laser Light at Room Temperature," Appl. Surf. Sci., 253(11), pp. 5017–5028.

[37] Silva, E. M. R., Monteiro, W. A., Rossi, W., and Lima, M. S. F., 2000, "Absorption of Nd:YAG Laser Beam by Metallic Alloys," J. Mater. Sci. Lett., 19(23), pp. 2095–2097.
[38] Zavala-Arredondo, M., Boone, N., Willmott, J., Childs, D. T. D., Ivanov, P., Groom, K. M., and Mumtaz, K., 2017, "Laser Diode Area Melting for High Speed Additive Manufacturing of Metallic Components," Mater. Des., 117, pp. 305–315.
[39] Allmen, M. v, and Blatter, A., 1995, *Laser-Beam Interactions with Materials: Physical Principles and Applications*, Springer-Verlag, Berlin Heidelberg.
[40] Bergström, D., 2008, "The Absorption of Laser Light by Rough Metal Surfaces," PhD thesis, Luleå University of Technology.
[41] Kainer, K. U., 2006, *Metal Matrix Composites: Custom-Made Materials for Automotive and Aerospace Engineering*, John Wiley & Sons.
[42] The Ceramic Society of Japan, 2012, *Advanced Ceramic Technologies & Products*, Springer Science & Business Media, Tokyo.
[43] Hashim, J., 1999, "The Production of Metal Matrix Composites Using the Stir Casting Technique," doctoral, Dublin City University.
[44] Mussatto, A., Ahad, I. U., Mousavian, R. T., Delaure, Y., and Brabazon, D., 2020, "Advanced Production Routes for Metal Matrix Composites," Eng. Rep.
[45] Samal, P., Vundavilli, P. R., Meher, A., and Mahapatra, M. M., 2020, "Recent Progress in Aluminum Metal Matrix Composites: A Review on Processing, Mechanical and Wear Properties," J. Manuf. Process., 59, pp. 131–152.
[46] Kumar Sharma, A., Bhandari, R., Aherwar, A., Rimašauskienė, R., and Pinca-Bretotean, C., 2020, "A Study of Advancement in Application Opportunities of Aluminum Metal Matrix Composites," Mater. Today Proc., 26, pp. 2419–2424.
[47] Toor, Z. S., 2017, "Applications of Aluminum-Matrix Composites in Satellite: A Review," J. Space Technol., 7(1), pp. 1–6.
[48] Bhoi, N. K., Singh, H., and Pratap, S., 2020, "Developments in the Aluminum Metal Matrix Composites Reinforced by Micro/Nano Particles – A Review," J. Compos. Mater., 54(6), pp. 813–833.
[49] Singh, H., Singh, K., Vardhan, S., Mohan, S., and Singh, V., 2021, "A Comprehensive Review of Aluminium Matrix Composite Reinforcement and Fabrication Methodologies," Funct. Compos. Struct., 3(1).
[50] Surappa, M. K., 2003, "Aluminium Matrix Composites: Challenges and Opportunities," Sadhana, 28(1), pp. 319–334.
[51] Senthil, S., Raguraman, M., and Thamarai Manalan, D., 2020, "Manufacturing Processes & Recent Applications of Aluminium Metal Matrix Composite Materials: A Review," Mater. Today Proc.
[52] Dutta, S., Gupta, S., and Roy, M., 2020, "Recent Developments in Magnesium Metal–Matrix Composites for Biomedical Applications: A Review," ACS Biomater. Sci. Eng., 6(9), pp. 4748–4773.
[53] Bommala, V. K., Krishna, M. G., and Rao, C. T., 2019, "Magnesium Matrix Composites for Biomedical Applications: A Review," J. Magnes. Alloys, 7(1), pp. 72–79.
[54] Su, J., Teng, J., Xu, Z., and Li, Y., 2020, "Biodegradable Magnesium-Matrix Composites: A Review," Int. J. Miner. Metall. Mater., 27(6), pp. 724–744.
[55] Hayat, M. D., Singh, H., He, Z., and Cao, P., 2019, "Titanium Metal Matrix Composites: An Overview," Compos. Part Appl. Sci. Manuf., 121, pp. 418–438.
[56] Lütjering, G., and Williams, J. C., eds., 2007, "Titanium Matrix Composites," *Titanium*, Springer, Berlin, Heidelberg, pp. 367–382.

[57] Mall, S., and Nichols, T., 1997, *Titanium Matrix Composites: Mechanical Behavior*, CRC Press, Florida.
[58] Singerman, S., Jackson, J. J., and Lynn, M., 1996, "Titanium Metal Matrix Composites for Aerospace Applications," *Proceedings of Eighth International Symposium on Superalloys*, Superalloys, Champion, PA, pp. 579–586.
[59] Imbaby, M., and Jiang, K., 2011, "A Fabrication Process of Composite Micro Components Using Super Fine Stainless Steel and Ceramic Nano Powders," *Advances in Nanocomposites - Synthesis, Characterization and Industrial Applications*, IntechOpen, Rijeka, Croatia, pp. 679–684.
[60] Gun, T., and Simsir, M., 2017, "Investigation of Mechanical Properties of Fe-Based Metal Matrix Composites by Warm Compaction for Gear Production," Acta Phys. Pol. A, 131(3), pp. 443–447.
[61] Kumar, V. V., and Kumaran, S. S., 2019, "Friction Material Composite: Types of Brake Friction Material Formulations and Effects of Various Ingredients on Brake Performance–a Review," Mater. Res. Express, 6(8).
[62] Xiao, Z. Y., Ngai, T. L., Wen, L. P., and Li, Y. Y., 2007, "Preparation of Warm Compacted NbC Reinforced Iron-Based Composite and Its Tribological Behavior," Mater. Sci. Forum, 534–536, pp. 913–916.
[63] Zhou, c, Moon, J. R., and Peacock, S., 2013, "Rotary Forging of Sintered Iron Based Composites," Powder Metall., pp. 33–38.
[64] Asif, M., Chandra, K., and Misra, P. S., 2011, "Development of Iron Based Brake Friction MMC Used for Military Aircraft Application by A New P/M Route," J. Miner. Mater. Charact. Eng., 10(8), pp. 693–705.
[65] Jamwal, A., Mittal, P., Agrawal, R., Gupta, S., Kumar, D., Sadasivuni, K. K., and Gupta, P., 2020, "Towards Sustainable Copper Matrix Composites: Manufacturing Routes with Structural, Mechanical, Electrical and Corrosion Behaviour," J. Compos. Mater., 54(19), pp. 2635–2649.
[66] Gautam, Y. K., Somani, N., Kumar, M., and Sharma, S. K., 2018, "A Review on Fabrication and Characterization of Copper Metal Matrix Composite (CMMC)," AIP Conf. Proc., 2018(1).
[67] Tan, Z., Li, J., and Zhang, Z., 2021, "Experimental and Numerical Studies on Fabrication of Nanoparticle Reinforced Aluminum Matrix Composites by Friction Stir Additive Manufacturing," J. Mater. Res. Technol., 12, pp. 1898–1912.
[68] Shao, C., Zhao, S., Wang, X., Zhu, Y., Zhang, Z., and Ritchie, R. O., 2019, "Architecture of High-Strength Aluminum–Matrix Composites Processed by a Novel Microcasting Technique," NPG Asia Mater., 11(1), pp. 1–12.
[69] Liu, Q., Fan, G., Tan, Z., Guo, Q., Xiong, D., Su, Y., Li, Z., and Zhang, D., 2021, "Reinforcement with Intragranular Dispersion of Carbon Nanotubes in Aluminum Matrix Composites," Compos. Part B Eng., 217, p. 108915.
[70] Ma, X., Zhao, Y. F., Tian, W. J., Qian, Z., Chen, H. W., Wu, Y. Y., and Liu, X. F., 2016, "A Novel Al Matrix Composite Reinforced by Nano-AlN p Network," Sci. Rep., 6(1).
[71] Zhu, J., Jiang, W., Li, G., Guan, F., Yu, Y., and Fan, Z., 2020, "Microstructure and Mechanical Properties of SiCnp/Al6082 Aluminum Matrix Composites Prepared by Squeeze Casting Combined with Stir Casting," J. Mater. Process. Technol., 283.
[72] Zhang, H., Feng, P., and Akhtar, F., 2017, "Aluminium Matrix Tungsten Aluminide and Tungsten Reinforced Composites by Solid-State Diffusion Mechanism," Sci. Rep., 7(1).
[73] Kumar, S. D., Ravichandran, M., Jeevika, A., Stalin, B., Kailasanathan, C., and Karthick, A., 2021, "Effect of ZrB2 on Microstructural, Mechanical and Corrosion

Behaviour of Aluminium (AA7178) Alloy Matrix Composite Prepared by the Stir Casting Route," Ceram. Int., 47(9), pp. 12951–12962.
[74] Yuan, Z., Tian, W., Li, F., Fu, Q., Wang, X., Qian, W., and An, W., 2020, "Effect of Heat Treatment on the Interface of High-Entropy Alloy Particles Reinforced Aluminum Matrix Composites," J. Alloys Compd., 822.
[75] Tiwari, J. K., Mandal, A., Sathish, N., Agrawal, A. K., and Srivastava, A. K., 2020, "Investigation of Porosity, Microstructure and Mechanical Properties of Additively Manufactured Graphene Reinforced AlSi10Mg Composite," Addit. Manuf., 33.
[76] Zhang, X., Hou, X., Pan, D., Pan, B., Liu, L., Chen, B., Kondoh, K., and Li, S., 2020, "Designable Interfacial Structure and Its Influence on Interface Reaction and Performance of MWCNTs Reinforced Aluminum Matrix Composites," Mater. Sci. Eng. A, 793.
[77] Xiang, S., Wang, X., Gupta, M., Wu, K., Hu, X., and Zheng, M., 2016, "Graphene Nanoplatelets Induced Heterogeneous Bimodal Structural Magnesium Matrix Composites with Enhanced Mechanical Properties," Sci. Rep., 6(1).
[78] Dinaharan, I., Zhang, S., Chen, G., and Shi, Q., 2020, "Titanium Particulate Reinforced AZ31 Magnesium Matrix Composites with Improved Ductility Prepared Using Friction Stir Processing," Mater. Sci. Eng. A, 772.
[79] Turan, M. E., Sun, Y., and Akgul, Y., 2018, "Mechanical, Tribological and Corrosion Properties of Fullerene Reinforced Magnesium Matrix Composites Fabricated by Semi Powder Metallurgy," J. Alloys Compd., 740, pp. 1149–1158.
[80] Sahoo, S. K., Sahoo, B. N., and Panigrahi, S. K., 2020, "Effect of In-Situ Sub-Micron Sized TiB2 Reinforcement on Microstructure and Mechanical Properties in ZE41 Magnesium Matrix Composites," Mater. Sci. Eng. A, 773.
[81] Dezfuli, S. N., Huan, Z., Mol, A., Leeflang, S., Chang, J., and Zhou, J., 2017, "Advanced Bredigite-Containing Magnesium-Matrix Composites for Biodegradable Bone Implant Applications," Mater. Sci. Eng. C, 79, pp. 647–660.
[82] Sahoo, B. N., and Panigrahi, S. K., 2016, "Synthesis, Characterization and Mechanical Properties of in-Situ (TiC-TiB2) Reinforced Magnesium Matrix Composite," Mater. Des., 109, pp. 300–313.
[83] Selvam, B., Marimuthu, P., Narayanasamy, R., Anandakrishnan, V., Tun, K. S., Gupta, M., and Kamaraj, M., 2014, "Dry Sliding Wear Behaviour of Zinc Oxide Reinforced Magnesium Matrix Nano-Composites," Mater. Des., 58, pp. 475–481.
[84] Deng, K. K., Wu, K., Wu, Y. W., Nie, K. B., and Zheng, M. Y., 2010, "Effect of Submicron Size SiC Particulates on Microstructure and Mechanical Properties of AZ91 Magnesium Matrix Composites," J. Alloys Compd., 504(2), pp. 542–547.
[85] Niu, X., Shen, H., Fu, J., and Feng, J., 2021, "Effective Control of Microstructure Evolution in AZ91D Magnesium Alloy by SiC Nanoparticles in Laser Powder-Bed Fusion," Mater. Des., 206.
[86] Sklenička, V., Svoboda, M., Pahutová, M., Kuchařová, K., and Langdon, T. G., 2001, "Microstructural Processes in Creep of an AZ 91 Magnesium-Based Composite and Its Matrix Alloy," Mater. Sci. Eng. A, 319–321, pp. 741–745.
[87] Neubauer, E., Vály, L., Kitzmantel, M., Grech, D., Ortega, A. R., Montealegre-Meléndez, I., and Arévalo, C., 2016, "Titanium Matrix Composites with High Specific Stiffness," Key Eng. Mater., 704, pp. 38–43.
[88] Pouzet, S., Peyre, P., Gorny, C., Castelnau, O., Baudin, T., Brisset, F., Colin, C., and Gadaud, P., 2016, "Additive Layer Manufacturing of Titanium Matrix Composites Using the Direct Metal Deposition Laser Process," Mater. Sci. Eng. A, 677, pp. 171–181.

[89] Ma, F., Liu, P., Li, W., Liu, X., Chen, X., Zhang, K., Pan, D., and Lu, W., 2016, "The Mechanical Behavior Dependence on the TiB Whisker Realignment during Hot-Working in Titanium Matrix Composites," Sci. Rep., 6(1).
[90] Cao, H., and Liang, Y., 2020, "The Microstructures and Mechanical Properties of Graphene-Reinforced Titanium Matrix Composites," J. Alloys Compd., 812.
[91] Wei, W., Zhang, Q., Wu, W., Cao, H., Shen, J., Fan, S., and Duan, X., 2020, "Agglomeration-Free Nanoscale TiC Reinforced Titanium Matrix Composites Achieved by in-Situ Laser Additive Manufacturing," Scr. Mater., 187, pp. 310–316.
[92] Zhang, F., Du, M., Fan, K., Ye, C., and Zhang, B., 2020, "Fabrication and Mechanical Properties of Network Structured Titanium Alloy Matrix Composites Reinforced with Ti2AlC Particulates," Mater. Sci. Eng. A, 776.
[93] Saba, F., Zhang, F., Liu, S., and Liu, T., 2019, "Reinforcement Size Dependence of Mechanical Properties and Strengthening Mechanisms in Diamond Reinforced Titanium Metal Matrix Composites," Compos. Part B Eng., 167, pp. 7–19.
[94] Cao, Z., Wang, X., Li, J., Wu, Y., Zhang, H., Guo, J., and Wang, S., 2017, "Reinforcement with Graphene Nanoflakes in Titanium Matrix Composites," J. Alloys Compd., 696, pp. 498–502.
[95] Huang, L., Wang, L., Qian, M., and Zou, J., 2017, "High Tensile-Strength and Ductile Titanium Matrix Composites Strengthened by TiB Nanowires," Scr. Mater., 141, pp. 133–137.
[96] Qin, Y., Geng, L., and Ni, D., 2011, "Dry Sliding Wear Behavior of Extruded Titanium Matrix Composite Reinforced by in Situ TiB Whisker and TiC Particle," J. Mater. Sci., 46(14), pp. 4980–4985.
[97] Guan, D., He, X., Zhang, R., Li, R., and Qu, X., 2018, "Tribological and Corrosion Properties of PM 316L Matrix Composites Reinforced by in Situ Polymer-Derived Ceramics," Vacuum, 148, pp. 319–326.
[98] Pagounis, E., Lindroos, V. K., and Talvitie, M., 1996, "Influence of Matrix Structure on the Abrasion Wear Resistance and Toughness of a Hot Isostatic Pressed White Iron Matrix Composite," Metall. Mater. Trans. A, 27(12), pp. 4183–4191.
[99] Tjong, S. C., and Lau, K. C., 1999, "Sliding Wear of Stainless Steel Matrix Composite Reinforced with TiB2 Particles," Mater. Lett., 41(4), pp. 153–158.
[100] Qiu, B., Xing, S. M., and Dong, Q., 2017, "Wear Behaviour of Iron Matrix Composite Reinforced by ZTA Particles in Impact Abrasion," IOP Conf. Ser. Mater. Sci. Eng., 269.
[101] Lima, W. M., Velasco, F., and Torralba, J. M., 1999, "Stainless Steel Matrix Composites Reinforced with AlCr2," Mater. Sci. Forum, 299–300, pp. 431–438.
[102] Salman, O. O., Funk, A., Waske, A., Eckert, J., and Scudino, S., 2018, "Additive Manufacturing of a 316L Steel Matrix Composite Reinforced with CeO2 Particles: Process Optimization by Adjusting the Laser Scanning Speed," Technologies, 6(1), p. 25.
[103] Hadjem-Hamouche, Z., Chevalier, J.-P., Cui, Y., and Bonnet, F., 2012, "Deformation Behavior and Damage Evaluation in a New Titanium Diboride (TiB2) Steel-Based Composite," Steel Res. Int., 83(6), pp. 538–545.
[104] Chen, H., Gu, D., Zhang, H., Xi, L., Lu, T., Deng, L., Kühn, U., and Kosiba, K., 2021, "Novel WC-Reinforced Iron-Based Composites with Excellent Mechanical Properties Synthesized by Laser Additive Manufacturing: Underlying Role of Reinforcement Weight Fraction," J. Mater. Process. Technol., 289.
[105] Pelleg, J., 1999, "Reactions in the Matrix and Interface of the Fe–SiC Metal Matrix Composite System," Mater. Sci. Eng. A, 269(1), pp. 225–241.

[106] Parveez, B., and Wani, M. F., 2021, “Tribological Behaviour of Nano-Zirconia Reinforced Iron-Based Self-Lubricating Composites for Bearing Applications,” Tribol. Int., 159.
[107] Wang, H., Zhang, Z.-H., Zhang, H.-M., Hu, Z.-Y., Li, S.-L., and Cheng, X.-W., 2017, “Novel Synthesizing and Characterization of Copper Matrix Composites Reinforced with Carbon Nanotubes,” Mater. Sci. Eng. A, 696, pp. 80–89.
[108] Salvo, C., Mangalaraja, R. V., Udayabashkar, R., Lopez, M., and Aguilar, C., 2019, “Enhanced Mechanical and Electrical Properties of Novel Graphene Reinforced Copper Matrix Composites,” J. Alloys Compd., 777, pp. 309–316.
[109] Deng, H., Yi, J., Xia, C., and Yi, Y., 2017, “Mechanical Properties and Microstructure Characterization of Well-Dispersed Carbon Nanotubes Reinforced Copper Matrix Composites,” J. Alloys Compd., 727, pp. 260–268.
[110] Yih, P., and Chung, D. D. L., 1999, “Brass-Matrix Silicon Carbide Whisker Composites Prepared by Powder Metallurgy,” J. Mater. Sci., 34(2), pp. 359–364.
[111] Salvo, C., Chicardi, E., Hernández-Saz, J., Aguilar, C., Gnanaprakasam, P., and Mangalaraja, R. V., 2021, “Microstructure, Electrical and Mechanical Properties of Ti2AlN MAX Phase Reinforced Copper Matrix Composites Processed by Hot Pressing,” Mater. Charact., 171.
[112] Bahador, A., Umeda, J., Hamzah, E., Yusof, F., Li, X., and Kondoh, K., 2020, “Synergistic Strengthening Mechanisms of Copper Matrix Composites with TiO2 Nanoparticles,” Mater. Sci. Eng. A, 772.
[113] Dinaharan, I., Saravanakumar, S., Kalaiselvan, K., and Gopalakrishnan, S., 2017, “Microstructure and Sliding Wear Characterization of Cu/TiB2 Copper Matrix Composites Fabricated via Friction Stir Processing,” J. Asian Ceram. Soc., 5(3), pp. 295–303.
[114] Zhou, H., Yao, P., Xiao, Y., Fan, K., Zhang, Z., Gong, T., Zhao, L., Deng, M., Liu, C., and Ling, P., 2019, “Friction and Wear Maps of Copper Metal Matrix Composites with Different Iron Volume Content,” Tribol. Int., 132, pp. 199–210.
[115] Gao, S., Nan, Z., Li, Y., Zhao, N., Liu, Q., Xu, G., Cheng, X., and Yang, J., 2020, “Copper Matrix Thermal Conductive Composites with Low Thermal Expansion for Electronic Packaging,” Ceram. Int., 46(11, Part A), pp. 18019–18025.
[116] Mai, Y. J., Chen, F. X., Lian, W. Q., Zhang, L. Y., Liu, C. S., and Jie, X. H., 2018, “Preparation and Tribological Behavior of Copper Matrix Composites Reinforced with Nickel Nanoparticles Anchored Graphene Nanosheets,” J. Alloys Compd., 756, pp. 1–7.
[117] AlMangour, B., 2016, “In-Situ TiC Particle Reinforced 316L Stainless Steel Matrix Nanocomposites: Powder Preparation by Mechanical Alloying and Selective Laser Melting Behaviour,” *26th Annual International Solid Freeform Fabrication Symposium*, University of Texas at Austin, Texas, USA.
[118] Plaut, R. L., Herrera, C., Escriba, D. M., Rios, P. R., and Padilha, A. F., 2007, “A Short Review on Wrought Austenitic Stainless Steels at High Temperatures: Processing, Microstructure, Properties and Performance,” Mater. Res., 10(4), pp. 453–460.
[119] Yu, Y., Shironita, S., Souma, K., and Umeda, M., 2018, “Effect of Chromium Content on the Corrosion Resistance of Ferritic Stainless Steels in Sulfuric Acid Solution,” Heliyon, 4(11).
[120] Farrer, J. C. M., 2004, *The Alloy Tree: A Guide to Low-Alloy Steels, Stainless Steels, and Nickel-Base Alloys*, Woodhead Publishing Limited, Cambridge.
[121] Berns, H., Gavriljuk, V., and Riedner, S., 2013, *High Interstitial Stainless Austenitic Steels*, Springer-Verlag, Berlin Heidelberg.

[122] Holmberg, B., 2002, *Stainless Steels: Their Properties and Their Suitability for Welding*, Avesta Polarit Stainless, Sweden.
[123] McGuire, M. F., 2008, *Stainless Steels for Design Engineers*, ASM International, Ohio.
[124] AL-Mangour, B., 2015, "Powder Metallurgy of Stainless Steel: State-of-the Art, Challenges, and Development," Stainless Teel: Microstructure, Mechanical Properties and Methods of Application," Nova Sci. Publ., pp. 37–80.
[125] Dutta Majumdar, J., Kumar, A., and Li, L., 2009, "Direct Laser Cladding of SiC Dispersed AISI 316L Stainless Steel," Tribol. Int., 42(5), pp. 750–753.
[126] Yan, J., Zhou, Y., Gu, R., Zhang, X., Quach, W.-M., and Yan, M., 2019, "A Comprehensive Study of Steel Powders (316L, H13, P20 and 18Ni300) for Their Selective Laser Melting Additive Manufacturing," Metals, 9(1).
[127] AK Steel, 2007, *Stainless 316, 316L, 317, 317L*, AK Steel Corporation, 7100-0096 7/07, West Chester.
[128] PSP, 2011, *Alloy 316/316L Specifications: UNS S31600 / S31603*, Penn Stainless Products, Pennsylvania.
[129] Zhou, D., Qiu, F., Wang, H., and Jiang, Q., 2014, "Manufacture of Nano-Sized Particle-Reinforced Metal Matrix Composites: A Review," Acta Metall. Sin. Engl. Lett., 27(5), pp. 798–805.
[130] Casati, R., and Vedani, M., 2014, "Metal Matrix Composites Reinforced by Nano-Particles—A Review," Metals, 4(1), pp. 65–83.
[131] Groover, M. P., 2010, *Fundamentals of Modern Manufacturing: Materials, Processes, and Systems*, John Wiley & Sons, United States of America.
[132] Yang, W., and Lee, W. B., 1993, "Strengthening Mechanisms," *Mesoplasticity and Its Applications*, W. Yang, and W.B. Lee, eds., Springer, Berlin, Heidelberg, pp. 191–216.
[133] Hansen, N., and Ralph, B., 1986, "Additive Strengthening Mechanisms in Dispersion Hardened Polycrystals," Acta Metall., 34(10), pp. 1955–1962.
[134] Rosso, M., 2006, "Ceramic and Metal Matrix Composites: Routes and Properties," J. Mater. Process. Technol., 175(1), pp. 364–375.
[135] Williams, J. J., Piotrowski, G., Saha, R., and Chawla, N., 2002, "Effect of Overaging and Particle Size on Tensile Deformation and Fracture of Particle-Reinforced Aluminum Matrix Composites," Metall. Mater. Trans. A, 33(12), pp. 3861–3869.
[136] Gibbons, J. H., 1988, *Advanced Materials by Design: New Structural Materials Technologies*, U.S. Government Printing Office, Washington.
[137] Rohatgi, P. K., and Schultz, B., 2007, "Lightweight Metal Matrix Nanocomposites - Stretching the Boundaries of Metals," Mater. Matters, 2.4(16).
[138] Dammak, M., Ksaeir, I., Brinza, O., and Gasperini, O., 2013, "Experimental Analysis of Damage of Fe-TiB2 Metal Matrix Composites under Complex Loading," *21ème Congrès Français de Mécanique*, 21ème Congrès Français de Mécanique, Paris, France.
[139] Yi, Z.-Z., Xie, Z.-P., Huang, Y., Ma, J.-T., and Cheng, Y.-B., 2002, "Study on Gelcasting and Properties of Recrystallized Silicon Carbide," Ceram. Int., 28(4), pp. 369–376.
[140] Kavecký, Š., Janeková, B., Madejová, J., and Šajgalík, P., 2000, "Silicon Carbide Powder Synthesis by Chemical Vapour Deposition from Silane/Acetylene Reaction System," J. Eur. Ceram. Soc., 20(12), pp. 1939–1946.
[141] Cheung, R., 2006, *Silicon Carbide Microelectromechanical Systems for Harsh Environments*, World Scientific, Singapore.

[142] Riedel, R., 2000, *Handbook of Ceramic Hard Materials*, Wiley, Weinheim.
[143] Zetterling, C.-M., 2002, *Process Technology for Silicon Carbide Devices*, IET Inspec.
[144] Carter, C. B., and Norton, M. G., 2007, *Ceramic Materials: Science and Engineering*, Springer Science & Business Media, Washington.
[145] Basu, B., and Kalin, M., 2011, *Tribology of Ceramics and Composites: A Materials Science Perspective*, Wiley, New Jersey.
[146] Saddow, S. E., and Agarwal, A., 2004, *Advances in Silicon Carbide Processing and Applications*, Artech House.
[147] Harris, G. L., 1995, *Properties of Silicon Carbide*, IET Inspec.
[148] Pierson, H. O., 2013, *Handbook of Refractory Carbides & Nitrides: Properties, Characteristics, Processing and Applications*, Elsevier Science, New Jersey.
[149] Ruys, A. J., 2020, *Metal-Reinforced Ceramics*, Elsevier, Amsterdam.
[150] Gusev, A. I., 2021, "Mechanical Properties of Nonstoichiometric Cubic Titanium Carbide TiCy," Phys. Chem. Chem. Phys., 23(34), pp. 18558–18567.
[151] Kurlov, A. S., and Gusev, A. I., 2013, *Tungsten Carbides: Structure, Properties and Application in Hardmetals*, Springer Science & Business Media, Switzerland.
[152] Shackelford, J. F., and Alexander, W., 2001, *Materials Science and Engineering Handbook*, CRC Press.
[153] Cardarelli, F., 2008, *Materials Handbook: A Concise Desktop Reference*, Springer Science & Business Media, London.
[154] Chawla, N., and Chawla, K. K., 2006, *Metal Matrix Composites*, Springer Science & Business Media, New York.
[155] Chawla, N., and Chawla, K. K., 2013, *Metal Matrix Composites*, Springer Science & Business Media, New York.
[156] Everett, R., 2012, *Metal Matrix Composites: Processing and Interfaces*, Academic Press, San Diego.
[157] Park, S.-J., and Seo, M.-K., 2011, *Interface Science and Composites*, Academic Press, Amsterdam.
[158] Reddy, B. S. B., Das, K., and Das, S., 2007, "A Review on the Synthesis of in Situ Aluminum Based Composites by Thermal, Mechanical and Mechanical–Thermal Activation of Chemical Reactions," J. Mater. Sci., 42(22), pp. 9366–9378.
[159] Lee, K.-B., Kim, S.-H., Kim, D.-Y., Cha, P.-R., Kim, H.-S., Choi, H.-J., and Ahn, J.-P., 2019, "Aluminum Matrix Composites Manufactured Using Nitridation-Induced Self-Forming Process," Sci. Rep., 9(1).
[160] Ajayan, P. M., Schadler, L. S., and Braun, P. V., 2006, *Nanocomposite Science and Technology*, John Wiley & Sons, Weinheim.
[161] Aikin, R. M., 1997, "The Mechanical Properties of In-Situ Composites," JOM, 49(8).
[162] Ceschini, L., and Montanari, R., 2011, *Advances in Metal Matrix Composites*, Trans Tech Publications Ltd, Switzerland.
[163] Jo, I., 2014, "Lightweight Mg-Based Composites with Thermodynamically Stable Interfaces by in-Situ Combustion Synthesis," Ph.D., Colorado School of Mines.
[164] Yi, X.-S., Du, S., and Zhang, L., 2017, *Composite Materials Engineering: Different Types of Composite Materials*, Springer, Beijing.
[165] Jo, I., Jeon, S., Lee, E., Cho, S., and Lee, H., 2015, "Phase Formation and Interfacial Phenomena of the In-Situ Combustion Reaction of Al-Ti-C in TiC/Mg Composites," Mater. Trans., 56(5), pp. 661–664.
[166] Banerjee, R., and Manna, I., 2013, *Ceramic Nanocomposites*, Elsevier, Cambridge.

[167] Bartolo, P., Lemos, A., and Pereira, A., 2013, "High Value Manufacturing: Advanced Research in Virtual and Rapid Prototyping," *CRC Press*, Leiria, Portugal, p. 650.
[168] Thandalam, S. K., Ramanathan, S., and Sundarrajan, S., 2015, "Synthesis, Microstructural and Mechanical Properties of Ex Situ Zircon Particles (ZrSiO4) Reinforced Metal Matrix Composites (MMCs): A Review," J. Mater. Res. Technol., 4(3), pp. 333–347.
[169] Suarez, C. E., 2012, "Light Metals," *TMS Annual Meeting & Exhibition*, Springer, Orlando, p. 1007.
[170] Tjong, S. C., and Ma, Z. Y., 2000, "Microstructural and Mechanical Characteristics of in Situ Metal Matrix Composites," Mater. Sci. Eng. R Rep., 29(3), pp. 49–113.
[171] Chen, Y., and Chung, D. D. L., 1996, "In Situ Al-TiB Composite Obtained by Stir Casting," J. Mater. Sci., 31(2), pp. 311–315.
[172] Kondoh, K., 2015, "Titanium Metal Matrix Composites by Powder Metallurgy (PM) Routes," *Titanium Powder Metallurgy*, M. Qian, and F.H. (Sam) Froes, eds., Butterworth-Heinemann, Boston, pp. 277–297.
[173] Ponraj, N. V., Azhagurajan, A., Vettivel, S. C., Sahaya Shajan, X., Nabhiraj, P. Y., and Sivapragash, M., 2017, "Graphene Nanosheet as Reinforcement Agent in Copper Matrix Composite by Using Powder Metallurgy Method," Surf. Interfaces, 6, pp. 190–196.
[174] Ozkaya, S., and Canakci, A., 2016, "Effect of the B4C Content and the Milling Time on the Synthesis, Consolidation and Mechanical Properties of AlCuMg-B4C Nanocomposites Synthesized by Mechanical Milling," Powder Technol., 297, pp. 8–16.
[175] Fernandes, M. R. P., Martinelli, A. E., Klein, A. N., Hammes, G., Binder, C., and Nascimento, R. M., 2017, "Production of Nickel Matrix Composites Reinforced with Carbide Particles by Granulation of Fine Powders and Mechanical Pressing," Powder Technol., 305, pp. 673–678.
[176] Shirvanimoghaddam, K., Hamim, S. U., Karbalaei Akbari, M., Fakhrhoseini, S. M., Khayyam, H., Pakseresht, A. H., Ghasali, E., Zabet, M., Munir, K. S., Jia, S., Davim, J. P., and Naebe, M., 2017, "Carbon Fiber Reinforced Metal Matrix Composites: Fabrication Processes and Properties," Compos. Part Appl. Sci. Manuf., 92, pp. 70–96.
[177] German, R. M., 1994, *Powder Metallurgy Science*, Metal Powder Industries Federation, Princeton, New Jersey.
[178] Wei, D., Dave, R., and Pfeffer, R., 2002, "Mixing and Characterization of Nanosized Powders: An Assessment of Different Techniques," J. Nanoparticle Res., 4(1), pp. 21–41.
[179] Kaye, B. H., 1997, *Powder Mixing*, Springer Science & Business Media, London.
[180] Kalpakjian, S., and Schmid, S. R., 2014, *Manufacturing Engineering and Technology*, Pearson, New Jersey.
[181] Šalak, A., 1995, *Ferrous Powder Metallurgy*, Cambridge International Science Publishing, Cambridge.
[182] Gessinger, G. H., 2013, *Powder Metallurgy of Superalloys: Butterworths Monographs in Materials*, Elsevier, Switzerland.
[183] Kalpakjian, S., and Schmid, S. R., 2008, *Manufacturing Processes for Engineering Materials*, Pearson Education, New Jersey.
[184] ASM Committee, 1998, *ASM Handbook: Volume 7: Powder Metal Technologies and Applications*, ASM International.

[185] Thümmler, F., and Oberacker, R., 1993, *An Introduction to Powder Metallurgy*, Institute of Materials, London.
[186] Philips, T., Dwyer, J., and Zurecki, Z., 2006, "Controlling Properties of Sintered Steel Powder Metal Components Using Atmosphere Composition as a Variable," Air Prod. Chem. Inc.
[187] Sing, S. L., 2019, *Selective Laser Melting of Novel Titanium-Tantalum Alloy as Orthopaedic Biomaterial*, Springer, Singapore.
[188] Kamath, C., 2016, "Data Mining and Statistical Inference in Selective Laser Melting," Int. J. Adv. Manuf. Technol., 86(5), pp. 1659–1677.
[189] Su, X., and Yang, Y., 2012, "Research on Track Overlapping during Selective Laser Melting of Powders," J. Mater. Process. Technol., 212(10), pp. 2074–2079.
[190] Gong, H., Rafi, K., Gu, H., Starr, T., and Stucker, B., 2014, "Analysis of Defect Generation in Ti–6Al–4V Parts Made Using Powder Bed Fusion Additive Manufacturing Processes," Addit. Manuf., 1–4, pp. 87–98.
[191] Liu, Q. C., Elambasseril, J., Sun, S. J., Leary, M., Brandt, M., and Sharp, P. K., 2014, "The Effect of Manufacturing Defects on the Fatigue Behaviour of Ti-6Al-4V Specimens Fabricated Using Selective Laser Melting," Adv. Mater. Res., 891–892, pp. 1519–1524.
[192] Vilaro, T., Colin, C., and Bartout, J. D., 2011, "As-Fabricated and Heat-Treated Microstructures of the Ti-6Al-4V Alloy Processed by Selective Laser Melting," Metall. Mater. Trans. A, 42(10), pp. 3190–3199.
[193] Dong, Z., Liu, Y., Wen, W., Ge, J., and Liang, J., 2019, "Effect of Hatch Spacing on Melt Pool and As-Built Quality During Selective Laser Melting of Stainless Steel: Modeling and Experimental Approaches," Materials, 12(1), p. 50.
[194] Hong, M.-H., Min, B. K., and Kwon, T.-Y., 2016, "The Influence of Process Parameters on the Surface Roughness of a 3D-Printed Co–Cr Dental Alloy Produced via Selective Laser Melting," Appl. Sci., 6(12), p. 401.
[195] Peng, T., and Chen, C., 2018, "Influence of Energy Density on Energy Demand and Porosity of 316L Stainless Steel Fabricated by Selective Laser Melting," Int. J. Precis. Eng. Manuf.-Green Technol., 5(1), pp. 55–62.
[196] Xiong, W., Hao, L., Li, Y., Tang, D., Cui, Q., Feng, Z., and Yan, C., 2019, "Effect of Selective Laser Melting Parameters on Morphology, Microstructure, Densification and Mechanical Properties of Supersaturated Silver Alloy," Mater. Des., 170.
[197] Taha, M. A., Yousef, A. F., Gany, K. A., and Sabour, H. A., 2012, "On Selective Laser Melting of Ultra High Carbon Steel: Effect of Scan Speed and Post Heat Treatment," Mater. Sci. Eng. Technol., 43(11), pp. 913–923.
[198] Wang, J.-H., Ren, J., Liu, W., Wu, X.-Y., Gao, M.-X., and Bai, P.-K., 2018, "Effect of Selective Laser Melting Process Parameters on Microstructure and Properties of Co-Cr Alloy," Materials, 11(9).
[199] Maamoun, A. H., Xue, Y. F., Elbestawi, M. A., and Veldhuis, S. C., 2018, "Effect of Selective Laser Melting Process Parameters on the Quality of Al Alloy Parts: Powder Characterization, Density, Surface Roughness, and Dimensional Accuracy," Materials, 11(12).
[200] junfeng, L., and zhengying, W., 2017, "Process Optimization and Microstructure Characterization of Ti6Al4V Manufactured by Selective Laser Melting," IOP Conf. Ser. Mater. Sci. Eng., 269.
[201] Wang, S., Liu, Y., Shi, W., Qi, B., Yang, J., Zhang, F., Han, D., and Ma, Y., 2017, "Research on High Layer Thickness Fabricated of 316L by Selective Laser Melting," Materials, 10(9).

[202] Ma, M., Wang, Z., Gao, M., and Zeng, X., 2015, “Layer Thickness Dependence of Performance in High-Power Selective Laser Melting of 1Cr18Ni9Ti Stainless Steel,” J. Mater. Process. Technol., 215, pp. 142–150.
[203] Sufiiarov, V. Sh., Popovich, A. A., Borisov, E. V., Polozov, I. A., Masaylo, D. V., and Orlov, A. V., 2017, “The Effect of Layer Thickness at Selective Laser Melting,” Procedia Eng., 174, pp. 126–134.
[204] Shi, X., Ma, S., Liu, C., Chen, C., Wu, Q., Chen, X., and Lu, J., 2016, “Performance of High Layer Thickness in Selective Laser Melting of Ti6Al4V,” Materials, 9(12).
[205] Pizarro, J. M., and Savalani, M. M., 2016, “Effect of Preheat and Layer Thickness on Selective Laser Melting (SLM) of Magnesium,” Rapid Prototyp. J., 22(1), pp. 115–122.
[206] Dadbakhsh, S., and Hao, L., 2014, “Effect of Layer Thickness in Selective Laser Melting on Microstructure of Al/5 Wt.%Fe2O3 Powder Consolidated Parts,” Sci. World J., 2014.
[207] Fatemi, S. A., Ashany, J. Z., Aghchai, A. J., and Abolghasemi, A., 2017, “Experimental Investigation of Process Parameters on Layer Thickness and Density in Direct Metal Laser Sintering: A Response Surface Methodology Approach,” Virtual Phys. Prototyp., 12(2), pp. 133–140.
[208] Gusarov, A. V., Yadroitsev, I., Bertrand, Ph., and Smurov, I., 2007, “Heat Transfer Modelling and Stability Analysis of Selective Laser Melting,” Appl. Surf. Sci., 254(4), pp. 975–979.
[209] Bian, L., Usher, J., and Shamsaei, N., 2017, *Laser-Based Additive Manufacturing of Metal Parts: Modeling, Optimization, and Control of Mechanical Properties*, Taylor & Francis Incorporated, Florida.
[210] Gusarov, A. V., and Smurov, I., 2010, “Modeling the Interaction of Laser Radiation with Powder Bed at Selective Laser Melting,” Phys. Procedia, 5, pp. 381–394.
[211] Alkahari, M. R., Furumoto, T., Ueda, T., and Hosokawa, A., 2014, “Melt Pool and Single Track Formation in Selective Laser Sintering/Selective Laser Melting,” Adv. Mater. Res., 933, pp. 196–201.
[212] Dilip, J. J. S., Zhang, S., Teng, C., Zeng, K., Robinson, C., Pal, D., and Stucker, B., 2017, “Influence of Processing Parameters on the Evolution of Melt Pool, Porosity, and Microstructures in Ti-6Al-4V Alloy Parts Fabricated by Selective Laser Melting,” Prog. Addit. Manuf., 2(3), pp. 157–167.
[213] Yuan, P., and Gu, D., 2015, “Molten Pool Behaviour and Its Physical Mechanism during Selective Laser Melting of TiC/AlSi10Mg Nanocomposites: Simulation and Experiments,” J. Phys. Appl. Phys., 48(3).
[214] Wu, Y.-C., San, C.-H., Chang, C.-H., Lin, H.-J., Marwan, R., Baba, S., and Hwang, W.-S., 2018, “Numerical Modeling of Melt-Pool Behavior in Selective Laser Melting with Random Powder Distribution and Experimental Validation,” J. Mater. Process. Technol., 254, pp. 72–78.
[215] Yang, H., Yang, J., Huang, W., Wang, Z., and Zeng, X., 2018, “The Printability, Microstructure, Crystallographic Features and Microhardness of Selective Laser Melted Inconel 718 Thin Wall,” Mater. Des., 156, pp. 407–418.
[216] Yang, J., Han, J., Yu, H., Yin, J., Gao, M., Wang, Z., and Zeng, X., 2016, “Role of Molten Pool Mode on Formability, Microstructure and Mechanical Properties of Selective Laser Melted Ti-6Al-4V Alloy,” Mater. Des., 110, pp. 558–570.

[217] Tan, J. H., Wong, W. L. E., and Dalgarno, K. W., 2017, “An Overview of Powder Granulometry on Feedstock and Part Performance in the Selective Laser Melting Process,” Addit. Manuf., 18, pp. 228–255.
[218] Ladewig, A., Schlick, G., Fisser, M., Schulze, V., and Glatzel, U., 2016, “Influence of the Shielding Gas Flow on the Removal of Process By-Products in the Selective Laser Melting Process,” Addit. Manuf., 10, pp. 1–9.
[219] O’Neill, W., Sutcliffe, C. J., Morgan, R., Landsborough, A., and Hon, K. K. B., 1999, “Investigation on Multi-Layer Direct Metal Laser Sintering of 316L Stainless Steel Powder Beds,” CIRP Ann., 48(1), pp. 151–154.
[220] Han, Q., Geng, Y., Setchi, R., Lacan, F., Gu, D., and Evans, S. L., 2017, “Macro and Nanoscale Wear Behaviour of Al-Al2O3 Nanocomposites Fabricated by Selective Laser Melting,” Compos. Part B Eng., 127, pp. 26–35.
[221] Spears, T. G., and Gold, S. A., 2016, “In-Process Sensing in Selective Laser Melting (SLM) Additive Manufacturing,” Integrating Mater. Manuf. Innov., 5(1).
[222] O’Neill, W., Sutcliffe, C. J., Morgan, R., and Hon, K. K. B., 1998, “Investigation of Short Pulse Nd: YAG Laser Interaction with Stainless Steel Powder Beds,” Proc. Solid Free. Fabr. Symp., 9, pp. 147–160.
[223] King, W. E., Barth, H. D., Castillo, V. M., Gallegos, G. F., Gibbs, J. W., Hahn, D. E., Kamath, C., and Rubenchik, A. M., 2014, “Observation of Keyhole-Mode Laser Melting in Laser Powder-Bed Fusion Additive Manufacturing,” J. Mater. Process. Technol., 214(12), pp. 2915–2925.
[224] Kruth, J. P., Froyen, L., Van Vaerenbergh, J., Mercelis, P., Rombouts, M., and Lauwers, B., 2004, “Selective Laser Melting of Iron-Based Powder,” J. Mater. Process. Technol., 149(1), pp. 616–622.
[225] Wang, D., Wu, S., Fu, F., Mai, S., Yang, Y., Liu, Y., and Song, C., 2017, “Mechanisms and Characteristics of Spatter Generation in SLM Processing and Its Effect on the Properties,” Mater. Des., 117, pp. 121–130.
[226] Anwar, A. B., and Pham, Q.-C., 2018, “Study of the Spatter Distribution on the Powder Bed during Selective Laser Melting,” Addit. Manuf., 22, pp. 86–97.
[227] Taheri Andani, M., Dehghani, R., Karamooz-Ravari, M. R., Mirzaeifar, R., and Ni, J., 2017, “Spatter Formation in Selective Laser Melting Process Using Multi-Laser Technology,” Mater. Des., 131, pp. 460–469.
[228] Taheri Andani, M., Dehghani, R., Karamooz-Ravari, M. R., Mirzaeifar, R., and Ni, J., 2018, “A Study on the Effect of Energy Input on Spatter Particles Creation during Selective Laser Melting Process,” Addit. Manuf., 20, pp. 33–43.
[229] Simonelli, M., Tuck, C., Aboulkhair, N. T., Maskery, I., Ashcroft, I., Wildman, R. D., and Hague, R., 2015, “A Study on the Laser Spatter and the Oxidation Reactions During Selective Laser Melting of 316L Stainless Steel, Al-Si10-Mg, and Ti-6Al-4V,” Metall. Mater. Trans. A, 46(9), pp. 3842–3851.
[230] Liu, Y., Yang, Y., Mai, S., Wang, D., and Song, C., 2015, “Investigation into Spatter Behavior during Selective Laser Melting of AISI 316L Stainless Steel Powder,” Mater. Des., 87, pp. 797–806.
[231] Gunenthiram, V., Peyre, P., Schneider, M., Dal, M., Coste, F., Koutiri, I., and Fabbro, R., 2018, “Experimental Analysis of Spatter Generation and Melt-Pool Behavior during the Powder Bed Laser Beam Melting Process,” J. Mater. Process. Technol., 251, pp. 376–386.
[232] Konda Gokuldoss, P., Kolla, S., and Eckert, J., 2017, “Additive Manufacturing Processes: Selective Laser Melting, Electron Beam Melting and Binder Jetting—Selection Guidelines,” Materials, 10(6).

[233] Zavala-Arredondo, M., Ali, H., Groom, K. M., and Mumtaz, K., 2018, "Investigating the Melt Pool Properties and Thermal Effects of Multi-Laser Diode Area Melting," Int. J. Adv. Manuf. Technol., 97(1), pp. 1383–1396.
[234] Birol, Y., 1996, "Microstructural Characterization of a Rapidly-Solidified Al-12 Wt% Si Alloy," J. Mater. Sci., 31(8), pp. 2139–2143.
[235] Lavernia, E. J., and Srivatsan, T. S., 2010, "The Rapid Solidification Processing of Materials: Science, Principles, Technology, Advances, and Applications," J. Mater. Sci., 45(2), pp. 287–325.
[236] DebRoy, T., Wei, H. L., Zuback, J. S., Mukherjee, T., Elmer, J. W., Milewski, J. O., Beese, A. M., Wilson-Heid, A., De, A., and Zhang, W., 2018, "Additive Manufacturing of Metallic Components – Process, Structure and Properties," Prog. Mater. Sci., 92, pp. 112–224.
[237] Ion, J. C., 2005, *Laser Processing of Engineering Materials: Principles, Procedure and Industrial Application*, Elsevier, Butterworth-Heinemann, United States of America.
[238] Kou, S., 2003, *Welding Metallurgy*, John Wiley & Sons, New Jersey.
[239] Tang, C., Tan, J. L., and Wong, C. H., 2018, "A Numerical Investigation on the Physical Mechanisms of Single Track Defects in Selective Laser Melting," Int. J. Heat Mass Transf., 126, pp. 957–968.
[240] Kaufman, J. G., and Rooy, E. L., 2004, *Aluminum Alloy Castings: Properties, Processes, and Applications*, ASM International, United States of America.
[241] Khairallah, S. A., Anderson, A. T., Rubenchik, A., and King, W. E., 2016, "Laser Powder-Bed Fusion Additive Manufacturing: Physics of Complex Melt Flow and Formation Mechanisms of Pores, Spatter, and Denudation Zones," Acta Mater., 108, pp. 36–45.
[242] Aboulkhair, N. T., Everitt, N. M., Ashcroft, I., and Tuck, C., 2014, "Reducing Porosity in AlSi10Mg Parts Processed by Selective Laser Melting," Addit. Manuf., 1–4, pp. 77–86.
[243] Coeck, S., Bisht, M., Plas, J., and Verbist, F., 2019, "Prediction of Lack of Fusion Porosity in Selective Laser Melting Based on Melt Pool Monitoring Data," Addit. Manuf., 25, pp. 347–356.
[244] Darvish, K., Chen, Z. W., and Pasang, T., 2016, "Reducing Lack of Fusion during Selective Laser Melting of CoCrMo Alloy: Effect of Laser Power on Geometrical Features of Tracks," Mater. Des., 112, pp. 357–366.
[245] Zhou, X., Liu, X., Zhang, D., Shen, Z., and Liu, W., 2015, "Balling Phenomena in Selective Laser Melted Tungsten," J. Mater. Process. Technol., 222, pp. 33–42.
[246] Gu, D., and Shen, Y., 2009, "Balling Phenomena in Direct Laser Sintering of Stainless Steel Powder: Metallurgical Mechanisms and Control Methods," Mater. Des., 30(8), pp. 2903–2910.
[247] Li, R., Liu, J., Shi, Y., Wang, L., and Jiang, W., 2012, "Balling Behavior of Stainless Steel and Nickel Powder during Selective Laser Melting Process," Int. J. Adv. Manuf. Technol., 59(9), pp. 1025–1035.
[248] Körner, C., Attar, E., and Heinl, P., 2011, "Mesoscopic Simulation of Selective Beam Melting Processes," J. Mater. Process. Technol., 211(6), pp. 978–987.
[249] Pyka, G., Kerckhofs, G., Papantoniou, I., Speirs, M., Schrooten, J., and Wevers, M., 2013, "Surface Roughness and Morphology Customization of Additive Manufactured Open Porous Ti6Al4V Structures," Materials, 6(10), pp. 4737–4757.
[250] Leary, M., 2017, "Surface Roughness Optimisation for Selective Laser Melting (SLM): Accommodating Relevant and Irrelevant Surfaces," *Laser Additive Manufacturing*, M. Brandt, ed., Woodhead Publishing, pp. 99–118.

[251] Demir, A. G., Colombo, P., and Previtali, B., 2017, "From Pulsed to Continuous Wave Emission in SLM with Contemporary Fiber Laser Sources: Effect of Temporal and Spatial Pulse Overlap in Part Quality," Int. J. Adv. Manuf. Technol., 91(5), pp. 2701–2714.
[252] Nickel, A. H., Barnett, D. M., and Prinz, F. B., 2001, "Thermal Stresses and Deposition Patterns in Layered Manufacturing," Mater. Sci. Eng. A, 317(1), pp. 59–64.
[253] Mishurova, T., Cabeza, S., Thiede, T., Nadammal, N., Kromm, A., Klaus, M., Genzel, C., Haberland, C., and Bruno, G., 2018, "The Influence of the Support Structure on Residual Stress and Distortion in SLM Inconel 718 Parts," Metall. Mater. Trans. A, 49(7), pp. 3038–3046.
[254] Totten, G. E., and MacKenzie, D. S., 2003, *Handbook of Aluminum: Physical Metallurgy and Processes*, CRC Press, United States of America.
[255] Xing, W., Ouyang, D., Li, N., and Liu, L., 2018, "Estimation of Residual Stress in Selective Laser Melting of a Zr-Based Amorphous Alloy," Materials, 11(8).
[256] Gupta, M., 2018, *3D Printing of Metals*, Multidisciplinary Digital Publishing Institute, Singapore.
[257] Sewell, N., Hao, L., and Dadbakhsh, S., 2012, "Effect of Selective Laser Melting Layout on the Quality of Stainless Steel Parts," Rapid Prototyp. J., 18(3), pp. 241–249.
[258] Parry, L., Ashcroft, I. A., and Wildman, R. D., 2016, "Understanding the Effect of Laser Scan Strategy on Residual Stress in Selective Laser Melting through Thermo-Mechanical Simulation," Addit. Manuf., 12, pp. 1–15.
[259] Li, C., Liu, Z. Y., Fang, X. Y., and Guo, Y. B., 2018, "Residual Stress in Metal Additive Manufacturing," *4th Conference on Surface Integrity*, pp. 348–353.
[260] Zhang, B., Li, Y., and Bai, Q., 2017, "Defect Formation Mechanisms in Selective Laser Melting: A Review," Chin. J. Mech. Eng., 30(3), pp. 515–527.
[261] Wissenbach, K., Höges, S., Robotti, P., Molinari, A., Facchini, L., and Magalini, E., 2010, "Ductility of a Ti-6Al-4V Alloy Produced by Selective Laser Melting of Prealloyed Powders," Rapid Prototyp. J., 16(6), pp. 450–459.
[262] Gu, D., Hagedorn, Y.-C., Meiners, W., Meng, G., Batista, R. J. S., Wissenbach, K., and Poprawe, R., 2012, "Densification Behavior, Microstructure Evolution, and Wear Performance of Selective Laser Melting Processed Commercially Pure Titanium," Acta Mater., 60(9), pp. 3849–3860.
[263] Mercelis, P., and Kruth, J., 2006, "Residual Stresses in Selective Laser Sintering and Selective Laser Melting," Rapid Prototyp. J., 12(5), pp. 254–265.
[264] Fu, C. H., and Guo, Y. B., 2014, "Three-Dimensional Temperature Gradient Mechanism in Selective Laser Melting of Ti-6Al-4V," J. Manuf. Sci. Eng., 136(6).
[265] Liu, Y., Yang, Y., and Wang, D., 2017, "Investigation into the Shrinkage in Z-Direction of Components Manufactured by Selective Laser Melting (SLM)," Int. J. Adv. Manuf. Technol., 90(9), pp. 2913–2923.
[266] Dai, K., and Shaw, L., 2005, "Finite Element Analysis of the Effect of Volume Shrinkage during Laser Densification," Acta Mater., 53(18), pp. 4743–4754.
[267] Zhu, H. H., Lu, L., and Fuh, J. Y. H., 2006, "Study on Shrinkage Behaviour of Direct Laser Sintering Metallic Powder," J. Eng. Manuf., 220(2), pp. 183–190.
[268] Ning, Y., Wong, Y. S., Fuh, J. Y. H., and Loh, H. T., 2006, "An Approach to Minimize Build Errors in Direct Metal Laser Sintering," IEEE Trans. Autom. Sci. Eng., 3(1), pp. 73–80.

[269] Lu, J., Luo, Z., Yang, Y., and Wang, D., 2012, “Accuracy and Density Optimization in Directly Fabricating Customized Orthodontic Production by Selective Laser Melting,” Rapid Prototyp. J., 18(6), pp. 482–489.
[270] Loh, L.-E., Chua, C.-K., Yeong, W.-Y., Song, J., Mapar, M., Sing, S.-L., Liu, Z.-H., and Zhang, D.-Q., 2015, “Numerical Investigation and an Effective Modelling on the Selective Laser Melting (SLM) Process with Aluminium Alloy 6061,” Int. J. Heat Mass Transf., 80, pp. 288–300.
[271] Edwards, P., and Ramulu, M., 2014, “Fatigue Performance Evaluation of Selective Laser Melted Ti–6Al–4V,” Mater. Sci. Eng. A, 598, pp. 327–337.
[272] Yan, F., Xiong, W., and Faierson, E. J., 2017, “Grain Structure Control of Additively Manufactured Metallic Materials,” Materials, 10(11).
[273] Kunze, K., Etter, T., Grässlin, J., and Shklover, V., 2015, “Texture, Anisotropy in Microstructure and Mechanical Properties of IN738LC Alloy Processed by Selective Laser Melting (SLM),” Mater. Sci. Eng. A, 620, pp. 213–222.
[274] Popovich, V. A., Borisov, E. V., Popovich, A. A., Sufiiarov, V. Sh., Masaylo, D. V., and Alzina, L., 2017, “Functionally Graded Inconel 718 Processed by Additive Manufacturing: Crystallographic Texture, Anisotropy of Microstructure and Mechanical Properties,” Mater. Des., 114, pp. 441–449.
[275] Gong, X., Lydon, J., Cooper, K., and Chou, K., 2014, “Beam Speed Effects on Ti–6Al–4V Microstructures in Electron Beam Additive Manufacturing,” J. Mater. Res., 29(17), pp. 1951–1959.
[276] Scharowsky, T., Juechter, V., Singer, R. F., and Körner, C., 2015, “Influence of the Scanning Strategy on the Microstructure and Mechanical Properties in Selective Electron Beam Melting of Ti–6Al–4V,” Adv. Eng. Mater., 17(11), pp. 1573–1578.
[277] Marya, M., Singh, V., Marya, S., and Hascoet, J. Y., 2015, “Microstructural Development and Technical Challenges in Laser Additive Manufacturing: Case Study with a 316L Industrial Part,” Metall. Mater. Trans. B, 46(4), pp. 1654–1665.
[278] Vaithilingam, J., Goodridge, R. D., Hague, R. J. M., Christie, S. D. R., and Edmondson, S., 2016, “The Effect of Laser Remelting on the Surface Chemistry of Ti6al4V Components Fabricated by Selective Laser Melting,” J. Mater. Process. Technol., 232, pp. 1–8.
[279] Chen, M., Li, X., Ji, G., Wu, Y., Chen, Z., Baekelant, W., Vanmeensel, K., Wang, H., and Kruth, J.-P., 2017, “Novel Composite Powders with Uniform TiB2 Nano-Particle Distribution for 3D Printing,” Appl. Sci., 7(3), pp. 1–9.
[280] Perminov, A., Bartzsch, G., Franke, A., Biermann, H., and Volkova, O., 2021, “Manufacturing Fe–TiC Composite Powder via Inert Gas Atomization by Forming Reinforcement Phase In Situ,” Adv. Eng. Mater., 23(3), pp. 1–11.
[281] Yeh, T. Y., and Peng, K. Y., 2016, “Characterization of Simultaneously Gas Atomized Ti/TiC Composite Powders,” Key Eng. Mater., 704, pp. 302–307.
[282] Yamanoglu, R., Zeren, M., and German, R. M., 2012, “Solidification Characteristics of Atomized AlCu4Mg1-SiC Composite Powders,” J. Min. Metall. B Metall., 48(1), pp. 73–79.
[283] Wang, C., Liu, Y., Liu, H., Yang, T., Chen, X., Yang, S., and Liu, X., 2015, “A Novel Self-Assembling Al-Based Composite Powder with High Hydrogen Generation Efficiency,” Sci. Rep., 5(1).
[284] Mair, P., and Kaserer, L., 2021, “Microstructure and Mechanical Properties of a TiB2-Modified Al–Cu Alloy Processed by Laser Powder-Bed Fusion,” Mater. Sci. Eng. A, 799.

[285] Li, X., Heisterüber, L., Achelis, L., and Fritsching, U., 2016, “Multiscale Descriptions of Particle-Droplet Interactions in Multiphase Spray Processing,” Int. J. Multiph. Flow, 80, pp. 15–28.
[286] Eslamian, M., Rak, J., and Ashgriz, N., 2008, “Preparation of Aluminum/Silicon Carbide Metal Matrix Composites Using Centrifugal Atomization,” Powder Technol., 184(1), pp. 11–20.
[287] Wu, Y., and Lavernia, E. J., 1992, “Interaction Mechanisms between Ceramic Particles and Atomized Metallic Droplets,” Metall. Trans. A, 23(10), pp. 2923–2937.
[288] Li, X., Heisteruber, L., Achelis, L., Uhlenwinkel, V., and Fritsching, U., 2011, “Spray Process Modelling in Metal Matrix Composite Powder Production,” At. Sprays, 21(11), pp. 933–943.
[289] Song, B., Wang, Z., Yan, Q., Zhang, Y., Zhang, J., Cai, C., Wei, Q., and Shi, Y., 2017, “Integral Method of Preparation and Fabrication of Metal Matrix Composite: Selective Laser Melting of in-Situ Nano/Submicro-Sized Carbides Reinforced Iron Matrix Composites,” Mater. Sci. Eng. A, 707, pp. 478–487.
[290] Verma, P. K., Warghane, S., Nichul, U., Kumar, P., Dhole, A., and Hiwarkar, V., 2021, “Effect of Boron Addition on Microstructure, Hardness and Wear Performance of Ti-6Al-4 V Alloy Manufactured by Laser Powder Bed Fusion Additive Manufacturing,” Mater. Charact., 172.
[291] Gu, D., Wang, H., and Zhang, G., 2014, “Selective Laser Melting Additive Manufacturing of Ti-Based Nanocomposites: The Role of Nanopowder,” Metall. Mater. Trans. A, 45(1), pp. 464–476.
[292] Zhao, T., Dahmen, M., Cai, W., Alkhayat, M., Schaible, J., Albus, P., Zhong, C., Hong, C., Biermann, T., Zhang, H., Gu, D., Weisheit, A., Gasser, A., and Schleifenbaum, J. H., 2020, “Laser Metal Deposition for Additive Manufacturing of AA5024 and Nanoparticulate TiC Modified AA5024 Alloy Composites Prepared with Balling Milling Process,” Opt. Laser Technol., 131.
[293] Zhang, F., Mei, M., Al-Hamdani, K., Tan, H., and Clare, A. T., 2018, “Novel Nucleation Mechanisms through Satelliting in Direct Metal Deposition of Ti-15Mo,” Mater. Lett., 213, pp. 197–200.
[294] Zeng, X., Yu, J., Fu, D., Zhang, H., and Teng, J., 2018, “Wear Characteristics of Hybrid Aluminum-Matrix Composites Reinforced with Well-Dispersed Reduced Graphene Oxide Nanosheets and Silicon Carbide Particulates,” Vacuum, 155, pp. 364–375.
[295] Zhang, X., Song, F., Wei, Z., Yang, W., and Dai, Z., 2017, “Microstructural and Mechanical Characterization of In-Situ TiC/Ti Titanium Matrix Composites Fabricated by Graphene/Ti Sintering Reaction,” Mater. Sci. Eng. A, 705, pp. 153–159.
[296] Li, M., Wu, X., Yang, Y., Wei, Q., Yan, C., Cai, C., Liu, J., Li, W., and Shi, Y., 2018, “TiAl/RGO (Reduced Graphene Oxide) Bulk Composites with Refined Microstructure and Enhanced Nanohardness Fabricated by Selective Laser Melting (SLM),” Mater. Charact., 143, pp. 197–205.
[297] Zhou, W., Sun, X., Kikuchi, K., Nomura, N., Yoshimi, K., and Kawasaki, A., 2018, “In Situ Synthesized TiC/Mo-Based Composites via Laser Powder Bed Fusion,” Mater. Des., 146, pp. 116–124.
[298] Ren, S., Chen, J., He, X., and Qu, X., 2018, “Effect of Matrix-Alloying-Element Chromium on the Microstructure and Properties of Graphite Flakes/Copper Composites Fabricated by Hot Pressing Sintering,” Carbon, 127, pp. 412–423.

[299] Zhang, L., and Hou, G., 2018, “Aluminum/Graphene Composites with Enhanced Heat-Dissipation Properties by in-Situ Reduction of Graphene Oxide on Aluminum Particles,” J. Alloys Compd., 748, pp. 854–860.
[300] Chen, H., Hong, R., Liu, Q., Li, S., Huang, F., Lu, Y., Wang, L., Li, K., and Zhang, H., 2018, “CNFs@carbonaceous Co/CoO Composite Derived from CNFs Penetrated through ZIF-67 for High-Efficient Electromagnetic Wave Absorption Material,” J. Alloys Compd., 752, pp. 115–122.
[301] Han, T., Li, J., Zhao, N., Shi, C., Liu, E., He, F., Ma, L., Li, Q., and He, C., 2017, “In-Situ Fabrication of Nano-Sized TiO2 Reinforced Cu Matrix Composites with Well-Balanced Mechanical Properties and Electrical Conductivity,” Powder Technol., 321, pp. 66–73.
[302] Zhou, W., Sun, X., Kikuchi, K., Nomura, N., Yoshimi, K., and Kawasaki, A., 2018, “Carbon Nanotubes as a Unique Agent to Fabricate Nanoceramic/Metal Composite Powders for Additive Manufacturing,” Mater. Des., 137, pp. 276–285.
[303] Martin, J. H., Yahata, B. D., Clough, E. C., Mayer, J. A., Hundley, J. M., and Schaedler, T. A., 2018, “Additive Manufacturing of Metal Matrix Composites via Nanofunctionalization,” MRS Commun., 8(2), pp. 297–302.
[304] Saboori, A., Moheimani, S. K., Dadkhah, M., Pavese, M., Badini, C., and Fino, P., 2018, “An Overview of Key Challenges in the Fabrication of Metal Matrix Nanocomposites Reinforced by Graphene Nanoplatelets,” Metals, 8(3).
[305] Mahmood, M. A., Popescu, A. C., and Mihailescu, I. N., 2020, “Metal Matrix Composites Synthesized by Laser-Melting Deposition: A Review,” Materials, 13(11).
[306] Garg, P., Jamwal, A., Kumar, D., Sadasivuni, K. K., Hussain, C. M., and Gupta, P., 2019, “Advance Research Progresses in Aluminium Matrix Composites: Manufacturing & Applications,” J. Mater. Res. Technol., 8(5), pp. 4924–4939.
[307] Tjong, S. C., and Ma, Z. Y., 2000, “Microstructural and Mechanical Characteristics of in Situ Metal Matrix Composites,” Mater. Sci. Eng. R Rep., 29(3), pp. 49–113.
[308] Li, N., Liu, W., Wang, Y., Zhao, Z., Yan, T., Zhang, G., and Xiong, H., 2021, “Laser Additive Manufacturing on Metal Matrix Composites: A Review,” Chin. J. Mech. Eng., 34(1).
[309] Angelo, P. C., and Sabramanian, R., 2009, *Powder Metallurgy: Science, Technology and Applications*, PHI Learning, New Delhi.
[310] Suthar, J., and Patel, K. M., 2018, “Processing Issues, Machining, and Applications of Aluminum Metal Matrix Composites,” Mater. Manuf. Process., 33(5), pp. 499–527.
[311] Meier, C., Weissbach, R., Weinberg, J., Wall, W. A., and Hart, A. J., 2019, “Critical Influences of Particle Size and Adhesion on the Powder Layer Uniformity in Metal Additive Manufacturing,” J. Mater. Process. Technol., 266, pp. 484–501.
[312] Ge, Q., Gu, D., Dai, D., Ma, C., Sun, Y., Shi, X., Li, Y., Zhang, H., and Chen, H., 2021, “Mechanisms of Laser Energy Absorption and Melting Behavior during Selective Laser Melting of Titanium-Matrix Composite: Role of Ceramic Addition,” J. Phys. Appl. Phys., 54(11).
[313] Tolochko, N. K., Khlopkov, Y. V., Mozzharov, S. E., Ignatiev, M. B., Laoui, T., and Titov, V. I., 2000, “Absorptance of Powder Materials Suitable for Laser Sintering,” Rapid Prototyp. J., 6(3), pp. 155–161.
[314] Zhang, J., Gu, D., Yang, Y., Zhang, H., Chen, H., Dai, D., and Lin, K., 2019, “Influence of Particle Size on Laser Absorption and Scanning Track Formation

Mechanisms of Pure Tungsten Powder During Selective Laser Melting," Engineering, 5(4), pp. 736–745.
[315] Yang, Y., Gu, D., Dai, D., and Ma, C., 2018, "Laser Energy Absorption Behavior of Powder Particles Using Ray Tracing Method during Selective Laser Melting Additive Manufacturing of Aluminum Alloy," Mater. Des., 143, pp. 12–19.
[316] Constantin, L., Kraiem, N., Wu, Z., Cui, B., Battaglia, J.-L., Garnier, C., Silvain, J.-F., and Lu, Y. F., 2021, "Manufacturing of Complex Diamond-Based Composite Structures via Laser Powder-Bed Fusion," Addit. Manuf., 40.
[317] Sercombe, T. B., and Li, X., 2016, "Selective Laser Melting of Aluminium and Aluminium Metal Matrix Composites: Review," Mater. Technol., 31(2), pp. 77–85.
[318] Tang, S., Ummethala, R., Suryanarayana, C., Eckert, J., Prashanth, K. G., and Wang, Z., "Additive Manufacturing of Aluminum-Based Metal Matrix Composites—A Review," Adv. Eng. Mater.
[319] Jäcklein, M., Pfaff, A., and Hoschke, K., 2020, "Developing Tungsten-Filled Metal Matrix Composite Materials Using Laser Powder Bed Fusion," Appl. Sci., 10(24).
[320] Ertugrul, O., Park, H.-S., Onel, K., and Willert-Porada, M., 2015, "Structure and Properties of SiC and Emery Powder Reinforced PM 316l Matrix Composites Produced by Microwave and Conventional Sintering," Powder Metall., 58(1), pp. 41–50.
[321] Patankar, S. N., and Tan, M. J., 2000, "Role of Reinforcement in Sintering of SiC/316L Stainless Steel Composite," Powder Metall., 43(4), pp. 350–352.
[322] Patankar, S. N., Chandrasekaran, M., and Tan, M. J., 2000, "Matrix Reinforcement Interaction in SiC/316L Stainless Steel Composite," J. Mater. Sci. Lett., 19(7), pp. 613–615.
[323] Lin, S., and Xiong, W., 2012, "Microstructure and Abrasive Behaviors of TiC-316L Composites Prepared by Warm Compaction and Microwave Sintering," Adv. Powder Technol., 23(3), pp. 419–425.
[324] Pagounis, E., and Lindroos, V. K., 1998, "Processing and Properties of Particulate Reinforced Steel Matrix Composites," Mater. Sci. Eng. A, 246(1), pp. 221–234.
[325] Jin, C., and Plucknett, K. P., 2016, "Microstructure Instability in TiC-316L Stainless Steel Cermets," Int. J. Refract. Met. Hard Mater., 58, pp. 74–83.
[326] Simchi, A., and Petzoldt, F., 2009, "Cosintering of Powder Injection Molding Parts Made from Ultrafine WC-Co and 316L Stainless Steel Powders for Fabrication of Novel Composite Structures," Metall. Mater. Trans. A, 41(1).
[327] Kawakami, Y., Tamai, F., Enjoji, T., Takashima, K., and Otsu, M., 2007, "Wear Resistance Properties of Tungsten Carbide/Stainless Steel Composite Materials Prepared by Pulsed Current Sintering," Mater. Sci. Forum, 534–536, pp. 1573–1576.
[328] Chuankrerkkul, N., Borwornkiatkaew, W., Pornpijit, A., and Charojrochkul, S., 2011, "Processing, Microstructure and Properties of 316L Stainless Steel-Tungsten Carbide Composites," Malays. J. Microsc., 7, pp. 31–35.
[329] Zou, Y., Tan, C., Qiu, Z., Ma, W., Kuang, M., and Zeng, D., 2021, "Additively Manufactured SiC-Reinforced Stainless Steel with Excellent Strength and Wear Resistance," Addit. Manuf., 41.
[330] AlMangour, B., Grzesiak, D., Cheng, J., and Ertas, Y., 2018, "Thermal Behavior of the Molten Pool, Microstructural Evolution, and Tribological Performance during Selective Laser Melting of TiC/316L Stainless Steel Nanocomposites: Experimental and Simulation Methods," J. Mater. Process. Technol., 257, pp. 288–301.

[331] AlMangour, B., Grzesiak, D., and Yang, J.-M., 2017, "In-Situ Formation of Novel TiC-Particle-Reinforced 316L Stainless Steel Bulk-Form Composites by Selective Laser Melting," J. Alloys Compd., 706, pp. 409–418.
[332] AlMangour, B., Grzesiak, D., Borkar, T., and Yang, J.-M., 2018, "Densification Behavior, Microstructural Evolution, and Mechanical Properties of TiC/316L Stainless Steel Nanocomposites Fabricated by Selective Laser Melting," Mater. Des., 138, pp. 119–128.
[333] AlMangour, B., Grzesiak, D., and Jenn-MingYang, 2016, "Selective Laser Melting of TiC Reinforced 316L Stainless Steel Matrix Nanocomposites: Influence of Starting TiC Particle Size and Volume Content," Mater. Des., 104, pp. 141–151.
[334] Grzesiak, D., AlMangour, B., Krawczyk, M., Baek, M.-S., and Lee, K.-A., 2019, "Selective Laser Melting of TiC Reinforced Stainless Steel Nanocomposites: Mechanical Behaviour at Elevated Temperatures," Mater. Lett., 256.
[335] Zhao, S., Shen, X., Yang, J., Teng, W., and Wang, Y., 2018, "Densification Behavior and Mechanical Properties of Nanocrystalline TiC Reinforced 316L Stainless Steel Composite Parts Fabricated by Selective Laser Melting," Opt. Laser Technol., 103, pp. 239–250.
[336] Kotadia, H. R., Gibbons, G., Das, A., and Howes, P. D., 2021, "A Review of Laser Powder Bed Fusion Additive Manufacturing of Aluminium Alloys: Microstructure and Properties," Addit. Manuf., 46.
[337] Tofail, S. A. M., Koumoulos, E. P., Bandyopadhyay, A., Bose, S., O'Donoghue, L., and Charitidis, C., 2018, "Additive Manufacturing: Scientific and Technological Challenges, Market Uptake and Opportunities," Mater. Today, 21(1), pp. 22–37.
[338] Mussatto, A., Ahad, I. U., Mousavian, R. T., Delaure, Y., and Brabazon, D., 2020, "Advanced Production Routes for Metal Matrix Composites," Eng. Rep., pp. 1–25.
[339] Thomas-Seale, L. E. J., Kirkman-Brown, J. C., Attallah, M. M., Espino, D. M., and Shepherd, D. E. T., 2018, "The Barriers to the Progression of Additive Manufacture: Perspectives from UK Industry," Int. J. Prod. Econ., 198, pp. 104–118.
[340] Liu, C., Le Roux, L., Körner, C., Tabaste, O., Lacan, F., and Bigot, S., 2020, "Digital Twin-Enabled Collaborative Data Management for Metal Additive Manufacturing Systems," J. Manuf. Syst.
[341] Schmidt, M., Merklein, M., Bourell, D., Dimitrov, D., Hausotte, T., Wegener, K., Overmeyer, L., Vollertsen, F., and Levy, G. N., 2017, "Laser Based Additive Manufacturing in Industry and Academia," CIRP Ann., 66(2), pp. 561–583.
[342] Spears, T. G., and Gold, S. A., 2016, "In-Process Sensing in Selective Laser Melting (SLM) Additive Manufacturing," Integrating Mater. Manuf. Innov., 5(1), pp. 16–40.
[343] Dowling, L., Kennedy, J., O'Shaughnessy, S., and Trimble, D., 2020, "A Review of Critical Repeatability and Reproducibility Issues in Powder Bed Fusion," Mater. Des., 186, p. 108346.
[344] Oliveira, J. P., LaLonde, A. D., and Ma, J., 2020, "Processing Parameters in Laser Powder Bed Fusion Metal Additive Manufacturing," Mater. Des., 193(108762).
[345] ISO/ASTM52921, 2019, *Standard Terminology for Additive Manufacturing - Coordinate Systems and Test Methodologies*, ASTM International, West Conshohocken, PA.
[346] Karimi, P., Sadeghi, E., Ålgårdh, J., Harlin, P., and Andersson, J., 2020, "Effect of Build Location on Microstructural Characteristics and Corrosion Behavior of EB-PBF Built Alloy 718," Int. J. Adv. Manuf. Technol., 106(7), pp. 3597–3607.
[347] Calignano, F., 2018, "Investigation of the Accuracy and Roughness in the Laser Powder Bed Fusion Process," Virtual Phys. Prototyp., 13(2), pp. 97–104.

[348] Hitzler, L., Hirsch, J., Merkel, M., Hall, W., and Öchsner, A., 2017, "Position Dependent Surface Quality in Selective Laser Melting," Mater. Werkst., 48(5), pp. 327–334.
[349] Mertová, K., Džugan, J., Roudnická, M., Daniel, M., Vojtěch, D., Seifi, M., and Lewandowski, J. J., 2020, "Build Size and Orientation Influence on Mechanical Properties of Powder Bed Fusion Deposited Titanium Parts," Metals, 10(10), p. 1340.
[350] Croccolo, D., Agostinis, M. D., Fini, S., Olmi, G., Bogojevic, N., and Ciric-Kostic, S., 2018, "Effects of Build Orientation and Thickness of Allowance on the Fatigue Behaviour of 15–5 PH Stainless Steel Manufactured by DMLS," Fatigue Fract. Eng. Mater. Struct., 41(4), pp. 900–916.
[351] Shen, H., Rometsch, P., Wu, X., and Huang, A., 2020, "Influence of Gas Flow Speed on Laser Plume Attenuation and Powder Bed Particle Pickup in Laser Powder Bed Fusion," JOM, 72(3), pp. 1039–1051.
[352] Obeidi, M. A., Mussatto, A., Groarke, R., Vijayaraghavan, R. K., Conway, A., Rossi Kaschel, F., McCarthy, E., Clarkin, O., O'Connor, R., and Brabazon, D., 2020, "Comprehensive Assessment of Spatter Material Generated during Selective Laser Melting of Stainless Steel," Mater. Today Commun., 25, p. 101294.
[353] Chua, G. K. H., Choong, Y. Y. C., and Wong, C. H., 2018, "Investigation of the Effects on the Print Location during Selective Laser Melting Process," *Proceedings of the 3rd International Conference on Progress in Additive Manufacturing*, Pro-AM Conference Papers, Singapore, pp. 613–618.
[354] Hrabe, N., and Quinn, T., 2013, "Effects of Processing on Microstructure and Mechanical Properties of a Titanium Alloy (Ti–6Al–4V) Fabricated Using Electron Beam Melting (EBM), Part 2: Energy Input, Orientation, and Location," Mater. Sci. Eng. A, 573, pp. 271–277.
[355] Re, F. D., Scherillo, F., Contaldi, V., Palumbo, B., Squillace, A., Corrado, P., and Petta, P. D., 2019, "Mechanical Properties Characterisation of AlSi10Mg Parts Produced by Laser Powder Bed Fusion Additive Manufacturing," Int. J. Mater. Res., 110(5), pp. 436–446.
[356] Seifi, M., Dahar, M., Aman, R., Harrysson, O., Beuth, J., and Lewandowski, J. J., 2015, "Evaluation of Orientation Dependence of Fracture Toughness and Fatigue Crack Propagation Behavior of As-Deposited ARCAM EBM Ti-6Al-4V," JOM, 67(3), pp. 597–607.
[357] Drexler, M., Lexow, M., and Drummer, D., 2015, "Selective Laser Melting of Polymer Powder - Part Mechanics as Function of Exposure Speed," Phys. Procedia, 78, pp. 328–336.
[358] Grasso, M., and Colosimo, B. M., 2017, "Process Defects and in Situ Monitoring Methods in Metal Powder Bed Fusion: A Review," Meas. Sci. Technol., 28(4), pp. 1–25.
[359] Moorthy, S., 2017, "Modeling and Characterization of Mechanical Properties in Laser Powder Bed Fusion Additive Manufactured Inconel 718," Masters theses, Colorado School of Mines.
[360] Soltani-Tehrani, A., Pegues, J., and Shamsaei, N., 2020, "Fatigue Behavior of Additively Manufactured 17-4 PH Stainless Steel: The Effects of Part Location and Powder Re-Use," Addit. Manuf., 36, p. 101398.
[361] Mussatto, A., Groarke, R., O'Neill, A., Obeidi, M. A., Delaure, Y., and Brabazon, D., 2021, "Influences of Powder Morphology and Spreading Parameters on the Powder Bed Topography Uniformity in Powder Bed Fusion Metal Additive Manufacturing," Addit. Manuf., 38, p. 101807.

[362] Cordova, L., Bor, T., de Smit, M., Campos, M., and Tinga, T., 2020, "Measuring the Spreadability of Pre-Treated and Moisturized Powders for Laser Powder Bed Fusion," Addit. Manuf., 32, p. 101082.
[363] Gibson, B. T., and Lowden, R. A., 2018, *Process Development for Selective Laser Melting of Molybdenum*, ORNL/SPR-2018/1045, Oak Ridge National Laboratory, United States.
[364] Alfaify, A., 2019, "The Effect of Changing Particle Size Distribution and Layer Thickness on the Density of Parts Manufactured Using the Laser Powder Bed Fusion Process," PhD thesis, University of Sheffield.
[365] ASTM E8/E8M, 2009, *Standard Test Methods for Tension Testing of Metallic Materials*, ASTM International, West Conshohocken, PA.
[366] ASTM B962, 2017, *Standard Test Methods for Density of Compacted or Sintered Powder Metallurgy (PM) Products Using Archimedes' Principle*, ASTM International, West Conshohocken, PA.
[367] ASTM E92, 2017, *Standard Test Methods for Vickers Hardness and Knoop Hardness of Metallic Materials*, West Conshohocken, PA.
[368] Zhang, B., Li, Y., and Bai, Q., 2017, "Defect Formation Mechanisms in Selective Laser Melting: A Review," Chin. J. Mech. Eng., 30(3), pp. 515–527.
[369] Louvis, E., Fox, P., and Sutcliffe, C. J., 2011, "Selective Laser Melting of Aluminium Components," J. Mater. Process. Technol., 211(2), pp. 275–284.
[370] Das, S., 2003, "Physical Aspects of Process Control in Selective Laser Sintering of Metals," Adv. Eng. Mater., 5(10), pp. 701–711.
[371] Vilaro, T., Colin, C., and Bartout, J. D., 2011, "As-Fabricated and Heat-Treated Microstructures of the Ti-6Al-4V Alloy Processed by Selective Laser Melting," Metall. Mater. Trans. A, 42(10), pp. 3190–3199.
[372] de Terris, T., Andreau, O., Peyre, P., Adamski, F., Koutiri, I., Gorny, C., and Dupuy, C., 2019, "Optimization and Comparison of Porosity Rate Measurement Methods of Selective Laser Melted Metallic Parts," Addit. Manuf., 28, pp. 802–813.
[373] Yadroitsev, I., Gusarov, A., Yadroitsava, I., and Smurov, I., 2010, "Single Track Formation in Selective Laser Melting of Metal Powders," J. Mater. Process. Technol., 210(12), pp. 1624–1631.
[374] DebRoy, T., Wei, H. L., Zuback, J. S., Mukherjee, T., Elmer, J. W., Milewski, J. O., Beese, A. M., Wilson-Heid, A., De, A., and Zhang, W., 2018, "Additive Manufacturing of Metallic Components – Process, Structure and Properties," Prog. Mater. Sci., 92, pp. 112–224.
[375] Gunenthiram, V., Peyre, P., Schneider, M., Dal, M., Coste, F., and Fabbro, R., 2017, "Analysis of Laser–Melt Pool–Powder Bed Interaction during the Selective Laser Melting of a Stainless Steel," J. Laser Appl., 29(2), p. 022303.
[376] Reijonen, J., Revuelta, A., Riipinen, T., Ruusuvuori, K., and Puukko, P., 2020, "On the Effect of Shielding Gas Flow on Porosity and Melt Pool Geometry in Laser Powder Bed Fusion Additive Manufacturing," Addit. Manuf., 32.
[377] Marattukalam, J. J., Karlsson, D., Pacheco, V., Beran, P., Wiklund, U., Jansson, U., Hjörvarsson, B., and Sahlberg, M., 2020, "The Effect of Laser Scanning Strategies on Texture, Mechanical Properties, and Site-Specific Grain Orientation in Selective Laser Melted 316L SS," Mater. Des., 193, p. 108852.
[378] Liu, Y., Pang, Z., and Zhang, J., 2017, "Comparative Study on the Influence of Subsequent Thermal Cycling on Microstructure and Mechanical Properties of Selective Laser Melted 316L Stainless Steel," Appl. Phys. A, 123(11), p. 688.
[379] Laleh, M., Hughes, A. E., Xu, W., Haghdadi, N., Wang, K., Cizek, P., Gibson, I., and Tan, M. Y., 2019, "On the Unusual Intergranular Corrosion Resistance of 316L

Stainless Steel Additively Manufactured by Selective Laser Melting," Corros. Sci., 161, p. 108189.
[380] Rowe, L. C., 1977, "The Application of Corrosion Principles to Engineering Design," SAE Trans., 86, pp. 1379–1392.
[381] Virtanen, S., Schmuki, P., and Frankel, G. S., 2003, "Intergranular Corrosion Morphology and Growth Kinetics in High Strength Aluminium Alloys," *Critical Factors in Localized Corrosion IV: A Symposium in Honor of the 65th Birthday of Hans Böhni : Proceedings of the International Symposium*, The Electrochemical Society, Salt Lake City, United States, pp. 159–167.
[382] Ball, P., 2008, "Steel Toughened by Pancakes: New Treatment Set to Improve Steel's Properties at Low Cost," Nature, p. news.2008.851.
[383] Bahl, S., Mishra, S., Yazar, K. U., Kola, I. R., Chatterjee, K., and Suwas, S., 2019, "Non-Equilibrium Microstructure, Crystallographic Texture and Morphological Texture Synergistically Result in Unusual Mechanical Properties of 3D Printed 316L Stainless Steel," Addit. Manuf., 28, pp. 65–77.
[384] Obeidi, M. A., Uí Mhurchadha, S. M., Raghavendra, R., Conway, A., Souto, C., Tormey, D., Ahad, I. U., and Brabazon, D., 2021, "Comparison of the Porosity and Mechanical Performance of 316L Stainless Steel Manufactured on Different Laser Powder Bed Fusion Metal Additive Manufacturing Machines," J. Mater. Res. Technol., 13, pp. 2361–2374.
[385] Wang, Y. M., Voisin, T., McKeown, J. T., Ye, J., Calta, N. P., Li, Z., Zeng, Z., Zhang, Y., Chen, W., Roehling, T. T., Ott, R. T., Santala, M. K., Depond, P. J., Matthews, M. J., Hamza, A. V., and Zhu, T., 2018, "Additively Manufactured Hierarchical Stainless Steels with High Strength and Ductility," Nat. Mater., 17(1), pp. 63–71.
[386] Gallmeyer, T. G., Moorthy, S., Kappes, B. B., Mills, M. J., Amin-Ahmadi, B., and Stebner, A. P., 2020, "Knowledge of Process-Structure-Property Relationships to Engineer Better Heat Treatments for Laser Powder Bed Fusion Additive Manufactured Inconel 718," Addit. Manuf., 31.
[387] Liu, L., Ding, Q., Zhong, Y., Zou, J., Wu, J., Chiu, Y.-L., Li, J., Zhang, Z., Yu, Q., and Shen, Z., 2018, "Dislocation Network in Additive Manufactured Steel Breaks Strength–Ductility Trade-Off," Mater. Today, 21(4), pp. 354–361.
[388] Wang, X., Muñiz-Lerma, J. A., Sánchez-Mata, O., Attarian Shandiz, M., and Brochu, M., 2018, "Microstructure and Mechanical Properties of Stainless Steel 316L Vertical Struts Manufactured by Laser Powder Bed Fusion Process," Mater. Sci. Eng. A, 736, pp. 27–40.
[389] Röttger, A., Boes, J., Theisen, W., Thiele, M., Esen, C., Edelmann, A., and Hellmann, R., 2020, "Microstructure and Mechanical Properties of 316L Austenitic Stainless Steel Processed by Different SLM Devices," Int. J. Adv. Manuf. Technol., 108(3), pp. 769–783.
[390] Kempf, A., and Hilgenberg, K., 2020, "Influence of Sub-Cell Structure on the Mechanical Properties of AlSi10Mg Manufactured by Laser Powder Bed Fusion," Mater. Sci. Eng. A, 776.
[391] Cui, L., Jiang, F., Deng, D., Xin, T., Sun, X., Mousavian, R. T., Peng, R. L., Yang, Z., and Moverare, J., 2021, "Cyclic Response of Additive Manufactured 316L Stainless Steel: The Role of Cell Structures," Scr. Mater., 205.
[392] Callister, W., and Rethwisch, D. G., 2018, *Fundamentals of Materials Science and Engineering: An Integrated Approach*, John Wiley & Sons, New Jersey.

[393] Eschner, N., Weiser, L., Häfner, B., and Lanza, G., 2020, "Classification of Specimen Density in Laser Powder Bed Fusion (L-PBF) Using in-Process Structure-Borne Acoustic Process Emissions," Addit. Manuf., 34, p. 101324.
[394] Pal, S., Lojen, G., Kokol, V., and Drstvenšek, I., 2019, "Reducing Porosity at the Starting Layers above Supporting Bars of the Parts Made by Selective Laser Melting," Powder Technol., 355, pp. 268–277.
[395] Nath, S. D., Irrinki, H., Gupta, G., Kearns, M., Gulsoy, O., and Atre, S., 2019, "Microstructure-Property Relationships of 420 Stainless Steel Fabricated by Laser-Powder Bed Fusion," Powder Technol., 343, pp. 738–746.
[396] Bai, Y., Wagner, G., and Williams, C. B., 2017, "Effect of Particle Size Distribution on Powder Packing and Sintering in Binder Jetting Additive Manufacturing of Metals," J. Manuf. Sci. Eng., 139(8).
[397] Mindt, H. W., Megahed, M., Lavery, N. P., Holmes, M. A., and Brown, S. G. R., 2016, "Powder Bed Layer Characteristics: The Overseen First-Order Process Input," Metall. Mater. Trans. A, 47(8), pp. 3811–3822.
[398] Mao, K. S., Sun, C., Huang, Y., Shiau, C.-H., Garner, F. A., Freyer, P. D., and Wharry, J. P., 2019, "Grain Orientation Dependence of Nanoindentation and Deformation-Induced Martensitic Phase Transformation in Neutron Irradiated AISI 304L Stainless Steel," Materialia, 5, p. 100208.
[399] Fischer-Cripps, A. C., 2006, "Critical Review of Analysis and Interpretation of Nanoindentation Test Data," Surf. Coat. Technol., 200(14), pp. 4153–4165.
[400] Broitman, E., 2016, "Indentation Hardness Measurements at Macro-, Micro-, and Nanoscale: A Critical Overview," Tribol. Lett., 65(1), p. 23.
[401] Yakout, M., Elbestawi, M. A., and Veldhuis, S. C., 2019, "Density and Mechanical Properties in Selective Laser Melting of Invar 36 and Stainless Steel 316L," J. Mater. Process. Technol., 266, pp. 397–420.
[402] Musil, J., Kunc, F., Zeman, H., and Poláková, H., 2002, "Relationships between Hardness, Young's Modulus and Elastic Recovery in Hard Nanocomposite Coatings," Surf. Coat. Technol., 154(2), pp. 304–313.
[403] Briscoe, B. J., Fiori, L., and Pelillo, E., 1998, "Nano-Indentation of Polymeric Surfaces," J. Phys. Appl. Phys., 31(19), pp. 2395–2405.
[404] Nasim, M., Li, Y., and Wen, C., 2021, "Individual Layer Thickness-Dependent Nanoindentation and Nanotribological Behaviors of Ta/Co Nanolaminates," Tribol. Int., 156, p. 106845.
[405] Hynowska, A., Pellicer, E., Fornell, J., González, S., van Steenberge, N., Suriñach, S., Gebert, A., Calin, M., Eckert, J., Baró, M. D., and Sort, J., 2012, "Nanostructured β-Phase Ti–31.0Fe–9.0Sn and Sub-Mm Structured Ti–39.3Nb–13.3Zr–10.7Ta Alloys for Biomedical Applications: Microstructure Benefits on the Mechanical and Corrosion Performances," Mater. Sci. Eng. C, 32(8), pp. 2418–2425.
[406] Tiamiyu, A. A., Tari, V., Szpunar, J. A., Odeshi, A. G., and Khan, A. K., 2018, "Effects of Grain Refinement on the Quasi-Static Compressive Behavior of AISI 321 Austenitic Stainless Steel: EBSD, TEM, and XRD Studies," Int. J. Plast., 107, pp. 79–99.
[407] Tiamiyu, A. A., Odeshi, A. G., and Szpunar, J. A., 2018, "Multiple Strengthening Sources and Adiabatic Shear Banding during High Strain-Rate Deformation of AISI 321 Austenitic Stainless Steel: Effects of Grain Size and Strain Rate," Mater. Sci. Eng. A, 711, pp. 233–249.
[408] Ghanbari, S., and Bahr, D. F., 2019, "An Energy-Based Nanoindentation Method to Assess Localized Residual Stresses and Mechanical Properties on Shot-Peened Materials," J. Mater. Res., 34(7), pp. 1121–1129.

[409] Lee, J., Lee, C., and Kim, B., 2009, "Reverse Analysis of Nano-Indentation Using Different Representative Strains and Residual Indentation Profiles," Mater. Des., 30(9), pp. 3395–3404.
[410] Yan, F. K., Liu, G. Z., Tao, N. R., and Lu, K., 2012, "Strength and Ductility of 316L Austenitic Stainless Steel Strengthened by Nano-Scale Twin Bundles," Acta Mater., 60(3), pp. 1059–1071.
[411] Calcagnotto, M., Ponge, D., and Raabe, D., 2010, "Effect of Grain Refinement to 1μm on Strength and Toughness of Dual-Phase Steels," Mater. Sci. Eng. A, 527(29), pp. 7832–7840.
[412] Bartolomeu, F., Buciumeanu, M., Pinto, E., Alves, N., Carvalho, O., Silva, F. S., and Miranda, G., 2017, "316L Stainless Steel Mechanical and Tribological Behavior—A Comparison between Selective Laser Melting, Hot Pressing and Conventional Casting," Addit. Manuf., 16, pp. 81–89.
[413] Wang, Y. M., Voisin, T., McKeown, J. T., Ye, J., Calta, N. P., Li, Z., Zeng, Z., Zhang, Y., Chen, W., Roehling, T. T., Ott, R. T., Santala, M. K., Depond, P. J., Matthews, M. J., Hamza, A. V., and Zhu, T., 2018, "Additively Manufactured Hierarchical Stainless Steels with High Strength and Ductility," Nat. Mater., 17(1), pp. 63–71.
[414] Anwar, A. B., and Pham, Q.-C., 2017, "Selective Laser Melting of AlSi10Mg: Effects of Scan Direction, Part Placement and Inert Gas Flow Velocity on Tensile Strength," J. Mater. Process. Technol., 240, pp. 388–396.
[415] Rollett, A. D., and Kocks, U. F., 1993, *A Review of the Stages of Work Hardening*, LA-UR-93-2339; CONF-9304166-1, Los Alamos National Lab, New Mexico.
[416] Kurz, W., and Fisher, D. J., 1998, *Fundamentals of Solidification*, Trans Tech Publications Ltd, Zurich, Switzerland.
[417] Kocks, U. F., and Mecking, H., 2003, "Physics and Phenomenology of Strain Hardening: The FCC Case," Prog. Mater. Sci., 48(3), pp. 171–273.
[418] Zehetbauer, M., and Seumer, V., 1993, "Cold Work Hardening in Stages IV and V of F.C.C. Metals—I. Experiments and Interpretation," Acta Metall. Mater., 41(2), pp. 577–588.
[419] El-Danaf, E., Kalidindi, S. R., Doherty, R. D., and Necker, C., 2000, "Deformation Texture Transition in Brass: Critical Role of Micro-Scale Shear Bands," Acta Mater., 48(10), pp. 2665–2673.
[420] Wenk, H. R., 1985, *Preferred Orientation in Deformed Metal and Rocks: An Introduction to Modern Texture Analysis*, Academic Press Inc., California.
[421] Mussatto, A., Groarke, R., A-Hameed, A., Ahad, I. U. I., Vijayaraghavan, R. K., O'Neill, A., McNally, P., Delaure, Y., and Brabazon, D., 2019, "Evaluation via Powder Metallurgy of Nano-Reinforced Iron Powders Developed for Selective Laser Melting Applications," Mater. Des., 182, p. 108046.
[422] Sun, Z., Tan, X., Tor, S. B., and Chua, C. K., 2018, "Simultaneously Enhanced Strength and Ductility for 3D-Printed Stainless Steel 316L by Selective Laser Melting," NPG Asia Mater., 10(4), pp. 127–136.
[423] Khorsand Zak, A., Abd. Majid, W. H., Abrishami, M. E., and Yousefi, R., 2011, "X-Ray Analysis of ZnO Nanoparticles by Williamson–Hall and Size–Strain Plot Methods," Solid State Sci., 13(1), pp. 251–256.
[424] Fultz, B., and Howe, J. M., 2012, *Transmission Electron Microscopy and Diffractometry of Materials*, Springer Science & Business Media, Heidelberg.
[425] Humphreys, F. J., and Hatherly, M., 1995, *Recrystallization and Related Annealing Phenomena*, Elsevier Science Ltd, Oxford.

[426] Mola, J., 2017, “Considerations in the Design of Formable Austenitic Stainless Steels Based on Deformation-Induced Processes,” *Austenitic Stainless Steels - New Aspects*, IntechOpen, Croatia, pp. 7–28.
[427] Woo, W., Naeem, M., Jeong, J.-S., Lee, C.-M., Harjo, S., Kawasaki, T., He, H., and Wang, X.-L., 2020, “Comparison of Dislocation Density, Twin Fault Probability, and Stacking Fault Energy between CrCoNi and CrCoNiFe Medium Entropy Alloys Deformed at 293 and 140K,” Mater. Sci. Eng. A, 781, p. 139224.
[428] Schramm, R. E., and Reed, R. P., 1975, “Stacking Fault Energies of Seven Commercial Austenitic Stainless Steels,” Metall. Trans. A, 6(7), p. 1345.
[429] Teklu, A., Ledbetter, H., Kim, S., Boatner, L. A., McGuire, M., and Keppens, V., 2004, “Single-Crystal Elastic Constants of Fe-15Ni-15Cr Alloy,” Metall. Mater. Trans. A, 35(10), pp. 3149–3154.
[430] Wu, X. X., San, X. Y., Liang, X. G., Gong, Y. L., and Zhu, X. K., 2013, “Effect of Stacking Fault Energy on Mechanical Behavior of Cold-Forging Cu and Cu Alloys,” Mater. Des., 47, pp. 372–376.
[431] Branicio, P. S., Zhang, J. Y., and Srolovitz, D. J., 2013, “Effect of Strain on the Stacking Fault Energy of Copper: A First-Principles Study,” Phys. Rev. B, 88(6), p. 064104.
[432] Achmad, T. L., Fu, W., Chen, H., Zhang, C., and Yang, Z.-G., 2018, “Effect of Strain on the Intrinsic Stacking Fault Energy of Fcc Co: A First-Principles Study,” J. Mater. Sci., 53(14), pp. 10217–10230.
[433] Dovgyy, B., Piglione, A., Hooper, P. A., and Pham, M.-S., 2020, “Comprehensive Assessment of the Printability of CoNiCrFeMn in Laser Powder Bed Fusion,” Mater. Des., 194.
[434] Wan, H. Y., Zhou, Z. J., Li, C. P., Chen, G. F., and Zhang, G. P., 2018, “Effect of Scanning Strategy on Grain Structure and Crystallographic Texture of Inconel 718 Processed by Selective Laser Melting,” J. Mater. Sci. Technol., 34(10), pp. 1799–1804.
[435] Chen, L., Richter, B., Zhang, X., Bertsch, K. B., Thoma, D. J., and Pfefferkorn, F. E., 2021, “Effect of Laser Polishing on the Microstructure and Mechanical Properties of Stainless Steel 316L Fabricated by Laser Powder Bed Fusion,” Mater. Sci. Eng. A, 802.
[436] Riabov, D., Leicht, A., Ahlström, J., and Hryha, E., 2021, “Investigation of the Strengthening Mechanism in 316L Stainless Steel Produced with Laser Powder Bed Fusion,” Mater. Sci. Eng. A, 822.
[437] Voisin, T., Forien, J.-B., Perron, A., Aubry, S., Bertin, N., Samanta, A., Baker, A., and Wang, Y. M., 2021, “New Insights on Cellular Structures Strengthening Mechanisms and Thermal Stability of an Austenitic Stainless Steel Fabricated by Laser Powder-Bed-Fusion,” Acta Mater., 203.
[438] Hong, Y., Zhou, C., Zheng, Y., Zhang, L., and Zheng, J., 2021, “The Cellular Boundary with High Density of Dislocations Governed the Strengthening Mechanism in Selective Laser Melted 316L Stainless Steel,” Mater. Sci. Eng. A, 799.
[439] Donik, Č., Kraner, J., Paulin, I., and Godec, M., 2020, “Influence of the Energy Density for Selective Laser Melting on the Microstructure and Mechanical Properties of Stainless Steel,” Metals, 10(7).
[440] Leicht, A., Rashidi, M., Klement, U., and Hryha, E., 2020, “Effect of Process Parameters on the Microstructure, Tensile Strength and Productivity of 316L Parts Produced by Laser Powder Bed Fusion,” Mater. Charact., 159.

[441] Jaskari, M., Ghosh, S., Miettunen, I., Karjalainen, P., and Järvenpää, A., 2021, "Tensile Properties and Deformation of AISI 316L Additively Manufactured with Various Energy Densities," Materials, 14(19).
[442] Stansbury, E. E., and Buchanan, R. A., 2000, *Fundamentals of Electrochemical Corrosion*, ASM International, Ohio.
[443] ASTM G102-89, 2015, *Practice for Calculation of Corrosion Rates and Related Information from Electrochemical Measurements*, ASTM International, West Conshohocken, PA.
[444] Milošev, I., and Strehblow, H.-H., 2000, "The Behavior of Stainless Steels in Physiological Solution Containing Complexing Agent Studied by X-Ray Photoelectron Spectroscopy," J. Biomed. Mater. Res., 52(2), pp. 404–412.
[445] Chen, H., Zhang, C., Jia, D., Wellmann, D., and Liu, W., 2020, "Corrosion Behaviors of Selective Laser Melted Aluminum Alloys: A Review," Metals, 10(1), p. 102.
[446] Yuan, X.-Z. (Riny), Song, C., Wang, H., and Zhang, J., 2009, *Electrochemical Impedance Spectroscopy in PEM Fuel Cells: Fundamentals and Applications*, Springer Science & Business Media.
[447] Lvovich, V. F., 2012, *Impedance Spectroscopy: Applications to Electrochemical and Dielectric Phenomena*, John Wiley & Sons.
[448] Brug, G. J., van den Eeden, A. L. G., Sluyters-Rehbach, M., and Sluyters, J. H., 1984, "The Analysis of Electrode Impedances Complicated by the Presence of a Constant Phase Element," J. Electroanal. Chem. Interfacial Electrochem., 176(1), pp. 275–295.
[449] Orazem, M. E., and Tribollet, B., 2011, *Electrochemical Impedance Spectroscopy*, John Wiley & Sons.
[450] Lodhi, M. J. K., Deen, K. M., Greenlee-Wacker, M. C., and Haider, W., 2019, "Additively Manufactured 316L Stainless Steel with Improved Corrosion Resistance and Biological Response for Biomedical Applications," Addit. Manuf., 27, pp. 8–19.
[451] Balusamy, T., Kumar, S., and Sankara Narayanan, T. S. N., 2010, "Effect of Surface Nanocrystallization on the Corrosion Behaviour of AISI 409 Stainless Steel," Corros. Sci., 52(11), pp. 3826–3834.
[452] Di Schino, A., and Kenny, J. M., 2002, "Effects of the Grain Size on the Corrosion Behavior of Refined AISI 304 Austenitic Stainless Steels," J. Mater. Sci. Lett., 21(20), pp. 1631–1634.
[453] Helmholtz, H., 1879, "Studien Über Electrische Grenzschichten," Ann. Phys., 243(7), pp. 337–382.
[454] Burt, R., Birkett, G., and Zhao, X. S., 2014, "A Review of Molecular Modelling of Electric Double Layer Capacitors," Phys. Chem. Chem. Phys., 16(14), pp. 6519–6538.
[455] Brown, S. D., Tauler, R., and Walczak, B., 2020, *Comprehensive Chemometrics: Chemical and Biochemical Data Analysis*, Elsevier, Amsterdam, Netherlands.
[456] Huang, D. J., and Li, H., 2021, "A Machine Learning Guided Investigation of Quality Repeatability in Metal Laser Powder Bed Fusion Additive Manufacturing," Mater. Des., 203, p. 109606.
[457] Ladewig, A., Schlick, G., Fisser, M., Schulze, V., and Glatzel, U., 2016, "Influence of the Shielding Gas Flow on the Removal of Process By-Products in the Selective Laser Melting Process," Addit. Manuf., 10, pp. 1–9.
[458] Ma, L., Wiame, F., Maurice, V., and Marcus, P., 2019, "Origin of Nanoscale Heterogeneity in the Surface Oxide Film Protecting Stainless Steel against Corrosion," Npj Mater. Degrad., 3(1), pp. 1–9.

[459] Mraied, H., Wang, W., and Cai, W., 2019, “Influence of Chemical Heterogeneity and Microstructure on the Corrosion Resistance of Biodegradable WE43 Magnesium Alloys,” J. Mater. Chem. B, 7(41), pp. 6399–6411.
[460] Moshiri, M., Candeo, S., Carmignato, S., Mohanty, S., and Tosello, G., 2019, “Benchmarking of Laser Powder Bed Fusion Machines,” J. Manuf. Mater. Process., 3(4), p. 85.
[461] Ahmed, A., Majeed, A., Atta, Z., and Jia, G., 2019, “Dimensional Quality and Distortion Analysis of Thin-Walled Alloy Parts of AlSi10Mg Manufactured by Selective Laser Melting,” J. Manuf. Mater. Process., 3(2), p. 51.
[462] Meyer, B., 2012, *Accuracy in Additive Manufacturing: A Common Mistake Is to Confuse High Resolution with Accuracy*, Penton Media, Inc.
[463] Qin, Y., Qi, Q., Scott, P. J., and Jiang, X., 2019, “Status, Comparison, and Future of the Representations of Additive Manufacturing Data,” Comput.-Aided Des., 111, pp. 44–64.
[464] Energetics Incorporated, 2013, *Measurement Science Roadmap for Metal-Based Additive Manufacturing*, National Institute of Standards and Technology, U.S. Department of Commerce, Maryland.
[465] Franchitti, S., Borrelli, R., Pirozzi, C., Carrino, L., Polini, W., Sorrentino, L., and Gazzerro, A., 2018, “Investigation on Electron Beam Melting: Dimensional Accuracy and Process Repeatability,” Vacuum, 157, pp. 340–348.
[466] Kim, D. B., Witherell, P., Lu, Y., and Feng, S., 2017, “Toward a Digital Thread and Data Package for Metals-Additive Manufacturing,” Smart Sustain. Manuf. Syst., 1(1), pp. 75–99.
[467] Plesser, H. E., 2018, “Reproducibility vs. Replicability: A Brief History of a Confused Terminology,” Front. Neuroinformatics, 11(76), pp. 1–4.
[468] McArthur, S. L., 2019, “Repeatability, Reproducibility, and Replicability: Tackling the 3R Challenge in Biointerface Science and Engineering,” Biointerphases, 14(2), p. 020201.
[469] ISO 5725-1, 1994, *Accuracy (Trueness and Precision) of Measurement Methods and Results - Part 1: General Principles and Definitions*, International Organization for Standardization, Geneva, Switzerland.
[470] National Academies of Sciences, Engineering, and Medicine, 2019, *Reproducibility and Replicability in Science*, The National Academies Press, Washington, DC.
[471] ASTM International, “Additive Manufacturing Technology Standards” [Online]. Available: https://www.astm.org/Standards/additive-manufacturing-technology-standards.html.
[472] ISO/ASTM52900, 2015, *Standard Terminology for Additive Manufacturing - General Principles - Terminology*, ASTM International, West Conshohocken, PA.
[473] Schmeiser, F., Krohmer, E., Schell, N., Uhlmann, E., and Reimers, W., 2020, “Experimental Observation of Stress Formation during Selective Laser Melting Using in Situ X-Ray Diffraction,” Addit. Manuf., 32.
[474] Gibson, I., Rosen, D., and Stucker, B., 2015, *Additive Manufacturing Technologies: 3D Printing, Rapid Prototyping, and Direct Digital Manufacturing*, Springer.
[475] Childerhouse, T., and Jackson, M., 2019, “Near Net Shape Manufacture of Titanium Alloy Components from Powder and Wire: A Review of State-of-the-Art Process Routes,” Metals, 9(6), p. 689.

[476] Kruth, J.-P., Levy, G., Klocke, F., and Childs, T. H. C., 2007, "Consolidation Phenomena in Laser and Powder-Bed Based Layered Manufacturing," CIRP Ann., 56(2), pp. 730–759.
[477] Das, S., 2003, "Physical Aspects of Process Control in Selective Laser Sintering of Metals," Adv. Eng. Mater., 5(10), pp. 701–711.
[478] Gu, D., Xia, M., and Dai, D., 2019, "On the Role of Powder Flow Behavior in Fluid Thermodynamics and Laser Processability of Ni-Based Composites by Selective Laser Melting," Int. J. Mach. Tools Manuf., 137, pp. 67–78.
[479] Escano, L. I., Parab, N. D., Xiong, L., Guo, Q., Zhao, C., Fezzaa, K., Everhart, W., Sun, T., and Chen, L., 2018, "Revealing Particle-Scale Powder Spreading Dynamics in Powder-Bed-Based Additive Manufacturing Process by High-Speed x-Ray Imaging," Sci. Rep., 8(1), pp. 1–11.
[480] Narayan, R., 2019, *Rapid Prototyping of Biomaterials: Techniques in Additive Manufacturing*, Woodhead Publishing.
[481] Yang, L., Hsu, K., Baughman, B., Godfrey, D., Medina, F., Menon, M., and Wiener, S., 2017, *Additive Manufacturing of Metals: The Technology, Materials, Design and Production*, Springer.
[482] Mussatto, A., Groarke, R., A-Hameed, A., Ahad, I. U. I., Vijayaraghavan, R. K., O'Neill, A., McNally, P., Delaure, Y., and Brabazon, D., 2019, "Evaluation via Powder Metallurgy of Nano-Reinforced Iron Powders Developed for Selective Laser Melting Applications," Mater. Des., 182.
[483] Brika, S. E., Letenneur, M., Dion, C. A., and Brailovski, V., 2020, "Influence of Particle Morphology and Size Distribution on the Powder Flowability and Laser Powder Bed Fusion Manufacturability of Ti-6Al-4V Alloy," Addit. Manuf., 31.
[484] Pleass, C., and Jothi, S., 2018, "Influence of Powder Characteristics and Additive Manufacturing Process Parameters on the Microstructure and Mechanical Behaviour of Inconel 625 Fabricated by Selective Laser Melting," Addit. Manuf., 24, pp. 419–431.
[485] Baitimerov, R., Lykov, P., Zherebtsov, D., Radionova, L., Shultc, A., and Prashanth, K. G., 2018, "Influence of Powder Characteristics on Processability of AlSi12 Alloy Fabricated by Selective Laser Melting," Materials, 11(5).
[486] Murray, J. W., Simonelli, M., Speidel, A., Grant, D. M., and Clare, A. T., 2019, "Spheroidisation of Metal Powder by Pulsed Electron Beam Irradiation," Powder Technol., 350, pp. 100–106.
[487] Wang, L., Li, E. L., Shen, H., Zou, R. P., Yu, A. B., and Zhou, Z. Y., 2019, "Adhesion Effects on Spreading of Metal Powders in Selective Laser Melting," Powder Technol.
[488] Beitz, S., Uerlich, R., Bokelmann, T., Diener, A., Vietor, T., and Kwade, A., 2019, "Influence of Powder Deposition on Powder Bed and Specimen Properties," Materials, 12(2), p. 297.
[489] Zielinski, J., Vervoort, S., Mindt, H.-W., and Megahed, M., 2017, "Influence of Powder Bed Characteristics on Material Quality in Additive Manufacturing," BHM Berg- Hüttenmänn. Monatshefte, 162(5), pp. 192–198.
[490] Hesse, N., Dechet, M. A., Bonilla, J. S. G., Lübbert, C., Roth, S., Bück, A., Schmidt, J., and Peukert, W., 2019, "Analysis of Tribo-Charging during Powder Spreading in Selective Laser Sintering: Assessment of Polyamide 12 Powder Ageing Effects on Charging Behavior," Polymers, 11(4).
[491] Chen, H., Wei, Q., Zhang, Y., Chen, F., Shi, Y., and Yan, W., 2019, "Powder-Spreading Mechanisms in Powder-Bed-Based Additive Manufacturing: Experiments and Computational Modeling," Acta Mater., 179, pp. 158–171.

[492] Xiang, Z., Yin, M., Deng, Z., Mei, X., and Yin, G., 2016, "Simulation of Forming Process of Powder Bed for Additive Manufacturing," J. Manuf. Sci. Eng., 138(8).
[493] Shaheen, M. Y., Thornton, A. R., Luding, S., and Weinhart, T., 2019, "Discrete Particle Simulation of the Spreading Process in Additive Manufacturing," *Proceedings of the 8th International Conference on Discrete Element Methods (DEM8)*, Netherlands.
[494] Nagarajan, B., Hu, Z., Song, X., Zhai, W., and Wei, J., 2019, "Development of Micro Selective Laser Melting: The State of the Art and Future Perspectives," Engineering, 5(4), pp. 702–720.
[495] Manakari, V., Parande, G., and Gupta, M., 2017, "Selective Laser Melting of Magnesium and Magnesium Alloy Powders: A Review," Metals, 7(1), p. 2.
[496] Bidare, P., Bitharas, I., Ward, R. M., Attallah, M. M., and Moore, A. J., 2018, "Fluid and Particle Dynamics in Laser Powder Bed Fusion," Acta Mater., 142, pp. 107–120.
[497] Ly, S., Rubenchik, A. M., Khairallah, S. A., Guss, G., and Matthews, M. J., 2017, "Metal Vapor Micro-Jet Controls Material Redistribution in Laser Powder Bed Fusion Additive Manufacturing," Sci. Rep., 7(1), pp. 1–12.
[498] American National Standards Institute, 2018, *Standardization Roadmap for Additive Manufacturing: PM2 Spreadability*, version 2.
[499] Snow, Z., Martukanitz, R., and Joshi, S., 2019, "On the Development of Powder Spreadability Metrics and Feedstock Requirements for Powder Bed Fusion Additive Manufacturing," Addit. Manuf., 28, pp. 78–86.
[500] Fouda, Y. M., and Bayly, A. E., 2019, "A DEM Study of Powder Spreading in Additive Layer Manufacturing," Granul. Matter, 22(1), p. 10.
[501] Ma, Y., Evans, T. M., Philips, N., and Cunningham, N., 2020, "Numerical Simulation of the Effect of Fine Fraction on the Flowability of Powders in Additive Manufacturing," Powder Technol., 360, pp. 608–621.
[502] Meier, C., Weissbach, R., Weinberg, J., Wall, W. A., and Hart, A. J., 2019, "Critical Influences of Particle Size and Adhesion on the Powder Layer Uniformity in Metal Additive Manufacturing," J. Mater. Process. Technol., 266, pp. 484–501.
[503] Chen, H., Wei, Q., Wen, S., Li, Z., and Shi, Y., 2017, "Flow Behavior of Powder Particles in Layering Process of Selective Laser Melting: Numerical Modeling and Experimental Verification Based on Discrete Element Method," Int. J. Mach. Tools Manuf., 123, pp. 146–159.
[504] Haeri, S., 2017, "Optimisation of Blade Type Spreaders for Powder Bed Preparation in Additive Manufacturing Using DEM Simulations," Powder Technol., 321, pp. 94–104.
[505] Haeri, S., Wang, Y., Ghita, O., and Sun, J., 2017, "Discrete Element Simulation and Experimental Study of Powder Spreading Process in Additive Manufacturing," Powder Technol., 306, pp. 45–54.
[506] Nan, W., Pasha, M., Bonakdar, T., Lopez, A., Zafar, U., Nadimi, S., and Ghadiri, M., 2018, "Jamming during Particle Spreading in Additive Manufacturing," Powder Technol., 338, pp. 253–262.
[507] Cordova, L., Bor, T., de Smit, M., Campos, M., and Tinga, T., 2020, "Measuring the Spreadability of Pre-Treated and Moisturized Powders for Laser Powder Bed Fusion," Addit. Manuf., 32.
[508] Muñiz-Lerma, J. A., Nommeots-Nomm, A., Waters, K. E., and Brochu, M., 2018, "A Comprehensive Approach to Powder Feedstock Characterization for Powder Bed Fusion Additive Manufacturing: A Case Study on AlSi7Mg," Materials, 11(12).

[509] Mindt, H. W., Megahed, M., Lavery, N. P., Holmes, M. A., and Brown, S. G. R., 2016, "Powder Bed Layer Characteristics: The Overseen First-Order Process Input," Metall. Mater. Trans. A, 47(8), pp. 3811–3822.
[510] *ASTM F3049-14, Standard Guide for Characterizing Properties of Metal Powders Used for Additive Manufacturing Processes, ASTM International, West Conshohocken, PA, 2014*.
[511] *ASTM B213-13, Standard Test Methods for Flow Rate of Metal Powders Using the Hall Flowmeter Funnel, ASTM International, West Conshohocken, PA, 2013*.
[512] Lumay, G., Boschini, F., Traina, K., Bontempi, S., Remy, J.-C., Cloots, R., and Vandewalle, N., 2012, "Measuring the Flowing Properties of Powders and Grains," Powder Technol., 224, pp. 19–27.
[513] Reichold, T. V., Ruiz, P. D., and Huntley, J. M., 2020, "Nine-Hundred-Channel Single-Shot Surface Roughness Measurement Using Hyperspectral Interferometry," Meas. Sci. Technol., 31(4).
[514] Reichold, T. V., Ruiz, P. D., and Huntley, J. M., 2019, "2500-Channel Single-Shot Areal Profilometer Using Hyperspectral Interferometry with a Pinhole Array," Opt. Lasers Eng., 122, pp. 37–48.
[515] Forouzbakhsh, F., Rezanejad Gatabi, J., and Rezanejad Gatabi, I., 2009, "A New Measurement Method for Ultrasonic Surface Roughness Measurements," Measurement, 42(5), pp. 702–705.
[516] Chang, H.-K., Kim, J.-H., Kim, I. H., Jang, D. Y., and Han, D. C., 2007, "In-Process Surface Roughness Prediction Using Displacement Signals from Spindle Motion," Int. J. Mach. Tools Manuf., 47(6), pp. 1021–1026.
[517] Möbius, M. E., Lauderdale, B. E., Nagel, S. R., and Jaeger, H. M., 2001, "Size Separation of Granular Particles," Nature, 414(6861), pp. 270–270.
[518] Devriendt, L., Gatumel, C., and Berthiaux, H., 2013, "Experimental Evidence of Mixture Segregation by Particle Size Distribution," Part. Sci. Technol., 31(6), pp. 653–657.
[519] Tang, P., and Puri, V. M., 2004, "Methods for Minimizing Segregation: A Review," Part. Sci. Technol., 22(4), pp. 321–337.
[520] Nan, W., Pasha, M., and Ghadiri, M., 2020, "Numerical Simulation of Particle Flow and Segregation during Roller Spreading Process in Additive Manufacturing," Powder Technol., 364, pp. 811–821.
[521] Jacob, G., Brown, C. U., and Donmez, M. A., 2018, "The Influence of Spreading Metal Powders with Different Particle Size Distributions on the Powder Bed Density in Laser-Based Powder Bed Fusion Processes," NIST Pubs, 100–17.
[522] Ghosh, S., Mahmoudi, M., Johnson, L., Elwany, A., Arroyave, R., and Allaire, D., 2019, "Uncertainty Analysis of Microsegregation during Laser Powder Bed Fusion," Model. Simul. Mater. Sci. Eng., 27(3).
[523] Boley, C. D., Khairallah, S. A., and Rubenchik, A. M., 2015, "Calculation of Laser Absorption by Metal Powders in Additive Manufacturing," Appl. Opt., 54(9), pp. 2477–2482.
[524] Liu, A. Z., Zhang, D., Lam, L. P., and Ng, W. H., 2017, "Multi-Blade Recoater," Pat. WO2017143145A1, UCT Additive Manufacturing Center Pte. Ltd.
[525] Obeidi, M. A., Mussatto, A., Groarke, R., Vijayaraghavan, R. K., Conway, A., Rossi Kaschel, F., McCarthy, E., Clarkin, O., O'Connor, R., and Brabazon, D., 2020, "Comprehensive Assessment of Spatter Material Generated during Selective Laser Melting of Stainless Steel," Mater. Today Commun., 25, p. 101294.
[526] Casati, R., Vedani, M., Casati, R., and Vedani, M., 2014, "Metal Matrix Composites Reinforced by Nano-Particles - A Review," Metals, 4(1), pp. 65–83.

[527] Zhou, D., Qiu, F., Wang, H., Jiang, Q., Zhou, D., Qiu, F., Wang, H., and Jiang, Q., 2014, "Manufacture of Nano-Sized Particle-Reinforced Metal Matrix Composites: A Review, Manufacture of Nano-Sized Particle-Reinforced Metal Matrix Composites: A Review," Acta Metall. Sin. Lett., 27(5), pp. 798–805.
[528] Fernandes, M. R. P., Martinelli, A. E., Klein, A. N., Hammes, G., Binder, C., and Nascimento, R. M., 2017, "Production of Nickel Matrix Composites Reinforced with Carbide Particles by Granulation of Fine Powders and Mechanical Pressing," Powder Technol., 305, pp. 673–678.
[529] Thandalam, S. K., Ramanathan, S., and Sundarrajan, S., 2015, "Synthesis, Microstructural and Mechanical Properties of Ex Situ Zircon Particles (ZrSiO4) Reinforced Metal Matrix Composites (MMCs): A Review," J. Mater. Res. Technol., 4(3), pp. 333–347.
[530] Munir, K. S., Kingshott, P., and Wen, C., 2015, "Carbon Nanotube Reinforced Titanium Metal Matrix Composites Prepared by Powder Metallurgy—A Review," Crit. Rev. Solid State Mater. Sci., 40(1), pp. 38–55.
[531] Shirvanimoghaddam, K., Hamim, S. U., Karbalaei Akbari, M., Fakhrhoseini, S. M., Khayyam, H., Pakseresht, A. H., Ghasali, E., Zabet, M., Munir, K. S., Jia, S., Davim, J. P., and Naebe, M., 2017, "Carbon Fiber Reinforced Metal Matrix Composites: Fabrication Processes and Properties," Compos. Part Appl. Sci. Manuf., 92, pp. 70–96.
[532] Nassar, A. E., and Nassar, E. E., 2017, "Properties of Aluminum Matrix Nano Composites Prepared by Powder Metallurgy Processing," J. King Saud Univ. - Eng. Sci., 29(3), pp. 295–299.
[533] Strondl, A., Lyckfeldt, O., Brodin, H., and Ackelid, U., 2015, "Characterization and Control of Powder Properties for Additive Manufacturing," JOM, 67(3), pp. 549–554.
[534] Azevedo, J. M. C., CabreraSerrenho, A., and Allwood, J. M., 2018, "Energy and Material Efficiency of Steel Powder Metallurgy," Powder Technol., 328, pp. 329–336.
[535] Clyne, T. W., 2001, "Composites: Interfaces," *Encyclopedia of Materials: Science and Technology*, K.H.J. Buschow, R.W. Cahn, M.C. Flemings, B. Ilschner, E.J. Kramer, S. Mahajan, and P. Veyssière, eds., Elsevier, Oxford, pp. 1382–1391.
[536] Vani, V. V., and Chak, S. K., 2018, "The Effect of Process Parameters in Aluminum Metal Matrix Composites with Powder Metallurgy," Manuf. Rev., 5, p. 7.
[537] Huang, L. J., Geng, L., Xu, H. Y., and Peng, H. X., 2011, "In Situ TiC Particles Reinforced Ti6Al4V Matrix Composite with a Network Reinforcement Architecture," Mater. Sci. Eng. A, 528(6), pp. 2859–2862.
[538] Huang, L. J., Geng, L., and Peng, H.-X., 2015, "Microstructurally Inhomogeneous Composites: Is a Homogeneous Reinforcement Distribution Optimal?," Prog. Mater. Sci., 71, pp. 93–168.
[539] Shahid, R. N., and Scudino, S., 2018, "Strengthening of Al-Fe 3 Al Composites by the Generation of Harmonic Structures," Sci. Rep., 8(1).
[540] Bai, M., Song, B., Reddy, L., and Hussain, T., 2019, "Preparation of MCrAlY–Al2O3 Composite Coatings with Enhanced Oxidation Resistance through a Novel Powder Manufacturing Process," J. Therm. Spray Technol., 28(3), pp. 433–443.
[541] Song, B., Wang, Z., Yan, Q., Zhang, Y., Zhang, J., Cai, C., Wei, Q., and Shi, Y., 2017, "Integral Method of Preparation and Fabrication of Metal Matrix Composite: Selective Laser Melting of in-Situ Nano/Submicro-Sized Carbides Reinforced Iron Matrix Composites," Mater. Sci. Eng. A, 707, pp. 478–487.

[542] Gu, D., Wang, H., and Zhang, G., 2014, “Selective Laser Melting Additive Manufacturing of Ti-Based Nanocomposites: The Role of Nanopowder,” Metall. Mater. Trans. A, 45(1), pp. 464–476.
[543] Zhang, F., Mei, M., Al-Hamdani, K., Tan, H., and Clare, A. T., 2018, “Novel Nucleation Mechanisms through Satelliting in Direct Metal Deposition of Ti-15Mo,” Mater. Lett., 213, pp. 197–200.
[544] Martin, J. H., Yahata, B. D., Clough, E. C., Mayer, J. A., Hundley, J. M., and Schaedler, T. A., 2018, “Additive Manufacturing of Metal Matrix Composites via Nanofunctionalization,” MRS Commun., 8(2), pp. 297–302.
[545] Black, J. T., and kohser, R. A., 2011, *Materials and Processes in Manufacturing*, John Wiley & Sons, United States of America.
[546] Asthana, R., Kumar, A., and Dahotre, N. B., 2006, *Materials Processing and Manufacturing Science*, Elsevier, United States of America.
[547] Spierings, A. B., Voegtlin, M., Bauer, T., and Wegener, K., 2016, “Powder Flowability Characterisation Methodology for Powder-Bed-Based Metal Additive Manufacturing,” Prog. Addit. Manuf., 1(1), pp. 9–20.
[548] Baitimerov, R., Lykov, P., Zherebtsov, D., Radionova, L., Shultc, A., and Prashanth, K. G., 2018, “Influence of Powder Characteristics on Processability of AlSi12 Alloy Fabricated by Selective Laser Melting,” Materials, 11(5).
[549] Freeman, R., 2007, “Measuring the Flow Properties of Consolidated, Conditioned and Aerated Powders - A Comparative Study Using a Powder Rheometer and a Rotational Shear Cell,” Powder Technol., 174(1), pp. 25–33.
[550] Krantz, M., Zhang, H., and Zhu, J., 2009, “Characterization of Powder Flow: Static and Dynamic Testing,” Powder Technol., 194(3), pp. 239–245.
[551] Liu, B., Wildman, R., Tuck, C. R., Ashcroft, I., and Hague, R. J. M., 2011, “Investigation the Effect of Particle Size Distribution on Processing Parameters Optimisation in Selective Laser Melting Process,” Additive Manufacturing Research Group, Loughborough University.
[552] Hatami, S., Lyckfeldt, O., Tönnäng, L., and Fransson, K., 2017, “Flow Properties of Tool Steel Powders for Selective Laser Melting – Influence of Thermal and Mechanical Powder Treatments,” Powder Metall., 60(5), pp. 353–362.
[553] Clayton, J., 2014, “Optimising Metal Powders for Additive Manufacturing,” Met. Powder Rep., 69(5), pp. 14–17.
[554] Nguyen, Q. B., Nai, M. L. S., Zhu, Z., Sun, C.-N., Wei, J., and Zhou, W., 2017, “Characteristics of Inconel Powders for Powder-Bed Additive Manufacturing,” Engineering, 3(5), pp. 695–700.
[555] Ludwig, B., and Miller, T. F., 2015, “Rheological and Surface Chemical Characterization of Alkoxysilane Treated, Fine Aluminum Powders Showing Enhanced Flowability and Fluidization Behavior for Delivery Applications,” Powder Technol., 283, pp. 380–388.
[556] Sotomayor, M. E., Várez, A., and Levenfeld, B., 2010, “Influence of Powder Particle Size Distribution on Rheological Properties of 316L Powder Injection Moulding Feedstocks,” Powder Technol., 200(1), pp. 30–36.
[557] Pleass, C., and Jothi, S., 2018, “Influence of Powder Characteristics and Additive Manufacturing Process Parameters on the Microstructure and Mechanical Behaviour of Inconel 625 Fabricated by Selective Laser Melting,” Addit. Manuf., 24, pp. 419–431.
[558] Yun, H., Dong, L., Wang, W., Bing, Z., and Xiangyun, L., 2018, “Study on the Flowability of TC4 Alloy Powder for 3D Printing,” Mater. Sci. Eng., 439.

[559] Tan, J. H., Wong, W. L. E., and Dalgarno, K. W., 2017, "An Overview of Powder Granulometry on Feedstock and Part Performance in the Selective Laser Melting Process," Addit. Manuf., 18, pp. 228–255.
[560] Liu, J., Silveira, J., Groarke, R., Parab, S., Singh, H., McCarthy, E., Karazi, S., Mussatto, A., Houghtaling, J., Ahad, I. U., Naher, S., and Brabazon, D., 2019, "Effect of Powder Metallurgy Synthesis Parameters for Pure Aluminium on Resultant Mechanical Properties," Int. J. Mater. Form., 12(1), pp. 79–87.
[561] Gülsoy, H. Ö., 2008, "Production of Injection Moulded 316L Stainless Steels Reinforced with TiC(N) Particles," Mater. Sci. Technol., 24(12), pp. 1484–1491.
[562] Gülsoy, H. Ö., Baykara, T., and Özbek, S., 2011, "Injection Moulding of 316L Stainless Steels Reinforced with Nanosize Alumina Particles," Powder Metall., 54(3), pp. 360–365.
[563] Klar, E., and Samal, P. K., 2007, *Powder Metallurgy Stainless Steels: Processing, Microstructures, and Properties*, ASM International, Ohio.
[564] Larsen, R. M., and Thorsen, K. A., 1994, "Equilibria and Kinetics of Gas–Metal Reactions During Sintering of Austenitic Stainless Steel," Powder Metall., 37(1), pp. 61–66.
[565] Arh, B., and Tehovnik, F., 2007, "The Oxidation and Reduction of Chromium during the Elaboration of Stainless Steels in an Electric Arc Furnace," Mater. Technol., 41(5), pp. 203–211.
[566] Buffat, P. A., and Borel, J. P., 1976, "Size Effect on the Melting Temperature of Gold Particles," Phys. Rev. A, 13(6), pp. 2287–2298.
[567] Lai, S. L., Guo, J. Y., Petrova, V., Ramanath, G., and Allen, L. H., 1996, "Size-Dependent Melting Properties of Small Tin Particles: Nanocalorimetric Measurements," Phys. Rev. Lett., 77(1), pp. 99–102.
[568] Little, S. A., Begou, T., Collins, R. W., and Marsillac, S., 2012, "Optical Detection of Melting Point Depression for Silver Nanoparticles via in Situ Real Time Spectroscopic Ellipsometry," Appl. Phys. Lett., 100(5).
[569] Sun, J., and Simon, S. L., 2007, "The Melting Behavior of Aluminum Nanoparticles," Thermochim. Acta, 463(1), pp. 32–40.
[570] Meyyappan, M., and Sunkara, M. K., 2009, *Inorganic Nanowires: Applications, Properties, and Characterization*, CRC Press, London.
[571] Yang, C., Wong, C. P., and Yuen, M. M. F., 2013, "Printed Electrically Conductive Composites: Conductive Filler Designs and Surface Engineering," J. Mater. Chem. C, 1(26), pp. 4052–4069.
[572] Allen, G. L., Bayles, R. A., Gile, W. W., and Jesser, W. A., 1986, "Small Particle Melting of Pure Metals," Thin Solid Films, 144(2), pp. 297–308.
[573] Menamparambath, M. M., Muhammed Ajmal, C., Kim, K. H., Yang, D., Roh, J., Park, H. C., Kwak, C., Choi, J.-Y., and Baik, S., 2015, "Silver Nanowires Decorated with Silver Nanoparticles for Low-Haze Flexible Transparent Conductive Films," Sci. Rep., 5.
[574] El Fawkhry, M. K., and Mattar, T., 2018, "Influence of Diffusion and Wetting on the SiC Reinforcement of the Cast Surface of Low Alloy Steel," Int. J. Met., 12(1), pp. 139–147.
[575] Wu, C. L., Zhang, S., Zhang, C. H., Zhang, J. B., Liu, Y., and Chen, J., 2019, "Effects of SiC Content on Phase Evolution and Corrosion Behavior of SiC-Reinforced 316L Stainless Steel Matrix Composites by Laser Melting Deposition," Opt. Laser Technol., 115, pp. 134–139.
[576] Carvalho, O., Madeira, S., Buciumeanu, M., Soares, D., Silva, F., and Miranda, G., 2016, "Pressure and Sintering Temperature Influence on the Interface Reaction

of SiCp/410L Stainless Steel Composites," J. Compos. Mater., 50(15), pp. 2005–2015.
[577] Sorbello, F., Flewitt, P. E. J., Crocker, A. G., and Smith, G. E., 2008, "A Consideration of Cleavage Crack Propagation in Fe2Si Steel," Key Eng. Mater.
[578] Mari, D., Miguel, L., and Nebel, C., 2014, *Comprehensive Hard Materials*, Newnes.
[579] Chattopadhyay, R., 2001, *Surface Wear: Analysis, Treatment, and Prevention*, ASM International.
[580] Buytoz, S., 2006, "Microstructural Properties of SiC Based Hardfacing on Low Alloy Steel," Surf. Coat. Technol., 200(12), pp. 3734–3742.
[581] Cuevas, A. C., Becerril, E. B., Martínez, M. S., and Ruiz, J. L., 2018, *Metal Matrix Composites: Wetting and Infiltration*, Springer.
[582] Chand, S., and Chandrasekhar, P., 2020, "Influence of B4C/BN on Solid Particle Erosion of Al6061 Metal Matrix Hybrid Composites Fabricated through Powder Metallurgy Technique," Ceram. Int., 46(11, Part A), pp. 17621–17630.
[583] Mussatto, A., Ahad, I. U., Mousavian, R. T., Delaure, Y., and Brabazon, D., 2021, "Advanced Production Routes for Metal Matrix Composites," Eng. Rep., 3(5, e12330).
[584] Cantor, B., Dunne, F. P. E., and Stone, I. C., 2003, *Metal and Ceramic Matrix Composites*, CRC Press, Florida.
[585] Kim, J.-K., Tjong, S. C., and Mai, Y.-W., 2018, "4.2 Effect of Interface Strength on Metal Matrix Composites Properties," *Comprehensive Composite Materials II*, P.W.R. Beaumont, and C.H. Zweben, eds., Elsevier, Oxford, pp. 22–59.
[586] Prasad Behera, M., Dougherty, T., Singamneni, S., and De Silva, K., 2020, "Selective Laser Melting of Aluminium Metal-Matrix Composites and the Challenges," Mater. Today Proc., 33, pp. 5729–5733.
[587] Han, T., Liu, E., Li, J., Zhao, N., and He, C., 2020, "A Bottom-up Strategy toward Metal Nano-Particles Modified Graphene Nanoplates for Fabricating Aluminum Matrix Composites and Interface Study," J. Mater. Sci. Technol., 46, pp. 21–32.
[588] Han, T., Wang, F., Li, J., Zhao, N., and He, C., 2021, "Simultaneously Enhanced Strength and Ductility of Al Matrix Composites through the Introduction of Intragranular Nano-Sized Graphene Nanoplates," Compos. Part B Eng., 212(108700).
[589] Behera, M. P., Dougherty, T., and Singamneni, S., 2019, "Conventional and Additive Manufacturing with Metal Matrix Composites: A Perspective," Procedia Manuf., 30, pp. 159–166.
[590] Cepeda-Jiménez, C. M., and Pérez-Prado, M. T., 2018, "4.12 Processing of Nanoparticulate Metal Matrix Composites," *Comprehensive Composite Materials II*, P.W.R. Beaumont, and C.H. Zweben, eds., Elsevier, Oxford, pp. 313–330.
[591] Rajkumar, K., and Aravindan, S., 2013, "Tribological Behavior of Microwave Processed Copper–Nanographite Composites," Tribol. Int., 57, pp. 282–296.
[592] Withers, P. J., and Clyne, T. W., eds., 1993, "The Interfacial Region," *An Introduction to Metal Matrix Composites*, Cambridge University Press, Cambridge, pp. 166–217.
[593] Yu, W. H., Sing, S. L., Chua, C. K., Kuo, C. N., and Tian, X. L., 2019, "Particle-Reinforced Metal Matrix Nanocomposites Fabricated by Selective Laser Melting: A State of the Art Review," Prog. Mater. Sci., 104, pp. 330–379.
[594] Sahoo, B. P., and Das, D., 2019, "Critical Review on Liquid State Processing of Aluminium Based Metal Matrix Nano-Composites," Mater. Today Proc., 19, pp. 493–500.

[595] Dasgupta, R., 2012, “Aluminium Alloy-Based Metal Matrix Composites: A Potential Material for Wear Resistant Applications,” ISRN Metall., 2012(e594573).
[596] Ashby, M. F., and Maine, E. M. A., 2000, “3.29 - Design Aspects of Metal Matrix Composite Usage,” *Comprehensive Composite Materials*, A. Kelly, and C. Zweben, eds., Pergamon, Oxford, pp. 779–795.
[597] Zhao, X., Wei, Q. S., Gao, N., Zheng, E. L., Shi, Y. S., and Yang, S. F., 2019, “Rapid Fabrication of TiN/AISI 420 Stainless Steel Composite by Selective Laser Melting Additive Manufacturing,” J. Mater. Process. Technol., 270, pp. 8–19.
[598] Dadbakhsh, S., Mertens, R., Hao, L., Humbeeck, J. V., and Kruth, J.-P., 2019, “Selective Laser Melting to Manufacture ‘In Situ’ Metal Matrix Composites: A Review,” Adv. Eng. Mater., 21(3).
[599] Jäcklein, M., Pfaff, A., and Hoschke, K., 2020, “Developing Tungsten-Filled Metal Matrix Composite Materials Using Laser Powder Bed Fusion,” Appl. Sci., 10(24).
[600] Popov, V. V., Grilli, M. L., Koptyug, A., Jaworska, L., Katz-Demyanetz, A., Klobčar, D., Balos, S., Postolnyi, B. O., and Goel, S., 2021, “Powder Bed Fusion Additive Manufacturing Using Critical Raw Materials: A Review,” Materials, 14(4).
[601] Kotadia, H. R., Gibbons, G., Das, A., and Howes, P. D., 2021, “A Review of Laser Powder Bed Fusion Additive Manufacturing of Aluminium Alloys: Microstructure and Properties,” Addit. Manuf., 46.
[602] Bhuvanesh Kumar, M., and Sathiya, P., 2021, “Methods and Materials for Additive Manufacturing: A Critical Review on Advancements and Challenges,” Thin-Walled Struct., 159.
[603] Zou, Y., Tan, C., Qiu, Z., Ma, W., Kuang, M., and Zeng, D., 2021, “Additively Manufactured SiC-Reinforced Stainless Steel with Excellent Strength and Wear Resistance,” Addit. Manuf., 41.
[604] Wei, C., Chueh, Y.-H., Zhang, X., Huang, Y., Chen, Q., and Li, L., 2019, “Easy-To-Remove Composite Support Material and Procedure in Additive Manufacturing of Metallic Components Using Multiple Material Laser-Based Powder Bed Fusion,” J. Manuf. Sci. Eng., 141(7).
[605] Jia, H., Sun, H., Wang, H., Wu, Y., and Wang, H., 2021, “Scanning Strategy in Selective Laser Melting (SLM): A Review,” Int. J. Adv. Manuf. Technol., 113(9), pp. 2413–2435.
[606] Zhang, W., Tong, M., and Harrison, N. M., 2020, “Scanning Strategies Effect on Temperature, Residual Stress and Deformation by Multi-Laser Beam Powder Bed Fusion Manufacturing,” Addit. Manuf., 36.
[607] Serrano-Munoz, I., Mishurova, T., Thiede, T., Sprengel, M., Kromm, A., Nadammal, N., Nolze, G., Saliwan-Neumann, R., Evans, A., and Bruno, G., 2020, “The Residual Stress in As-Built Laser Powder Bed Fusion IN718 Alloy as a Consequence of the Scanning Strategy Induced Microstructure,” Sci. Rep., 10(1).
[608] Cheng, B., Shrestha, S., and Chou, K., 2016, “Stress and Deformation Evaluations of Scanning Strategy Effect in Selective Laser Melting,” Addit. Manuf., 12, pp. 240–251.
[609] Obeidi, M. A., Monu, M., Hughes, C., Bourke, D., Dogu, M. N., Francis, J., Zhang, M., Ahad, I. U., and Brabazon, D., 2021, “Laser Beam Powder Bed Fusion of Nitinol Shape Memory Alloy (SMA),” J. Mater. Res. Technol., 14, pp. 2554–2570.
[610] Jarfors, A. E. W., Shashidhar, A. C. G. H., Yepur, H. K., Steggo, J., Andersson, N.-E., and Stolt, R., 2021, “Build Strategy and Impact Strength of SLM Produced Maraging Steel (1.2709),” Metals, 11(1), p. 51.

[611] Jiang, J., and Ma, Y., 2020, "Path Planning Strategies to Optimize Accuracy, Quality, Build Time and Material Use in Additive Manufacturing: A Review," Micromachines, 11(7), p. 633.
[612] Catchpole-Smith, S., Aboulkhair, N., Parry, L., Tuck, C., Ashcroft, I. A., and Clare, A., 2017, "Fractal Scan Strategies for Selective Laser Melting of 'Unweldable' Nickel Superalloys," Addit. Manuf., 15, pp. 113–122.
[613] Yang, J., Bin, H., Zhang, X., and Liu, Z., 2003, "Fractal Scanning Path Generation and Control System for Selective Laser Sintering (SLS)," Int. J. Mach. Tools Manuf., 43(3), pp. 293–300.
[614] Bo, Q., Yu-sheng, S., Qing-song, W., and Hai-bo, W., 2012, "The Helix Scan Strategy Applied to the Selective Laser Melting," Int. J. Adv. Manuf. Technol., 63(5), pp. 631–640.
[615] Yang, Y., Loh, H. T., Fuh, J. Y. H., and Wang, Y. G., 2002, "Equidistant Path Generation for Improving Scanning Efficiency in Layered Manufacturing," Rapid Prototyp. J., 8(1), pp. 30–37.
[616] Ding, D., Pan, Z., Cuiuri, D., and Li, H., 2015, "A Practical Path Planning Methodology for Wire and Arc Additive Manufacturing of Thin-Walled Structures," Robot. Comput.-Integr. Manuf., 34, pp. 8–19.
[617] Jafari, D., Vaneker, T. H. J., and Gibson, I., 2021, "Wire and Arc Additive Manufacturing: Opportunities and Challenges to Control the Quality and Accuracy of Manufactured Parts," Mater. Des., 202.
[618] Ding, D., Pan, Z., Cuiuri, D., Li, H., and Larkin, N., 2016, "Adaptive Path Planning for Wire-Feed Additive Manufacturing Using Medial Axis Transformation," J. Clean. Prod., 133, pp. 942–952.
[619] Zhao, D., and Guo, W., 2019, "Shape and Performance Controlled Advanced Design for Additive Manufacturing: A Review of Slicing and Path Planning," J. Manuf. Sci. Eng., 142(1).
[620] Zhang, L., Ding, L., Ullah, S., Hu, T., Xu, Y., Chen, L., and Hanif, M., 2020, "An Improved Medial Axis Path Generation Algorithm for Selective Laser Melting," Rapid Prototyp. J., 26(10), pp. 1751–1759.
[621] Mussatto, A., Groarke, R., A-Hameed, A., Ahad, I. U. I., Vijayaraghavan, R. K., O'Neill, A., McNally, P., Delaure, Y., and Brabazon, D., 2019, "Evaluation via Powder Metallurgy of Nano-Reinforced Iron Powders Developed for Selective Laser Melting Applications," Mater. Des., 182.
[622] Mussatto, A., Groarke, R., O'Neill, A., Obeidi, M. A., Delaure, Y., and Brabazon, D., 2021, "Influences of Powder Morphology and Spreading Parameters on the Powder Bed Topography Uniformity in Powder Bed Fusion Metal Additive Manufacturing," Addit. Manuf., 38.
[623] Mussatto, A., Groarke, R., Vijayaraghavan, R. K., Hughes, C., Obeidi, M. A., Doğu, M. N., Yalçin, M. A., McNally, P. J., Delaure, Y., and Brabazon, D., 2022, "Assessing Dependency of Part Properties on the Printing Location in Laser-Powder Bed Fusion Metal Additive Manufacturing," Mater. Today Commun., 30.
[624] ASTM E92, 2017, *Standard Test Methods for Vickers Hardness and Knoop Hardness of Metallic Materials*, West Conshohocken, PA.
[625] Mohr, G., Altenburg, S. J., and Hilgenberg, K., 2020, "Effects of Inter Layer Time and Build Height on Resulting Properties of 316L Stainless Steel Processed by Laser Powder Bed Fusion," Addit. Manuf., 32.
[626] Leicht, A., Yu, C. H., Luzin, V., Klement, U., and Hryha, E., 2020, "Effect of Scan Rotation on the Microstructure Development and Mechanical Properties of 316L Parts Produced by Laser Powder Bed Fusion," Mater. Charact., 163.

[627] Heiden, M. J., Deibler, L. A., Rodelas, J. M., Koepke, J. R., Tung, D. J., Saiz, D. J., and Jared, B. H., 2019, "Evolution of 316L Stainless Steel Feedstock Due to Laser Powder Bed Fusion Process," Addit. Manuf., 25, pp. 84–103.
[628] Duval-Chaneac, M. S., Gao, N., Khan, R. H. U., Giles, M., Georgilas, K., Zhao, X., and Reed, P. A. S., 2021, "Fatigue Crack Growth in IN718/316L Multi-Materials Layered Structures Fabricated by Laser Powder Bed Fusion," Int. J. Fatigue, 152, p. 106454.
[629] Pineau, A., Benzerga, A. A., and Pardoen, T., 2016, "Failure of Metals I: Brittle and Ductile Fracture," Acta Mater., 107, pp. 424–483.
[630] Bian, L., Shamsaei, N., and Usher, J. M., 2017, *Laser-Based Additive Manufacturing of Metal Parts: Modeling, Optimization, and Control of Mechanical Properties*, CRC Press, Florida.
[631] Barkia, B., Aubry, P., Haghi-Ashtiani, P., Auger, T., Gosmain, L., Schuster, F., and Maskrot, H., 2020, "On the Origin of the High Tensile Strength and Ductility of Additively Manufactured 316L Stainless Steel: Multiscale Investigation," J. Mater. Sci. Technol., 41, pp. 209–218.
[632] Sun, Z., Tan, X., Tor, S. B., and Chua, C. K., 2018, "Simultaneously Enhanced Strength and Ductility for 3D-Printed Stainless Steel 316L by Selective Laser Melting," NPG Asia Mater., 10(4), pp. 127–136.
[633] Sun, Z., Tan, X., Tor, S. B., and Yeong, W. Y., 2016, "Selective Laser Melting of Stainless Steel 316L with Low Porosity and High Build Rates," Mater. Des., 104, pp. 197–204.
[634] Pham, M.-S., Dovgyy, B., Hooper, P. A., Gourlay, C. M., and Piglione, A., 2020, "The Role of Side-Branching in Microstructure Development in Laser Powder-Bed Fusion," Nat. Commun., 11(1), p. 749.
[635] Gäumann, M., Henry, S., Cléton, F., Wagnière, J.-D., and Kurz, W., 1999, "Epitaxial Laser Metal Forming: Analysis of Microstructure Formation," Mater. Sci. Eng. A, 271(1), pp. 232–241.
[636] Boettinger, W. J., Coriell, S. R., Greer, A. L., Karma, A., Kurz, W., Rappaz, M., and Trivedi, R., 2000, "Solidification Microstructures: Recent Developments, Future Directions," Acta Mater., 48(1), pp. 43–70.
[637] Wu, C. S., Wang, L., Ren, W. J., and Zhang, X. Y., 2014, "Plasma Arc Welding: Process, Sensing, Control and Modeling," J. Manuf. Process., 16(1), pp. 74–85.
[638] Chen, S. B., and Lv, N., 2014, "Research Evolution on Intelligentized Technologies for Arc Welding Process," J. Manuf. Process., 16(1), pp. 109–122.
[639] Liskevych, O., and Scotti, A., 2015, "Influence of the CO2 Content on Operational Performance of Short-Circuit GMAW," Weld. World, 59(2), pp. 217–224.
[640] Criss, E. M., Smith, R. J., and Meyers, M. A., 2015, "Failure Mechanisms in Cobalt Welded with a Silver–Copper Filler," Mater. Sci. Eng. A, 645, pp. 369–382.
[641] Xu, H., Xu, L. D., Zhang, S. J., and Han, Q., 2006, "Effect of the Alloy Composition on the Grain Refinement of Aluminum Alloys," Scr. Mater., 54(12), pp. 2191–2196.
[642] Fan, Z., Gao, F., Wang, Y., Men, H., and Zhou, L., 2021, "Effect of Solutes on Grain Refinement," Prog. Mater. Sci.
[643] Gupta, M., and Surappa, M. K., 1995, "Effect of Increase in Heterogeneous Nucleation Sites on the Aging Behavior of 6061/SiC Metal Matrix Composites," Mater. Res. Bull., 30(8), pp. 1023–1030.

[644] Tosun, G., and Kurt, M., 2019, "The Porosity, Microstructure, and Hardness of Al-Mg Composites Reinforced with Micro Particle SiC/Al2O3 Produced Using Powder Metallurgy," Compos. Part B Eng., 174.
[645] Galy, C., Le Guen, E., Lacoste, E., and Arvieu, C., 2018, "Main Defects Observed in Aluminum Alloy Parts Produced by SLM: From Causes to Consequences," Addit. Manuf., 22, pp. 165–175.
[646] Wei, Q., Li, S., Han, C., Li, W., Cheng, L., Hao, L., and Shi, Y., 2015, "Selective Laser Melting of Stainless-Steel/Nano-Hydroxyapatite Composites for Medical Applications: Microstructure, Element Distribution, Crack and Mechanical Properties," J. Mater. Process. Technol., 222, pp. 444–453.
[647] Evans, A., Marchi, C. S., and Mortensen, A., 2003, *Metal Matrix Composites in Industry: An Introduction and a Survey*, Springer, New York.
[648] Clyne, T. W., and Withers, P. J., 1993, *An Introduction to Metal Matrix Composites*, Cambridge University Press, Cambridge.
[649] Bhushan, B., 2013, *Introduction to Tribology*, John Wiley & Sons, New York.
[650] Bowden, F. P., Bowden, F. P., and Tabor, D., 2001, *The Friction and Lubrication of Solids*, Clarendon Press, Oxford.
[651] Johnson, K. L., 1987, *Contact Mechanics*, Cambridge University Press, Camdridge.
[652] Goddard, J., and Wilman, H., 1962, "A Theory of Friction and Wear during the Abrasion of Metals," Wear, 5(2), pp. 114–135.
[653] Lafaye, S., Gauthier, C., and Schirrer, R., 2005, "A Surface Flow Line Model of a Scratching Tip: Apparent and True Local Friction Coefficients," Tribol. Int., 38(2), pp. 113–127.
[654] Bucaille, J. L., Felder, E., and Hochstetter, G., 2001, "Mechanical Analysis of the Scratch Test on Elastic and Perfectly Plastic Materials with the Three-Dimensional Finite Element Modeling," Wear, 249(5), pp. 422–432.
[655] Lafaye, S., Gauthier, C., and Schirrer, R., 2006, "Analysis of the Apparent Friction of Polymeric Surfaces," J. Mater. Sci., 41(19), pp. 6441–6452.
[656] Gauthier, C., Lafaye, S., and Schirrer, R., 2001, "Elastic Recovery of a Scratch in a Polymeric Surface: Experiments and Analysis," Tribol. Int., 34(7), pp. 469–479.
[657] Lafaye, S., Gauthier, C., and Schirrer, R., 2006, "The Ploughing Friction: Analytical Model with Elastic Recovery for a Conical Tip with a Blunted Spherical Extremity," Tribol. Lett., 21(2), pp. 95–99.
[658] Lafaye, S., and Troyon, M., 2006, "On the Friction Behaviour in Nanoscratch Testing," Wear, 261(7), pp. 905–913.
[659] Mishra, M., and Szlufarska, I., 2012, "Analytical Model for Plowing Friction at Nanoscale," Tribol. Lett., 45(3), pp. 417–426.
[660] Yang, X., Tang, F., Hao, X., and Li, Z., 2021, "Oxide Evolution During the Solidification of 316L Stainless Steel from Additive Manufacturing Powders with Different Oxygen Contents," Metall. Mater. Trans. B, 52(4), pp. 2253–2262.
[661] Harun, W. S. W., Asri, R. I. M., Romlay, F. R. M., Sharif, S., Jan, N. H. M., and Tsumori, F., 2018, "Surface Characterisation and Corrosion Behaviour of Oxide Layer for SLMed-316L Stainless Steel," J. Alloys Compd., 748, pp. 1044–1052.
[662] Habib, K. A., Damra, M. S., Saura, J. J., Cervera, I., and Bellés, J., 2011, "Breakdown and Evolution of the Protective Oxide Scales of AISI 304 and AISI 316 Stainless Steels under High-Temperature Oxidation," Int. J. Corros., 2011.
[663] Maurice, V., Yang, W. P., and Marcus, P., 1998, "X-Ray Photoelectron Spectroscopy and Scanning Tunneling Microscopy Study of Passive Films Formed on (100) Fe-18Cr-13Ni Single-Crystal Surfaces," J. Electrochem. Soc., 145(3).

[664] Apell, J., Wonneberger, R., Seyring, M., Stöcker, H., Rettenmayr, M., and Undisz, A., 2021, "Early Oxidation Stages of a Co-Cr-Fe-Mn-Ni-Si Complex Concentrated Alloy with Cr, Mn, and Si Contents Matching Those of 316L Stainless Steel," Corros. Sci., 190.
[665] Wang, Z., Paschalidou, E.-M., Seyeux, A., Zanna, S., Maurice, V., and Marcus, P., 2019, "Mechanisms of Cr and Mo Enrichments in the Passive Oxide Film on 316L Austenitic Stainless Steel," Front. Mater., 6.
[666] Holcomb, G. R., Tylczak, J., and Carney, C., 2015, "Oxidation of CoCrFeMnNi High Entropy Alloys," JOM, 67(10), pp. 2326–2339.
[667] Wang, Z., Di-Franco, F., Seyeux, A., Zanna, S., Maurice, V., and Marcus, P., 2019, "Passivation-Induced Physicochemical Alterations of the Native Surface Oxide Film on 316L Austenitic Stainless Steel," J. Electrochem. Soc., 166(11), pp. 3376–3388.
[668] Wang, L., Seyeux, A., and Marcus, P., 2020, "Ion Transport Mechanisms in the Oxide Film Formed on 316L Stainless Steel Surfaces Studied by ToF-SIMS with 18O2 Isotopic Tracer," J. Electrochem. Soc., 167(10).
[669] Huang, X., Xiao, K., Fang, X., Xiong, Z., Wei, L., Zhu, P., and Li, X., 2020, "Oxidation Behavior of 316L Austenitic Stainless Steel in High Temperature Air with Long-Term Exposure," Mater. Res. Express, 7(6).
[670] Wang, L., Seyeux, A., and Marcus, P., 2020, "Thermal Stability of the Passive Film Formed on 316L Stainless Steel Surface Studied by ToF-SIMS," Corros. Sci., 165.
[671] Maurice, V., Peng, H., H. Klein, L., Seyeux, A., Zanna, S., and Marcus, P., 2015, "Effects of Molybdenum on the Composition and Nanoscale Morphology of Passivated Austenitic Stainless Steel Surfaces," Faraday Discuss., 180(0), pp. 151–170.
[672] Raj, K. A., Arunkumar, M. P., Kanigalpula, P. K. C., and Karthikeyan, M., 2019, "Tribological and Vibrational Characteristics of AISI 316L Tested at Elevated Temperature and 600 Torr Vacuum," Def. Technol., 15(1), pp. 58–64.
[673] O'Donnell, L. J., Michal, G. M., Ernst, F., Kahn, H., and Heuer, A. H., 2010, "Wear Maps for Low Temperature Carburised 316L Austenitic Stainless Steel Sliding against Alumina," Surf. Eng., 26(4), pp. 284–292.
[674] Saka, N., Eleiche, A. M., and Suh, N. P., 1977, "Wear of Metals at High Sliding Speeds," Wear, 44(1), pp. 109–125.
[675] Stack, M. M., Corlett, N., and Zhou, S., 1997, "A Methodology for the Construction of the Erosion-Corrosion Map in Aqueous Environments," Wear, 203–204, pp. 474–488.
[676] Geringer, J., and Macdonald, D. D., 2012, "Modeling Fretting-Corrosion Wear of 316L SS against Poly(Methyl Methacrylate) with the Point Defect Model: Fundamental Theory, Assessment, and Outlook," Electrochimica Acta, 79, pp. 17–30.
[677] Jian, S.-R., Teng, I.-J., Yang, P.-F., Lai, Y.-S., Lu, J.-M., Chang, J.-G., and Ju, S.-P., 2008, "Surface Morphological and Nanomechanical Properties of PLD-Derived ZnO Thin Films," Nanoscale Res. Lett., 3(5), pp. 186–193.
[678] Chen, J., Shi, J., Wang, Y., Sun, J., Han, J., Sun, K., and Fang, L., 2018, "Nanoindentation and Deformation Behaviors of Silicon Covered with Amorphous SiO 2 : A Molecular Dynamic Study," RSC Adv., 8(23), pp. 12597–12607.
[679] Zambrano, O. A., Coronado, J. J., and Rodríguez, S. A., 2015, "Mechanical Properties and Phases Determination of Low Carbon Steel Oxide Scales Formed at 1200°C in Air," Surf. Coat. Technol., 282, pp. 155–162.

[680] Hu, Z., Ning, K., and Lu, K., 2016, "Study of Spark Plasma Sintered Nanostructured Ferritic Steel Alloy with Silicon Carbide Addition," Mater. Sci. Eng. A, 670, pp. 75–80.
[681] Lacaze, J., and Sundman, B., 1991, "An Assessment of the Fe-C-Si System," Metall. Trans. A, 22(10), pp. 2211–2223.
[682] Wu, C. L., Zhang, S., Zhang, C. H., Zhang, J. B., Liu, Y., and Chen, J., 2019, "Effects of SiC Content on Phase Evolution and Corrosion Behavior of SiC-Reinforced 316L Stainless Steel Matrix Composites by Laser Melting Deposition," Opt. Laser Technol., 115, pp. 134–139.
[683] Polmear, I., 2005, *Light Alloys: From Traditional Alloys to Nanocrystals*, Butterworth-Heinemann, Oxford.
[684] Porter, D. A., and Easterling, K. E., 1992, *Phase Transformations in Metals and Alloys, Third Edition (Revised Reprint)*, CRC Press, London.
[685] Smallman, R. E., and Bishop, R. J., 1995, *Metals and Materials: Science, Processes, Applications*, Butterworth-Heinemann, Oxford.
[686] Sola, A., and Nouri, A., 2019, "Microstructural Porosity in Additive Manufacturing: The Formation and Detection of Pores in Metal Parts Fabricated by Powder Bed Fusion," J. Adv. Manuf. Process., 1(3).
[687] Herzog, D., Seyda, V., Wycisk, E., and Emmelmann, C., 2016, "Additive Manufacturing of Metals," Acta Mater., 117, pp. 371–392.
[688] Liverani, E., Toschi, S., Ceschini, L., and Fortunato, A., 2017, "Effect of Selective Laser Melting (SLM) Process Parameters on Microstructure and Mechanical Properties of 316L Austenitic Stainless Steel," J. Mater. Process. Technol., 249, pp. 255–263.
[689] Reijonen, J., Revuelta, A., Riipinen, T., Ruusuvuori, K., and Puukko, P., 2020, "On the Effect of Shielding Gas Flow on Porosity and Melt Pool Geometry in Laser Powder Bed Fusion Additive Manufacturing," Addit. Manuf., 32.
[690] King, W. E., Barth, H. D., Castillo, V. M., Gallegos, G. F., Gibbs, J. W., Hahn, D. E., Kamath, C., and Rubenchik, A. M., 2014, "Observation of Keyhole-Mode Laser Melting in Laser Powder-Bed Fusion Additive Manufacturing," J. Mater. Process. Technol., 214(12), pp. 2915–2925.
[691] Gan, Z., Kafka, O. L., Parab, N., Zhao, C., Fang, L., Heinonen, O., Sun, T., and Liu, W. K., 2021, "Universal Scaling Laws of Keyhole Stability and Porosity in 3D Printing of Metals," Nat. Commun., 12(1).
[692] Wang, L., Mohammadpour, M., Yang, B., Gao, X., Lavoie, J.-P., Kleine, K., Kong, F., and Kovacevic, R., 2020, "Monitoring of Keyhole Entrance and Molten Pool with Quality Analysis during Adjustable Ring Mode Laser Welding," Appl. Opt., 59(6), pp. 1576–1584.
[693] Sokolov, M., Franciosa, P., Al Botros, R., and Ceglarek, D., 2020, "Keyhole Mapping to Enable Closed-Loop Weld Penetration Depth Control for Remote Laser Welding of Aluminum Components Using Optical Coherence Tomography," J. Laser Appl., 32(3).
[694] Wu, C., Jia, C., and Chen, M. A., 2010, "A Control System for Keyhole Plasma Arc Welding of Stainless Steel Plates with Medium Thickness," Weld. J., 89, pp. 225–231.
[695] Goncalves Assuncao, E., 2012, "Investigation of Conduction to Keyhole Mode Transition," doctoral thesis, Cranfield University.
[696] Cherry, J. A., Davies, H. M., Mehmood, S., Lavery, N. P., Brown, S. G. R., and Sienz, J., 2015, "Investigation into the Effect of Process Parameters on

Microstructural and Physical Properties of 316L Stainless Steel Parts by Selective Laser Melting," Int. J. Adv. Manuf. Technol., 76(5), pp. 869–879.
[697] Xiong, W., Hao, L., Li, Y., Tang, D., Cui, Q., Feng, Z., and Yan, C., 2019, "Effect of Selective Laser Melting Parameters on Morphology, Microstructure, Densification and Mechanical Properties of Supersaturated Silver Alloy," Mater. Des., 170.
[698] Wang, H., and Zou, Y., 2019, "Microscale Interaction between Laser and Metal Powder in Powder-Bed Additive Manufacturing: Conduction Mode versus Keyhole Mode," Int. J. Heat Mass Transf., 142.
[699] Papula, S., Song, M., Pateras, A., Chen, X.-B., Brandt, M., Easton, M., Yagodzinskyy, Y., Virkkunen, I., and Hänninen, H., 2019, "Selective Laser Melting of Duplex Stainless Steel 2205: Effect of Post-Processing Heat Treatment on Microstructure, Mechanical Properties, and Corrosion Resistance," Materials, 12(15).
[700] Andreau, O., Koutiri, I., Peyre, P., Penot, J.-D., Saintier, N., Pessard, E., De Terris, T., Dupuy, C., and Baudin, T., 2019, "Texture Control of 316L Parts by Modulation of the Melt Pool Morphology in Selective Laser Melting," J. Mater. Process. Technol., 264, pp. 21–31.
[701] Niendorf, T., Leuders, S., Riemer, A., Richard, H. A., Tröster, T., and Schwarze, D., 2013, "Highly Anisotropic Steel Processed by Selective Laser Melting," Metall. Mater. Trans. B, 44(4), pp. 794–796.
[702] Liang, Y., Zhou, W., Liu, Y., Li, Z., Yang, Y., Xi, H., and Wu, Z., 2021, "Energy Absorption and Deformation Behavior of 3D Printed Triply Periodic Minimal Surface Stainless Steel Cellular Structures under Compression," Steel Res. Int., 92(3).
[703] Dovgyy, B., Piglione, A., Hooper, P. A., and Pham, M.-S., 2020, "Comprehensive Assessment of the Printability of CoNiCrFeMn in Laser Powder Bed Fusion," Mater. Des., 194.
[704] Salman, O. O., Brenne, F., Niendorf, T., Eckert, J., Prashanth, K. G., He, T., and Scudino, S., 2019, "Impact of the Scanning Strategy on the Mechanical Behavior of 316L Steel Synthesized by Selective Laser Melting," J. Manuf. Process., 45, pp. 255–261.
[705] Qiu, C., Kindi, M. A., Aladawi, A. S., and Hatmi, I. A., 2018, "A Comprehensive Study on Microstructure and Tensile Behaviour of a Selectively Laser Melted Stainless Steel," Sci. Rep., 8(1).
[706] Gu, D., Guo, M., Zhang, H., Sun, Y., Wang, R., and Zhang, L., 2020, "Effects of Laser Scanning Strategies on Selective Laser Melting of Pure Tungsten," 2(2).
[707] Nong, X. D., and Zhou, X. L., 2021, "Effect of Scanning Strategy on the Microstructure, Texture, and Mechanical Properties of 15-5PH Stainless Steel Processed by Selective Laser Melting," Mater. Charact., 174.
[708] Thijs, L., Kempen, K., Kruth, J.-P., and Van Humbeeck, J., 2013, "Fine-Structured Aluminium Products with Controllable Texture by Selective Laser Melting of Pre-Alloyed AlSi10Mg Powder," Acta Mater., 61(5), pp. 1809–1819.
[709] AlMangour, B., Grzesiak, D., and Yang, J.-M., 2017, "Scanning Strategies for Texture and Anisotropy Tailoring during Selective Laser Melting of TiC/316L Stainless Steel Nanocomposites," J. Alloys Compd., 728, pp. 424–435.
[710] Carter, L. N., Martin, C., Withers, P. J., and Attallah, M. M., 2014, "The Influence of the Laser Scan Strategy on Grain Structure and Cracking Behaviour in SLM Powder-Bed Fabricated Nickel Superalloy," J. Alloys Compd., 615, pp. 338–347.
[711] Nadammal, N., Mishurova, T., Fritsch, T., Serrano-Munoz, I., Kromm, A., Haberland, C., Portella, P. D., and Bruno, G., 2021, "Critical Role of Scan Strategies

on the Development of Microstructure, Texture, and Residual Stresses during Laser Powder Bed Fusion Additive Manufacturing," Addit. Manuf., 38.
[712] Casati, R., Lemke, J., and Vedani, M., 2016, "Microstructure and Fracture Behavior of 316L Austenitic Stainless Steel Produced by Selective Laser Melting," J. Mater. Sci. Technol., 32(8), pp. 738–744.
[713] Dryepondt, S., Nandwana, P., Fernandez-Zelaia, P., and List, F., 2021, "Microstructure and High Temperature Tensile Properties of 316L Fabricated by Laser Powder-Bed Fusion," Addit. Manuf., 37.
[714] Pham, M. S., Dovgyy, B., and Hooper, P. A., 2017, "Twinning Induced Plasticity in Austenitic Stainless Steel 316L Made by Additive Manufacturing," Mater. Sci. Eng. A, 704, pp. 102–111.
[715] Zhao, C., Bai, Y., Zhang, Y., Wang, X., Xue, J. M., and Wang, H., 2021, "Influence of Scanning Strategy and Building Direction on Microstructure and Corrosion Behaviour of Selective Laser Melted 316L Stainless Steel," Mater. Des., 209.
[716] Chen, L., Richter, B., Zhang, X., Bertsch, K. B., Thoma, D. J., and Pfefferkorn, F. E., 2021, "Effect of Laser Polishing on the Microstructure and Mechanical Properties of Stainless Steel 316L Fabricated by Laser Powder Bed Fusion," Mater. Sci. Eng. A, 802.
[717] Wang, D., Song, C., Yang, Y., and Bai, Y., 2016, "Investigation of Crystal Growth Mechanism during Selective Laser Melting and Mechanical Property Characterization of 316L Stainless Steel Parts," Mater. Des., 100, pp. 291–299.
[718] Yin, Y. J., Sun, J. Q., Guo, J., Kan, X. F., and Yang, D. C., 2019, "Mechanism of High Yield Strength and Yield Ratio of 316 L Stainless Steel by Additive Manufacturing," Mater. Sci. Eng. A, 744, pp. 773–777.
[719] Birnbaum, A. J., Steuben, J. C., Barrick, E. J., Iliopoulos, A. P., and Michopoulos, J. G., 2019, "Intrinsic Strain Aging, Σ3 Boundaries, and Origins of Cellular Substructure in Additively Manufactured 316L," Addit. Manuf., 29.
[720] Sprouster, D. J., Streit Cunningham, W., Halada, G. P., Yan, H., Pattammattel, A., Huang, X., Olds, D., Tilton, M., Chu, Y. S., Dooryhee, E., Manogharan, G. P., and Trelewicz, J. R., 2021, "Dislocation Microstructure and Its Influence on Corrosion Behavior in Laser Additively Manufactured 316L Stainless Steel," Addit. Manuf., 47.
[721] Zhong, Y., Liu, L., Wikman, S., Cui, D., and Shen, Z., 2016, "Intragranular Cellular Segregation Network Structure Strengthening 316L Stainless Steel Prepared by Selective Laser Melting," J. Nucl. Mater., 470, pp. 170–178.
[722] Hettesheimer, T., Hirzel, S., and Roß, H. B., 2018, "Energy Savings through Additive Manufacturing: An Analysis of Selective Laser Sintering for Automotive and Aircraft Components," Energy Effic., 11(5), pp. 1227–1245.
[723] Salman, O. O., Gammer, C., Chaubey, A. K., Eckert, J., and Scudino, S., 2019, "Effect of Heat Treatment on Microstructure and Mechanical Properties of 316L Steel Synthesized by Selective Laser Melting," Mater. Sci. Eng. A, 748, pp. 205–212.
[724] Yap, C. Y., Chua, C. K., Dong, Z. L., Liu, Z. H., Zhang, D. Q., Loh, L. E., and Sing, S. L., 2015, "Review of Selective Laser Melting: Materials and Applications," Appl. Phys. Rev., 2(4).
[725] Wei, C., Li, L., Zhang, X., and Chueh, Y.-H., 2018, "3D Printing of Multiple Metallic Materials via Modified Selective Laser Melting," CIRP Ann., 67(1), pp. 245–248.

[726] Gu, H., Wei, C., Li, L., Han, Q., Setchi, R., Ryan, M., and Li, Q., 2020, "Multi-Physics Modelling of Molten Pool Development and Track Formation in Multi-Track, Multi-Layer and Multi-Material Selective Laser Melting," Int. J. Heat Mass Transf., 151, p. 119458.
[727] Veron, F., Lanoue, F., Baco-Carles, V., Kiryukhina, K., Vendier, O., and Tailhades, P., 2020, "Selective Laser Powder Bed Fusion for Manufacturing of 3D Metal-Ceramic Multi-Materials Assemblies," Addit. Manuf., 50.
[728] Tan, C., Zhou, K., Ma, W., and Min, L., 2018, "Interfacial Characteristic and Mechanical Performance of Maraging Steel-Copper Functional Bimetal Produced by Selective Laser Melting Based Hybrid Manufacture," Mater. Des., 155, pp. 77–85.
[729] Mussatto, A., Ahad, I. U., Mousavian, R. T., Delaure, Y., and Brabazon, D., 2021, "Advanced Production Routes for Metal Matrix Composites," Eng. Rep., 3(5).
[730] Wiscombe, T., 2012, "Beyond Assemblies: System Convergence and Multi-Materiality," Bioinspir. Biomim., 7(1).
[731] Neirinck, B., Li, X., and Hick, M., 2021, "Powder Deposition Systems Used in Powder Bed-Based Multimetal Additive Manufacturing," Acc. Mater. Res., 2(6), pp. 387–393.
[732] Wang, H., Chen, J., Luo, H., Wang, D., Song, C., Yao, X., Chen, P., and Yan, M., 2022, "Bimetal Printing of High Entropy Alloy/Metallic Glass by Laser Powder Bed Fusion Additive Manufacturing," Intermetallics, 141.
[733] Koopmann, J., Voigt, J., and Niendorf, T., 2019, "Additive Manufacturing of a Steel–Ceramic Multi-Material by Selective Laser Melting," Metall. Mater. Trans. B, 50(2), pp. 1042–1051.
[734] Chen, J., Yang, Y., Song, C., Zhang, M., Wu, S., and Wang, D., 2019, "Interfacial Microstructure and Mechanical Properties of 316L /CuSn10 Multi-Material Bimetallic Structure Fabricated by Selective Laser Melting," Mater. Sci. Eng. A, 752, pp. 75–85.
[735] Tan, C., Wang, D., Ma, W., and Zhou, K., 2021, "Ultra-Strong Bond Interface in Additively Manufactured Iron-Based Multi-Materials," Mater. Sci. Eng. A, 802.
[736] Zhang, X., Wei, C., Chueh, Y.-H., and Li, L., 2018, "An Integrated Dual Ultrasonic Selective Powder Dispensing Platform for Three-Dimensional Printing of Multiple Material Metal/Glass Objects in Selective Laser Melting," J. Manuf. Sci. Eng., 141(1).
[737] Sing, S. L., Huang, S., Goh, G. D., Goh, G. L., Tey, C. F., Tan, J. H. K., and Yeong, W. Y., 2021, "Emerging Metallic Systems for Additive Manufacturing: In-Situ Alloying and Multi-Metal Processing in Laser Powder Bed Fusion," Prog. Mater. Sci., 119.
[738] Mahamood, R. M., and Akinlabi, E. T., 2015, "Laser Metal Deposition of Functionally Graded Ti6Al4V/TiC," Mater. Des., 84, pp. 402–410.
[739] Li, Y., Feng, Z., Hao, L., Huang, L., Xin, C., Wang, Y., Bilotti, E., Essa, K., Zhang, H., Li, Z., Yan, F., and Peijs, T., 2020, "A Review on Functionally Graded Materials and Structures via Additive Manufacturing: From Multi-Scale Design to Versatile Functional Properties," Adv. Mater. Technol., 5(6).
[740] Wei, C., and Li, L., 2021, "Recent Progress and Scientific Challenges in Multi-Material Additive Manufacturing via Laser-Based Powder Bed Fusion," Virtual Phys. Prototyp., 16(3), pp. 347–371.
[741] Chen, K., Wang, C., Hong, Q., Wen, S., Zhou, Y., Yan, C., and Shi, Y., 2020, "Selective Laser Melting 316L/CuSn10 Multi-Materials: Processing Optimization, Interfacial Characterization and Mechanical Property," J. Mater. Process. Technol., 283.

[742] Walker, J., Middendorf, J. R., Lesko, C. C. C., and Gockel, J., 2021, "Multi-Material Laser Powder Bed Fusion Additive Manufacturing in 3-Dimensions," Manuf. Lett.
[743] Sing, S. L., Lam, L. P., Zhang, D. Q., Liu, Z. H., and Chua, C. K., 2015, "Interfacial Characterization of SLM Parts in Multi-Material Processing: Intermetallic Phase Formation between AlSi10Mg and C18400 Copper Alloy," Mater. Charact., 107, pp. 220–227.
[744] Mussatto, A., Groarke, R., A-Hameed, A., Ahad, I. U. I., Vijayaraghavan, R. K., O'Neill, A., McNally, P., Delaure, Y., and Brabazon, D., 2019, "Evaluation via Powder Metallurgy of Nano-Reinforced Iron Powders Developed for Selective Laser Melting Applications," Mater. Des., 182.
[745] Wei, C., Sun, Z., Chen, Q., Liu, Z., and Li, L., 2019, "Additive Manufacturing of Horizontal and 3D Functionally Graded 316L/Cu10Sn Components via Multiple Material Selective Laser Melting," J. Manuf. Sci. Eng., 141(8).
[746] Diener, S., Zocca, A., and Günster, J., 2021, "Literature Review: Methods for Achieving High Powder Bed Densities in Ceramic Powder Bed Based Additive Manufacturing," Open Ceram., 8.
[747] Mussatto, A., Groarke, R., O'Neill, A., Obeidi, M. A., Delaure, Y., and Brabazon, D., 2021, "Influences of Powder Morphology and Spreading Parameters on the Powder Bed Topography Uniformity in Powder Bed Fusion Metal Additive Manufacturing," Addit. Manuf., 38.
[748] Mair, P., Kaserer, L., Braun, J., Weinberger, N., Letofsky-Papst, I., and Leichtfried, G., 2021, "Microstructure and Mechanical Properties of a TiB2-Modified Al–Cu Alloy Processed by Laser Powder-Bed Fusion," Mater. Sci. Eng. A, 799.
[749] Chen, M., Li, X., Ji, G., Wu, Y., Chen, Z., Baekelant, W., Vanmeensel, K., Wang, H., and Kruth, J.-P., 2017, "Novel Composite Powders with Uniform TiB2 Nano-Particle Distribution for 3D Printing," Appl. Sci., 7(3), p. 250.
[750] Zhang, C., Wang, R., Cai, Z., Peng, C., Feng, Y., and Zhang, L., 2015, "Effects of Dual-Layer Coatings on Microstructure and Thermal Conductivity of Diamond/Cu Composites Prepared by Vacuum Hot Pressing," Surf. Coat. Technol., 277, pp. 299–307.
[751] Wang, S., Zhu, S., Cheng, J., Qiao, Z., Yang, J., and Liu, W., 2017, "Microstructural, Mechanical and Tribological Properties of Al Matrix Composites Reinforced with Cu Coated Ti3AlC2," J. Alloys Compd., 690, pp. 612–620.
[752] Kruth, J.-P., Levy, G., Klocke, F., and Childs, T. H. C., 2007, "Consolidation Phenomena in Laser and Powder-Bed Based Layered Manufacturing," CIRP Ann., 56(2), pp. 730–759.
[753] Nadammal, N., Mishurova, T., Fritsch, T., Serrano-Munoz, I., Kromm, A., Haberland, C., Portella, P. D., and Bruno, G., 2021, "Critical Role of Scan Strategies on the Development of Microstructure, Texture, and Residual Stresses during Laser Powder Bed Fusion Additive Manufacturing," Addit. Manuf., 38.
[754] Wan, H. Y., Zhou, Z. J., Li, C. P., Chen, G. F., and Zhang, G. P., 2018, "Effect of Scanning Strategy on Grain Structure and Crystallographic Texture of Inconel 718 Processed by Selective Laser Melting," J. Mater. Sci. Technol., 34(10), pp. 1799–1804.
[755] Thijs, L., Kempen, K., Kruth, J.-P., and Van Humbeeck, J., 2013, "Fine-Structured Aluminium Products with Controllable Texture by Selective Laser Melting of Pre-Alloyed AlSi10Mg Powder," Acta Mater., 61(5), pp. 1809–1819.

[756] Scipioni Bertoli, U., MacDonald, B. E., and Schoenung, J. M., 2019, "Stability of Cellular Microstructure in Laser Powder Bed Fusion of 316L Stainless Steel," Mater. Sci. Eng. A, 739, pp. 109–117.
[757] Cheng, M., Xiao, X., Luo, G., and Song, L., 2021, "Integrated Control of Molten Pool Morphology and Solidification Texture by Adjusting Pulse Duration in Laser Additive Manufacturing of Inconel 718," Opt. Laser Technol., 142.
[758] Hagihara, K., Ishimoto, T., Suzuki, M., Ozasa, R., Matsugaki, A., Wang, P., and Nakano, T., 2021, "Factor Which Governs the Feature of Texture Developed during Additive Manufacturing; Clarified from the Study on Hexagonal C40-NbSi2," Scr. Mater., 203.
[759] Zhao, S., Shen, X., Yang, J., Teng, W., and Wang, Y., 2018, "Densification Behavior and Mechanical Properties of Nanocrystalline TiC Reinforced 316L Stainless Steel Composite Parts Fabricated by Selective Laser Melting," Opt. Laser Technol., 103, pp. 239–250.
[760] Langi, E., Zhao, L. G., Jamshidi, P., Attallah, M. M., Silberschmidt, V. V., Willcock, H., and Vogt, F., 2021, "Microstructural and Mechanical Characterization of Thin-Walled Tube Manufactured with Selective Laser Melting for Stent Application," J. Mater. Eng. Perform., 30(1), pp. 696–710.
[761] Murkute, P., Pasebani, S., and Isgor, O. B., 2019, "Production of Corrosion-Resistant 316L Stainless Steel Clads on Carbon Steel Using Powder Bed Fusion-Selective Laser Melting," J. Mater. Process. Technol., 273.
[762] Hong, Y., Zhou, C., Zheng, Y., Zhang, L., and Zheng, J., 2021, "The Room Temperature Creep of Selective Laser Melted 316L Stainless Steel Investigated by Nanoindentation," J. Mater. Eng. Perform., 30(9), pp. 6502–6510.
[763] Tjong, S. C., 2007, "Novel Nanoparticle-Reinforced Metal Matrix Composites with Enhanced Mechanical Properties," Adv. Eng. Mater., 9(8), pp. 639–652.
[764] Mussatto, A., Groarke, R., Vijayaraghavan, R. K., Obeidi, M. A., McNally, P. J., Nicolosi, V., Delaure, Y., and Brabazon, D., 2022, "Laser-Powder Bed Fusion of Silicon Carbide Reinforced 316L Stainless Steel Using a Sinusoidal Laser Scanning Strategy," J. Mater. Res. Technol., 18, pp. 2672–2698.
[765] Qiu, C., Kindi, M. A., Aladawi, A. S., and Hatmi, I. A., 2018, "A Comprehensive Study on Microstructure and Tensile Behaviour of a Selectively Laser Melted Stainless Steel," Sci. Rep., 8(1).
[766] Yin, H., Song, M., Deng, P., Li, L., Prorok, B. C., and Lou, X., 2021, "Thermal Stability and Microstructural Evolution of Additively Manufactured 316L Stainless Steel by Laser Powder Bed Fusion at 500–800 °C," Addit. Manuf., 41.
[767] Lippold, J. C., 2015, *Welding Metallurgy and Weldability*, John Wiley & Sons, New Jersey.
[768] Upadhyay, M. V., Slama, M. B. H., Gaudez, S., Mohanan, N., Yedra, L., Hallais, S., Héripré, E., and Tanguy, A., 2021, "Non-Oxide Precipitates in Additively Manufactured Austenitic Stainless Steel," Sci. Rep., 11(1).
[769] Folkhard, E., 2012, *Welding Metallurgy of Stainless Steels*, Springer Science & Business Media, Vienna, Austria.
[770] Dutta Majumdar, J., Kumar, A., and Li, L., 2009, "Direct Laser Cladding of SiC Dispersed AISI 316L Stainless Steel," Tribol. Int., 42(5), pp. 750–753.
[771] Dilip, J. J. S., Zhang, S., Teng, C., Zeng, K., Robinson, C., Pal, D., and Stucker, B., 2017, "Influence of Processing Parameters on the Evolution of Melt Pool, Porosity, and Microstructures in Ti-6Al-4V Alloy Parts Fabricated by Selective Laser Melting," Prog. Addit. Manuf., 2(3), pp. 157–167.

[772] Wakai, Y., Ogura, T., Nakano, S., Sato, N., Kajino, S., and Suzuki, S., 2020, "Melting Behavior in Laser Powder Bed Fusion Revealed by in Situ X-Ray and Thermal Imaging," Int. J. Adv. Manuf. Technol., 110(3), pp. 1047–1059.
[773] Fan, Z., Lu, M., and Huang, H., 2018, "Selective Laser Melting of Alumina: A Single Track Study," Ceram. Int., 44(8), pp. 9484–9493.
[774] Fischer, R., Ting, A., DiComo, G., Prosser, J., Peñano, J., Hafizi, B., and Sprangle, P., 2009, "Absorption and Scattering of 1.06 Um Laser Radiation from Oceanic Aerosols," Appl. Opt., 48(36), pp. 6990–6999.
[775] Semak, V. V., Gerakis, A., and Shneider, M. N., 2019, "Measurement of Temperature Dependent Absorption Coefficient of Water at 1064nm Wavelength," AIP Adv., 9(8).
[776] Putri, K. Y., Yulianto, N., and Herbani, Y., 2017, "Study on Acoustic Detections of Nd:YAG Laser Induced Breakdown at Different Wavelengths," J. Phys. Conf. Ser., 817.
[777] Ho, J. R., Grigoropoulos, C. P., and Humphrey, J. a. C., 1995, "Computational Study of Heat Transfer and Gas Dynamics in the Pulsed Laser Evaporation of Metals," J. Appl. Phys., 78(7), pp. 4696–4709.
[778] Matthews, M. J., Guss, G., Khairallah, S. A., Rubenchik, A. M., Depond, P. J., and King, W. E., 2016, "Denudation of Metal Powder Layers in Laser Powder Bed Fusion Processes," Acta Mater., 114, pp. 33–42.
[779] Sun, Z., Tan, X., Tor, S. B., and Chua, C. K., 2018, "Simultaneously Enhanced Strength and Ductility for 3D-Printed Stainless Steel 316L by Selective Laser Melting," NPG Asia Mater., 10(4), pp. 127–136.
[780] Zhao, C., Fezzaa, K., Cunningham, R. W., Wen, H., De Carlo, F., Chen, L., Rollett, A. D., and Sun, T., 2017, "Real-Time Monitoring of Laser Powder Bed Fusion Process Using High-Speed X-Ray Imaging and Diffraction," Sci. Rep., 7(1), p. 3602.
[781] Liu, S. Y., Li, H. Q., Qin, C. X., Zong, R., and Fang, X. Y., 2020, "The Effect of Energy Density on Texture and Mechanical Anisotropy in Selective Laser Melted Inconel 718," Mater. Des., 191.
[782] Weingarten, C., Buchbinder, D., Pirch, N., Meiners, W., Wissenbach, K., and Poprawe, R., 2015, "Formation and Reduction of Hydrogen Porosity during Selective Laser Melting of AlSi10Mg," J. Mater. Process. Technol., 221, pp. 112–120.
[783] Haiyan, G., Xiaoming, R., Jianguo, S., Wang, C., Baode, S., Qing, Z., Jun, W., and Zili, L., 2012, *Fe-X-C Crystal Grain Refiner and Preparation Method Thereof*, Patent Number CN102277523B, Shanghai Jiaotong University, Baoshan Iron and Steel Co Ltd, China.
[784] Kusoglu, I. M., Gökce, B., and Barcikowski, S., 2020, "Use of (Nano-)Additives in Laser Powder Bed Fusion of Al Powder Feedstocks: Research Directions within the Last Decade," Procedia CIRP, 94, pp. 11–16.
[785] Fan, Z., Gao, F., Wang, Y., Men, H., and Zhou, L., 2022, "Effect of Solutes on Grain Refinement," Prog. Mater. Sci., 123(A Festschrift in Honor of Brian Cantor).
[786] Matlock, D. K., and Speer, J. G., 2010, "Processing Opportunities for New Advanced High-Strength Sheet Steels," Mater. Manuf. Process., 25(1–3), pp. 7–13.
[787] Watari, T., Nansai, K., and Nakajima, K., 2021, "Major Metals Demand, Supply, and Environmental Impacts to 2100: A Critical Review," Resour. Conserv. Recycl., 164.
[788] Salvo, C., Mangalaraja, R. V., Udayabashkar, R., Lopez, M., and Aguilar, C., 2019, "Enhanced Mechanical and Electrical Properties of Novel Graphene Reinforced Copper Matrix Composites," J. Alloys Compd., 777, pp. 309–316.

[789] Gao, S., Nan, Z., Li, Y., Zhao, N., Liu, Q., Xu, G., Cheng, X., and Yang, J., 2020, “Copper Matrix Thermal Conductive Composites with Low Thermal Expansion for Electronic Packaging,” Ceram. Int., 46(11, Part A), pp. 18019–18025.
[790] Sillani, F., de Gasparo, F., Schmid, M., and Wegener, K., 2021, “Influence of Packing Density and Fillers on Thermal Conductivity of Polymer Powders for Additive Manufacturing,” Int. J. Adv. Manuf. Technol., 117(7), pp. 2049–2058.
[791] Ummartyotin, S., Bunnak, N., Juntaro, J., Sain, M., and Manuspiya, H., 2012, “Synthesis of Colloidal Silver Nanoparticles for Printed Electronics,” Comptes Rendus Chim., 15(6), pp. 539–544.
[792] Luo, D., Xiao, Y., Hardwick, L., Snell, R., Way, M., Sanuy Morell, X., Livera, F., Ludford, N., Panwisawas, C., Dong, H., and Goodall, R., 2021, “High Entropy Alloys as Filler Metals for Joining,” Entropy, 23(1), p. 78.
[793] Chuang, T. H., Tsao, L. C., Tsai, T. C., Yeh, M. S., and Wu, C. S., 2000, “Development of a Low-Melting-Point Filler Metal for Brazing Aluminum Alloys,” Metall. Mater. Trans. A, 31(9), pp. 2239–2245.
[794] Muhrat, A., Puga, H., and Barbosa, J., 2018, “Low-Temperature Brazing of Titanium Using Al-Based Filler Alloys,” Adv. Mater. Sci. Eng., 2018.
[795] Way, M., Willingham, J., and Goodall, R., 2020, “Brazing Filler Metals,” Int. Mater. Rev., 65(5), pp. 257–285.
[796] Zavala-Arredondo, M., Boone, N., Willmott, J., Childs, D. T. D., Ivanov, P., Groom, K. M., and Mumtaz, K., 2017, “Laser Diode Area Melting for High Speed Additive Manufacturing of Metallic Components,” Mater. Des., 117, pp. 305–315.
[797] Li, N., Liu, W., Wang, Y., Zhao, Z., Yan, T., Zhang, G., and Xiong, H., 2021, “Laser Additive Manufacturing on Metal Matrix Composites: A Review,” Chin. J. Mech. Eng., 34(1), p. 38.
[798] Jadhav, S. D., Dhekne, P. P., Brodu, E., Van Hooreweder, B., Dadbakhsh, S., Kruth, J.-P., Van Humbeeck, J., and Vanmeensel, K., 2021, “Laser Powder Bed Fusion Additive Manufacturing of Highly Conductive Parts Made of Optically Absorptive Carburized CuCr1 Powder,” Mater. Des., 198.
[799] Gu, D., Yang, Y., Xi, L., Yang, J., and Xia, M., 2019, “Laser Absorption Behavior of Randomly Packed Powder-Bed during Selective Laser Melting of SiC and TiB2 Reinforced Al Matrix Composites,” Opt. Laser Technol., 119.
[800] Constantin, L., Kraiem, N., Wu, Z., Cui, B., Battaglia, J.-L., Garnier, C., Silvain, J.-F., and Lu, Y. F., 2021, “Manufacturing of Complex Diamond-Based Composite Structures via Laser Powder-Bed Fusion,” Addit. Manuf., 40.
[801] Lahoz, R., Natividad, E., Mayoral, Á., Rentenberger, C., Díaz-Fernández, D., Félix, E. J., Soriano, L., Kautek, W., and Bomati-Miguel, O., 2020, “Pursuit of Optimal Synthetic Conditions for Obtaining Colloidal Zero-Valent Iron Nanoparticles by Scanning Pulsed Laser Ablation in Liquids,” J. Ind. Eng. Chem., 81, pp. 340–351.
[802] Jiménez, A., Bidare, P., Hassanin, H., Tarlochan, F., Dimov, S., and Essa, K., 2021, “Powder-Based Laser Hybrid Additive Manufacturing of Metals: A Review,” Int. J. Adv. Manuf. Technol., 114(1), pp. 63–96.
[803] Walachowicz, F., Bernsdorf, I., Papenfuss, U., Zeller, C., Graichen, A., Navrotsky, V., Rajvanshi, N., and Kiener, C., 2017, “Comparative Energy, Resource and Recycling Lifecycle Analysis of the Industrial Repair Process of Gas Turbine Burners Using Conventional Machining and Additive Manufacturing,” J. Ind. Ecol., 21(S1), pp. S203–S215.

[804] Bidare, P., Jiménez, A., Hassanin, H., and Essa, K., 2021, “Porosity, Cracks, and Mechanical Properties of Additively Manufactured Tooling Alloys: A Review,” Adv. Manuf.
[805] Rahito, Wahab, D. A., and Azman, A. H., 2019, “Additive Manufacturing for Repair and Restoration in Remanufacturing: An Overview from Object Design and Systems Perspectives,” Processes, 7(11), p. 802.
[806] Aswal, V. K., Jain, J. K., and Sonia, P., 2021, “Review on the Behavior of Various Parameters on Heat Distribution in the SAW Process,” Mater. Today Proc., 47, pp. 6734–6739.
[807] Baghel, A., Sharma, C., Rathee, S., and Srivastava, M., 2021, “Influence of Activated Flux on Micro-Structural and Mechanical Properties of AISI 1018 during MIG Welding,” Mater. Today Proc., 47, pp. 6947–6952.
[808] Obeidi, M. A., Conway, A., Mussatto, A., Dogu, M. N., Sreenilayam, S. P., Ayub, H., Ahad, I. U., and Brabazon, D., 2022, “Effects of Powder Compression and Laser Re-Melting on the Microstructure and Mechanical Properties of Additively Manufactured Parts in Laser-Powder Bed Fusion,” Results Mater., 13.